Precision measurement of neutrino oscillation parameters at INO ICAL

By

Lakshmi S Mohan
Enrolment Number : PHYS01200904008
Bhabha Atomic Reseaarch Centre
Mumbai - 400 085

A thesis submitted to
The Board of Studies in Physical Sciences

In partial fulfillment of requirements
For the Degree of
DOCTOR OF PHILOSOPHY
of
HOMI BHABHA NATIONAL INSTITUTE

October, 2015

Homi Bhabha National Institute

Recommendations of the Viva Voce Board

As members of the Viva Voce Board, we certify that we have read the dissertation prepared by **Lakshmi S Mohan** (PHYS01200904008) entitled "Precision measurement of neutrino oscillation parameters at INO ICAL" and recommend that it may be accepted as fulfilling the dissertation requirement for the Degree of Doctor of philosophy.

Date:

Chairman -

Date:

Guide / Convener -

Date:

Member 1 -

Date:

Member 2 -

Date:

Member 3 -

Date:

External Examiner -

Final approval and acceptance of this dissertation is contingent upon the candidate's submission of the final copies of the dissertation to HBNI.

I hereby certify that I have read this dissertation prepared under my direction and recommend that it may be accepted as fulfilling the dissertation requirement.

Date:

Place: Guide

STATEMENT BY AUTHOR

This dissertation has been submitted in partial fulfillment of requirements for an advanced degree at Homi Bhabha National Institute (HBNI) and is deposited in the Library to be made available to borrowers under rules of the HBNI.

Brief quotations from this dissertation are allowable without special permission, provided that accurate acknowledgement of source is made. Requests for permission for extended quotation from or reproduction of this manuscript in whole or in part may be granted by the Competent Authority of HBNI when in his or her judgement the proposed use of the material is in the interests of scholarship. In all other instances, however, permission must be obtained from the author.

Lakshmi S Mohan

(Enrolment Number : PHYS01200904008)

Date:

Place:

Declaration

I hereby declare that the investigation presented in the thesis has been carried out by me. The work is original and has not been submitted earlier as a whole or in part for a degree/diploma at this or any other Institution/University.

Lakshmi S Mohan

(Enrolment Number : PHYS01200904008)

Date:

Place:

Dedicated to

My Parents

ACKNOWLEDGEMENTS

Dreams and aspirations

I honestly don't know where to start this acknowledgement. I am wordless right now to express the depth of my gratitude to all the people who have guided, supported, pushed, pulled and cared for an ordinary girl who just wanted to do Physics all her life. And the girl was lucky enough to have joined the most ambitious basic science projects in India and be part of a huge academic family aka the INO collaboration. :)

No words will be sufficient enough to express how lucky I feel to have been guided by Prof. D. Indumathi, IMSc, one of the most brilliant Physicists I have ever known. Without the excellent guidance Ma'am gave and the support both academic and personal and her loving care, I would never have reached this point. Ma'am's wisdom and knowledge are unparalleled and farsighted nature and prudence, something to learn from. I express, from the bottom of my heart, my many thanks and gratitude to Indu Ma'am, for being kind, patient and loving to an ordinary student like me and for the immense support and motivation all throughout this PhD period. Thank you Ma'am for being my guide and light all these years.

I thank Prof. M.V.N.Murthy, IMSc, for all the guidance given to us young students. As the co-ordinator of the hadron group of the INO ICAL collaboration he gave us the opportunity to work under his guidance. Again the guidance and care Prof. Murthy gave cannot be expressed in words. The neutrino physics lectures he used to give us on Saturdays were really memorable. I express my heartfelt gratitude and thanks to Prof.M.V.N.Murthy for the great guidance and support he gave to a budding student. Again words will not be enough to express my gratitude.

I thank Prof.Nita Sinha, IMSc for the care and support she has given me as a student. I also express my heartfelt thanks to Prof. G. Rajasekharan, IMSc and CMI, for being an inspiration to a young student like me. I was lucky enough to be part of the INO collaboration and work in the Institute of Mathematical Sciences and interact with these great scientists and teachers.

I thank my doctoral committee members, Prof.James Libby, IITM and Prof. Prafulla Behera IITM, for the timely advises and comments and support. Being in a collaboration is a great experience. INO is special in that it gave me an opportunity to go to several institutes and work there. That also means that I had the opportunity to be taught by

many amazing scientists. In the Tata Institute of Fundamental Reseaarch (TIFR) Mumbai, where I did my PhD course work, I was taught by some of the most amazing scientists. I thank Prof. Naba K Mondal, INO project director for all the guidance and support he has offered not only as the director of such a mega science project but also as an enthusiastic teacher who used to spend time discussing detector physics with us in the first year of PhD. Prof. Mondal's great dedication to science is inspirational and the ease with which he sees the whole picture of an analysis and makes the right comments can only come with experience and passion to science. Thank you Sir for being so energetic and caring. I express my heartfelt gratitude to Prof. Amol Dighe, who not only taught us neutrino physics during course work, but also happened to be my collaborator's guide and one of the coordinators of the ICAL physics group. His classes were really enjoyable. Being a member of the hadron group, I got the opportunity to discuss with him even though a little. Thank you Sir, for all the kind suggestions both in the discussions and in the physics meetings and careful readings of all the drafts.

I express my heartfelt gratitude to Prof. Gobinda Majumder, who taught us during our course work and is the author of the ICAL simulation code which we students have been using for all the PhD works. I thank Prof. Majumder for all the prompt help and clarifications he has given regarding detector simulations during the PhD time. I thank Prof.Kajari Mazumdar, Prof. Vandana Nanal, Prof. R.G.K Pillai, Prof. Sudeshna Banerjee, TIFR, and Prof. L.M.Pant, BARC, who taught us and enlightened us on various fields during our course work in the first year of PhD and cared for us. I express my heartfelt thanks to Dr. Satyanarayana Bheesette, for being our mentor and for all the care and support bestowed on students.

I express my gratitude to Prof. Md. Naimuddin, Delhi university and Prof. Prafulla Behera, IITM, for co-ordinating all the detector simulation meetings and all the suggestions and discussions regarding detector simulations. I express my heartfelt thanks to Prof.Amol Dighe, TIFR and Prof.Srubabati Goswami, PRL, for co-ordinating the physics simulation meetings and the wise suggestions and comments. I also thank Prof. Sandhya Choubey, earlier coordinator of physics group along with Prof.D. Indumathi, and a member of the hadron simulations group, for the suggestions and comments and support. I thank Prof.Y. P. Viyogi, VECC; Prof. Vivek Datar, BARC and Prof. Brajesh Choudhary, Delhi University for the careful reading, suggestions and comments on the hadron simulation reports. I also express my thanks to Prof. Uma Shankar, IITB; Prof. Satyajit Saha,

SINP and Prof. Sanjib Kumar Agarwalla, IOP. I express my heartfelt thanks to Ms.Asmita Redij, for the development of the ICAL simulation code and the clarifications she would offer.

I express my thanks to the scientific staff in TIFR involved with the R&D of RPCs, Mr. S. Kalmani, Mr. L. V Reddy, Mr.Ravindra R Shinde, Mr. Mandar Saraf, Mr. Manas Bhuyan, Mr. S. Chavan, Mr. G. Ghodke and Mr. P. Nagraj, Ms. N. Srivastava and Mr. V. Pavan Kumar for all the computer related helps in TIFR. I have to express my heartfelt gratitude towards the system administrators of the Institute of Mathematical Sciences, Sri.G. Subramoniam and Sri. Raveendra Reddy B, for the amazing computing facilities, enabling fast and efficient computing. I express my gratitude to Sri.Mangala Pandi, project system administrators, IMSc for all the prompt help regarding the cluster machines in IMSc were I used to run all the simulations required for my work. I express my heartfelt thanks to Mr. Srinivasan and Mr. Jahir Hussain, technical assistants, computer section for all the help they have given regarding all kinds of computers and computing. Without the excellent clusters of IMSc my PhD would not have been a reality! Bravo Satpura6!

At this point I express my gratitude to all members of the INO collaboration who have been lending their direct and indirect support and care all throughout. INO collaboration meetings were all memorable and it was a great experience being part of the collaboration being able to interact with so many people and learn from them. I also express my heartfelt thanks to the administrative staff of both TIFR and IMSc for taking care of all our official matters, be it salary or accommodation or anything else and giving all the support so that we could do our research work without bothering about anything else. I thank the Department of Atomic Energy (DAE), India and the Department of Science and Technology (DST), India for jointly funding this research.

I thank with great respect all the teachers who have taught me in school, college and university. Without their guidance and support I would not have made it to the beginning of the PhD. I express my heartfelt thanks to Prof.K. Indulekha, Prof. C. Venugopal and Prof. N.V.Unnikrishnan, Mahatma Gandhi University, for the care and support given to me as a student. I humbly bow my head in the memories of Late. Prof. G.V.Vijayagovindan M.G.University and Late. Prof. Rahul Basu, IMSc, who guided me to high energy physics and whom I will always remember with great respect.

I express my special thanks to my student collaborators Moon Moon Devi, Dr. Anushree

Ghosh, and Daljeet Kaur. It was pleasure working with you all. Moon Moon thank you for being my friend apart from being a great collaborator and for being there to push, pull, scold, support, love and care in times of need and for that nudge you would give for making me confident enough to be independent. I express my heartfelt thanks to Kanishka Rawat, for being a steadfast friend and for all the love and care she has given me again in times of need. Again, thanks to my two great pillars of support Moon Moon and Kanishka for being those strong friends who not only gave me the gift of friendship, but to whom I could give the gift of friendship and care as well.

Friends are those who keep life colourful. I thank my INO student friends Meghna, Mathimalar, Neha, Animesh, Sumanta, Vivek, Nitali, Anushree, Sudeshna, Chandan, Amina, Raveendra, Rajesh Ganai, Varchaswi, Ali, Abhik and Deepak for being part of this INO student family. A very special thanks to Dr.Saveetha and Senthil, IMSc, for being friends and members of the IMSc group. Also special thanks to the students in the Chennai group Meghna, Divya, Aleena, Rebin and Saddique. Special thanks to Dr. Susnata Seth, Post Doc at TIFR. I also thank Dr.Shreedevi K Masuti, Dr.Pradeesha Ashok and Sruthi Murali who were my flat mates in IMSc. The times I spent with you as flatmates are memorable and will be missed. Thank you deeply for the love and care you all kindly bestowed on me. I also thank Sriluckshmy P V, my flatmate and research scholar in IMSc. I cannot end the list of friends I want to acknowledge without mentioning Dr.Meenadevi, Debasmita Mukherjee, Ria Sain, Jilmy, Minati, Tanmay Mitra and Dr.Jaya Maji and baby Arama, who have been kind enough to be my friends in IMSc. I also thank Abhrajit Laskar and Rajesh Singh, my office mates for being studious and hard working, looking at whom I could come back on track if ever I felt like slacking off.

This comes last, nevertheless very important, for family is what keeps you firm and extends all love and care always. I thank my family for the biggest support anybody could ever give. Words won't be sufficient to express how deeply I am indebted to my parents Sri.R. Mohanachandran and Smt.N. S. Sandhyakumari. All my urge to study has come from them only. As a kid I used to make them tell me about their younger days and unknowingly picked up the lesson that they came up in life because of their education. My parents took all the best efforts to give me the best possible education. I am lucky to have been born as the daughter of such loving parents. Hopefully someday I will make them proud. I also thank my relatives, especially my grandmother and grandaunts who actually supported and gave courage to my parents when they were afraid of sending me

to a distant place for PhD. I thank all my near and distant family members for all the care and support they have given me. Thank you all for being that great support all the time.

An eight year old girl read about the Solar System in a children's magazine special edition. It was so impressive to know that we live on a planet which is part of something bigger. Then in school she learned that the solar system is part of a galaxy and the galaxy is part of the universe and so on. The girl used to dream about roaming in the skies on the clouds or travelling the whole universe touching stars and going inside them and travelling forever enjoying the myriad wonders out there. I am thankful that, that girl has not changed, even though she has grown up and her outer world and life in general have changed. Thankfully she never gave up on her dream and somehow managed to battle obstacles and get past them, difficult they might have been. And she still dreams that someday she will traverse those places in the visible night sky she admires and those invisible places out there.

Thank you Nature, for being so mysteriously beautiful, holding never ending surprises.

LIST OF PUBLICATIONS

- **Published in refereed journals**

1. M.M. Devi, A. Ghosh, D. Kaur, **S.M. Lakshmi**, *et al.*, "Hadron energy response of the Iron Calorimeter de- tector at the India-based Neutrino Observatory", *JINST* **8**, P11003, 2013 [arXiv:1304.5115 [physics.ins-det]].
2. **S.M. Lakshmi**, A. Ghosh, M.M. Devi, D. Kaur, *et al.*, "Simulation studies of hadron energy resolution as a function of iron plate thickness at INO-ICAL", *JINST* **9**, T09003, 2014 [arXiv:1401.2779 [physics.ins-det]].

- **Manuscript in preparation**

1. M.M. Devi, **S.M. Lakshmi**, A. Dighe and D. Indumathi, "The physics reach of ICAL using hadron direction resolution", 2015.
2. **S.M. Lakshmi**, D. Indumathi, N. Sinha, "Probing sensitivities to atmospheric neutrino oscillation parameters by the addition of higher energies in muons and constraining the neutrino-antineutrino flux ratio", 2015.

- **Other publications**

1. **Lakshmi S Mohan** : "Hadron energy response as a function of plate thickness and angular resolution of hadrons at the ICAL detector in INO", abstract, XX DAE-BRNS, High Energy Physics Symposium, January 13-18, 2013, Visva-Bharati, Santiniketan, India.
2. **Lakshmi S Mohan**, For the INO collaboration, "Hadron energy resolution as a function of plate thickness and theta resolution of hadrons at the Iron Calorimeter Detector in India based Neutrino Observatory", Proceedings of NUFACT 2013, IHEP, Beijing, China.
3. Gonzalo Martínez-Lema, **Lakshmi S. Mohan**, Maddalena Antonello and Izabela Kochanek, "Hands on ICARUS: reconstruction of ν_μ charged-current events", Proceedings of Gran Sasso Summer Institute 2014 Hands-On Experimental Underground Physics at LNGS, accepted to be published in Proceedings of Science.

4. S. Ahmed et al., The ICAL collaboration, "Physics Potential of the ICAL detector at the India-based Neutrino Observatory (INO)", arXiv:1505.07380 [physics.ins-det], 2015.

Lakshmi S Mohan

(Enrolment Number : PHYS01200904008)

Date:

Place:

Synopsis

0.1 Introduction

The study of neutrinos is one of the most interesting areas of particle physics today. Although theoretically proposed in 1930 by Pauli [1] as a "desperate remedy" for energy and angular momentum conservation in β-decays, and first experimentally detected in 1956 [2, 3], not much was known about this particle because of its weak interactions and extremely small cross sections, except that there are three flavours of neutrinos corresponding to each flavour of charged leptons and their antiparticles. It was with the discovery of neutrino flavour oscillations [4, 5] in solar [6, 7] and atmospheric neutrinos [8] that the fact that neutrinos have very tiny but non-zero masses of the order of a few electron volts (eV) was proved. Neutrino oscillations cannot occur, according to the Standard Model of Particle Physics, since they are considered massless in this theory. Apart from requiring neutrinos to have different masses, in addition, the flavour states must non-trivially mix in order to observe these flavour oscillations.

The parametrisation of neutrino oscillations has been done using a unitary transformation matrix which connects the flavour eigenstates (i.e., ν_l, where $l = e, \mu, \tau$) with the mass eigenstates (i.e., ν_i, where $i = 1, 2, 3$). This matrix consists of elements which are expressed as functions of three mixing angles θ_{12}, θ_{13} and θ_{23} and the CP violating phase δ_{CP} (the Majorana phases are not considered here). While these three angles determine the oscillation amplitude, the frequency will be determined by the mass squared differences $\Delta m^2_{ij} = m^2_i - m^2_j$. Though solar [6, 7] and reactor neutrino [9, 10] experiments have established neutrino oscillations and determined both the magnitude and sign of the solar mass squared difference Δm^2_{21}, only the magnitude of Δm^2_{32} (or Δm^2_{31}), the atmospheric mass square difference, is known. The determination of the sign of this quantity is an open puzzle in neutrino physics and will determine the type of mass ordering of neutrinos or the neutrino mass hierarchy. The hierarchy is normal (NH) if $m_1 < m_2 < m_3$ and is inverted if $m_3 < m_1 < m_2$ (since it is known that $m_1 < m_2$). Different experiments all over the world are probing different aspects of neutrino oscillations by observing neutrinos from different sources. The latest major discovery in neutrino physics, that the across generation 1–3 mixing angle is not only different from zero, but also reasonably large, i.e., $\theta_{13} \sim 9^\circ$ [11–14] has given a boost to the experiments all over the world especially those probing hierarchy and CP violation [15–17]. It is in regard to the measurement of neutrino mass hierarchy that a magnetised iron calorimeter gains importance due to the fact that it can distinguish between neutrinos and anti-neutrinos by distinguishing the final state leptons and anti-leptons with the help of a magnetic field. Not only can such a detector determine the mass ordering by studying earth matter effects on neutrino oscillations (because the earth being made up of matter behaves differently to neutrinos and anti-neutrinos), but it will enhance the precision on measurements of θ_{23} and $\Delta m^2_{32(31)}$.

The proposed India-based Neutrino Observatory (INO) [18, 19] which will house a 50 kiloton Iron Calorimeter (ICAL) detector in the observatory to be located at the Bodi West Hills, of Theni district Tamil Nadu, will observe atmospheric neutrinos and study their

oscillations. These atmospheric neutrinos produced in the atmosphere by the decay of secondary cosmic rays in the upper atmosphere are in the few GeV energy range (from $\sim$ 0.1 GeV to 500 GeV; with flux falling rapidly as the energy increases). The ICAL detector will consist of three modules of dimension 16 m $\times$ 16 m $\times$ 14.45 m; each module will have magnetic coils to produce a central field of about 1.5 Tesla. There will be 151 horizontal layers of iron plates of thickness 5.6 cm, stacked one above the other with a separation of 4 cm, interspersed with glass resistive plate chambers (RPCs) in the gaps. The iron plates will both act as the passive detector with which the neutrinos (anti-neutrinos) interact and also serve to make the detector an electromagnet. RPCs which are the active detector elements will detect the charged particles produced in the neutrinos (anti-neutrinos) interactions with iron. The charged current interactions of ν_μ and $\overline{\nu_\mu}$ are of main interest in ICAL and the detector is optimised for the detection of μ^- and μ^+, distinguished from each other by means of the magnetic field. In addition to the charged leptons, hadrons are also produced in the interactions which can be used as observables in the neutrino oscillation studies, thus adding to the sensitivity to oscillation parameters. The ICAL may also probe new physics such as CPT violation, help in the search for sterile neutrinos and magnetic monopoles. It opens a possibility of probing dark matter too.

This synopsis gives a brief account of the simulation studies conducted on the response of the ICAL to hadrons; in particular, the sensitivity of ICAL to determine the energy [20, 21] and direction of hadrons propagating through it. These sensitivities, as well as the response of ICAL to muons (which have been studied independently [22]) have been used to conduct a detailed physics simulation on the reach of ICAL with respect to some of the neutrino oscillation parameters including mass hierarchy, Δm^2_{32} and θ_{23}.

0.2 Energy and direction resolutions of hadrons in ICAL

This section describes the GEANT-4 [23] based simulation studies to calibrate the hadron response of ICAL. There can be more than one hadron in a single interaction. Since there is no information on the energy deposition in the RPC, individual hadrons cannot be separated and reconstructed calorimetrically. The only observable that can be used is the number of hits in the hadron shower. The origin of these hadrons is briefly described first.

0.2.1 Neutrino interaction processes

The three broad categories through which ν_μ and $\overline{\nu_\mu}$ interact with iron are, quasi-elastic (QE), resonance (RES) and deep inelastic scattering (DIS). There can be charged current (CC) as well as neutral current (NC) interactions, but the main interest is on charged current interactions of ν_μ and $\overline{\nu}_\mu$ which will produce $\mu^\pm$ and hadrons in the final state. Quasi elastic processes are dominant in the sub-GeV energy range. They do not have any hadrons in the final state in addition to the recoil nucleons. With increase in energy, RES

and DIS become dominant; at a few GeV, DIS becomes the most dominant one. Resonance events mostly contain a single pion in the final state (though a very small fraction may contain multiple pions), whereas DIS events produce multiple hadrons. Neutrino CC and NC events have been generated for these studies using the NUANCE neutrino generator [24]. To reconstruct the energy and direction of a neutrino the energies and directions of the final state particles have to be reconstructed. Unlike muons (which are minimum ionising particles) which leave a clean track in the detector, hadrons in ICAL only shower. The only way to reconstruct hadrons in ICAL is to make use of the shower hit information, the number of hits coding for net energy and the hit position for net direction of all hadrons in the shower.

0.2.2 Hadron energy resolution

The study of the energy resolution of single pions propagated in the ICAL detector simulated in GEANT-4 was first done. Since ICAL consists of two sets of strips in the X and Y directions arranged perpendicular to each other, the (x, y, z) positions of the hits along with the number of hits in both X direction and Y direction separately can be obtained. To avoid false double counting of hits (ghost hits), the maximum of the hits out of those produced in X and Y layers are taken for each event. The simulation studies are confined to single pions only, since pions constitute the majority of hadrons ($\sim 80\%$) in the shower and it has been observed through simulations of $\pi^{\pm}, \pi^0, K^{\pm}, K^0$ and protons of fixed energies propagated through ICAL, that the detector cannot distinguish between different hadrons. The number of hits can be calibrated to the energy of the pion which gives the distribution. The mean number of hits increases with energy and is related to the pion energy by the relation :

$$\bar{n}(E) \;=\; n_0 \left[1 - \exp\left(-E/E_0\right)\right], \tag{1}$$

where n_0 and E_0 are constants. In the 1–15 GeV energy range, the fits yield $n_0 \sim 53$ and $E_0 \sim 24.25$ GeV. In the limit $E \ll E_0$, the relation becomes linear; the hadron energy resolution can then be defined as :

$$\sigma/E \;=\; \Delta E/E \;=\; \Delta n(E)/\bar{n}(E), \tag{2}$$

since energy is calibrated to the number of hits. The energy resolution is obtained by fitting σ/E according to :

$$\frac{\sigma}{E} \;=\; \sqrt{\frac{a^2}{E} + b^2}\,, \tag{3}$$

where a and b are constants.

To determine the energy resolution, both the arithmetic mean and sigma of the actual distribution or the mean and sigma obtained from a functional fit to the hit distribution can be used. It has been observed that the hit distributions are not symmetric at low energies especially below ~ 6 GeV. Hence a Gaussian function cannot fit below this energy.

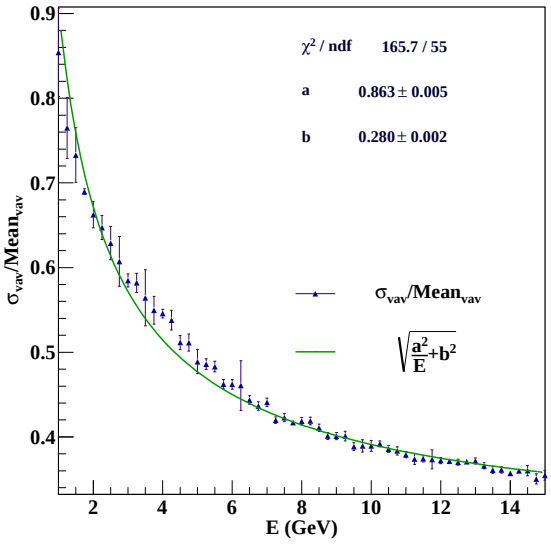

Figure 1: Energy resolution of fixed energy single pions deterined through fits to a Vavilov distribution as a function of incident pion energy in GeV, fitted with Eq. 3.

On the other hand, Vavilov distribution function [25, 26], which estimates the energy loss of particles propagating in moderately thick absorbers like iron fits well to the hadron hit distribution in ICAL which is asymmetric at lower energies. With the increase in energy these become Gaussian in shape. The Vavilov distribution is characterised by two parameters κ and β and approximates to a Landau distribution when $\kappa \leqslant 0.05$ and to a Gaussian for $\kappa \geqslant 10$. The mean and sigma, $Mean_{vav}$ and σ_{vav} are then used in the estimation of single pion energy resolution using Eq. 3. The energy resolution as a function of the pion energy is shown in Fig. 1. The energy resolution varies from 91.7% at 1 GeV to 35.5 % at 15 GeV. This work is reported in detail in Ref. [20].

Energy resolution of hadrons as a function of iron plate thickness

The default plate thickness in ICAL is 5.6 cm and the results discussed in Section 3.5 above were obtained with this default geometry. However it is interesting to study the effect of changing plate thickness on hadron energy resolution since the hadron energy plays a crucial role in enhancing the sensitivity of ICAL to oscillation parameters [27] and any improvement in the hadron energy resolution will further improve ICAL's physics potential. GEANT-4 based simulation studies [21] of fixed energy single pions propagating from vertices randomised in the central region of ICAL were conducted in this regard, using eleven different plate thicknesses including the default value 5.6 cm. The plate thicknesses used were 1.5 cm to 5 cm in steps of 0.5 cm, 5.6 cm, 6 cm and 8 cm respectively, in the hadron energy range 2–15 GeV. It is seen that the mean number of hits increases with increase in energy and decrease in thickness; thus the largest number of hits are for 1.5 cm plate at a given energy. The width of the distribution also follows the same trend, with the histograms becoming more and more symmetric (Gaussian) with smaller thickness and increasing energy. Since the study is confined to the effect of vary-

ing thickness on energy resolution, the arithmetic mean and RMS, $Mean_{arith}$ and σ_{arith} have been used to estimate the responses. The square of Eq. 3 has been used for this analysis, since it is linear in $1/E$; i.e.,

$$\left(\frac{\sigma}{E}\right)^2 = \frac{a^2}{E} + b^2, \tag{4}$$

where a is the stochastic coefficient and b is a constant. The plots of $(\sigma_{arith}/Mean_{arith})^2$ vs $1/E$ fitted with Eq. 4, give the values of a and b for various thicknesses. In the energy range 2–15 GeV, a varies from 0.71 to 0.99 and b from 0.23 to 0.29 respectively.

Thickness dependence can be parametrised in two ways, one in which the thickness dependence is attributed to stochastic coefficient a only and the other in which the dependence of the entire width is studied. The first takes the standard form :

$$a(t) = p_0 t^{p_1} + p_2, \tag{5}$$

where p_2 is the limiting resolution of hadrons for finite energy in the very small thickness limit. In the 2–15 GeV range, the values of $p_i,\ i = 0, 1, 2$, are 0.05, 0.94 and 0.64 respectively. This implies that there is always a residual resolution of hadrons due to the nature of strong interactions, detector geometry and other systematic effects even if the plate thickness is made infinitesimally small. It can be seen that the dependence is not a $\sqrt{t}$ one as shown by the value of p_1. The coefficient p_0 is small and p_2 being fairly large again emphasises the effect of residual resolution on the energy response. Stochastic coefficient a vs plate thickness t (cm), in three different energy range 2–4.75 GeV (low energy), 5–15 GeV (high energy) and 2–15 GeV is shown in Fig. 2. In the alternative approach, the a fit to $\sigma/\sqrt{E}$ is done with the equation:

$$\sigma/\sqrt{E} = q_0 t^{q_1} + q_2. \tag{6}$$

In the 2–15 GeV energy range, fit parameter q_1, the exponent of plate thickness decreases from $\sim$ 0.9 to 0.66, whereas q_0 increases from $\sim$ 0.06 to 0.14 with energy. The constant q_2 increases from $\sim$ 0.65 to 0.98 with energy and this behaviour is similar to that of the the previous approach.

Direction dependence of energy resolution and its thickness dependence has also been studied. As expected the resolution is worse in the horizontal direction and gets better as the direction becomes more vertical, but worse in the most vertical direction contrary to expectation, due to the presence of support structures in this direction and detector specific geometry.

e/h ratio in ICAL

Neutral pions can also be produced in these interactions and they behave differently from charged pions since the former decay electromagnetically. The effect of neutral hadrons

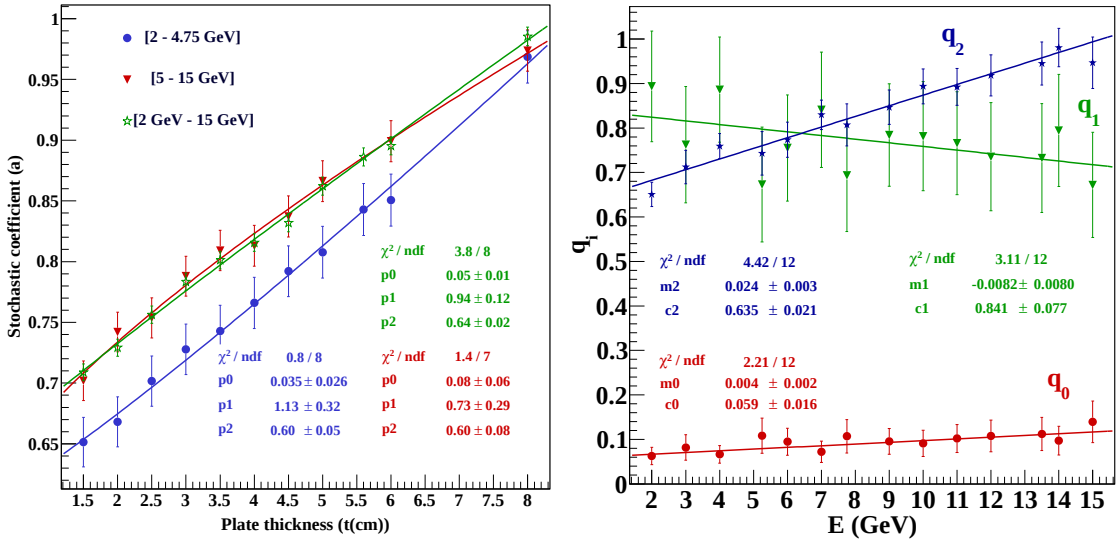

Figure 2: (Left) Thickness dependence of stochastic coefficient a in three different energy ranges and $\sigma/\sqrt{E}$ in the energy range 2–15 GeV. (Right) Values of the fit parameter q_i as defined in Eq. 6 as a function of the energy E.

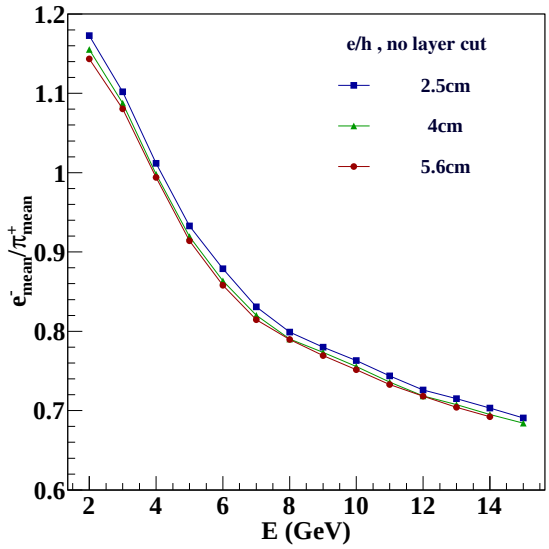

Figure 3: e/h ratio for 2.5, 4 and 5.6 cm thick iron plates as a function of energy in GeV.

on energy resolution is characterised by means of e/h ratio which is the ratio of electron response to charged pion response. GEANT-4 based simulation studies with different thicknesses and fixed energy charged single pions (π^+) and electrons (e^-) is done. The ratio is expressed as :

$$e/h \;=\; e^-_{mean}/\pi^+_{mean}, \tag{7}$$

where e^-_{mean} is the arithmetic mean of electron hit distribution and π^+_{mean} is the arithmetic mean of π^+ hit distribution. A detector with e/h = 1 is compensating. The values of e/h for three sample thicknesses 2.5 cm, 4 cm and 5.6 cm as functions of E (GeV) are shown in Fig. 3. It can be seen that the ratio decreases with energy.

Using the value of e/h obtained from this analysis, the average response of hadrons obtained from charged current muon neutrino interaction in ICAL using the NUANCE neutrino generator can be estimated as :

$$R_{had} \;=\; h\left[(1-F_0)+F_0\times\frac{e}{h}\right], \tag{8}$$

where F_0 is the neutral pion fraction in the sample. Using the values 0.34 for F_0 and 0.9 for an energy averaged e/h respectively, $R_{had} \;=\; 0.97h$, which is not very different from h. This explains why the resolution of multiple hadrons from NUANCE [24] generated neutrino events is almost the same as that of fixed energy single pions as discussed in [20].

The work on the thickness dependence of hadron energy resolution as well as the e/h ratio of ICAL detector are reported in detail in Ref. [21].

0.2.3 Direction resolution of hadron shower in ICAL

Reconstructing the direction of the incident neutrino requires knowing the direction of the final state muon and hadron shower, in charged current interactions. The only usable information regarding hadrons is their hit information and in this case the position information. The direction of hadron shower can be reconstructed using the hit information and timing of the hits by the method named as "raw hit" method. The advantage of this method is that it can be used in the case of both charged current and neutral current events since no charged lepton vertex is needed to reconstruct the direction using this method. The direction is reconstructed by fitting the average hits in XZ plane and YZ plane separately with a straight line. This is done to avoid "ghost hits". The slopes from the fits are used to reconstruct θ and ϕ of the shower using the equations :

$$m_x = r\cos\theta/(r\sin\theta\cos\phi) = \tan\omega \;;\; m_y = r\cos\theta/(r\sin\theta\sin\phi) = \tan\lambda. \tag{9}$$

Thus, θ and ϕ can be obtained as :

$$\tan\phi = \tan\omega/\tan\lambda \;;\; \cot\theta = \tan\omega\;\cos\phi. \tag{10}$$

The slopes m_x and m_y being products of trigonometric functions result in degeneracy in reconstructed direction θ. Timing of the hits is used to break this degeneracy and determine the quadrant of θ.

The simulation studies have been conducted for both fixed energy single pions from GEANT-4 and multiple hadrons from NUANCE generated neutrino events. The former includes studies with both θ and ϕ of the pions fixed and by fixing θ only randomising ϕ over the range 0–2π. The former gives a direction resolution of $\sim 9.01^\circ$ at 2 GeV and 8.5° at 10 GeV in the $\theta = 30^\circ$ and $\phi = 30^\circ$ direction. This is the best resolution for fixed energy single pions with fixed direction. Direction resolution of hadrons was also separately studied elsewhere; there, the techniques could only be applied to charged current muon

events since it was crucial to know the vertex of interaction (obtained from the muon track). The work on hadron direction resoltion will be reported in Ref. [28].

0.3 Physics simulation studies: An improved analysis

Earlier oscillation analyses of ICAL physics, both with observed muon energy and direction $(E_\mu, \cos\theta_\mu)$ [29, 30] and with muon momentum and hadron energy $(E_\mu, \cos\theta_\mu, E'_{had})$ [27] have been conducted only in the observed muon energy range of 1–11 GeV (0.8–10.8 GeV in [29, 30]) and including 10 systematic errors (pulls). These have been named as '2D' and '3D' methods. It is interesting to see the effect of adding higher energy bins in the observed muon energy since ICAL is looking at atmospheric neutrinos. Even though the fluxes are small at these energies, it has been seen in the study discussed here that the higher energy events contribute significantly to the enhancement of sensitivity to oscillation parameters. The analysis is briefly discussed here.

0.3.1 A brief description of the analysis

Since real data is not available, "data" has been simulated and used for analysis. Unoscillated events for 1000 years are generated using NUANCE neutrino generator and scaled down to the required number of years to reduce the effect of fluctuations in theory. The analysis procedure is described briefly here.

1. Generation of events : The events of interest, viz., charged current muon neutrino (anti-neutrino) (CC ν_μ and CC $\overline{\nu}_\mu$) events are generated using NUANCE neutrino generator version 3.5 [24]. Unoscillated events are generated according to the atmospheric neutrino flux at Super Kamiokande (SK) site as calculated in Honda 3D flux table. A very large set of data sample is generated, here for 1000 years, to reduce statistical fluctuations, and then this sample is scaled down to the required number of years for which the analysis has to be carried out.

2. Inclusion of detector responses, efficiencies and oscillations : The detector responses for muon momentum and direction and hadron energy in the central region of the detector, given according to the look-up table prepared by INO collaboration [20, 22] for these quantities have been used for the analysis. The efficiency of detecting each event has been taken as the efficiency with which a muon is reconstructed and this is the same for both 2D and 3D analysis. Charge identification (CID) efficiency has been incorporated to analyse neutrino and anti-neutrino events separately. Events are smeared according to the detector response and are binned into the observed bins. Oscillations are applied to each event, using a 3-flavour oscillation code that accounts in detail for the Earth Matter (PREM) profile [31]. It should be noted that the oscillations are applied on an event-by-event basis.

3. Binning scheme : There are two different analyses, one in which the events are binned in observed muon energy and direction only $(E_\mu, \cos\theta_\mu)$ which is called the 2D analysis and the other in which the bins are in observed $E_\mu, \cos\theta_\mu, E'_{had}$ which is the 3D analysis. The observed muon energy has 15 bins from 0.5–25 GeV as compared to the old 1–11 GeV analyses. The observed muon direction $\cos\theta_\mu$ ranges from -1 to $+1$ in 21 bins and there are 4 hadron energy bins from 0–15 GeV. All bins are non-uniform and are separate for each polarity of muon.

4. χ^2 analysis and addition of extra pull : The χ^2 analysis is done by determining the χ^2 corresponding to each observed bin mentioned above. Since neutrino detection experiments are low counting experiments, Poissonian χ^2 is used to take into account the small number of events per bin. Five systematic errors have been used for each polarity of muon in the analysis using method of pulls [32]: 20% flux normalisation error, 10% cross section error, 5% tilt error, 5% zenith angle error and 5% overall systematics. An extra pull is added in the current analysis as a constraint on the ν_μ-$\overline{\nu}_\mu$ flux ratio which is also found to enhance the physics potential of ICAL.

In the case with just 10 pulls, the Poissonian χ^2 is a sum of the individual χ^2s for μ^+ and μ^- events:

$$\chi^2_\pm = min_{\xi_l^\pm} \sum_{i=1}^{N_{E_\mu^{obs}}} \sum_{j=1}^{N_{\cos\theta_\mu^{obs}}} \left(\sum_{k=1}^{N_{E'^{obs}_{had}}} \right) 2 \left[\left(T^\pm_{ij(k)} - D^\pm_{ij(k)} \right) - D^\pm_{ij(k)} \ln \left(\frac{T^\pm_{ij(k)}}{D^\pm_{ij(k)}} \right) \right] + \sum_{l^\pm=1}^{5} \xi^2_{l^\pm}, \tag{11}$$

where $T^\pm_{ij(k)} = T^{0\pm}_{ij(k)} \left(1 + \sum_{l^\pm=1}^{5} \pi^{l^\pm}_{ij(k)} \xi_{l^\pm} \right)$ is the number of theory (expected) events in each bin with systematic errors, $T^{0\pm}_{ij(k)}$ is the number of theory (expected) events in each bin without systematic errors, $D^\pm_{ij(k)}$ is the number of "data" (observed) events in each bin, i, j, k are the observed bin indices, $\xi_{l^\pm}$ are the pulls, $\pi_{l^\pm}$ are the systematic uncertainties with $l = 1, \ldots, 5$.

For the case when the additional (ξ_6) pull is included, the χ^2 is no longer a sum because of the constraint between μ^+ and μ^- events:

$$\chi^2 = min_{\xi_l^\pm, \xi_6} \sum_{i=1}^{N_{E_\mu^{obs}}} \sum_{j=1}^{N_{\cos\theta_\mu^{obs}}} \left(\sum_{k=1}^{N_{E'^{obs}_{had}}} \right) 2 \left[\left(T^+_{ij(k)} - D^+_{ij(k)} \right) - D^+_{ij(k)} \ln \left(\frac{T^+_{ij(k)}}{D^+_{ij(k)}} \right) \right] +$$
$$2 \left[\left(T^-_{ij(k)} - D^-_{ij(k)} \right) - D^-_{ij(k)} \ln \left(\frac{T^-_{ij(k)}}{D^-_{ij(k)}} \right) \right] + \sum_{l^+=1}^{5} \xi^2_{l^+} + \sum_{l^-=1}^{5} \xi^2_{l^-} + \xi^2_6, \tag{12}$$

where 'D's represent the simulated "data" events as before and *theory* predicts the

observed (T) events as

$$T^{+}_{ij(k)} = T^{0+}_{ij(k)} \left(1 + \sum_{l^+=1}^{5} \pi^{l^+}_{ij(k)} \xi_{l^+} + \pi_6 \xi_6 \right),$$
$$T^{-}_{ij(k)} = T^{0-}_{ij(k)} \left(1 + \sum_{l^-=1}^{5} \pi^{l^-}_{ij(k)} \xi_{l^-} - \pi_6 \xi_6 \right).$$

Here ξ_6 is the 11^{th} pull and constraints the $\mu^+ : \mu^-$ ratio with $\pi_6 = 2.5\%$. Since the new pull acts as a constraint to the $\Phi_{\nu_\mu}/\Phi_{\overline{\nu}_\mu}$ ratio, the expressions for χ^2 from neutrino and anti-neutrino events cannot be written separately.

An 8% prior (at 1σ) on $\sin^2 2\theta_{13}$ is also added to obtain the total χ^2. Hence the total chisq is given as :

$$\chi^2_{ICAL} \;=\; \chi^2_{+} + \chi^2_{-} + \chi^2_{prior}, \tag{13}$$

when there are 10 pulls only and

$$\chi^2_{ICAL} \;=\; \chi^2 + \chi^2_{prior}, \tag{14}$$

when there are 11 pulls. A marginalisation over all the pull variables and over the allowed 3σ regions of the oscillation parameters relevant for atmospheric neutrinos has been carried out to obtain the results.

0.3.2 Precision measurement of θ_{23} and $|\Delta m^2_{eff}|$

The relative precision achieved on a parameter λ (here λ being $\sin^2\theta_{23}$ or Δm^2_{eff}) at 1σ is expressed as :

$$p(\lambda) \;=\; \frac{\lambda_{max-2\sigma} - \lambda_{min-2\sigma}}{4\lambda_{true}}, \tag{15}$$

where $\lambda_{max-2\sigma}$ and $\lambda_{min-2\sigma}$ are the maximum and minimum allowed values of λ at 2σ; λ_{true} is the true choice. Here the effective mass squared difference observed in atmospheric neutrino experiments is defined as :
$\Delta m^2_{\text{eff}} \;\equiv\; \Delta m^2_{31} - \Delta m^2_{21}\,(\cos^2\theta_{12} - \cos\delta_{CP}\sin\theta_{13}\sin 2\theta_{12}\tan\theta_{23})$.
The precisions achievable by ICAL with 500 kton year exposure (10 years of run) in different scenarios are listed in Table 1. The main observation is that the precision measurements improve with the current analysis and is significant in the case of $\sin^2\theta_{23}$ as can be seen from Table 1. The plots for $\Delta\chi^2_{ICAL}$ vs $\sin^2\theta_{23}$ and $|\Delta m^2_{eff}|$ are shown in Fig. 4 for different analyses. The improvement in the precision for ICAL can be seen. Other currently running main experiments measuring the precision of atmospheric neutrino oscillation parameters are MINOS [33] and T2K [34]. This improvement in the precision will contribute to the global analysis of this parameter and related quantities.

Binning Scheme	E_μ^{obs} (GeV)	No.of pulls	$P_{\sin^2\theta_{23}}\%$	$P_{\lvert\Delta m^2_{eff}\rvert}\%$
2D $(E_\mu^{obs}, \cos\theta_\mu^{obs})$	1–11	10	14.40	5.09
	0.5–25*	10	13.00	3.95
	0.5–25*	11	9.35	3.91
3D $(E_\mu^{obs}, \cos\theta_\mu^{obs}, E_{had}^{\prime obs})$	1–11	10	12.85	3.05
	0.5–25*	10	11.25	2.53
	0.5–25*	11	8.90	2.53

Table 1: Precision of $\sin^2\theta_{23}$ and $|\Delta m^2_{eff}|$ at 1σ, in different energy ranges, with different binning schemes and pulls, for 500 kton year exposure of ICAL. Here * are the results of this study; the others represent earlier studies with ICAL.

0.3.3 Sensitivity to mass hierarchy

The ability to distinguish true hierarchy from wrong hierarchy has been quantified as :

$$\Delta\chi^2_{MH} \;=\; \chi^2_{wrongMH} - \chi^2_{trueMH}, \tag{16}$$

where the true and wrong χ^2s are obtained by performing a fit to the "observed" events. Here normal hierarchy (NH) has been assumed as the true hierarchy. The sensitivities are depicted in Fig. 5. As has been pointed out earlier [27], these are sensitive to the values of θ_{13} and completely independent of the CP phase [19]. The addition of higher energy bins in observed muon energy improves both precision of oscillation parameters and mass hierarchy sensitivity. The additional pull significantly improves the precision on $\sin^2\theta_{23}$, but does not much affect that on $|\Delta m^2_{eff}|$ and hierarchy sensitivity. In summary, a more careful simulation analysis of the atmospheric neutrinos events at ICAL indicates that a considerable improvement in precision can be obtained. In particular, it constrains the value of θ_{23} significantly over earlier studies.

A detailed report of the physics analysis will be presented in Ref. [35].

0.4 Summary and future scope

0.4.1 Summary

The ICAL detector at the proposed INO experiment aims to study atmospheric neutrino oscillation parameters by detecting neutrinos produced in Earth's atmosphere. Though ICAL is optimised to detect muons, a great deal of information can be extracted from measuring hadron energy and momentum. Simulation studies of fixed energy single pion using ICAL detector simulated using GEANT-4 simulation packages have been used to estimate the response of hadrons in ICAL and their dependence on plate thickness. The hit distributions fitted with a Vavilov distribution function are seen to correctly reproduce the mean and σ of the distribution; the fit parameters are further used in physics studies to smear hadron energy. The thickness dependence of hadrons in ICAL is not a naive $\sqrt{t}$ dependence but shows that there is a significant "residual" resolution due to the characteristics of strong interactions, fluctuations and detector geometry. Also the e/h ratio

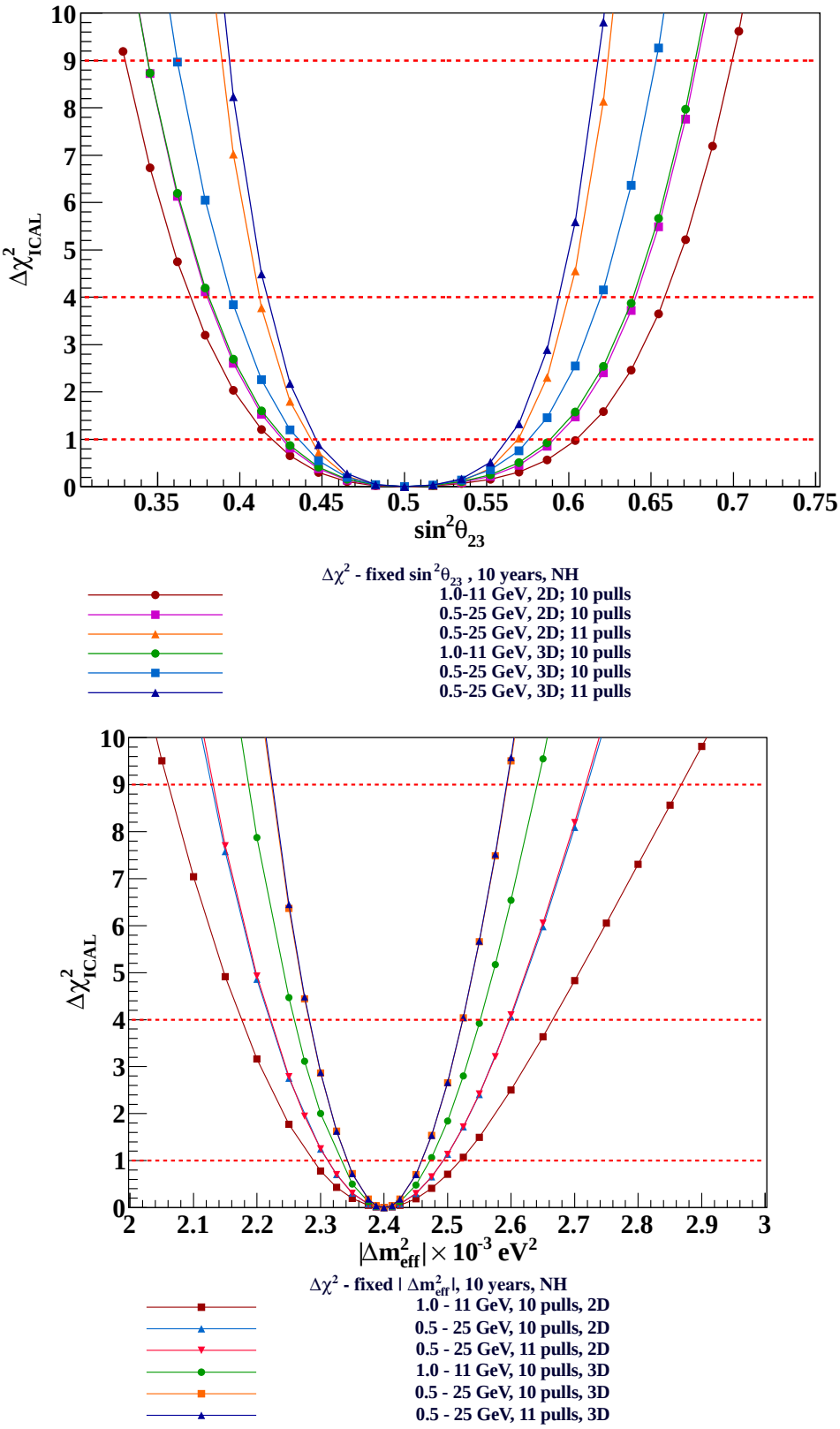

Figure 4: $\Delta\chi^2_{ICAL}$ vs $\sin^2\theta_{23}$ (top) and $\Delta\chi^2_{ICAL}$ vs $|\Delta m^2_{eff}|$ (bottom) for 500 kton year exposure of the ICAL and for different combinations of energy range and pulls, and the exclusion/inclusion of hadron energy information.

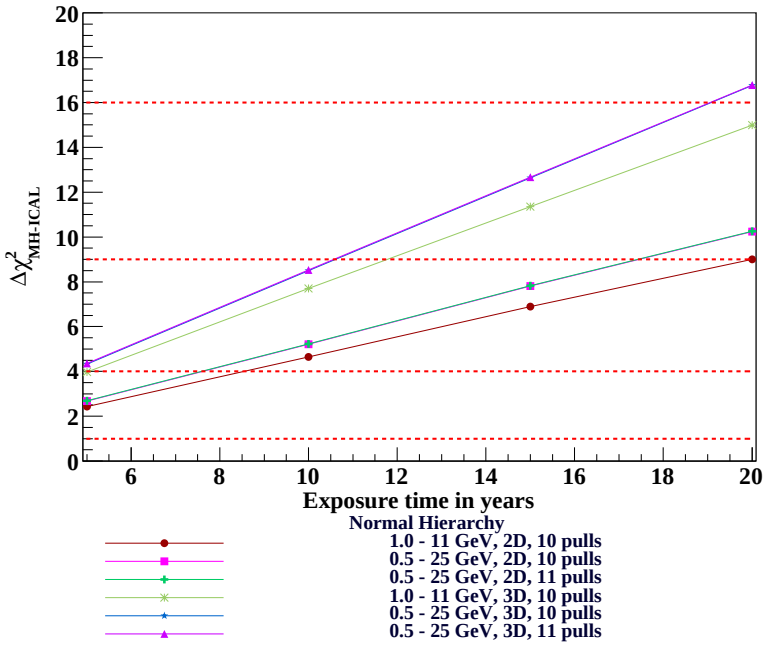

Figure 5: Hierarchy sensitivity for all cases assuming normal hierarchy (NH) as the true hierarchy. It can be seen that the increase in energy range improves the sensitivities for both 2D and 3D cases.

is estimated and used to check the resolution of multiple hadrons from neutrino interactions generated in NUANCE. Direction resolution of hadrons is estimated using "raw hit" method which uses only hadron hit position and timing to reconstruct the direction. Since this method does not require a charged lepton vertex for direction reconstruction, it can be used to reconstruct hadrons from neutral current events also.

The physics potential of ICAL in the higher observed energy range of muons is probed by extending observed muon energy from 0.5–25 GeV over earlier ranges from 1–11 GeV and adding an extra pull as a constraint on $\Phi_{\nu_\mu}/\Phi_{\overline{\nu}_\mu}$ ratio. Precision on both θ_{23} and Δm^2_{32} improves with the extension of the energy range. Hierarchy sensitivity also increases with higher energies. Though $|\Delta m^2_{eff}|$ precision does not improve further by the addition of the new pull, it improves $\sin^2\theta_{23}$ precision significantly. Hierarchy sensitivity is almost unaffected by the new pull.

0.4.2 Future scope

One of the main focuses of the studies reported in this synopsis is the response of hadrons produced in charged current muon neutrino interactions. However, it important to study the responses of electrons also in the ICAL detector since ν_e, $\overline{\nu}_e$ interactions with iron will also occur. As of now the electron shower resolution in ICAL is very poor and only coarsely calibrated. With some electron resolution one can probe in detail if ICAL will be able to see any event in the electron channel. Thus the separation of different types of events in ICAL also becomes important, since they affect the determination of sensitivities from different interaction channels. The proper identification of neutral current events are

also important since they can impact sterile neutrino searches. It is also important to have studies on newer algorithms to determine hadron shower direction in the detector. The effect of reducing strip width on the azimuthal angle (ϕ) determination of hadrons and its effect on the shower direction measurement has to be probed.

The sensitivity studies of ICAL reported here makes use of the atmospheric neutrino flux at Super Kamiokande site. The analysis with the neutrino flux at Theni where the observatory will be located is crucial. These flux tables are just being made available. Also studies on how the improved precisions and hierarchy sensitivities of ICAL can impact the global measurement of neutrino oscillation parameters have to be studied in detail. Sensitivity studies using hadron direction as the fourth observable in the binning scheme can also be probed. Finally, the significant improvement in θ_{23} obtained in this study will surely impact determination of the as-yet unknown octant of this mixing angle.

List of Figures

List of Tables

Abbreviation Notation and Nomenclature

INO	India-based Neutrino Observatory
ICAL	Iron Calorimeter
RPC	Resistive Plate Chamber
l	Lepton flavour (general) e, μ, τ
e	Electron
μ	Muon
τ	tau
ν_l	Neutrino of flavour l
ν_1, ν_2, ν_3	Neutrino mass eigenstates
$\bar{\nu}_l$	Anti-neutrino of flavour l
e^-	Electron
e^+	Positron
μ^-	Muon
μ^-	Anti-muon
p	Proton
n	Neutron
π^+	Positively charged pion
π^-	Negatively charged pion
π^0	Neutral pion
eV	Electron Volt
MeV	Mega electron volt
GeV	Giga electron volt
$\theta_{12}, \theta_{13}, \theta_{23}$	Neutrino mixing angles
Δm^2_{ij}	Neutrino mass squared differences
Δm^2_{eff}	Effective mass squared differences
CP	Charge conjugation and Parity (symmetry)
CPT	Charge conjugation, Parity and Time reversal (symmetry)
NH	Normal hierarchy
IH	Inverted hierarchy
L	Distance travelled by the neutrino
E	Energy of the neutrino
CC	Charged-Current (interaction)
NC	Neutral-Current (interaction)
ccmu	Charged current muon neutrino or anti-neutrino interaction
cce	Charged current electron neutrino or anti-neutrino interaction
ncmu	Neutral current muon neutrino or anti-neutrino interaction
nce	Neutral current electron neutrino or anti-neutrino interaction
QE	Quasi-elastic
RES	Resonance
DIS	Deep inelastic scattering
RH	Raw hit
RHM	Raw hit method
mo	muon only (analysis)
wh	with hadron (analysis)

Part I

Neutrinos and the ICAL detector

1 Introduction

1.1 The invisibles - yet detectable

The story of neutrino dates back to 1930, when Wolfgang Pauli proposed its existence as a "desperate remedy" [1] to save the law of conservation of energy, to correctly interpret the beta decay spectrum [36]. But neutrinos eluded detection till 1956 when they were detected in the experiment conducted by Reines and Cowan [2, 3]. There were still more mysteries to be unraveled in the coming decades of 20th century. The findings about this tiny particle were so astonishing that the urge to know more about it became greater by the day. Several experiments were established all over the world to probe different aspects of neutrinos. The India-based Neutrino Observatory (INO) is a proposed experiment in Bodi West Hills in southern India, which aims to study the properties of atmospheric neutrinos. Prior to understanding the neutrino physics potential of INO, it is necessary to understand some basics of neutrino physics. Let us have a look at it.

1.2 Neutrinos - some basics

The Standard Model of Particle Physics [37–43] has two types of particles in it, quarks and leptons. Each of them are divided into three doublets. The lepton doublets are as follows :

$$\begin{pmatrix} e \\ \nu_e \end{pmatrix} \begin{pmatrix} \mu \\ \nu_\mu \end{pmatrix} \begin{pmatrix} \tau \\ \nu_\tau \end{pmatrix}$$

Electron and its heavier versions have charge whereas neutrinos are charge neutral and in the Standard Model they are considered to be massless. But the fact that neutrinos exhibit flavour oscillations proves that they have mass and the ordering of the three neutrino masses is one of the main focus of neutrino oscillation physics now.

1.2.1 Classification of neutrinos based on sources

Neutrinos are produced in various processes and they can be classified on the basis of their sources. The important thing to remember is that depending on the sources the energies of these neutrinos and the processes by which they are produced vary. The study of the neutrinos from various sources can not only throw light upon the properties of neutrinos themselves but also on the production mechanisms and the sources themselves, especially when they are astrophysical. The sources of neutrinos can be classified as follows based on the energy of the neutrinos emitted from them.

1. **Big bang relic neutrinos** : These are neutrinos formed during Big Bang (BB) and are the second most abundant particles in the universe (the first being photons) with a density of about $\sim 330 cm^{-3}$. Due to their weak interaction, they decoupled from matter after about ~ 1 sec, at a temperature of $\simeq 10^{10}$ Kelvin; i.e., at an energy of ~ 1 MeV. The current energy of these neutrinos is about 1.95 K $\simeq 2 \times 10^{-4}$ eV. The combination of low energy and weak interaction cross section makes their detection very hard [44, 45].

2. **Terrestrial or geo neutrinos** : These are electron anti-neutrinos ($\bar{\nu}_e$) produced by the β decays of long lived natural isotopes like ^{238}U , ^{232}Th and ^{40}K. They have energies < 3 MeV. Study of these neutrinos can throw more light on the radiogenic heat production mechanisms in the Earth, the abundances of heat generating elements in the crust and the mantle and the study of the Earth's core [46].

3. The main sources of neutrinos of MeV energies are nuclear reactors, Sun and supernovae.

   (a) **Reactor neutrinos** : Nuclear reactors used for electric power production use various fissile elements such as ^{235}U, ^{238}Th, ^{239}Pu and ^{241}Pu. The β decay of the fission products produce large fluxes of electron anti-neutrinos $\bar{\nu}_e$ of mean energy ~ 3 MeV. The first experimental proof of neutrinos came from the detection of reactor neutrinos [2, 3].

   (b) **Solar neutrinos** : Sun is a major source of neutrinos which are produced by fusion reactions in the pp chain or the carbon-nitrogen-oxygen (CNO) cycle [47–50]; i.e.,

$$4p \rightarrow^4 He + 2e^+ + 2\nu_e. \tag{1.1}$$

Solar neutrinos have energies in the range of a few MeVs. Their flux at the Earth's surface is $\sim 6 \times 10^{10} cm^{-2} s^{-1}$ for $E_\nu \leqslant 0.42$ MeV and $5 \times 10^{6} cm^{-2} s^{-1}$ for 0.8 MeV $\leqslant E_\nu \leqslant 15$ MeV. The anomaly in the flux of solar neutrinos was the first evidence for neutrino oscillations [51–53].

(c) **Supernovae neutrinos :** These are emitted during the explosion of a supernova; i.e., when a massive star collapses into a neutron star [54, 55]. Majority of the binding energy of the star is radiated as neutrinos of all flavours and of energies 10 – 30 MeV. The emission lasts for a period of several tens of seconds with a luminosity almost 100 times larger than its optical luminosity. The first observed supernovae neutrinos were from 1987A, in the Large Magallenic Cloud galaxy [56–58].

4. The sources of neutrinos in the GeV energy ranges are the Earth's atmosphere and particle accelerators.

(a) **Atmospheric neutrinos** : Atmospheric neutrinos are produced in the Earth's atmosphere by means of cosmic rays [59]. The Kolar Gold Field experiment in India first discovered the atmospheric neutrinos [60]. The first oscillations of atmospheric neutrinos were observed by the Super-K detector in Japan [8]. High energy primary cosmic rays mainly composed of protons interact with the nuclei present in the Earth's atmosphere to produce secondary cosmic rays which consist mainly of pions and kaons. These particles decay into muons and muon neutrinos which further decay into electrons, electron neutrinos and muon neutrinos. The contribution to the neutrinos is mainly due to pion decay whereas kaon decay contributes a small fraction at higher energies. The decay processes are :

$$\pi^- \rightarrow \mu^- + \bar{\nu}_\mu \; ; \; \pi^+ \rightarrow \mu^+ + \nu_\mu; \tag{1.2}$$

$$\mu^- \rightarrow e^- + \nu_e + \bar{\nu}_\mu \; ; \; \mu^+ \rightarrow e^+ + \bar{\nu}_e + \nu_\mu. \tag{1.3}$$

The energy spectrum of these neutrinos peak at ~ 0.25 GeV and falls off as $E^{-2.7}$ as the energy increases. It is also important that the unoscillated flux ratio of ν_μ to that of ν_e, i.e $\Phi_{\nu_\mu}/\Phi_{\nu_e} \simeq 2$ in the GeV region. Typical energies of the atmospheric neutrinos are from about 0.1 MeV – 1000 GeV. Although the absolute flux

of atmospheric neutrinos is about $1\ cm^{-2}s^{-1}$ and the interaction cross sections only $\sim 10^{-38}\ cm^2$, it is worthwhile studying them, because of the wide range of energies and distances offered by them over which neutrino oscillations can be probed.

(b) **Accelerator neutrinos** : These are ν_μ or $\bar{\nu}_\mu$ of GeV ranges produced in particle accelerators where protons are accelerated, hit on a target which produces pions and kaons, which decay in flight inside a magnetic horn to give neutrinos. These magnetic horns help to focus the parent pion or kaon, thus indirectly causing the neutrinos to be emitted in a specific direction as a "beam" and also to selectively produce neutrino or anti-neutrino beams by choosing the parent particle accordingly. The advantage of using accelerator neutrinos is that a large flux of neutrinos can be obtained as compared to the atmospheric neutrinos, even though the oscillation parameters probed in both types of experiments are the same. It should be noted that even though accelerators give a large flux of neutrinos, probes over a wide range of energies and distances are not possible with them, thus making it necessary to tune the detectors precisely.

5. **Galactic and extra galactic neutrinos** : These are neutrinos which are produced as secondary products in the interactions of charged cosmic rays accelerated in shock processes inside the sources such as active galactic nuclei or gamma ray bursts. The decay of the charged pions produced in these hadronic interactions give rise to these ultra high energy neutrinos which travel without getting bent in the galactic magnetic field and hence carry information about the sources. The energy range of these neutrinos are of the order of TeVs and PeVs [61–63].

1.3 Neutrino oscillation physics

According to the Standard Model (SM) of Particle Physics, there are three flavours of neutrinos, namely ν_e, ν_μ, ν_τ (and their anti-particles $\bar{\nu}_e, \bar{\nu}_\mu, \bar{\nu}_\tau$) associated with each charged lepton in the lepton doublet. They are neutral particles, owing to which they experience only weak interactions [64]. In the Standard Model they are assumed to be massless. The detection of neutrinos from several sources like the Sun and the atmosphere showed that the flavour fluxes of neutrinos were not the same as predicted by theory. The only expla-

nation for this discrepancy was that one flavour of neutrinos oscillate to another flavour, which was confirmed by various experiments [7, 65, 66]. Such flavour oscillations can occur only if the neutrinos have masses which are non-zero and different from each other. Neutrinos indeed have masses even though very tiny and various experiments all over the world are trying to study the properties of neutrinos including their masses and mixing. The oscillations and mixing of neutrinos are explained in Section 1.4.

1.4 Three flavour neutrino oscillations

Flavour oscillations of neutrinos were first proposed by B. Pontecarvo [4, 5] in 1950s. In the formalism, the three neutrino flavour states are defined as the linear superpositions of three mass eigenstates; i.e.,

$$|\nu_\alpha\rangle = \sum_i U_{\alpha i}|\nu_i\rangle, \tag{1.4}$$

where $|\nu_\alpha\rangle$ is the flavour state, $\alpha = e, \mu, \tau$ and $|\nu_i\rangle$ is the mass eigenstate, i = 1,2,3 and $U_{\alpha i}$ is the unitary 3 $\times$ 3 mixing matrix called the U_{PMNS} mixing matrix named after Pontecarvo-Maki-Nakagawa-Sakata (PMNS) [67, 68]. The matrix can be written as :

$$U = \begin{pmatrix} c_{12}c_{13} & s_{12}c_{13} & s_{13}e^{-i\delta} \\ -c_{23}s_{12} - s_{23}s_{13}c_{12}e^{i\delta} & c_{23}c_{12} - s_{23}s_{13}s_{12}e^{i\delta} & s_{23}c_{13} \\ s_{23}s_{12} - c_{23}s_{13}c_{12}e^{i\delta} & -s_{23}c_{12} - c_{23}s_{13}s_{12}e^{i\delta} & c_{23}c_{13} \end{pmatrix}, \tag{1.5}$$

where $c_{ij} = \cos\theta_{ij}$, $s_{ij} = \sin\theta_{ij}$; θ_{ij} being the mixing angle between two mass eigenstates i and j; and δ is the CP violating (Dirac) phase. The matrix U diagonalises the 3 $\times$ 3 mass matrix M_ν^2 in the flavour basis (i.e the basis of e, μ, τ) :

$$U^\dagger M_\nu^2 U = \text{diag}(m_1^2, m_2^2, m_3^2), \tag{1.6}$$

where m_i represent the mass eigenstates, i = 1, 2, 3. Hence the fundamental neutrino parameters are the mixing angles θ_{ij}, the CP violating phase δ and the mass squared differences $\Delta_{ij} \equiv m_i^2 - m_j^2$; i, j = 1,2,3. One of the open questions in neutrino physics is the ordering of these masses. Experimental observations have proved that $m_2 > m_1$, but it is not known whether $m_3 \gg m_2$ or $m_3 \ll m_1$. This is known as the neutrino mass hierarchy problem. The case in which $m_3 > m_2 > m_1$ is known as the normal hierarchy (NH) and the other where $m_3 < m_1 < m_2$ (since it is already known that $m_1 < m_2$) is

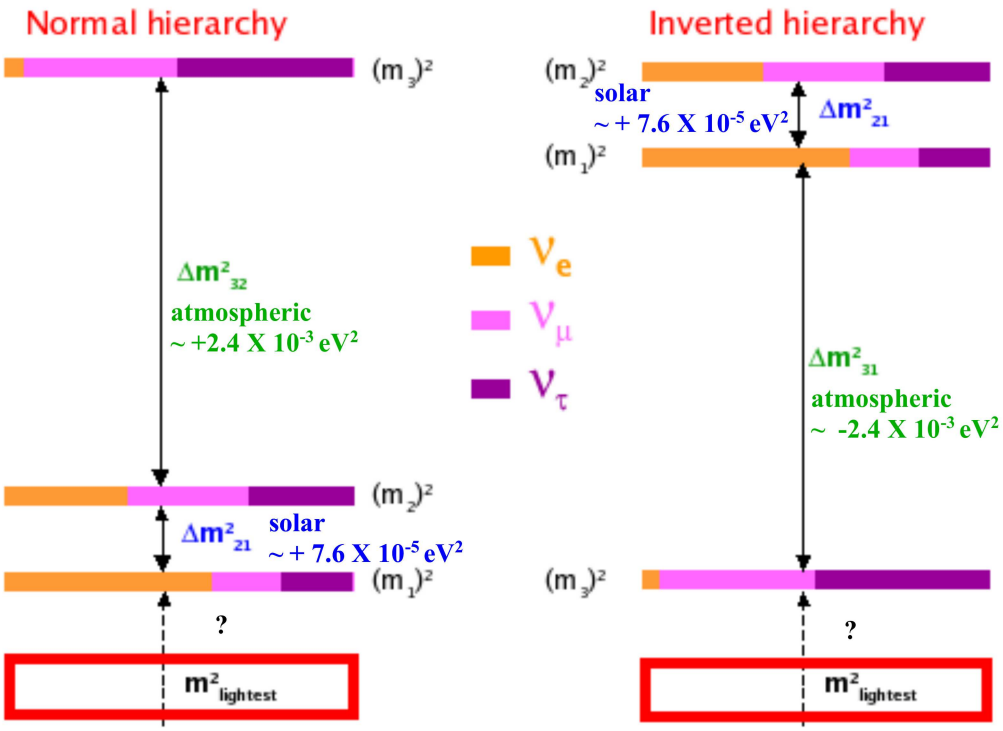

Figure 1.1: Neutrino mass ordering. Absolute zero of the mass scale is also unknown. Picture taken from [69].

known as the inverted hierarchy (IH). This is illustrated in Fig.1.1.

To determine the oscillation parameters, the transition probabilities from one neutrino flavour to the other can be calculated. The time evolution of the mass eigen states governed by Schrödinger equation is:

$$|\nu_i(t)\rangle \;=\; e^{-iE_it}|\nu_i(0)\rangle, \tag{1.7}$$

and consequently the time evolution of flavour states is given by:

$$|\nu_\alpha(t)\rangle \;=\; \sum_{\beta=e,\mu,\tau}\left(\sum_i U_{\alpha i}e^{-iE_it}U^*_{\beta i}\right)|\nu_\beta\rangle. \tag{1.8}$$

Hence the probability $P_{\alpha\beta}$ that a neutrino flavour $|\nu_\alpha\rangle$ of energy E will oscillate to another flavour $|\nu_\beta\rangle$ after travelling a distance L in vacuum is given by :

$$P_{\alpha\beta} \;=\; \delta_{\alpha\beta} - 4\sum_{i>j} Re\left[U_{\alpha i}U^*_{\beta i}U^*_{\alpha j}U_{\beta j}\right]\sin^2\left(\frac{\Delta m^2_{ij}L}{4E}\right) + 2\sum_{i>j} Im\left[U_{\alpha i}U^*_{\beta i}U^*_{\alpha j}U_{\beta j}\right]\sin\left(\frac{\Delta m^2_{ij}L}{2E}\right). \tag{1.9}$$

Similarly the probability $\bar{P}_{\alpha\beta}$ of an anti-neutrino flavour $|\bar{\nu}_\alpha\rangle$ oscillating to a flavour $|\bar{\nu}_\beta\rangle$ in vacuum is :

$$\bar{P}_{\alpha\beta} \;=\; \delta_{\alpha\beta} - 4\sum_{i>j} Re\left[U_{\alpha i}U^*_{\beta i}U^*_{\alpha j}U_{\beta j}\right]\sin^2\left(\frac{\Delta m^2_{ij}L}{4E}\right) - 2\sum_{i>j} Im\left[U_{\alpha i}U^*_{\beta i}U^*_{\alpha j}U_{\beta j}\right]\sin\left(\frac{\Delta m^2_{ij}L}{2E}\right). \tag{1.10}$$

The probability is called "transition probability" when $\alpha \neq \beta$ and "survival probability" when $\alpha = \beta$. The oscillation length L^{osc}_{ij} is defined such that the phase generated by Δm^2_{ij} becomes 2π; i.e.,

$$L^{osc}_{ij} \;=\; \frac{4\pi E}{\Delta m^2_{ij}} \;=\; 2.47\frac{E[MeV]}{\Delta m^2_{ij}[eV^2]}m \;=\; 2.47\frac{E[GeV]}{\Delta m^2_{ij}[eV^2]}km. \tag{1.11}$$

This quantity is used to design a neutrino experiment such that it is maximally sensitive to the parameter to be probed. Thus the energy and distance of the neutrinos required to obtain a certain level of sensitivity can be found out from Eq. 1.11.

1.4.1 Matter effects

Matter effects can alter the transition probabilities when neutrinos propagate through matter. Probing matter effects can help in determining the ordering of the neutrino mass eigenstates (whether it is NH or IH). The transition probabilities get modified when the neutrinos (anti-neutrinos) propagate through matter. The time evolution of neutrinos in the presence of matter is given by the expression :

$$i\frac{d}{dt}[\nu_\alpha] \;=\; \frac{1}{2E}\left[U\mathbb{M}^2U^\dagger + \mathbb{A}\right][\nu_\alpha], \tag{1.12}$$

where $[\nu_\alpha]$ is the flavour eigenstate vector and

$$[\nu_\alpha] = \begin{pmatrix} |\nu_e\rangle \\ |\nu_\mu\rangle \\ |\nu_\tau\rangle \end{pmatrix},\; \mathbb{M}^2 = \begin{pmatrix} 0 & 0 & 0 \\ 0 & \Delta m^2_{21} & 0 \\ 0 & 0 & \Delta m^2_{31} \end{pmatrix},\; \mathbb{A} = \begin{pmatrix} A_{CC} & 0 & 0 \\ 0 & 0 & 0 \\ 0 & 0 & 0 \end{pmatrix}.$$

The matter term (ignoring the diagonal neutral current contribution) is given by

$$A_{CC} \;=\; 2\sqrt{2}G_F n_e E \;=\; 7.63\times10^{-5}\text{eV}^2\;\rho(\text{gm/cc})\;E(\text{GeV}), \tag{1.13}$$

where, G_F is the Fermi constant and n_e is the electron number density in matter and ρ is the matter density. For anti-neutrinos the sign of A_{CC} and the phase δ in Eq. 1.12 get

reversed. Since $\Delta m^2_{21} \ll |\Delta m^2_{31}|$, the approximation $|\Delta m^2_{32}| \approx |\Delta m^2_{31}|$ can be made, making the propagation a single mass scale problem [70]. The modified mixing angles θ^m_{12} and θ^m_{13} in matter can be expressed as :

$$\sin 2\theta^m_{12} \approx \frac{\sin 2\theta_{12}}{\left[\left(\cos 2\theta_{12} - (A_{CC}/\Delta m^2_{21})\cos^2\theta_{13}\right)^2 + \sin^2 2\theta_{12}\right]^{1/2}}, \tag{1.14}$$

and

$$\sin 2\theta^m_{13} = \frac{\sin 2\theta_{13}}{\left[\left(\cos 2\theta_{13} - (A_{CC}/\Delta m^2_{32})\right)^2 + \sin^2 2\theta_{13}\right]^{1/2}}, \tag{1.15}$$

where, θ_{12} and θ_{13} are the vacuum mixing angles. The condition for MSW "resonance" [71, 72] in Eq.1.14 and Eq.1.15 are $\Delta m^2_{21}\cos 2\theta_{12} = A_{CC}\cos^2\theta_{13}$ and $\Delta m^2_{32}\cos 2\theta_{13} = A_{CC}$ respectively. For atmospheric neutrinos of multi GeV energies propagating through the Earth, Eq. 1.15 is more relevant. The term with Δm^2_{21} is negligible when considering the oscillation probability, due to the fact that the coefficient of this term is small [70]. Due to resonance, there is an enhancement in the $\nu_\mu \leftrightarrow \nu_e$ oscillations [33]. The resonance peak is fairly sharp owing to θ_{13} being small. For anti-neutrinos, $A_{CC} \to -A_{CC}$ and the resonance occurs for inverted mass hierarchy (IH), i.e., for $\Delta m^2_{31} < 0$. The sign of Δm^2_{31} is currently unknown; it can be immediately seen that this can be determined by knowing whether resonant-enhanced matter effects occur in the neutrino or anti-neutrino sector. Hence resonance/matter effects can probe the mass hierarchy (actually 2–3 mass ordering). The main effect due to propagation in matter arises due to θ^m_{13}, since $\sin 2\theta^m_{23} \approx \sin 2\theta_{23}$.

For GeV neutrinos, the main channels through which the oscillation studies are conducted are the $\nu_\mu \to \nu_\mu$, $\nu_e \to \nu_\mu$ and the $\nu_\mu \to \nu_e$ channels. The approximate survival probability for ν_μ in constant density matter can be written as:

$$P^m_{\mu\mu} \approx 1 - \sin^2 2\theta_{23}\left[\sin^2\theta^m_{13}\sin^2\Delta^m_{21} + \cos^2\theta^m_{13}\sin^2\Delta^m_{32}\right] - \sin^4\theta_{23}\sin^2 2\theta^m_{13}\sin^2\Delta^m_{31}, \tag{1.16}$$

and the transition probability for $\nu_e \to \nu_\mu$ can be written as:

$$P^m_{e\mu} \approx \sin^2\theta_{23}\sin^2 2\theta^m_{13}\sin^2\Delta^m_{31}, \tag{1.17}$$

where,

$$\Delta_{21}^{m} = \frac{1.27\Delta m_{32}^2 L}{E}\frac{1}{2}\left[\frac{\sin 2\theta_{13}}{\sin 2\theta_{13}^{m}} - 1 - \frac{A_{CC}}{\Delta m_{32}^2}\right],$$
$$\Delta_{32}^{m} = \frac{1.27\Delta m_{32}^2 L}{E}\frac{1}{2}\left[\frac{\sin 2\theta_{13}}{\sin 2\theta_{13}^{m}} + 1 + \frac{A_{CC}}{\Delta m_{32}^2}\right], \tag{1.18}$$
$$\Delta_{31}^{m} = \frac{1.27\Delta m_{32}^2 L}{E}\left[\frac{\sin 2\theta_{13}}{\sin 2\theta_{13}^{m}}\right].$$

It should be noted that all these three scales are of the same order of magnitude including Δ_{21}^{m}, which cannot be neglected for this reason. The corresponding probabilities for anti-neutrinos $\bar{P}_{\mu\mu}^{m}$ and $\bar{P}_{e\mu}^{m}$ are obtained by making $A_{CC} \rightarrow -A_{CC}$ in Eq. 1.16 and Eq. 1.17 respectively. The neutrino and anti-neutrino probabilities are invariant under $(A_{CC}, \Delta m_{32}^2) \rightarrow (-A_{CC}, -\Delta m_{32}^2)$. In the case of atmospheric neutrino experiments where the channels $\nu_\mu \rightarrow \nu_\mu$ ($\bar{\nu}_\mu \rightarrow \bar{\nu}_\mu$) and $\nu_e \rightarrow \nu_\mu$ ($\bar{\nu}_e \rightarrow \bar{\nu}_\mu$) both occur, the effects from both these channels will contribute.

But the $\nu_e \rightarrow \nu_\mu$ ($\bar{\nu}_e \rightarrow \bar{\nu}_\mu$) channel has much less sensitivity to the mass hierarchy because of the smaller electron neutrino flux as well as small θ_{13}. Hence the mass hierarchy discrimination is mainly quantified by the difference in the matter effects of the survival probabilities of ν_μ and $\bar{\nu}_\mu$:

$$\Delta P^{m} = P_{\mu\mu}^{m} - \bar{P}_{\mu\mu}^{m}. \tag{1.19}$$

sine the major effect is seen from the survival of muon-neutrinos and anti-neutrinos. It should also be noted that the effects due to the CP phase occur in the subleading terms only, which can be neglected in the case of atmospheric neutrinos. Hence the matter effects of atmospheric neutrinos are insensitive to the CP phase. The oscillation probabilities as functions of $\log(L_\nu/E_\nu)$, where L_ν is the distance traveled by the neutrino in km and E_ν is the neutrino energy in GeV, for different E_ν (GeV) are shown in Fig. 1.2. If θ is the zenith angle θ_z of the neutrino, the distance L_ν from the production point of the neutrino to the detector, L_ν is calculated as

$$L_\nu \;=\; \left[(R+h)^2 - R\sin^2\theta_z\right]^{1/2} - R\cos\theta_z, \tag{1.20}$$

where R = 6374 km is the radius of the Earth and $h \approx 15$ km, the average height in the atmosphere where neutrinos are produced. The plots shown are for normal hierarchy. For inverted hierarchy the plots just interchange.

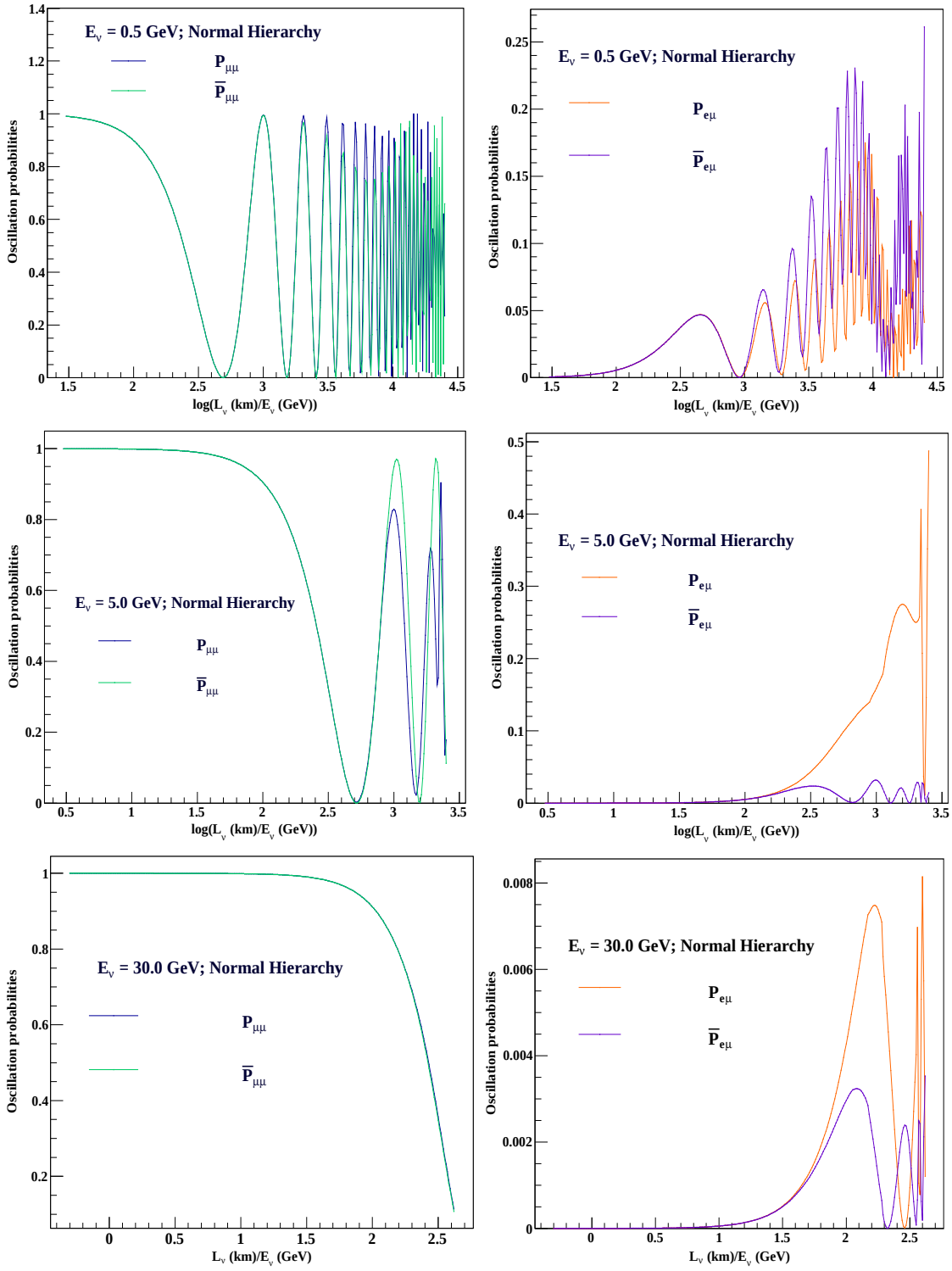

Figure 1.2: Survival probabilities $P_{\mu\mu}$ and $\bar{P}_{\mu\mu}$ (left) and oscillation probabilities $P_{e\mu}$ and $\bar{P}_{e\mu}$ (right) at E_ν = 0.5, 5 and 30 GeV as functions of $\log(L_\nu/E_\nu)$, where L_ν is the distance traveled by the neutrino in km and E_ν is the neutrino energy in GeV, for normal hierarchy. It can be seen that matter resonance occurs at 5 GeV for neutrinos for normal hierarchy. Matter resonance will occur for anti-neutrinos in inverted hierarchy. One important feature to be noted is that the range of $\log(L_\nu/E_\nu)$ spanned varies with neutrino energy. Hence the low energy 0.5 GeV neutrinos will span an L_ν/E_ν region from 1.5–4.4 and the highest energy shown in the figure viz, 30 GeV will span a region -0.3 to 2.6 (with the $\cos\theta$ ranging from 0–1).

The matter effects are more prominent for neutrinos in normal hierarchy and for anti-neutrinos with inverted hierarchy. Resonance occurs for neutrinos in normal hierarchy and for anti-neutrinos in inverted hierarchy. This is because the matter effects are enhanced when both A_{CC} and Δm^2_{32} have the same sign and are depleted when they have opposite signs as can be seen from Eqs. 1.16,1.17 and 1.19. This enables neutrino mass hierarchy distinction by studying the Earth matter effects.

Thus it can be seen that in the 3-flavour oscillation scenario the transition probabilities, both of neutrinos and anti-neutrinos, depend on all the oscillation parameters namely $\theta_{12},\ \theta_{13},\ \theta_{23},\ \Delta m^2_{21},\ \Delta m^2_{32}$ and the CP phase δ. Hence the precise measurement of the magnitude of all these quantities and determining the sign of the mass squared differences are very important. Several neutrino detectors, spanning over different baselines and energies are running and many more are being planned all over the world, including the INO, for this purpose. The next section lists some of the most important neutrino oscillation experiments. The list contains experiments which have finished taking data as well as currently running ones.

1.5 Some important neutrino oscillation experiments

Neutrino physics is an experiment driven field. Starting from the first detection of neutrinos which proved Pauli's theory to be right [2, 3] through the solar neutrino puzzle and its resolution, [73] to the recent measurement of θ_{13} [11], experiments have played a major role in formulating and improving our understanding of neutrinos. Some of the important neutrino oscillation experiments are listed in this section. The design of each experiment is optimally done specific to the sensitivity to the parameter to be measured.

1. **Homestake experiment** [51, 73–75]: This was a radiochemical experiment designed to detect and measure the electron neutrino (ν_e) flux from the sun. Only one third of the predicted flux [47] was detected in the experiment. This discrepancy with the theory led to the famous "solar neutrino problem" which was the first indication of flavour oscillations among neutrinos as well as non-zero neutrino masses.

2. **Sudbury Neutrino Observatory (SNO)**[7, 76, 77] : This was the solar neutrino experiment which used 2 ktons of heavy water to confirm solar neutrino oscillations by detecting solar neutrinos through both charged current and neutral current inter-

actions and also through elastic scattering with electrons. A deficit in the electron neutrino flux was observed by the detectors which probed only the charged current interaction channels. Using the other detection processes enabled SNO to detect the other neutrino flavours to which the ν_es from the Sun had oscillated to and to confirm for the first time the Standard Solar Model.

3. **Super Kamiokande (SK)** [78] : Super Kamiokande is a water Cherenkov detector in Japan. This is a versatile detector which has been used in the detection of solar [79–81], atmospheric [82, 83] and accelerator neutrinos [84–87]. The SK detector was first used for the detection of solar neutrinos, which confirmed the deficit in the flux and confirmed the direction of these neutrinos (i.e., they came from the Sun) and indicated neutrino oscillations. It also measured the day night asymmetry of solar neutrinos which suggested a large mixing angle solution [88, 89]. SK was the first detector to observe atmospheric neutrino oscillations [82, 83], i.e., the oscillation of muon neutrinos produced in the atmosphere. The flux of the up-coming ν_μs (generated on the other side of the Earth) was found to be half of the downgoing neutrino flux suggesting oscillations of ν_μ to other flavours. SK is also the far detector for two other experiments K2K and T2K, the former an accelerator experiment which sent a ν_μ beam from KEK situated 250 km away from Kamioka, the detection of which confirmed the oscillations observed in atmospheric neutrinos by showing a deficit in the flux of neutrinos observed at the detector. T2K experiment is a currently running experiment to determine the neutrino oscillation parameters using a neutrino beam from the J-PARC accelerator situated 295 km from the far detector which is the SK detector. This experiment has more flux than the K2K experiment and thus an enhanced physics potential. The predecessor of SK, Kamiokande-II observed the neutrinos from the Supernova 1987A [56].

4. **KamLAND** [9, 10, 90] : Kamioka Liquid Scintillator Antineutrino Detector is a scintillator based detector to detect electron anti-neutrinos $\bar{\nu}_e$ from reactors situated at a distance of an average of 180 km. The experiment established the oscillations of neutrinos and that they are massive by looking at the disappearance of the reactor $\bar{\nu}_e$. The experiment determined the value of Δm^2_{21} and θ_{12} precisely as $\Delta m^2_{21} = 7.9^{+0.6}_{-0.5} \times 10^{-5}\text{eV}^2$ and $\tan 2\theta_{12} = 0.40^{+0.10}_{-0.07}$ respectively. Kamland was the first to observe geo-neutrinos [91].

5. **Daya Bay** [92, 93] : Daya Bay is a reactor neutrino experiment which uses liquid scintillator loaded with gadolinium (Gd) to detect electron anti-neutrinos $\bar{\nu}_e$ from the Daya Bay Nuclear Power Plant (NPP) and the Ling Ao NPP in China. This experiment precisely measured the across-generation mixing angle θ_{13} by studying the disappearance of the reactor anti-neutrinos. The experiment determined the value of θ_{13} as $\sin^2 2\theta_{13} = 0.092 \pm 0.016(\text{stat}) \pm 0.005(\text{syst})$ [11] and was part of the group of reactor neutrino experiments that first established that θ_{13} is non-zero.

6. **RENO** [94] : Reactor Experiment for Neutrino Oscillation is another reactor experiment which used Gd doped liquid scintillator to detect reactor $\bar{\nu}_e$ from the Yonggwang Nuclear Power Plant in Korea. The experiment measured the value of θ_{13} as $\sin^2 2\theta_{13} = 0.113 \pm 0.013(\text{stat}) \pm 0.019(\text{syst})$ [12].

7. **Double CHOOZ** [95] : This is an upgrade of the reactor neutrino experiment where the reactor electron anti-neutrinos from the CHOOZ reactor are detected using liquid scintillators doped with Gd. The latest value of θ_{13} measured by this experiment alone is given by $\sin^2 2\theta_{13} = 0.109 \pm 0.030(\text{stat}) \pm 0.025(\text{syst})$ [13].

8. **MINOS** [96–98] : The Main Injector Neutrino Oscillation Search is an ongoing accelerator neutrino experiment. The experiment intends to measure θ_{23}, $\Delta m^2{}_{32}$, δ_{CP} and also determine the neutrino mass hierarchy and the octant of θ_{23}. The NuMI beam consisting of ν_μ and $\bar{\nu}_\mu$ of GeV energies produced at Fermilab travels a distance of 735 km to the far detector situated in Soudan mine. The far detector, a 5 kilo ton iron scintillator detector is magnetised and can distinguish ν_μ and $\bar{\nu}_\mu$ based on the charge of the muon produced in the neutrino interaction in the detector. This enables the detector to measure $|\Delta m^2_{32}|$ very precisely. MINOS can also detect atmospheric neutrinos. The current best limit at 68% CL on this oscillation parameter is given by the experiment as $|\Delta m^2_{32}| = [2.28 - 2.46] \times 10^{-3} eV^2$ for NH and $|\Delta m^2_{32}| = [2.32 - 2.53] \times 10^{-3} eV^2$ for IH [33].

9. **T2K** [86] : The Tokai to Kamioka experiment is also an ongoing accelerator experiment which detects the muon-neutrinos in the beam generated at J-PARC sent to the SK detector situated at a distance of 295 km away. This experiment also intends to probe the neutrino oscillation parameters in the atmospheric sector and also to search for sterile neutrinos as well as measure neutrino nucleus cross sections. Al-

though the precision on $|\Delta m^2_{32}|$ achievable by T2K is not as good as MINOS (since SK is not magnetised), T2K gives the current best precision on θ_{23} as $\sin^2\theta_{23} = 0.514^{+0.055}_{-0.056}$ for NH and $\sin^2\theta_{23} = 0.511 \pm 0.055$ for IH at 68% CL [34].

10. **NOνA** [99, 100] : The NuMI Off-axis ν_e Appearance experiment is an accelerator experiment which detects neutrinos from the NuMI beam using a far Totally Active Scintillator Detector (TASD) at Ash River, which is 810 km from the NuMI beam generator. The experiment intends to measure θ_{13} via the appearance of ν_e and $\bar{\nu}_e$ in the detector (the other current experiments looking at θ_{13} are all anti-neutrino disappearance experiments). NOνA also intends to determine the neutrino mass hierarchy, the octant of θ_{23} and the CP phase δ_{CP} via the appearance channel. This experiment also will measure θ_{23} and Δm^2_{32} by studying the $\nu_\mu \to \nu_\mu$ and $\bar{\nu}_\mu \to \bar{\nu}_\mu$ channels.

It should be noted that most reactor neutrino experiments which detect MeV energies of neutrinos have a long baseline of the order of one kilometer or so (KamLAND is an exception), whereas both the accelerator and atmospheric neutrino oscillation experiments which detect neutrinos of GeV energies have long baselines of the order of 100s – 1000s of kilometers. The sensitivity to the oscillation parameter to be measured is used to determine the L and E where the former is the baseline and the latter is the neutrino energy of a neutrino oscillation experiment. Apart from the experiments mentioned above, other experiments have been proposed to measure neutrino oscillation parameters. The chief among these are the experiments intending to determine neutrino mass hierarchy, namely Hyper-K [101], PINGU [102], JUNO [103] and ICAL at INO [18, 19]. Experiments like DUNE [15] intending to measure the CP violation phase have also been proposed. In addition experiments like OPERA [104] have searched for direct $\nu_\mu \to \nu_\tau$ oscillations and the observations of the neutrinos from the CNGS beam [105] have confirmed these oscillations. The current global fits of the neutrino oscillation parameters are given in the next section. Finally, there are many experiments to determine the neutrino mass directly (from beta decay) and also to find out whether neutrinos are Dirac or Majorana fermions – this is beyond the scope of the present study.

1.6 Current best values of various neutrino oscillation parameters

As mentioned in Section 1.5, several experiments have observed and studied various possible neutrino oscillation channels, established neutrino oscillations and have determined/are determining/will determine the values of the various oscillation parameters. The current global best fit values of all the neutrino oscillation parameters are shown in Fig. 1.3. The table is taken from [106]. (It should be noted that these are the latest values and are slightly different from those used for the analyses given in Chapter 6.) These

NuFIT 2.0 (2014)

	Normal Ordering ($\Delta\chi^2 = 0.97$)		Inverted Ordering (best fit)		Any Ordering
	bfp $\pm 1\sigma$	3σ range	bfp $\pm 1\sigma$	3σ range	3σ range
$\sin^2\theta_{12}$	$0.304^{+0.013}_{-0.012}$	$0.270 \to 0.344$	$0.304^{+0.013}_{-0.012}$	$0.270 \to 0.344$	$0.270 \to 0.344$
$\theta_{12}/^\circ$	$33.48^{+0.78}_{-0.75}$	$31.29 \to 35.91$	$33.48^{+0.78}_{-0.75}$	$31.29 \to 35.91$	$31.29 \to 35.91$
$\sin^2\theta_{23}$	$0.452^{+0.052}_{-0.028}$	$0.382 \to 0.643$	$0.579^{+0.025}_{-0.037}$	$0.389 \to 0.644$	$0.385 \to 0.644$
$\theta_{23}/^\circ$	$42.3^{+3.0}_{-1.6}$	$38.2 \to 53.3$	$49.5^{+1.5}_{-2.2}$	$38.6 \to 53.3$	$38.3 \to 53.3$
$\sin^2\theta_{13}$	$0.0218^{+0.0010}_{-0.0010}$	$0.0186 \to 0.0250$	$0.0219^{+0.0011}_{-0.0010}$	$0.0188 \to 0.0251$	$0.0188 \to 0.0251$
$\theta_{13}/^\circ$	$8.50^{+0.20}_{-0.21}$	$7.85 \to 9.10$	$8.51^{+0.20}_{-0.21}$	$7.87 \to 9.11$	$7.87 \to 9.11$
$\delta_{\rm CP}/^\circ$	306^{+39}_{-70}	$0 \to 360$	254^{+63}_{-62}	$0 \to 360$	$0 \to 360$
$\frac{\Delta m^2_{21}}{10^{-5}\ \text{eV}^2}$	$7.50^{+0.19}_{-0.17}$	$7.02 \to 8.09$	$7.50^{+0.19}_{-0.17}$	$7.02 \to 8.09$	$7.02 \to 8.09$
$\frac{\Delta m^2_{3\ell}}{10^{-3}\ \text{eV}^2}$	$+2.457^{+0.047}_{-0.047}$	$+2.317 \to +2.607$	$-2.449^{+0.048}_{-0.047}$	$-2.590 \to -2.307$	$\begin{bmatrix} +2.325 \to +2.599 \\ -2.590 \to -2.307 \end{bmatrix}$

Figure 1.3: The current global best fit values of neutrino oscillation parameters as given in [106, 107].

numbers will change in the course of time as more and more experiments to measure these parameters precisely will come up in future. The major unknown parameters are the mass hierarchy and δ_{CP} apart from the octant of θ_{23} which will be measured in the upcoming oscillation experiments.

1.7 Scope of INO among all the neutrino experiments in the world

As seen from the table in Fig. 1.3 in Section 1.6, the values of the two mixing angles θ_{12} and θ_{13} have been determined precisely and bounds have been put on the value of the mixing angle in the atmospheric sector θ_{23} by several experiments although it is the least well-determined mixing angle. Similarly, the value of the solar mass squared difference Δm^2_{21} and its sign ($m_1 < m_2$) have been determined and bounds have been put on the magnitude of the atmospheric mass square difference Δm^2_{32} (Δm^2_{31}) by experiments. The

most important open question in neutrino physics as of today is the sign of Δm^2_{32} (Δm^2_{31}), which will determine whether the neutrino masses are ordered in the normal fashion ($m_1 < m_2 < m_3$) or the inverted fashion ($m_3 < m_1 < m_2$). Other important questions are about the octant of θ_{23} and CP violation which are also being probed by many experiments. Since several experiments are sensitive to different channels and the property of the detector actually determines to what extent the experiment can be sensitive to neutrino oscillation parameters, it is important to design detectors which can answer specific questions. It is in such a context that the Iron Calorimeter (ICAL) detector at the proposed India-based Neutrino Observatory becomes important.

The proposed ICAL detector is a 50 kilo ton magnetisable detector which will be mainly sensitive to atmospheric muon neutrinos and anti-neutrinos. This detector, owing to its magnetisability, can distinguish between μ^- and μ^+ produced in the final state of a charged-current neutrino interaction with iron. Thus by looking at the charge of the muon, it can precisely tag an event as a neutrino or anti-neutrino event, which an unmagnetisable water Cherenkov detector cannot do. This inturn makes it ideal for the detection of neutrino and anti-neutrino events, separately, and thus determine the mass hierarchy of neutrinos by studying the Earth matter effects discussed in Section 1.4.1. The source of neutrinos in ICAL being atmospheric neutrinos opens up a new prospect of probing a wide range of distances L and energies E over which the oscillations can be studied. ICAL will be a huge detector, hence with reasonable exposure, there will be enough number of events with which the studies can be done. Not only can ICAL determine the neutrino mass hierarchy, but it can perform precision measurements of θ_{23} and Δm^2_{32}, which will further contribute to the global fits to these parameters. As of now ICAL is one of the experiments, despite being simple in design and working, that can do amazing physics and will definitely have an impact on the neutrino parameter values. It is also noteworthy that the ICAL can not only do neutrino oscillation studies, but also dark matter studies, searches for magnetic monopoles and even sterile neutrino searches [19].

1.8 Scope of this thesis

This thesis reports the detailed simulation studies of the ICAL detector and its physics potential, with emphasis on the hadrons produced in the neutrino interactions in the detector. Although ICAL detector is optimised for the detection and measurement of muons

and their momenta, the hadrons produced in the charged current interactions which produce these muons also carry much information which will enhance the sensitivity of the ICAL to oscillation parameters. Thus it is necessary to characterise the response of the detector to hadrons, their energy and direction have to be determined as precisely as possible. The description of the ICAL detector geometry and its various components along with the different interactions which can be detected are given in Chapter 2. A detailed report of the simulation studies of the energy resolution of hadrons in ICAL is presented in Chapter 3. The simulation studies on the reconstruction of hadron shower direction in ICAL are discussed in Chapter 4. The muon momentum resolution and charge identification capability of the ICAL have been studied elsewhere and are briefly presented in Chapter 5 for completeness. Since the charged-current interactions of muon neutrinos are of main interest in ICAL, the techniques to identify these events from other events such as the charged current electron neutrino events and neutral current events are also discussed in Chapter 5. The muon momentum and hadron energy resolutions obtained from the simulation studies are compiled as look-up tables and used in the oscillation analysis described in Chapter 6. A detailed simulation study on the sensitivity of ICAL to neutrino oscillation parameters in the extended energy range of 0.5–25 GeV of the observed muon is presented in Chapter 6. This study is a refinement over the earlier work presented in [27, 29, 30]. Two types of analyses, one which uses muon energy and direction information only and the other which makes use of muon energy,direction and hadron energy, are illustrated. Along with these, the effect of constraining the flux ratio of ν_μ and $\bar{\nu}_\mu$ is also studied. The conclusions and outlook derived from the analyses performed in these chapters along with the future scope are elucidated in Chapter 7.

2 ICAL @ INO

As mentioned in Chapter 1, one of the open questions in neutrino physics as of today is the mass ordering of neutrinos. To resolve this puzzle, several experiments [18, 19, 99–103] have been proposed and some are being built, all over the world. The experiment proposed in India, namely the India-based Neutrino Observatory (INO) [18, 19] will house a 50 kton magnetisable Iron Calorimeter detector (called ICAL) to detect atmospheric neutrinos and study neutrino oscillation parameters by probing the Earth matter effects of neutrinos as they propagate through various layers of the Earth. The detector will be located in Bodi West Hills in Theni District of Tamil Nadu, India, in a cavern built in the mountain such that there is a minimum rock cover of ~ 1 km on all sides to reduce the cosmic ray background. The main physics goals of the ICAL detector involve precision measurement of the oscillation parameters $\sin^2\theta_{23}$ and $|\Delta m^2_{32}|$ where θ_{23} is the mixing angle and the latter is the mass squared difference in the atmospheric sector. As mentioned above, ICAL also can determine the sign of Δm^2_{32}, i.e., the neutrino mass hierarchy. A brief description of the ICAL detector, to familiarise with the detector structure, is given in the following sections. The major components of the detector are iron plates which act as the passive detector with which the neutrinos interact and the active resistive plate chambers (RPCs) which detect the charged particles produced in these neutrino interactions.

2.1 Why a detector with iron and resistive plate chambers?

It is interesting to know why the combination of iron and RPCs has been chosen to build the detector. Two of the major deciding factors in the design of any detector will be the physics goals of the experiment and cost effectiveness. The iron-RPC combination is optimal for the kind of physics ICAL intends to study. The main reasons why ICAL will be built with iron are the following:

- The total number of unoscillated neutrino events in the detector can be expressed as :

$$N \sim \Phi \times \sigma \times n_d \times t, \tag{2.1}$$

where Φ is the unoscillated flux of neutrinos, σ is the interaction cross section, n_d is the number of targets in the detector, t is the exposure time. In the case of atmospheric neutrinos, the fluxes cannot be controlled. Oscillations will further decrease the neutrino flux. Interaction cross section also cannot be controlled since it is an intrinsic property of the particle. So with these constraints, to obtain a reasonable number of events so as to do oscillation studies, either the number of targets or the exposure time must be increased. To increase the number of targets, a large mass/volume, say a megaton/km^3 of a low density material like water (as in the case of Ice Cube detector), can be used, or a smaller mass/volume say of the order of kilo ton/m^3 of a high density material like iron (high Z material) can be used. The proposed ICAL detector consists of 50 kilo tons of iron as the target material; iron being a high Z material makes the detector a compact one which can detect a reasonable number of events in 5 or 10 years of exposure.

- The main physics studies in ICAL are the measurement of the neutrino oscillation parameters, i.e., the precision measurement of the neutrino mixing angle θ_{23} and the mass squared difference Δm^2_{32}. The sign of Δm^2_{32} i.e., neutrino mass hierarchy, can be determined by probing the earth matter effect as the neutrinos pass through the Earth. All these studies will mainly be done by the detection of charged current muon neutrino events, in which a ν_μ or $\bar{\nu}_\mu$ interacts with the iron nucleus and produces a μ^- or μ^+ accordingly. The iron in the detector now acts not only as the target material, but also as a magnet which can be used to distinguish these μ^- and μ^+ by using the direction of bending of these particles in the magnetic field. Thus it enables the identification of a particular type of charge which enhances the sensitivities of the ICAL to oscillation parameters as opposed to detectors which cannot be magnetised at all.

Determining the direction of the incoming neutrino is crucial in oscillation studies. To determine if a neutrino is upcoming or down-going, time information is important and the detector should have excellent timing resolution of the order of ~ 1 ns. The resistive plate chamber detectors (RPCs), which are gaseous detectors, have such a timing resolu-

tion and hence are used as the active detector elements to detect the charged particles in the final state of a neutrino interaction.

In addition to these, factors like cost effectiveness and the availability of detector technologies also play a role in determining the final design of the detector. Even though the structure of ICAL is a simple one, its physics potential is on par with other neutrino experiments. More details of the ICAL detector are given in the following sections.

2.2 ICAL detector geometry

The ICAL detector will be a modular cuboid in structure with three modules, each of dimensions 16 m $\times$ 16 m $\times$ 14.45 m in (X, Y, Z) respectively. Each module is separated from the other by a gap of 20 cm. Thus the detector will be 48 m long in the X direction with 151 iron plates of thickness 5.6 cm stacked one above the other in the Z direction. The Z direction is chosen such that it points vertically upwards so as to make the polar angle equal to the zenith angle θ. There is a separation of 4 cm between each iron plate in the Z direction, in which the active detector element RPCs will be accommodated. The iron plates are supported by $\sim$ 16 cm wide steel support structures at every 2 m. A schematic of the ICAL detector is given in Fig. 2.1.

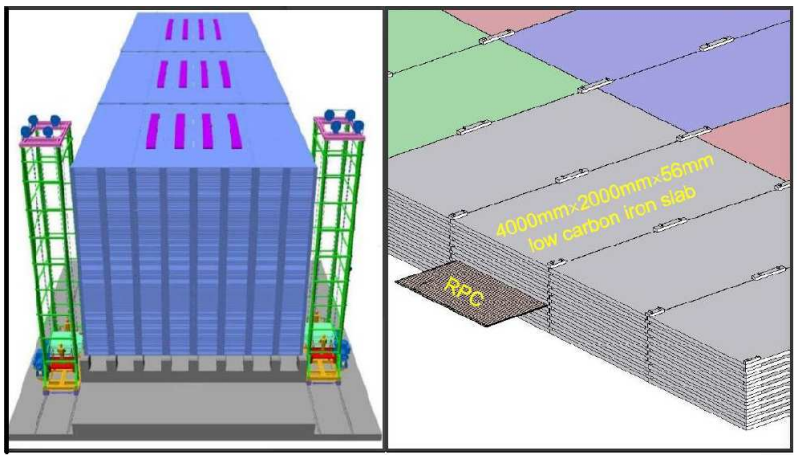

Figure 2.1: Schematic of the ICAL detector. (Left) Three modules of ICAL with coil slots. The longest axis is the X axis, the axis in the front portion of the figure is the Y axis and the one which points vertically upwards is the Z axis. (Right) Zoom of a portion of the detector with 5.6 cm thick iron plates; support structures are also visible.

The magnetic coils wrap around the central part of each module in 8 m long coil slots located at $x = x_0 \pm 4$ m and $|y| \leqslant 4$ m, where x_0 is the central X co-ordinate of each module. So each module is a separate magnet with individual coil slots. Different

regions of each module can be classified into different regions based on the strength of the magnetic field achievable, namely central, peripheral and side regions [22, 108] as shown in Fig. 2.2. The maximum field strength achievable in the central region of each module is $\sim$ 1.5 Tesla (T). A brief description of ICAL magnetic field is given in Section 2.2.1.

2.2.1 ICAL magnetic field

The most important feature of the ICAL detector is its ability to identify the charge of final state muons by means of a magnetic field. The simulated magnetic field map of ICAL in a single iron plate in the central module of the detector is shown in Fig. 2.2. The field in a single iron plate was simulated using MAGNET6.26 software [109].

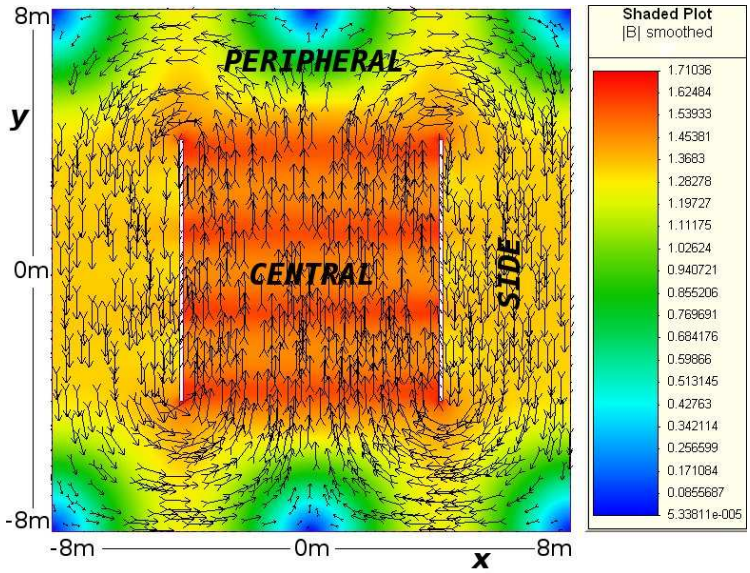

Figure 2.2: Magnetic field map in a single iron plate at $z = 0$ of the ICAL detector. The length and direction of the flux lines indicate the magnitude and direction of the field. In the central region, the field is uniform and has a strength of $\sim$ 1.5 T which provides the best reconstruction of muons in this region.

The field map was generated at the center of the central plate, i.e., at $z = 0$ and is assumed to be uniform over the entire 5.6 cm thickness of the iron plate. In the detector the magnetic field will be generated by electric current passing through the copper coils wound through the slots alloted for them as specified in Section 2.2. The arrows in the field map represent the magnetic field lines whose length and direction represent the magnitude and direction of the magnetic field. It can be seen that all the lines are parallel to the Y direction in the central 8 m $\times$ 8 m $\times$ 14.45 m region (i.e., $|x| \leqslant \pm$ 4 m, $|y| \leqslant \pm$ 4 m and $|z| \leqslant \pm$ 7.225 m) and this "central region" has the maximum field strength in the

whole module. It should be noted that both the magnitude and direction of the magnetic field are uniform in this region.

In the Y direction outside the central region, where $|y| \geqslant 4$ m, both the magnitude and direction of the magnetic field change maximally; the field strength falls to zero at the corners of the module. This region is called the "peripheral region" of the detector. Outside the coil slots in the X direction, where $|x| \geqslant |x_0| + 4$ m, there are two small regions, where the magnetic field strength is about 15% smaller than in the central region. These are called "side regions" where the direction of magnetic field is opposite to that of the central region. The reconstruction properties of the side regions in the central module are expected to be similar to that of the central region since they are contiguous with the side regions of the adjacent modules. Edge effects will affect the reconstruction of particles in the right side region of the right-most module and the left side region of the left-most module.

The reconstruction of muon energy and direction is very important for oscillation studies using ICAL. Studies on muon reconstruction in both the "central", "peripheral" and "side" regions have been carried out extensively. Details of these can be found in [22, 108] and is briefly discussed in Chapter 5. It should also be noted that in ICAL due to the spatial resolution which will be discussed in Section 2.3, the effect of magnetic field can be seen only for muons and not for hadrons and electrons even if the magnetic field is $\sim 1.5\ T$.

2.3 Resistive plate chambers

In any neutrino detector, neutrinos cannot be detected directly since they are neutral particles. The only way to detect neutrinos is to make them interact with a target material, iron in the case of ICAL, and then detect the charged particles in the final state. The detector elements which detect the charged particles are called active detectors. In the ICAL detector, glass resistive plate chambers (RPCs) [110] are the active detectors which detect the muons, electrons and hadrons in the final state. The structure and working of the RPCs are described briefly here.

A glass RPC is made using two 3 mm thick glass plates by sealing them together leaving a uniform gap of 2 mm in between them. To ensure that the uniform gap is maintained all throughout the area of the glass plates, plastic button spacers are placed

and glued inside the gap. The edges of the glass plates are glued with edge spacers and whole chamber is sealed, evacuated and leak tested before it is filled with the gas mixture to detect the passage of charged particles. The gas mixture consists of R134A ($\sim 95\%$), isobutane and trace amounts of SF_6, for ionisation production and quenching to reduce the excess number of electrons respectively. The gas mixture is flown continuously in the chamber at normal pressure, with a high DC voltage across (so that the electric field is about some 4 – 5 kV/mm) across them.

The resistive plate chamber works on the principle of the ionisation of the gas medium when a charged particle passes through it. When electrons are liberated by the passage of charged particles through the gas layer, there will be a sudden electric discharge which is quenched by the following mechanisms:

1. The electrode used in the RPC is glass which has a volume resistivity of $10^{12}\Omega$cm; this causes the prompt switching off of the field around the discharge point.
2. The quencher prevents secondary discharges from photo ionisation of gases.
3. The outer electrons of the discharge are captured using a gas with high electron affinity, thus reducing the size and transverse dimensions of the discharge.

These keep the signal localised and gives the location information of the charged particle passing through the detector. Thus the main purpose of the RPC detector in the ICAL is to provide the spatial co-ordinates of the locus of a particle as it passes through the detector. The glass electrodes coated with graphite having a surface resistivity ~200-300$k\Omega/cm^2$, are transparent to the electrical pulse produced in the gas. This allows a capacitive readout of the signal through external pick up electrodes which are placed on either side of the RPC with a mylar sheet separating them from the graphite coating for insulation. The pick up strips are made of 150 μm thick copper strips of width 1.96 cm each, and are placed on both sides of the RPC, orthogonal to each other in the $X-Y$ plane. Thus the signal from one side gives the position information in the X plane and that from the other gives the information from the Y plane. Thus the (x, y) co-ordinate of the particle can be obtained using an RPC. In addition to this, the layer of the RPC in which the signal is recorded gives the z co-ordinate of the particle. Timing resolution of the order of ns can be obtained using an RPC. In simulations, this is assumed to be about ~ 1 ns and the RPC is considered to be 95 $\%$ efficient from the RPC R $\&$ D done for the ICAL detector.

The signal from one strip is called a hit and gives the (x, y, z, t) information of particles. This enables the tracking of muons in the detector, which then enables the reconstruction of muon momentum and direction by observing its curvature. Also the bending of the track in the magnetic field gives information about the charge of the muon. In the case of hadrons, the individual particle tracks cannot be seen as in the case of muons since the spatial resolution of ICAL is coarse (but enough to study minimum ionising particles like muons) and because hadrons shower in the detector unlike muons. The information about the charge deposited in the detector by these particles is also not available. For muons it does not matter since their reconstruction is only through curvature method in ICAL. But for hadrons, the energy cannot be determined calorimetrically due to the lack of the information on energy deposited. Hence it is crucial in the case of hadrons to make use of the hit information to calibrate the energy and determine their direction. The first part of this thesis will present the GEANT4 [23] simulation studies of how the hit information of hadrons is used to determine their energy and direction responses. This will be combined with information on the muon response of ICAL (studied elsewhere) to perform simulation studies of the physics potential of ICAL. The ICAL geometry and magnetic field map have been implemented in a GEANT-4 based simulation code by the ICAL collaboration [19]. This code has been used in the current analysis. In addition, the NUANCE [24] neutrino generator was used to generate atmospheric neutrino events for the physics analysis in the second part of this thesis.

2.4 The different neutrino interactions in ICAL

The ICAL detector aims to study the neutrino oscillation parameters by detecting atmospheric neutrinos in the GeV energy range. The detector is optimised to detect muons of GeV energies. Various types of interactions can occur in the detector. Since the atmospheric neutrinos contain ν_μ and ν_e (and their anti-particles) in the approximate ratio 2:1, both these flavours can interact with the iron in the detector. The two channels through which they interact are the charged current channel and the neutral current channel.

The interactions in the charged current channel produce charged leptons along with hadrons in the final state both of which are detected by the RPCs. In the neutral current channel a neutrino of the same flavour and hadrons are present in the final state. Thus in the detector, only hadrons will be detected. The interactions of relevance in ICAL

Charged current	Neutral current
$\nu_l + N \rightarrow\ l^- + X$	$\nu_l + N \rightarrow \nu_l + X$
$\bar{\nu}_l + N \rightarrow\ l^+ + X$	$\bar{\nu}_l + N \rightarrow \bar{\nu}_l + X,$

Table 2.1: Here ν_l represents the neutrino flavour, l is the charged lepton associated with ν_l; $l\ =\ e, \mu, \tau$; N is the nucleon with which the neutrino interacts and X represents the final state hadrons.

are mainly the charged current interactions of ν_μ or $\bar{\nu}_\mu$ in the detector giving μ^- or μ^+ respectively along with the hadrons. Hence the detector is optimally designed to detect muons. Different types of processes can contribute to the production of the final state particles. The main broad categories among these processes include quasi elastic (QE), resonant production (RES) and deep inelastic scattering (DIS). In quasi elastic scattering a neutrino undergoes elastic scattering off a nucleon in the target material to produce a single or multiple nucleons; i.e., $\nu_l + n \rightarrow l^- + p$; $\bar{\nu}_l + p \rightarrow l^- + n$; these processes are dominant at low energies upto about 1 GeV. In resonance production the neutrino interaction causes the excitation of the target nucleon to a baryonic resonance which will further decay to a nucleon and a meson. For a charged current interaction, $\nu_l + N \rightarrow l^- + N^*\ ,\ N^* \rightarrow \pi + N'$, where N^* is the excited state, π is a pion and $N,\ N'\ =\ n,\ p$ respectively and for a neutral current interaction, $\nu_l + N \rightarrow \nu_l + N^*\ ,\ N^* \rightarrow \pi + N'$. These processes are dominant in the energy range of about 1–2 GeV. The deep inelastic scattering (DIS) occurs when a neutrino with adequate energy can "see" the individual quarks of a nucleon and interacts with them, producing a hadronic shower in the final state. The energy range in which DIS is dominant is beyond about $\sim$ 2 GeV. The above stated processes are empirically depicted in Table 2.2.

Process	CC	NC
QE	$\nu_l\ n \rightarrow l^-\ p$ $\bar{\nu}_l\ p \rightarrow l^+\ n$	$\nu_l\ p \rightarrow \nu_l\ p\ ;\ \nu_l\ n \rightarrow \nu_l\ n$ $\bar{\nu}_l\ p \rightarrow \bar{\nu}_l\ p\ ;\ \bar{\nu}_l\ n \rightarrow \bar{\nu}_l\ n$
RES	$\nu_l\ p \rightarrow l^-\ p\ \pi^+\ ;\ \bar{\nu}_l\ p \rightarrow l^+\ p\ \pi^-$ $\nu_l\ n \rightarrow l^-\ n\ \pi^+\ ;\ \bar{\nu}_l\ n \rightarrow l^+\ n\ \pi^-$ $\nu_l\ n \rightarrow l^-\ p\ \pi^0\ ;\ \bar{\nu}_l\ p \rightarrow l^+\ n\ \pi^0$	$\nu_l\ p \rightarrow \nu_l\ n\ \pi^+\ ;\ \bar{\nu}_l\ p \rightarrow \bar{\nu}_l\ n\ \pi^+$ $\nu_l\ n \rightarrow \nu_l\ p\ \pi^-\ ;\ \bar{\nu}_l\ n \rightarrow \bar{\nu}_l\ p\ \pi^-$ $\nu_l\ p \rightarrow \nu_l\ p\ \pi^0\ ;\ \bar{\nu}_l\ p \rightarrow \bar{\nu}_l\ p\ \pi^0$ $\nu_l\ n \rightarrow \nu_l\ n\ \pi^0\ ;\ \bar{\nu}_l\ n \rightarrow \bar{\nu}_l\ n\ \pi^0$
DIS	$\nu_l\ N \rightarrow l^-\ X\ ;\ \bar{\nu}_l\ N \rightarrow l^+\ X$	$\nu_l\ N \rightarrow \nu_l\ X\ ;\ \bar{\nu}_l\ N \rightarrow \bar{\nu}_l\ X$

Table 2.2: Interaction of a neutrino with a nucleon through charged current and neutral current channels, producing final state particles through various processes; ν_l is the neutrino flavour, l is the charged lepton associated with it, N is the nucleon and X is the final state hadron depending on the process.

The total cross sections of neutrinos and anti-neutrinos as a function of energy for these different processes are illustrated in Fig. 2.3 [111]. The cross sections give information about the dominant processes at each energy and help in calculating the event rates in

the detector. The processes of interest in the study of neutrino oscillations are the charged

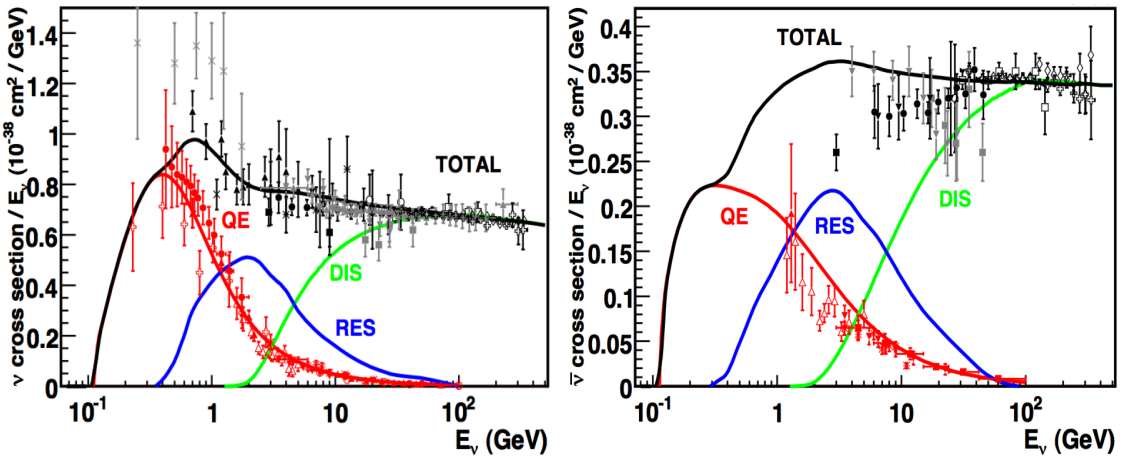

Figure 2.3: Total cross section per nucleon per unit energy for charged current neutrino interaction (left) and anti-neutrino interaction (right) as a function of energy for an isoscalar target [111]. Both data and theory predictions are shown. Figures are sourced from [111].

current interactions of muon- and electron- type neutrinos in the detector, for neutral current interactions do not carry oscillation information. Even though the ICAL is optimised for muon detection, ν_e and $\bar{\nu}_e$ charged current interactions will occur in ICAL and will be seen as showers since electrons will shower electromagnetically in the detector. Hence the separation of different types of events in ICAL is important so as to obtain correct physics results from oscillation analysis. It should be noted that the muons being minimum ionising particles in the detector will traverse more layers and leave less number of hits per layer, thus producing a clean "track" in the detector. Electrons, as mentioned above, will shower electromagnetically and will deposit large amount of energy within a shorter distance. Hadrons also will shower in the detector, but the showers contain both strong interaction part and an electromagnetic part. The separation of these events based on hit and layer information will be discussed briefly in Chapter 5.

Out of the different types of interactions, ν_μ and $\bar{\nu}_\mu$ are of more importance to ICAL. Knowing the energy and direction of the final state particles, the energy and direction of the incoming neutrino can be reconstructed. The detector is optimised for the detection of muons and has excellent energy and direction response for them and a very good charge identification efficiency. Even though hadrons only produce a shower in the detector, it is necessary to extract the information available about them. The study of the energy and direction resolution of hadrons will be discussed in detail in Chapters 3 and 4.

2.5 Atmospheric neutrino fluxes in ICAL

The source of neutrinos in ICAL is the Earth's atmosphere. Hence it is important to know about the flux of these neutrinos since it will eventually determine the mass of the detector and the exposure time required to collect enough number of events to perform neutrino oscillation studies. These neutrinos are produced by the decay of the secondary cosmic rays produced in the Earth's atmosphere when primary cosmic rays, mainly protons from galactic and extra-galactic sources, impinge on the Earth. Thus the flux of the atmospheric neutrinos depend upon the flux of these primary cosmic rays and their energies. The details of neutrino production are described in Section 2.5.1.

2.5.1 Atmospheric neutrino production mechanism

The production of atmospheric neutrinos was explained briefly in Section 1.2.1. The mechanism is explained again but in detailed in this section. The primary cosmic rays consist of high energy particles produced in both galactic and extra-galactic sources. Their energy spectrum extends to very high energies, even beyond $\sim 10^{10}$ GeV, but falls very rapidly with the increase in energy. In the GeV energy range, the primary cosmic rays comprises mainly protons, $\sim 9\%$ helium nuclei and a small fraction of heavy nuclei. These primary cosmic rays interact with the nuclei of the air molecules to produce secondary cosmic rays (mesons) mainly consisting of pions and a small fraction of kaons. These particles decay mainly into muons and associated neutrinos according to the decay chain:

$$\pi^{\pm} \rightarrow \mu^{\pm} + \nu_{\mu}(\bar{\nu}_{\mu}); \tag{2.2}$$

$$\mu^{\pm} \rightarrow e^{\pm} + \bar{\nu}_{\mu}(\nu_{\mu}) + \nu_{e}(\bar{\nu}_{e}), \tag{2.3}$$

where, $\pi^{\pm}$ represent the charged pions, $\mu^{\pm}$ anti-muon and muon, $e^{\pm}$ represent positron and electron and ν and $\bar{\nu}$ represent neutrino and anti-neutrino respectively.

Similarly, kaons also decay producing the two neutrino flavours ν_{μ} and ν_{e}, but their contribution to the atmospheric neutrino flux in the few GeV energy range is small compared to pions. It should be noted that only ν_{μ} and ν_{e} and their anti-neutrinos are produced in the atmosphere. The production of ν_{τ} requires mesons with heavy quarks to be produced which results in a negligible flux of ν_{τ} in atmospheric neutrinos. Hence, for atmospheric neutrino oscillation studies, the relevant neutrino fluxes are those of ν_{μ}, ν_{e}, $\bar{\nu}_{\mu}$

and $\bar{\nu}_e$ only. The cascading production of atmospheric neutrinos is illustrated in Fig. 2.4.

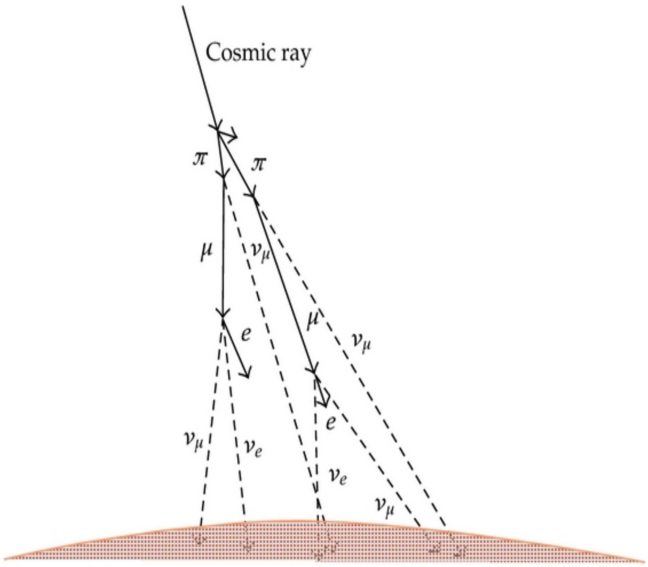

Figure 2.4: Schematic of atmospheric neutrino production [112].

The ratio of the neutrino fluxes,

$$R = \frac{(\Phi_{\nu_\mu} + \Phi_{\bar{\nu}_\mu})}{(\Phi_{\nu_e} + \Phi_{\bar{\nu}_e})} \approx 2. \tag{2.4}$$

The ratio is approximate since muons at high energies may not decay before reaching the Earth's surface, but remains > 2. The direction integrated fluxes and ratios of fluxes of different types of neutrinos in various flux models are illustrated in Fig. 2.5. A very important property of the atmospheric neutrino flux is that it is symmetric about a given direction on the Earth's surface; i.e.,

$$\Phi_\nu(E, \cos\theta = \Phi_\nu(E, -\cos\theta), \tag{2.5}$$

where θ is the zenith angle. This result is true for all energies $\gtrsim 3$ GeV (latitude dependent); at lower energies the geomagnetic effects cause deviations from this equality. Hence at higher energies, any asymmetry in the fluxes can be caused only by flavour oscillations during neutrino propagation. Even at lower energies where there are in-built asymmetries due to the geomagnetic effects at a specific location, major deviations from the equality can only be due to neutrino oscillations. Atmospheric neutrinos in the GeV ranges undergo oscillations while travelling through the Earth, hence a detector

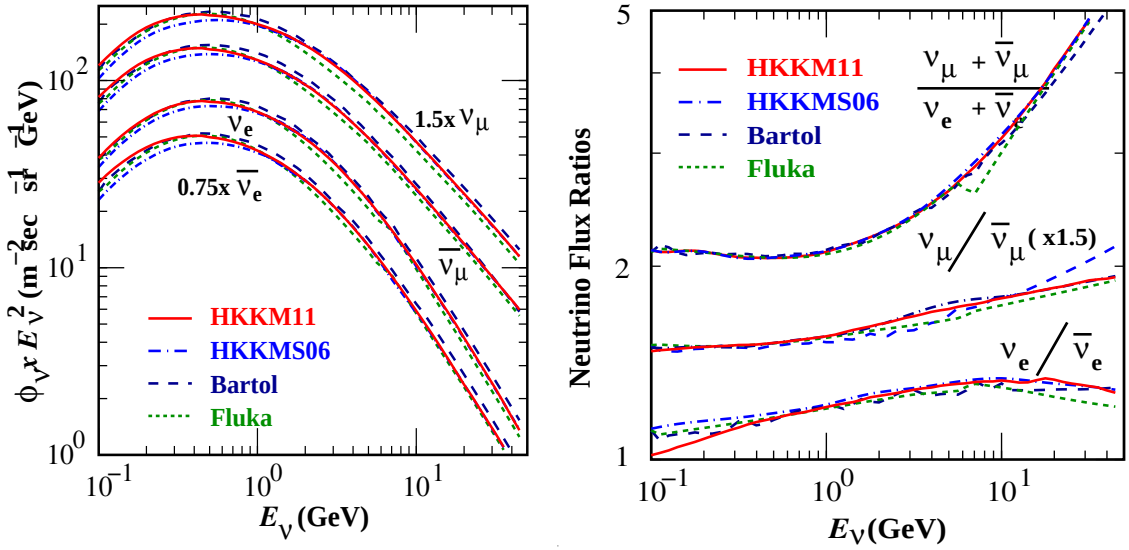

Figure 2.5: Direction integrated atmospheric neutrino fluxes in different models (left). Ratios of fluxes of different types of neutrinos as functions of energy (right) [113–116].

which detects atmospheric neutrinos from both sides of the Earth will see an up-down asymmetry; i.e., the flux of the up-coming neutrinos (coming through the Earth) is depleted whereas that of the down-going neutrinos is the same as expected. This asymmetry is the signature of atmospheric neutrino oscillations and was first seen by the Super Kamiokande (SK) collaboration, thus establishing oscillations in the atmospheric neutrino sector.

2.5.2 Atmospheric neutrino flux calculation

The energies of atmospheric neutrinos extend from hundreds of MeVs to TeV and beyond. Since there are so many energies and distances available in the case of atmospheric neutrinos, the physics that can be probed is wide. It is important to determine the flux of atmospheric neutrinos as precisely as possible to have a correct estimate of the number of detectable events in the energy range of interest. For this purpose, it is necessary to know the energy spectra of the primary cosmic rays, secondary muons and neutrinos. These are discussed briefly here.

- Primary cosmic ray energy spectrum : In the energy range 10 GeV to TeV region, the flux of primary cosmic rays decreases approximately as $E^{-2.7}$. This rapid fall in flux is reflected in the flux of the neutrinos produced subsequently. Well measured experiments upto tens of GeV have shown that the primary cosmic ray flux outside the Earth's atmosphere is isotropic and constant in time. The primary cosmic ray

proton spectrum can be fitter to a form

$$\Phi(E) = K\left[E + b\exp\left(-c\sqrt{E}\right)\right]^{\alpha}, \tag{2.6}$$

where, $\alpha = 2.74$, $K = 14900$, $b = 2.15$ and $c = 0.21$ [117].

- Secondary muon spectrum : The primary cosmic rays interacting with the air nuclei produce pions and kaons which decay to muons. The main input to the calculation of their fluxes are the hadronic cross sections. These cross sections have been measured well in the lower energy region upto hundred GeV by accelerator experiments. Those beyond the energies of accelerators are model dependent. Thus the composition of the secondary cosmic rays and their energy spectrum is well known upto TeV energies. This gives a good insight into the energy spectrum of the secondary muons produced by the decay of these mesons.

- Energy spectrum of atmospheric neutrinos: The atmospheric neutrinos which are produced during the decay of the secondary muons, in turn will depend on the properties of all the parent particles and their fluxes. To calculate the energy spectrum of these neutrinos, modelling of the interactions in the atmosphere according to altitude, impact of geomagnetic effects on cosmic ray and secondary fluxes and dependence of extensive air showers on longitude have to be done.

The precision with which the atmospheric neutrino flux on the Earth's surface can be determined is limited by the uncertainties in each of the above steps. As a result, an uncertainty of the order of 15–20% is introduced in the overall normalization.

It is interesting to see the zenith angle distributions of unoscillated atmospheric neutrinos at different energies. The fluxes averaged over azimuthal angles for three neutrino energies, calculated for Kamioka where the Super Kamiokande (SK) detector is situated, are shown in Fig. 2.6. From the figure it is evident that the flux is typically maximum in the $\cos\theta = 0$ direction, which is the horizontal direction. The muons have maximum proper time to decay in this direction leading to an increased number of neutrinos as compared to the other directions. It can also be seen that the ratio of the muon to electron neutrino flux also increases with the increase in energy and where the direction is more vertical (for up-coming or down-going neutrinos). This is because the muons have less proper time to decay thus making the second process in Eq. 2.3 less efficient. Another

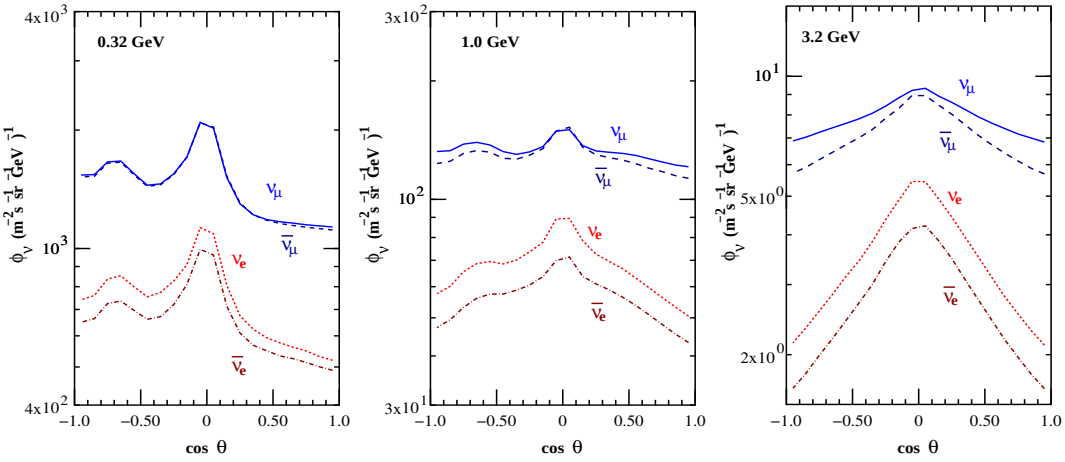

Figure 2.6: Atmospheric neutrino flux distributions averaged over azimuthal angles at three different neutrino energies namely 0.32 GeV, 1 GeV and 3.2 GeV, as a function of zenith angle at the Super Kamiokande site [117]. The flux scales are different for different energies. Here $\cos\theta = -1$ denotes the up-direction.

important observation is that the fluxes are asymmetric at lower energies arising from the bending of muons in the geomagnetic field. As the energy increases the fluxes become more and more symmetric and by 3.2 GeV they are fairly symmetric in zenith angle. Also the neutrino flux at lower energies is much higher than those at higher energies. For this reason, including these events in the oscillation analyses even though their contribution to oscillation sensitivities in ICAL is lesser as compared to the higher energy events, can help constrain the overall normalization of events which will in turn reduce fluctuations.

An important thing to remember is that the Honda flux used for physics analysis presented in this thesis assumes $\phi = 0$ direction as the South. Since the orientation of the ICAL cavern is not fixed right now, it is assumed that the $\phi = 0$ is along the length ($X - axis$) of ICAL and points south. Also according to Honda et al., the direction $-1 \leqslant \cos\theta \leqslant 0$ is the up-coming direction where the oscillation effects are present, whereas in the analysis, presented here, the up direction corresponds to $0 \leqslant \cos\theta \leqslant +1$ to match the convention for NUANCE. Only the notations are different, but physics remains the same. The atmospheric neutrino spectrum at Theni, where INO will be located, has been calculated by Honda et al. [118, 119] recently. However all the analyses presented in this thesis make use of the neutrino flux at Kamioka. The Theni flux has to be incorporated into the analyses and this is a future work which is beyond the scope of this thesis. the effect of this change is expected to be maximal at smaller energies where the Theni flux is smaller than the SK flux.

2.6 Neutrino oscillations relevant to ICAL

The main aim of ICAL detector is to determine the mass hierarchy of neutrinos by studying Earth matter effects during the passage of atmospheric neutrinos through the Earth. It also aims to study the precision measurement of the oscillation parameters θ_{23} and $|\Delta m^2{}_{32}|$. The physics probed by the ICAL will be discussed in this section.

The main aim of ICAL detector is to determine the neutrino mass hierarchy by probing the Earth matter effects. Due to matter effects all the oscillation parameters will be modified in matter as shown in Chapter 1. Since atmospheric neutrinos contain both ν_μ and ν_e in the ratio $\sim$ 2:1, there are many channels of oscillation available for study. Thus the probabilities $P_{\mu\mu}$, $P_{e\mu}$, $P_{\mu e}$ and $P_{\mu\tau}$ and the corresponding anti-neutrino probabilities are relevant in atmospheric neutrino oscillations. These probabilities and matter effects at fixed neutrino energies for normal hierarchy have been illustrated in Fig. 1.2. Depending on the detector resolutions, events from different channels can be detected with high efficiencies. In the case of ICAL, the detector is optimised for muon detection. Hence ICAL is most sensitive to $\nu_\mu \rightarrow \nu_\mu$ and $\nu_e \rightarrow \nu_\mu$ and the $\bar{\nu}_\mu \rightarrow \bar{\nu}_\mu$ and $\bar{\nu}_e \rightarrow \bar{\nu}_\mu$ channels in which the final state of oscillation is a ν_μ or $\bar{\nu}_\mu$. These ν_μ and $\bar{\nu}_\mu$ will interact with the iron in the detector through charged current interactions to give muons and hadrons in the final state. Since muons are minimum ionising particles at these energies, even with the detector configuration of 5.6 cm thick iron plates, they travel long distances in the detector and give a long track bent by the magnetic field according to the charge of the muon. The momentum and direction of these muons can be reconstructed using Kalman filter technique.

Hence it can be said that the ICAL is mainly sensitive to $P_{\mu\mu}$, $P_{e\mu}$, $\bar{P}_{\mu\mu}$ and $\bar{P}_{e\mu}$. The interactions of ν_e and $\bar{\nu}_e$ with iron can happen thus giving electrons, but currently the responses of electrons in ICAL have not been characterised and hence this channel is not considered in the analysis discussed in this thesis. The $\nu_\mu \rightarrow \nu_\tau$ oscillations can also occur but they are also not considered in the analysis discussed here. The analyses are done with charged current muon neutrino and muon anti-neutrino events only.

2.7 Summary

The ICAL detector has been designed in such a way that it is optimised for the detection of muons. As seen in Section 2.4, hadrons are also produced in these neutrino interactions. The most important point to remember about the muons and hadrons in ICAL is that muons leave clean tracks in the detector whereas hadrons leave only a shower in the detector in which the individual hadrons cannot be seen separately. Hence the effect of the magnetic field on these hadrons cannot also be observed in ICAL; any such effect will be washed out by the fact that the shower itself is wide and the hadron responses [20, 21] are worse compared to muon responses [22, 108] in ICAL. Even then the use of hadron energy information as an observable in the oscillation analysis improves the sensitivities tremendously [27]. Hence it is necessary to obtain the energy and direction responses of hadrons in ICAL. Detailed simulations of the hadron energy and direction responses in ICAL are presented in Chapters 3 and 4.

Even if the inclusion of hadron energy as a new observable increases the sensitivities of ICAL to oscillation parameters, these studies have earlier been done in the restricted energy range of 1–11 GeV of the observed muons. But it is very important to use the detector to its full potential. Hence a study on the oscillation parameters by extending and optimising the observed muon energy range is interesting. The detailed discussion about the effect of extending the energy range of observed muons on oscillation sensitivities of ICAL is presented in Chapter 6. In addition to extending the energy range, the effect of constraining the ν_μ-$\bar{\nu}_\mu$ flux ratio on oscillation sensitivities is also reported. It is seen that these further improve the precisions obtainable with the ICAL detector. It is worthwhile noting that despite having a simple geometry and the resolutions as will be discussed in the upcoming chapters, the physics potential of ICAL is simply awesome because of it being such a massive detector and most importantly magnetisable. This feature makes ICAL the best detector which can precisely determine mass hierarchy by making use of a very simple technique without having to worry about any other complications.

Part II

Simulation studies of the ICAL detector in a GEANT-4 based framework

3 Simulation studies of hadron energy response of the ICAL

3.1 Overview

Hadrons are produced in the final state during both the charged current and neutral current interactions of neutrinos and anti-neutrinos with the iron target in ICAL. To reconstruct the energy and direction of the incoming ν_μ and $\bar{\nu}_\mu$ it is essential to reconstruct the energies and directions of the muons and hadrons. Even though the ICAL detector is optimised for the detection of muons which leave clean tracks in the detector [22], the hadrons also leave their information as showers in the detector. Although ICAL cannot distinguish individual hadrons from one another, it is very important to study the energy and direction responses of these hadrons since they will provide additional information which will enhance the sensitivity of the ICAL detector to oscillation parameters [27]. Hadrons play a very crucial role in oscillation studies and it is necessary to extract as much information from them as possible.

This chapter mainly focuses on the simulation studies of hadron energy response of the ICAL detector. Detailed discussions on how to use the total number of hits in the hadron shower to calibrate hadron energy and an appropriate functional form which describes the hadron hit distributions at various energies are presented. It is also important to improve the hadron energy resolutions to further improve the sensitivity of the detector. The study of the effect of varying iron plate thickness on the hadron energy response is also discussed in detail. A study of the e/h ratio of the detector is also performed and reported in this chapter.

3.2 Hadrons in ICAL

When a neutrino interacts with the target nuclei inside the detector, it produces hadrons along with the final state lepton in the detector. There are both charged current and neutral current interactions of (anti-)neutrinos mainly via three different processes namely

quasi-elastic (QE), resonance (RES) and deep inelastic scattering (DIS). These can be represented as (shown in Table 3.1) : Here l is the charged lepton, N, N' are nucleons, and X

Processes	CC	NC
QE	$\overset{(-)}{\nu_l} N \rightarrow l^{\overset{(+)}{-}} N'$	$\overset{(-)}{\nu_l} N \rightarrow \overset{(-)}{\nu_l} N'$
RS & DIS	$\overset{(-)}{\nu_l} N \rightarrow l^{\overset{(+)}{-}} X$	$\overset{(-)}{\nu_l} N \rightarrow \overset{(-)}{\nu_l} X$

Table 3.1: The neutrino interaction processes.

corresponds to any set of possible final hadrons. In RES X typically corresponds to a pion and a nucleon , and multiple hadrons in DIS interactions. Since coherent interactions and interactions with electrons in the detector are rare at these energies, they are ignored.

It is necessary to have as precise reconstruction of the energies of the final state particles as possible to determine the oscillation parameters correctly. The response of muons has been studied elsewhere [22] and is briefly discussed in Chapter 5. To estimate the energy response of hadrons in ICAL, the hit information of these hadrons are used. It should be noted that ICAL cannot distinguish between individual hadrons due to its large pixel size of (2.8 cm $\times$ 2.8 cm) in X-Y direction and 9.6 cm in the Z direction. Also the total energy deposited cannot be measured calorimetrically by measuring the charge deposited. Hence the only way to estimate the hadron energy is to count the total number of hits at each energy and calibrate these hits to the energies. To study the response, fixed energy single pion events were first simulated at different energies in the GEANT4 based ICAL simulation code. Similarly to calculate the direction resolution of hadrons the hit information combined with the hit timing is used. This chapter thus highlights the main simulation results of hadrons (mainly pions) in ICAL.

3.3 General information about hadrons in ICAL

In any neutrino (or anti-neutrino) interaction, hadrons can be produced as described in Table 3.1. Of the different hadrons produced, 85% are pions (including charged ($\pi^{\pm}$) and neutral pions (π^0)) on the average. The rest consist of kaon, nucleons and the recoil nucleon. But this recoil nucleon is indistinguishable from the rest of the hadronic final state. Neutral pion decays within about $8.52 \times 10^{-17} s$ [120] into two gammas whereas the charged pions propagate through the detector and produce a cascade because of strong interactions. The visualization (using VICE event display program [121]) of a neutrino

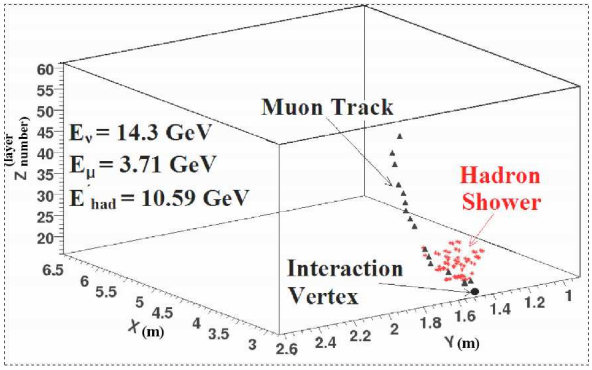

Figure 3.1: A charged current muon netrino interaction in ICAL. The incoming muon neutrino interacts with the iron in the detector to prodce a final state muon which gives a long track and hadrons which shower in the detector. The energy of the hadrons can be expressed as $E'_{had} = E_\nu - E_\mu$, where E_ν is the energy of the incoming neutrino and E_μ is the final state muon energy.

event generated using NUANCE (version 3.5) [24] and propagated through the simulated ICAL detector is shown in Fig. 3.1.

The major uncertainty in the determination of incident neutrino energy arises from that in the estimation of the energy of the final state hadrons. The energy balance for the the interaction $\nu_\mu N \rightarrow \mu X$ is given by :

$$E_\nu + E_N = E_\mu + E_{had} + E'_N, \tag{3.1}$$

where E_N is the initial nucleon energy when the nucleon is at rest, neglecting its small Fermi momentum and E'_N is the recoil nucleon energy which is indistinguishable from the energy E_{had} in the remaining hadrons. Hence for the calibration of detector response for multiple hadrons, the energy of observed hadrons is defined as

$$E'_{had} = E_\nu - E_\mu. \tag{3.2}$$

The detector response for hadrons has been calculated for both fixed energy single pions and multiple hadrons from neutrino interactions [20]. Let us look in detail how the energy response is computed for fixed energy single pions in ICAL, with the help of the GEANT4 based ICAL simulation.

3.4 Energy resolution of hadrons

As discussed in Section 3.3, since majority of the hadrons produced in neutrino interactions are pions, it is appropriate to study the energy response using fixed energy single

pions in the detector. For this purpose ICAL detector with iron plate thickness of 5.6 cm was simulated, and fixed energy single pions at different energies were propagated through the detector. To have a good statistics, 10000 events each were generated for each energy in the energy range 1 – 15 GeV, with vertices of the pions inside the fiducial volume 2 m $\times$ 2 m $\times$ 2 m in the central region of the detector. The energy range 1 – 15 GeV is chosen since this is the range of energies of interest of hadrons from atmospheric neutrino interactions. ICAL detector is not uniform in geometry. To prevent the geometry from affecting the energy resolution studies, an angle averaged calculation is done for this study. The zenith angle θ is smeared from $0 - -\pi$ were as the azimuth ϕ is smeared from 0–2π. The results presented in this section are average results. (A reference frame with the center of the detector taken as the origin is used to denote the angles. Here Z axis points vertically up and the plates are horizontal in the $X - Y$ plane.) When a charged particle passes through the detector whose active detector element is the RPC, it ionises the gas in the RPC and the charge is collected on both sides of the chamber with the help of copper strips. There are pick up strips of width 1.96 cm each, both in X and Y directions, placed perpendicular to each other above and below the glass plates so as to form pixels of size 1.96 cm $\times$ 1.96 cm. Signal can be collected from each strip and it is called a *hit*. This hit carries the $X - Y$ information and the layer number gives the information of the Z direction. The hits from either the X strips only, namely X_{hits} or from Y strips, namely Y_{hits} only can be chosen for analysis. It is possible that a particle gave a signal in say X strip and did not give in Y strip. So to avoid any ambiguity, the larger among these in each plane is chosen and is called *orighits* (i.e., orighits $= \max(X_{hits}, Y_{hits})$ if $X_{hits} > Y_{hits}$). It can be seen that the distributions of all these quantities are similar as shown in Fig. 3.2, still it is preferable to use the *orighits* for analysis to avoid any bias. Unless otherwise stated, the variable orighits is going to be used hereafter for all the calibration purposes.

The hit distributions of pions, kaons, and protons at different energies in the range 1 – 15 GeV are illustrated in Fig. 3.3. The hit patterns of the hadrons are similar, even though the peak position and spread depend on the particle. Because of this similarity and the large pixel size (1.96 cm $\times$ 1.96 cm) of ICAL in the $X - Y$ direction, individual hadrons cannot be distinguished from one another in the detector. There is a large variation in the number of hits for the same incident energy for different particles. This may be attributed partly to the smearing in angle and more dominantly due to strong interaction by means of which the hadrons interact with the detector elements. The distribution of neutral

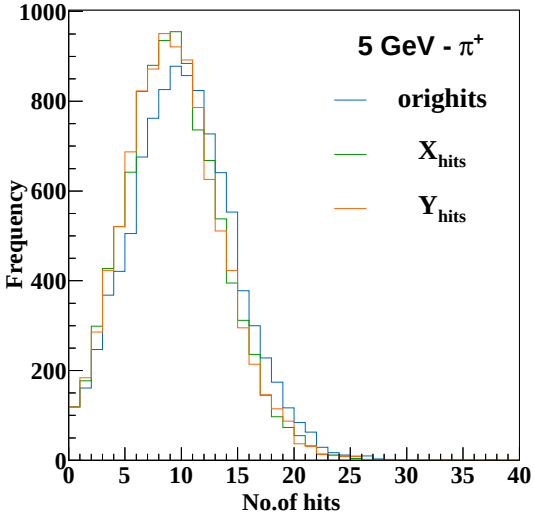

Figure 3.2: Distributions of X_{hits}, Y_{hits} and orighits for a 5 GeV π^+.

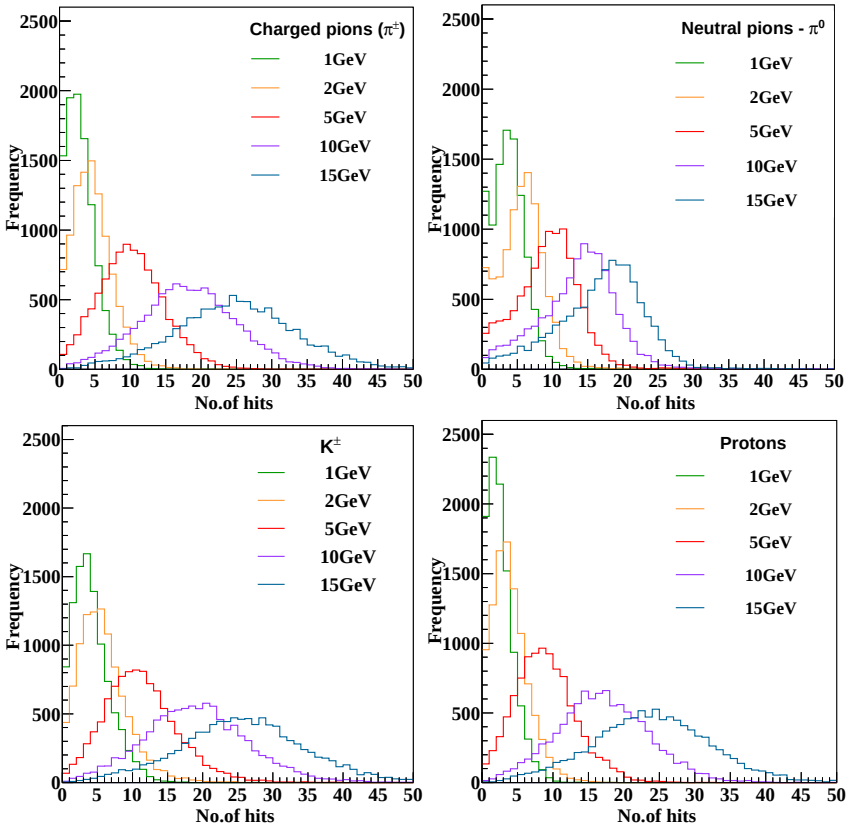

Figure 3.3: Hit distributions of at different energies (angle averaged) for charged ($\pi^{\pm}$) and neutral pions (π^0), kaons ($K^{\pm}$) and protons propagated from vertices in the central 2 m $\times$ 2 m $\times$ 2 m volume.

pions is an exception though, since it decays immediately into an e^+e^- pair, and this shower is actually electromagnetic rather than hadronic. In fact the distribution of π^0, electrons and gammas are identical. This will be discussed later in detail.

3.4.1 Energy response from hit pattern

Since hadrons form a shower and leave only hits in the ICAL detector , energy calibration has to be done using the hit distribution only. The hit distributions of single charged pions at two different energies are shown in Fig. 3.4.

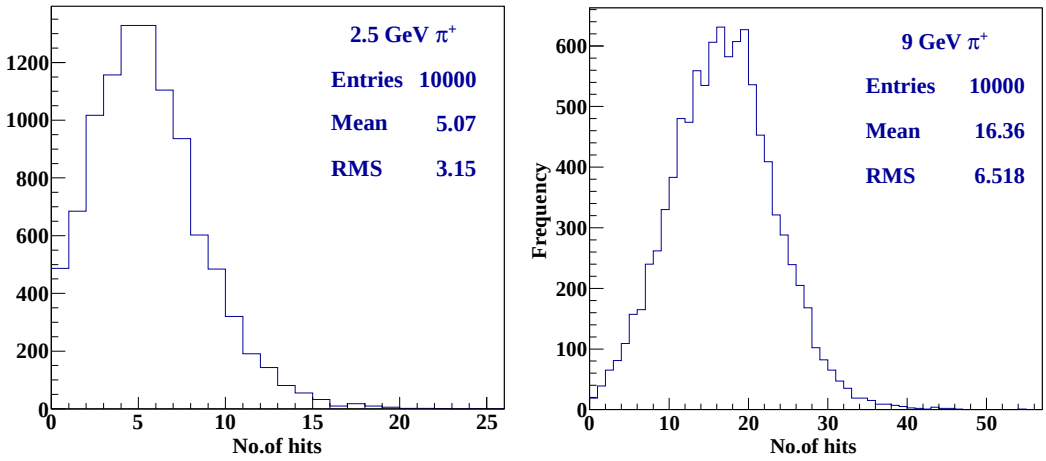

Figure 3.4: Hit distributions of single pions of energy 2.5 GeV (left) and 9 GeV (right) propagated from vertices randomised in the volume 2 m × 2 m × 2 m in the centre of the detector. It can be seen that the distributions are not symmetric but have long tails.

The distributions are not symmetric about the mean, but have long tails. The hit distributions at lower energies peak towards the low hit region which implies that there are fewer hits in the detector at lower energies, because of the presence of iron plates which are 5.6 cm thick. The particles of low energies cannot travel large distances and do not give signals in RPCS. As the energy increases, the particles are able to travel longer inside the detector and hence the hit distribution shifts to the right and becomes more symmetric. The tail in the distribution is due to the energy loss mechanisms inside the detector.

3.5 Energy resolutions of pions in ICAL

The behaviour of π^+ and π^- events were found to be similar in the detector. The arithmetic mean and RMS of the hit distributions of π^+ and π^- in the energy range 1 – 15 GeV are shown in Fig. 3.5. As expected the mean number of hits for π^+ and π^+ are identical within statistical fluctuations. Hence only π^+ have been used for all the analyses presented in the following sections.

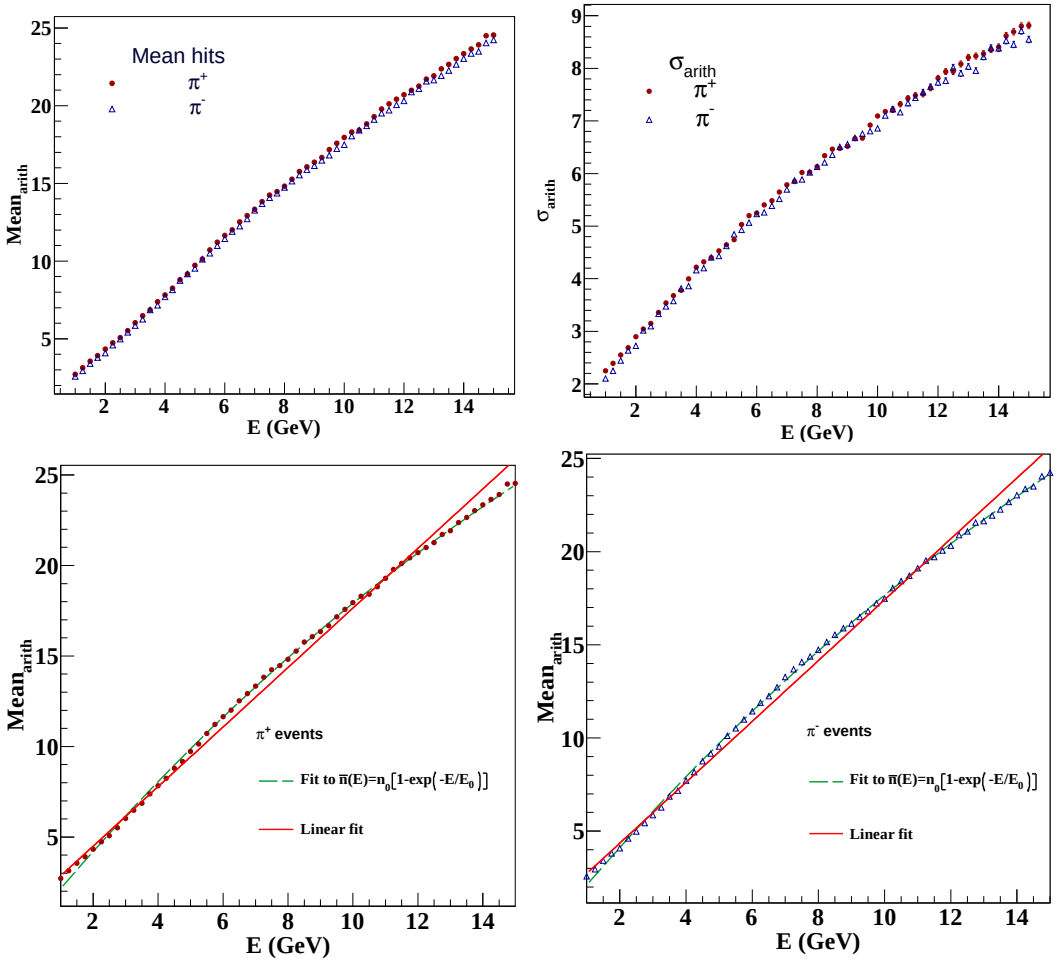

Figure 3.5: Arithmetic mean (top left) and sigma (top right) of hit distributions for π^+ and π^- at different energies, in 5.6 cm iron. It can be seen that the quantities are similar for both π^+ and π^-. The arithmetic means fitted with both Eq. 3.3 and linear fit are shown in the bottom panels, for π^+ (bottom left) and π^- (bottom right) respectively.

From Fig. 3.5 it can be seen that the arithmetic mean $\bar{n}(E)$ of the number of hits increases with increasing pion energy, and saturates at higher energies. It can be approximated by

$$\bar{n}(E) = n_0[1 - \exp(-E/E_0)], \tag{3.3}$$

where n_0 and E_0 are constants; n_0 and E_0 are sensitive to the energy ranges of the fit. The value of E_0 is found to be $\sim$ 30 GeV. Since the energies of interest for atmospheric neutrinos are much less than E_0, we may use Eq. (3.3) in its approximate linear form $\bar{n}(E) = n_0 E/E_0$. Fig. 3.5 also shows a fit to this linear form.

In the linear regime where ($E \ll E_0$),

$$\frac{\bar{n}(E)}{n_0} = \frac{E}{E_0}, \tag{3.4}$$

Hence the energy resolution may be written as

$$\frac{\sigma}{E} = \frac{\Delta n(E)}{\bar{n}(E)}, \tag{3.5}$$

where Δn is the RMS width of the distribution. Here onwards the notation σ/E will be used for energy resolution, and use Eq. (3.5) for the rest of the analysis.

The energy resolution of pions may be parametrized by

$$\frac{\sigma}{E} = \sqrt{\left(\frac{a}{\sqrt{E}}\right)^2 + b^2}\,, \tag{3.6}$$

where a and b are constants. The former constant a is often referred to as the stochastic coefficient (which incorporates both statistical and systematic uncertainties).

Mean and sigma of the hit distributions can be obtained as the arithmetic mean ($Mean_{arith}$) and sigma σ_{arith} or as the mean and sigma of a Gaussian fit ($Mean_{gaus}$ and σ_{gaus}) to the distribution. The hit distributions at 2.5 GeV and 9 GeV for π^+, fitted with Gaussian function are shown in Fig. 3.6. From the figure it can be seen that at lower en-

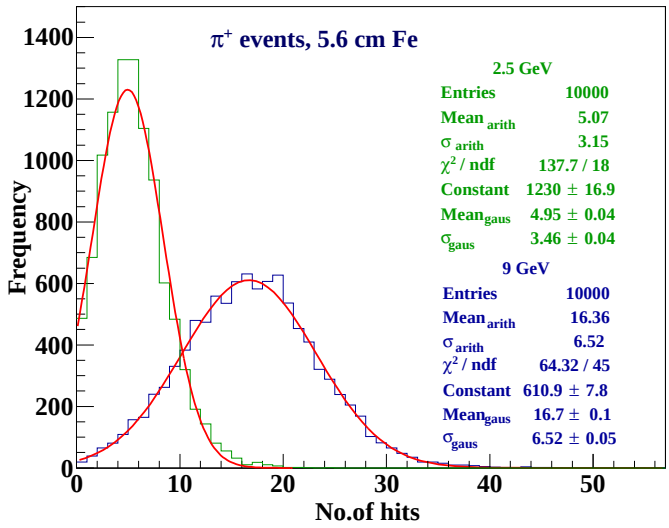

Figure 3.6: Hit distributions of 2.5 GeV and 9 GeV π^+, fitted with Gaussian function. The distribution being asymmetric at 2.5 GeV is not well approximated with a Gaussian, whereas at 9 GeV , it is. This can be attributed to the fact that there are lesser number of hits at lower energy whereas the number of hits increases as the energy increases.

ergies the distribution is asymmetric and doesn't fit well to the Gaussian, but at higher energies, Gaussian approximates the distribution very well. At lower energies the distribution has a tail towards the right. The hit distribution is made asymmetric by the low number of hits at low energies; as the energy increases, there are more number of hits and

the distribution shifts to the right, making it more symmetric. Thus at higher energies Gaussian can approximate the hadron hit distribution better than at lower energies.

The resolution of hadrons can be obtained either using the Gaussian mean and sigma ($Mean_{gaus}$ and σ_{gaus} obtained from fitting the hit distribution with a Gaussian or by simply using the arithmetic mean and sigma ($Mean_{arith}$ and σ_{arith}) of the distribution itself. It is seen that the latter gives a better resolution than the former. This is illustrated in Fig. 3.7; the resolutions are obtained in the 1 – 15 GeV energy range. Since the results for

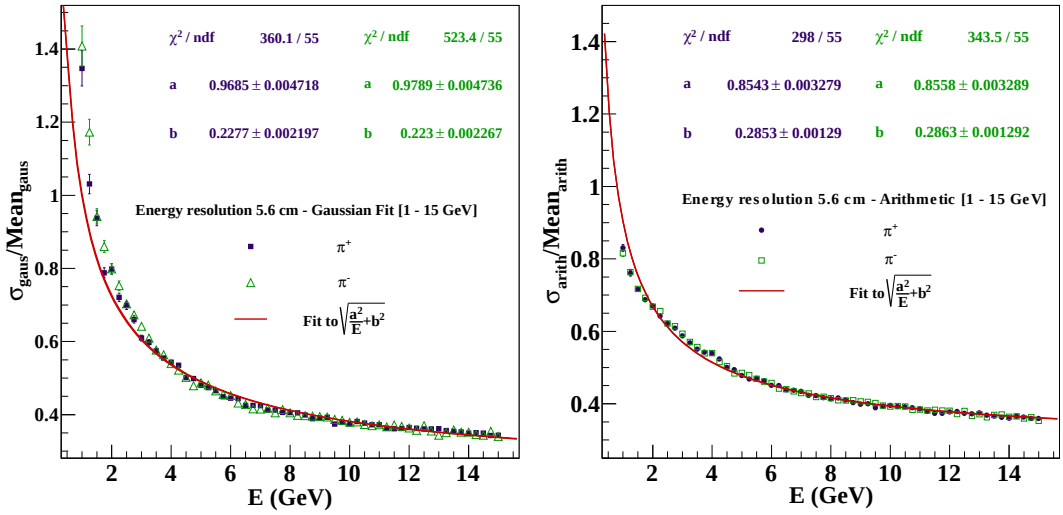

Figure 3.7: Resolutions of both π^+ and π^- in the energy range [1 – 15 GeV] obtained by fitting (left) $\sigma_{gaus}/Mean_{gaus}$ with Eq. 3.6 and (right) $\sigma_{arith}/Mean_{arith}$ with Eq. 3.6 respectively. It can be seen that Gaussian parameters give worse resolution than the arithmetic ones, since the Gaussian doesn't approximate the hit distribution well at low energies. It is evident from the left panel also that Gaussian mean and sigma result in worse energy resolution.

π^+ and π^- are similar, from now onwards analysis with π^+ only will be described unless otherwise specified. Since the Gaussian function doesn't fit the hit distribution well, it is not a good choice to describe the distribution itself. A function which can describe the hit distribution well both at high and low energies of interest here has to be used. It is found that the Vavilov function is a very good function for this purpose. It fits well to the asymmetric hit distributions below 6 GeV and tends to a Gaussian at energies above that. Hence it reproduces the width of the distribution accurately and provides an energy resolution which matches the one obtained directly from the arithmetic parameters. Details of this study are presented in [20]; more details on the Vavilov distribution are given in Appendix A.

The Vavilov distribution is parametrised by four parameters P_i, where i = 0, 1, 2 and 3 (Appendix A). Here P_0 is equivalent to κ and P_1 to β^2. The fifth parameter P_4 is the

normalisation factor. Given these parameters the hit distribution at a given energy can be reconstructed. The fit parameters as a function of energy are shown in Fig. 3.8.

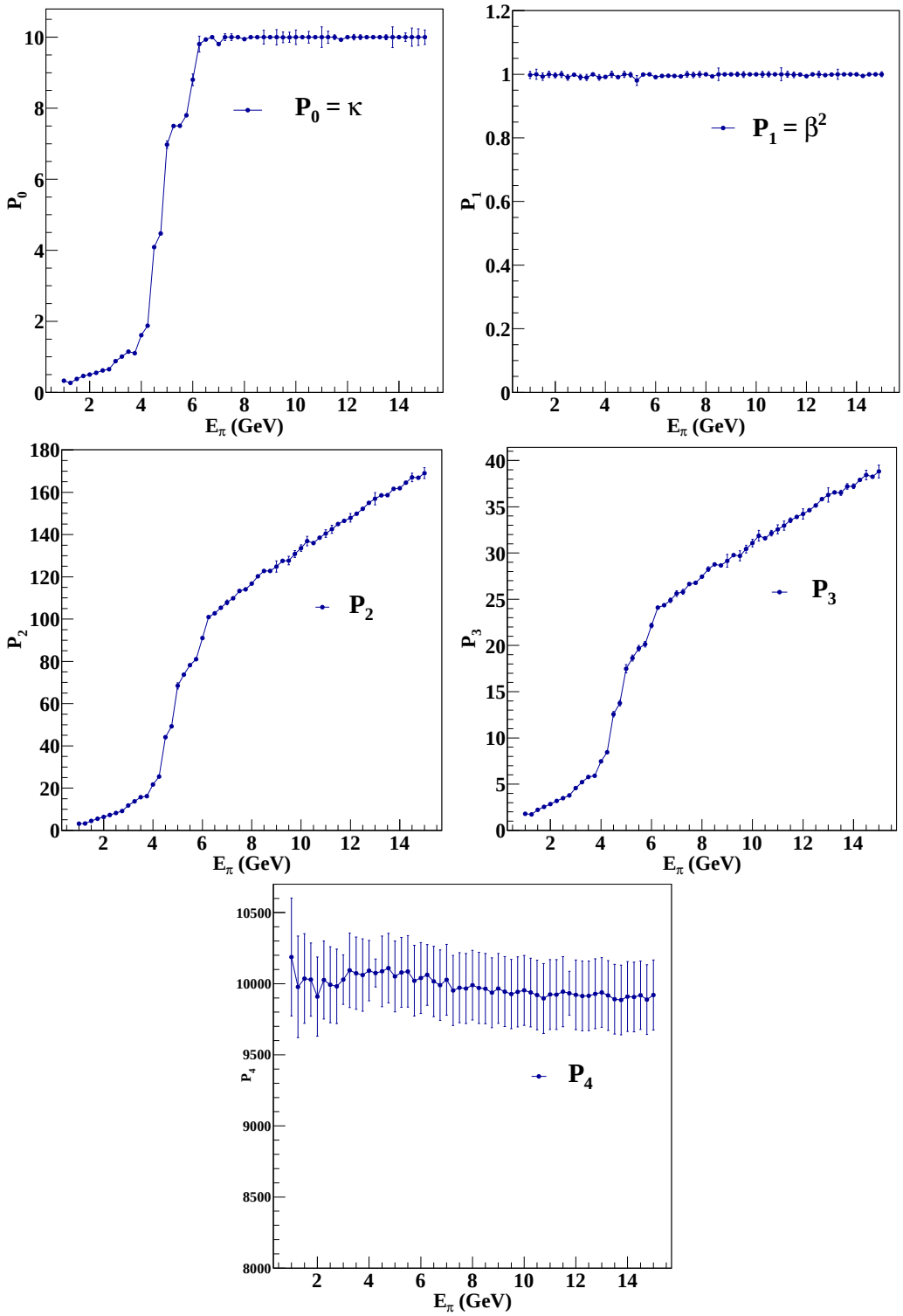

Figure 3.8: Fit parameters P_0, P_1, P_2, P_3 and P_4 of the Vavilov fit to the single pion hit distributions at different energies. From the value of P_0 at different energies, it can be seen that till about 6 GeV the hit distributions are Vavilov and approximate to Gaussian distribution after that. The fifth parameter P_4 is the normalisation factor.

For values of $\kappa \geqslant 10$, the vavilov distribution reduces to a Gaussian distribution; this is true for pion energies $E \geqslant 6$ GeV. This can be seen from Fig. 3.8. However at $E < 6$ GeV, the hit distributions have to be fitted with Vavilov function to reproduce the correct mean and sigma.

The comparison of the mean and sigma obtained from Vavilov fit, ($Mean_{vav}$ and σ_{vav}) with corresponding Gaussian and arithmetic quantities as functions of energy E (GeV) are shown in Fig. 3.9. From the figure it can be seen that both vavilov mean and sigma match with the corresponding arithmetic quantities in the entire energy range, whereas the Gaussian sigma σ_{gaus} never matches with the sigma of the actual hit distribution in the lower energy range [1–5.75 GeV]. Also, upto about $\sim$ 2 GeV, the Gaussian mean $Mean_{gaus}$ is less than the arithmetic mean $Mean_{arith}$, suggestive of the fact that the Gaussian distribution does not fit the hit distribution well at these energies and it is ideal to use the Vavilov function for fitting purposes.

In the higher energy region [6–15 GeV], the Gaussian mean is always slightly above the arithmetic mean, whereas the latter is matched by the Vavilov mean within error bars. Upto about $\sim$ 9.5 GeV, σ_{arith}, σ_{vav} and σ_{gaus} match very well within error bars, whereas beyond this energy, σ_{arith} is slightly higher than the other two. It should be noted though that Vavilov sigma approximates to Gaussian sigma and the two curves match. Hence Vavilov distribution is seen to fit the hit distribution well at all energies. The single pion energy resolution obtained by fitting $\sigma_{vav}/Mean_{vav}$ with Eq.3.6 is shown in Fig. 3.10.

Thus the Vavilov distribution function proves to be a very good candidate to fit the hit distribution of single pions. A similar study was conducted for multiple hadrons produced in neutrino interactions [20]. The hit distributions were fitted with Vavilov distribution and the fit parameters were obtained as for fixed energy single pions. These parameters are used to reconstruct the hadron hit distribution to smear the energy of hadrons in the physics analysis reported in Chapter 6. The study of energy response of multiple hadrons are reported in detail elsewhere [122]. However, in the succeeding sections, arithmetic mean and sigma ($Mean_{arith}$ and σ_{arith}) are used for analysis since they are not biased.

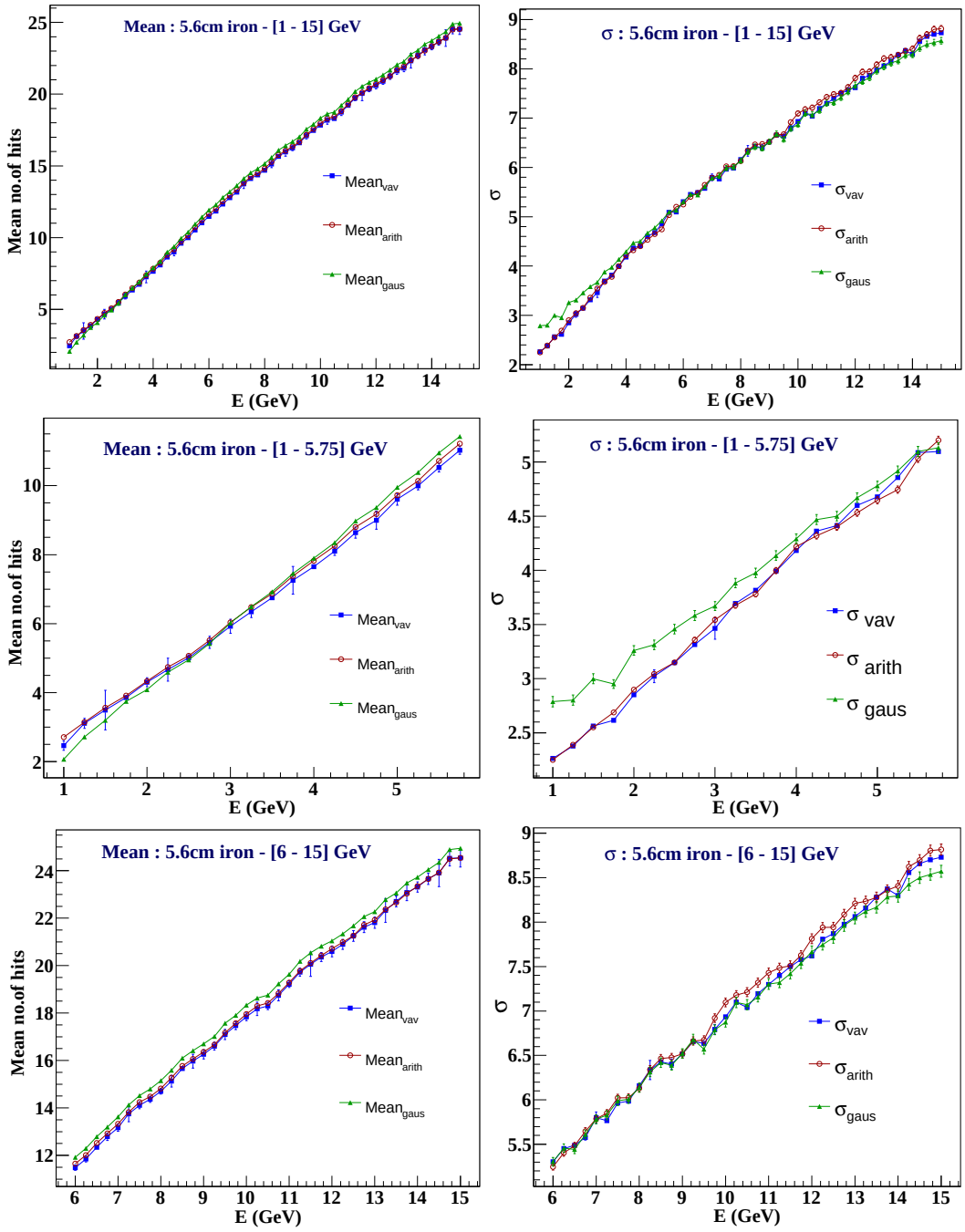

Figure 3.9: Comparison of Vavilov, arithmetic and Gaussian mean no.of hits (left) and sigmas (right) of pion hit distributions. The top panel depicts the values in the energy range [1 – 15 GeV] whereas the middle and bottom panels show those in the [1 – 5.75 GeV] (lower) and [6 – 15 GeV] (higher) energy ranges separately.

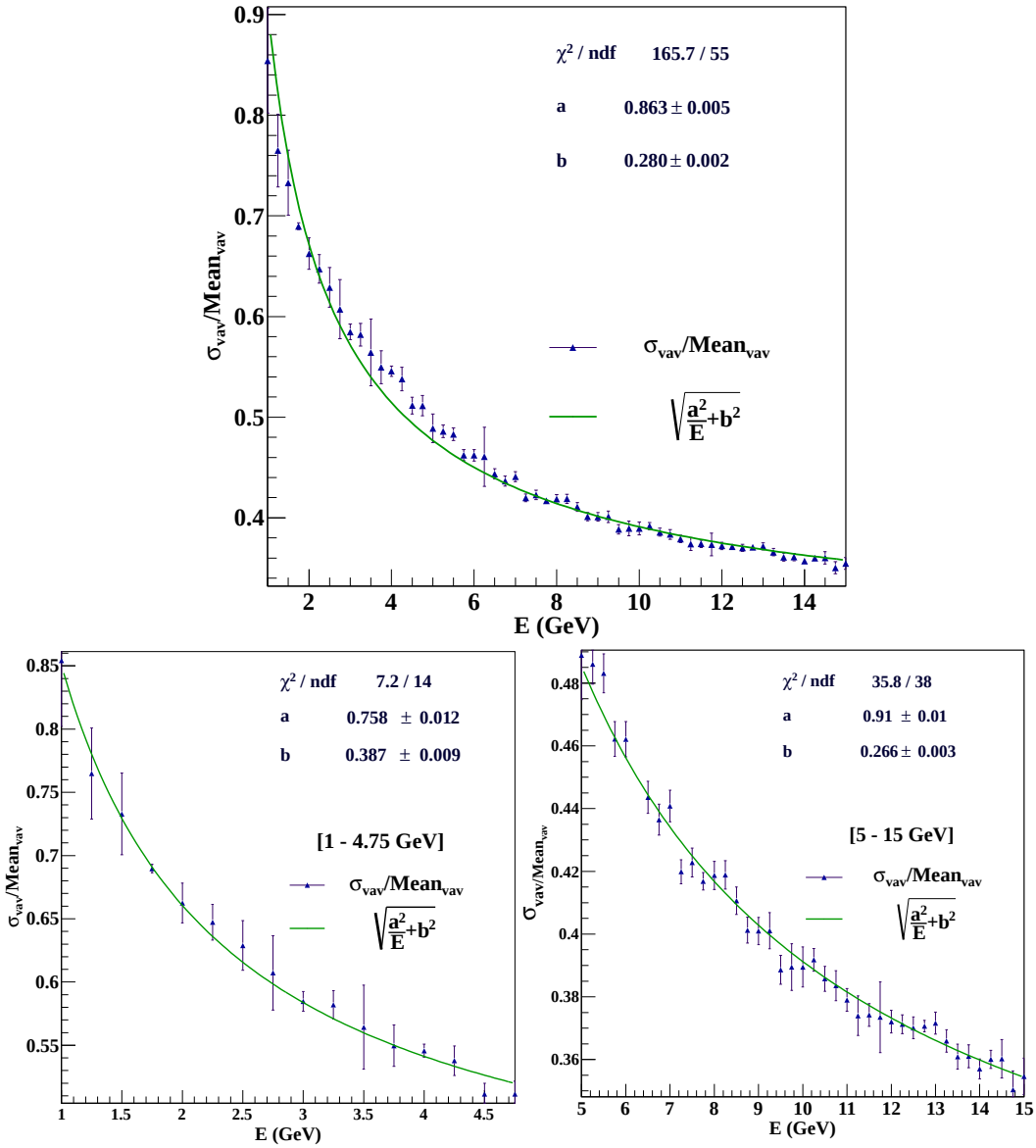

Figure 3.10: Energy resolution obtained by fitting $\sigma_{vav}/Mean_{vav}$ with Eq. 3.6, in the [1–15 GeV] energy range. It can be seen that the resolution obtained using Vavilov mean and sigma is similar to that obtained using the corresponding arithmetic quantities as shown in Fig. 3.7. The full energy range [1 – 15 GeV] can be split up into a lower and higher energy range to consider different processes. Bottom left and right panels show the energy resolutions in two separate energy ranges namely [1 – 4.75 GeV] which is the lower energy range and [5 – 15 GeV], the higher energy range respectively.

3.6 Hadron energy resolution as a function of iron plate thickness

This section will deal with the study of dependence of energy resolution on the thickness of the absorber, which is iron in ICAL, used in the detector. This study is relevant in terms of improvement of the resolution of hadrons, and thus the information it provides. The physics reach of INO ICAL is significantly improved by the addition of hadron energy information, as can be seen in Ref. [27]. Thus hadron energy resolution plays a crucial role in the study of oscillation parameters with ICAL. Hence it is important to investigate about and implement any possible detector configuration which can add information thus improving the reach of ICAL. The study of thickness dependence of hadron energy resolution is one such study in this direction. Even when improving the resolution of the detector is of interest to the physics to be probed by the ICAL, it is important that it be cost effective and hence the size, geometry and structural stability of the detector be optimised. It is also important that these studies be done specifically for the ICAL detector, which primarily is an atmospheric neutrino detector, in which the hadrons produced in the final state have energies of the order of a few GeVs as compared to those detected by dedicated hadron calorimeters in collider experiments [123–126]. There the hadrons have energies ranging from tens of GeVs to hundreds of GeVs and these studies indicate a square root dependence on the thickness t of the hadron energy resolution on the absorber thickness. The work on the thickness dependence of hadron energy resolution of the ICAL detector presented here intended to study the effect of plate thickness on the energy response of hadrons in the few GeV energy range and is of interest to neutrino experiments, which is otherwise not widely discussed in literature.

The current default geometry of ICAL has 5.6 cm thick iron plates stacked in 151 layers in the vertical (Z) direction. The total height of ICAL is 14.45 m. For the study of thickness dependence of hadron energy resolution, 11 thicknesses namely 1.5 cm, 2 cm, 2.5 cm, 3 cm, 3.5 cm, 4 cm, 4.5 cm, 5 cm, 5.6 cm, 6 cm and 8 cm have been considered. The plate thickness is changed in the GEANT4 simulation code keeping the height of the detector same. This means that the number of layers will vary accordingly. The simulations study has been conducted using both single pions generated using GEANT4 particle gun and also hadrons from NUANCE neutrino events. The detailed study presented is however using single pions. Since arithmetic mean ($Mean_{arith}$) and sigma (σ_{arith}) provide unbiased results, energy resolutions have been calculated using these quantities using

Eq. 3.5. Unlike in section.3.5, the square of the expression is used. Hence the energy resolution can be rewritten as :

$$\begin{aligned} \left(\frac{\sigma}{E}\right)^2 &= \left(\frac{\sigma_{arith}}{Mean_{arith}}\right)^2 \\ &= \left(\frac{a}{\sqrt{E}}\right)^2 + b^2 \,, \end{aligned} \tag{3.7}$$

which gives a linear relation between $(\sigma/E)^2$ and $1/E$ with a^2 as the slope and b^2 as the intercept. The parameters a and b are in general, thickness dependent.

3.6.1 Thickness dependence of energy resolution of fixed energy single pions

To study the dependence of the energy resolution of single pions on iron plate thickness, fixed energy single pions generated using GEANT4 simulation package are propagated through ICAL with different plate thicknesses. Again fixed energy single positive pions (π^+) have been used for the analysis. To obtain the hit information, fixed energy single pions are propagated from random vertices inside a volume of 2 m $\times$ 2 m $\times$ 2 m in the central region of the ICAL. This is to ensure that the events are completely contained inside the detector to avoid biasing the results due to edge effects. The direction of propagation is determined by their zenith angle θ and the azimuthal angle ϕ. The detector is geometrically oriented such that the x-axis corresponds to $\phi = 0$ and the z-axis corresponds to the vertically up direction, with $\theta = 0$. Unless otherwise specified, θ is smeared from 0 to π and ϕ from 0 to 2π in order to determine energy resolutions averaged over all directions. Energy of single pions is varied from 2 GeV to 15 GeV in steps of 0.25 GeV without smearing. For each energy and plate thickness, 10000 events are simulated.

The hit distributions at 5 GeV in all the different iron plates are shown in Fig. 3.11. As discussed in Section , the variable *orighits* has been used here also. It can be seen that the distributions are narrower for larger thicknesses implying that the particles travel short distances in thicker iron plates. The distributions become wider and shift to the right with decreasing plate thickness since particles can travel longer distances and hence leave more hits in the detector. Thus the mean number of hits is the least for 8 cm which is the thickest plate in this analysis and most for 1.5 cm, which is the thinnest plate. The detector magnetic field doesn't affect the hit distribution. This is due to the nature of the development of the shower and multiple scattering effects in the case of hadrons.

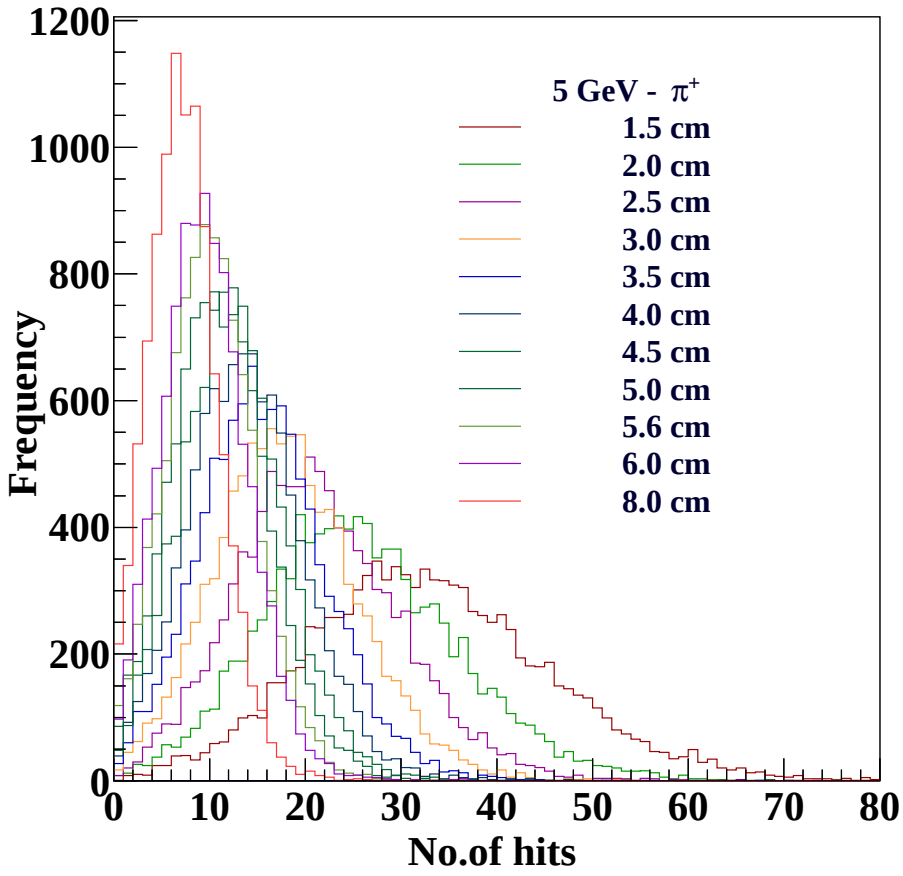

Figure 3.11: Hit distributions of 5 GeV single pions (π^+) in eleven different iron plate thicknesses.

The arithmetic mean ($Mean_{arith}$) and sigma (σ_{arith}) of the hit distributions as functions of energy in the range [2 – 15 GeV] for all the thicknesses are shown in Fig. 3.12. The mean number of hits increases with the increase in energy and also with decreasing plate thickness. This is because the particles travel more distances with increasing energy. On decreasing the plate thickness, they travel more distance through the active detector thus leaving more detectable hits in the hadron shower. The energy range [2 – 15 GeV] is further subdivided into two namely the low energy range from [2 – 4.75 GeV] and the high energy range [5 – 15 GeV]. In the former, all processes including quasi-elastic (nucleon recoil), resonance and deep inelastic scattering can contribute to a comparable extent to hadron production when a neutrino (or anti-neutrino) interacts in the detector. The high energy region is dominated by hadrons created via deep inelastic scattering. The mean number of hits and sigma of the hit distributions in these energy ranges are also shown in Fig. 3.12.

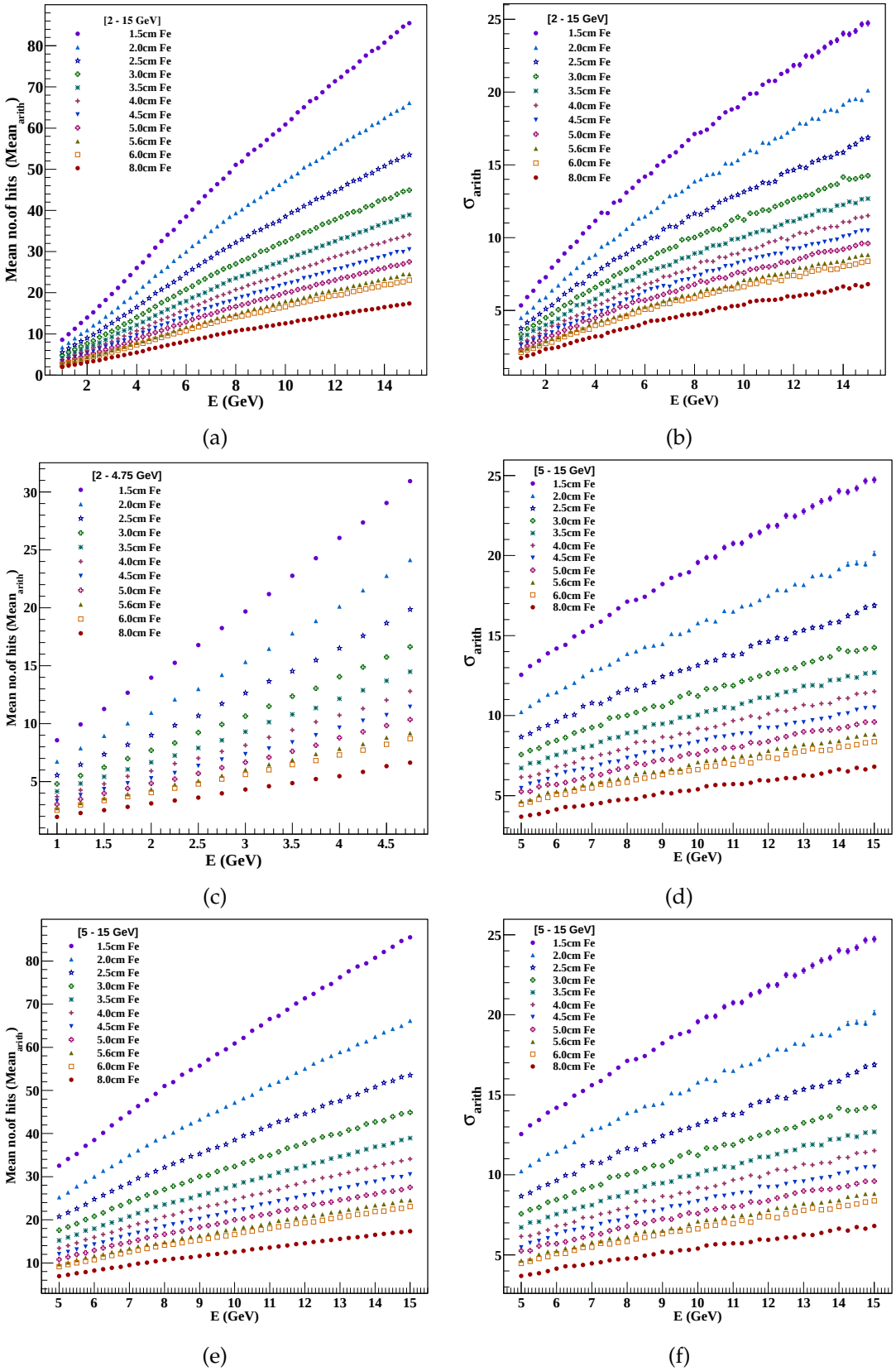

Figure 3.12: Left panels (a), (c) and (e) show the mean no.of hits ($Mean_{arith}$) in the energy ranges [2 – 15 GeV], [2 – 4.75 GeV] and [5 – 15 GeV] respectively, whereas the right panels (b), (d) and (f) show σ_{arith} in [2 – 15 GeV], [2 – 4.75 GeV] and [5 – 15 GeV] respectively; as functions of pion energy in GeV for different thicknesses. The Y-axes on the left panel are different.

Hadron energy resolution can be written as $\sigma_{arith}/Mean_{arith} = f(E,t)$ and its square is fitted to the form given in Eq. 3.7, where t is the absorber thickness (here iron plate thickness) in cm (which can alternatively be parametrised as t/t_0 where t_0 is a test thickness; here $t_0 = 1cm$. The specific functional form of the thickness dependence of the parameters a and b on the RHS of Eq. 3.7 has to be determined. Prior to this the values of a and b for different thicknesses should be determined separately in the low and high energy ranges.

3.6.1.1 Energy range [2 – 4.75 GeV]

Measurement of hadrons produced in this low energy range is crucial for atmospheric neutrino oscillations studies in ICAL detector. The quantity $(\sigma_{arith}/Mean_{arith})^2$, for the thicknesses from 1.5–8.0 cm, plotted as a function of $1/E$, where E is the pion energy in GeV, is shown in Fig. 3.13. The values of a and b obtained from the fit to Eq. 3.7 is shown

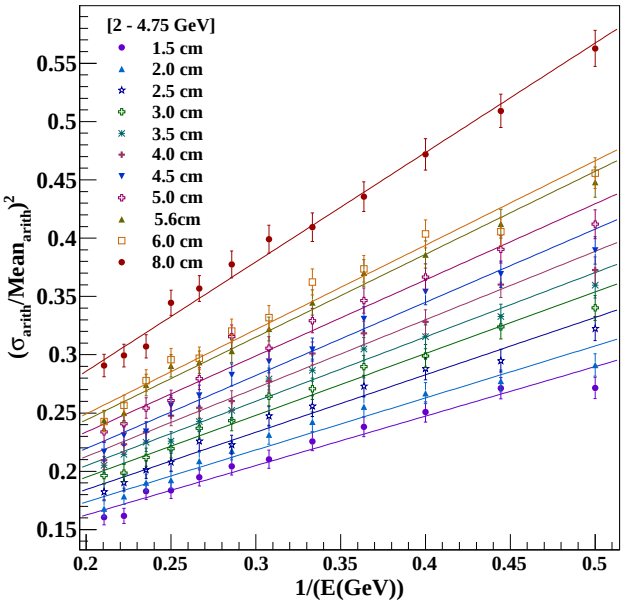

Figure 3.13: Plots of $(\sigma_{arith}/Mean_{arith})^2$ vs $1/E(GeV)$, where E is the pion energy in GeV, in the low energy range [2 – 4.75 GeV], for all thicknesses.

in Table. 3.2. It can be seen that a increases significantly with thickness. This is evinced by the increase in slope ($= a^2$) of the fit with thickness, with a increasing from $a = 0.651$ to $a = 0.969$ with the increase in thickness. However, the variation in b is only slight compared to that of a, with the value of b varying from $b = 0.279$ to $b = 0.313$ only.

t (cm)	a	b
1.5	0.651 ± 0.020	0.279 ± 0.015
2.0	0.668 ± 0.021	0.291 ± 0.015
2.5	0.702 ± 0.021	0.293 ± 0.015
3.0	0.728 ± 0.021	0.299 ± 0.016
3.5	0.743 ± 0.021	0.307 ± 0.016
4.0	0.766 ± 0.021	0.309 ± 0.016
4.5	0.792 ± 0.021	0.307 ± 0.017
5.0	0.808 ± 0.021	0.321 ± 0.017
5.6	0.843 ± 0.021	0.319 ± 0.017
6.0	0.851 ± 0.021	0.323 ± 0.017
8.0	0.969 ± 0.021	0.313 ± 0.020

Table 3.2: Fit parameters a and b obtained by fitting $(\sigma_{arith}/Mean_{arith})^2$ with Eq. 3.7, in the energy range [2 – 4.75 GeV].

3.6.1.2 Energy range [5 – 15 GeV]

The higher energy region is studied separately to probe a possible stronger E-dependence. From Fig. 3.14, it can be seen that the behaviour is similar to the low energy case.

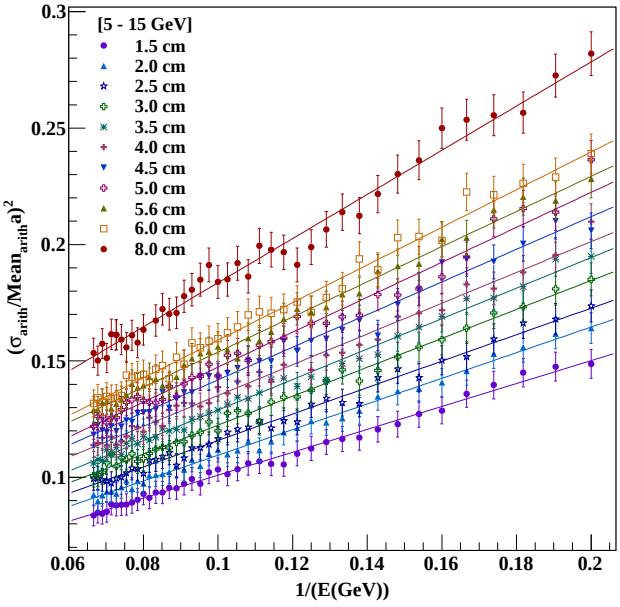

Figure 3.14: Plots of $(\sigma_{arith}/Mean_{arith})^2$ vs $1/E(GeV)$, where E is the pion energy in GeV, in the high energy range [5 – 15 GeV], for all thicknesses.

From Table. 3.3, it can be seen that the value of stochastic coefficient a varies between $a = 0.702$ and $a = 0.974$ in this region which is higher than in the lower energy case by up to 10%. The constant term b varies from 0.227 to 0.299 in this energy range.

t (cm)	a	b
1.5	0.702 ± 0.016	0.227 ± 0.006
2.0	0.742 ± 0.016	0.233 ± 0.006
2.5	0.756 ± 0.017	0.242 ± 0.006
3.0	0.788 ± 0.016	0.246 ± 0.006
3.5	0.809 ± 0.017	0.252 ± 0.006
4.0	0.813 ± 0.017	0.263 ± 0.006
4.5	0.837 ± 0.017	0.268 ± 0.006
5.0	0.866 ± 0.017	0.269 ± 0.006
5.6	0.868 ± 0.017	0.279 ± 0.006
6.0	0.899 ± 0.017	0.279 ± 0.006
8.0	0.974 ± 0.017	0.299 ± 0.006

Table 3.3: Fit parameters a and b obtained by fitting $(\sigma_{arith}/Mean_{arith})^2$ with Eq. 3.7, in the high energy range [5 – 15 GeV].

3.6.1.3 Full energy range [2 – 15 GeV]

The fits to Eq. 3.7 in the full energy range [2 – 15 GeV] are also obtained and are illustrated in Fig. 3.15. The values of a and b vary from $a = 0.709$ to $a = 0.985$ and $b = 0.226$ and $b = 0.294$ respectively as can be seen from Table. 3.3.

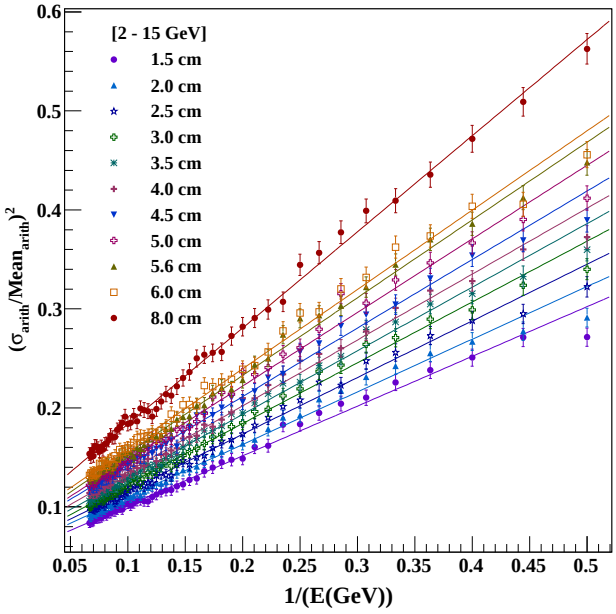

Figure 3.15: Plots of $(\sigma_{arith}/Mean_{arith})^2$ vs $1/E(GeV)$, where E is the pion energy in GeV, in the high energy range [2 – 15 GeV], for all thicknesses.

3.6.2 Parametrisation of plate thickness dependence

The functional form of thickness dependence can be expressed in two different ways. In the first approach, thickness dependence of only the stochastic coefficient a is considered,

t (cm)	a	b
1.5	0.709 $\pm$ 0.007	0.226 $\pm$ 0.003
2.0	0.729 $\pm$ 0.007	0.238 $\pm$ 0.003
2.5	0.756 $\pm$ 0.007	0.243 $\pm$ 0.003
3.0	0.783 $\pm$ 0.007	0.248 $\pm$ 0.003
3.5	0.801 $\pm$ 0.007	0.255 $\pm$ 0.003
4.0	0.816 $\pm$ 0.007	0.263 $\pm$ 0.003
4.5	0.832 $\pm$ 0.007	0.270 $\pm$ 0.003
5.0	0.862 $\pm$ 0.007	0.271 $\pm$ 0.003
5.6	0.886 $\pm$ 0.007	0.275 $\pm$ 0.003
6.0	0.895 $\pm$ 0.007	0.281 $\pm$ 0.003
8.0	0.985 $\pm$ 0.008	0.294 $\pm$ 0.004

Table 3.4: Fit parameters a and b obtained by fitting $(\sigma_{arith}/Mean_{arith})^2$ with Eq. 3.7, in the full energy range [2 – 15 GeV].

since the parameter b has a much smaller thickness dependence as can be seen from the analyses in different energy ranges. The dependence of the stochastic coefficient a on plate thickness can be parametrised in the standard form

$$a(t) = p_0 t^{p_1} + p_2 \ , \tag{3.8}$$

where, the exponent p_1 gives the thickness dependence of a. The constant term p_2 is the limiting resolution for hadrons for finite energy in the limit of very small thickness due to the nature of their interactions, detector geometry and other systematic effects. The parameters p_i, where $i = 0, 1, 2$, are estimated independently in the chosen energy ranges, to determine the thickness dependence of the stochastic coefficient a as mentioned before. Stochastic coefficient a vs plate thickness in (t(cm)) in the three different energy ranges [2 – 4.75 GeV], [5 – 15 GeV], [2 – 15 GeV], fitted with Eq. 3.8 is shown in Fig. 3.16. The values of $p_i,\ (i = 0, 1, 2)$ obtained from the fits are also shown. It can be seen that the parameter p_1 is clearly energy-sensitive and decreases in the higher energy range.

The analyses followed in the three energy ranges show that the thickness dependence is stronger than a $\sqrt{t}$ dependence. However,the smallness of the coefficient p_0, of the thickness parameter, in all cases, in comparison with the constant parameter p_2 should be noted. Irrespective of the energy range, p_2 remains around $p_2 \sim 0.60 \pm 0.08$ and contributes substantially to the energy resolution. Hence, *there will always be a residual resolution which cannot be improved further by the reduction of plate thickness*. This makes the option of going to smaller thicknesses less attractive than what the bare t-dependence indicates. For example, although the exponent of thickness term is $p_1 \sim 1.13$ at low energy, the energy

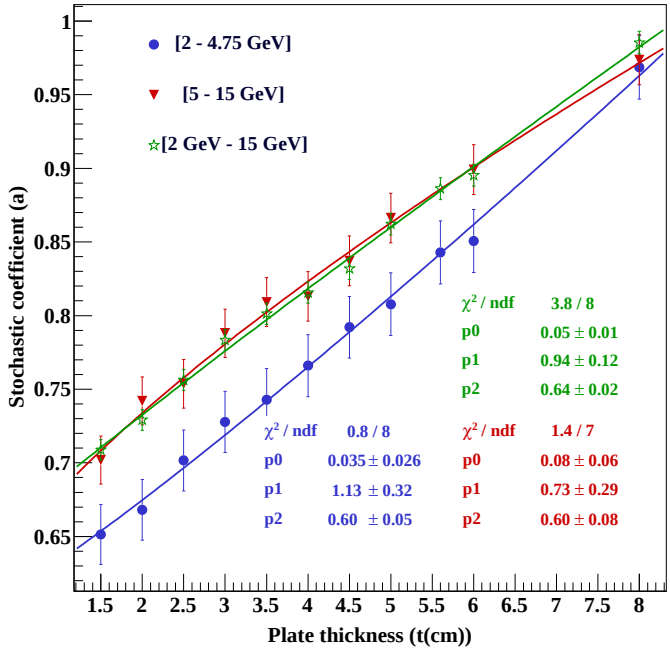

Figure 3.16: Stochastic coefficient a obtained from analysis in energy range [2 – 4.75 GeV], [5 – 15 GeV], [2 – 15 GeV] versus plate thickness t in cm, fitted with Eq. 3.8.

resolution worsens by only about 15% when the thickness is doubled from $t = 2.5$ to $t = 5$ cm rather than doubling as the bare t dependence indicates.

The alternative approach to thickness dependence analysis is to analyse the dependence of the entire quantity $\sigma/\sqrt{E}$ at different energies. The quantity $\sigma/\sqrt{E}$ at each energy is obtained as

$$\frac{\sigma}{\sqrt{E}} = \left(\frac{\sigma_{arith}}{Mean_{arith}}\right)\sqrt{E}\,, \tag{3.9}$$

where E is the energy of pion in GeV. A fit to $\sigma/\sqrt{E}$ with the equation

$$\sigma/\sqrt{E} = q_0 t^{q_1} + q_2\,, \tag{3.10}$$

similar in form with Eq. (3.8), reveals the trend as illustrated in Fig. 3.17. The exponent q_1 of the absorber thickness (t(cm)) decreases from ~ 0.9 to 0.66 in the [2–15 GeV] energy range, whereas its coefficient q_0 increases from ~ 0.06–0.14 with energy. The constant term q_2 increases from ~ 0.65–0.98 with energy E (GeV). Again, the smallness of the coefficient q_0 results in q_2 to dominate over the term $q_0 t^{q_1}$. Thus the behaviour of the parameters q_i, where $i = 0, 1, 2$ closely parallels that of the earlier analysis with the thickness dependence of a alone. The linear fits for the E dependence of the parameters q_0, q_1 and q_2 are also shown in Fig. 3.17. The trends indicate that the thickness exponent mildly decreases with

energy and may be compatible with the square-root dependence seen in earlier studies at higher beam energies [123, 127].

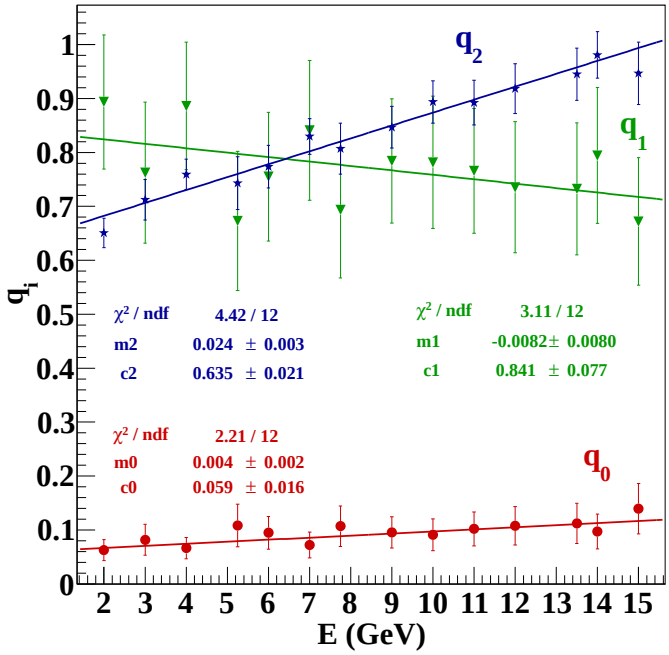

Figure 3.17: Variation of the parameters q_i obtained by fitting $\sigma/\sqrt{E}$ to Eq. (3.10) in the energy range 2–15 GeV. The linear fits through the points indicate the E dependence for each parameter $q_i,\ i = 0, 1, 2$.

3.7 Dependence of energy resolution on direction and thickness dependence

Naively, any particle travelling through a thickness t at angle $\cos\theta$ will in principle "encounter" an effective thickness of $t/\cos\theta$. Naively the thickness dependence can be explored through this angle dependence. In the actual detector with a given geometry, comprising of support structures, the orientation and arrangement of the detector elements will add non-trivial dependence on thickness. Thus the trends of direction dependence may be slightly different than expected.

In section 3.6, hadrons smeared in all directions in both polar and azimuthal angles, θ and ϕ were considered. In this section the energy resolution in various bins of incident polar angle θ of hadrons is done. In each θ bin, the azimuthal angle ϕ is smeared from 0–2π. The θ bins are defined symmetrically over the up/down directions in intervals of 0.2 in $|\cos\theta|$, with bin centers corresponding to $|\cos\theta_{in}|$ = 0.9, 0.7, 0.5, 0.3 and 0.1 respectively. The bins with the largest $|\cos\theta|$ are nearly perpendicular to the iron plates (and we refer

to them as vertical events) while the ones with the smallest values are practically parallel to them (and we label them as horizontal events). In an ideal ICAL with no support structures in the geometry, the energy resolutions are expected to be the best in the vertical directions and worse in the horizontal direction.

The mean number of hits ($Mean_{arith}$) and rms of the hit distribution (σ_{arith}) in different $\cos\theta$ bins for the default iron thickness of 5.6 cm is shown in Fig. 3.18. It can be seen that the mean hits increases as the angular bins become more vertical as expected. Widths of the distributions increase as the bins become more horizontal, except in the bin $\cos\theta = [0.8\text{–}1.0]$. This is due to the presence of support structures at every 2 m in both the x- and y-directions in the detector geometry, thus reducing the effective region of sensitive detector in the vertical direction, with a consequent loss of resolution. (In other words, the support structures have no sensitive detector which can pick up an electronic signal, hence the loss of hit information wherever they are present thus worsening the energy resolution in the vertical direction.)

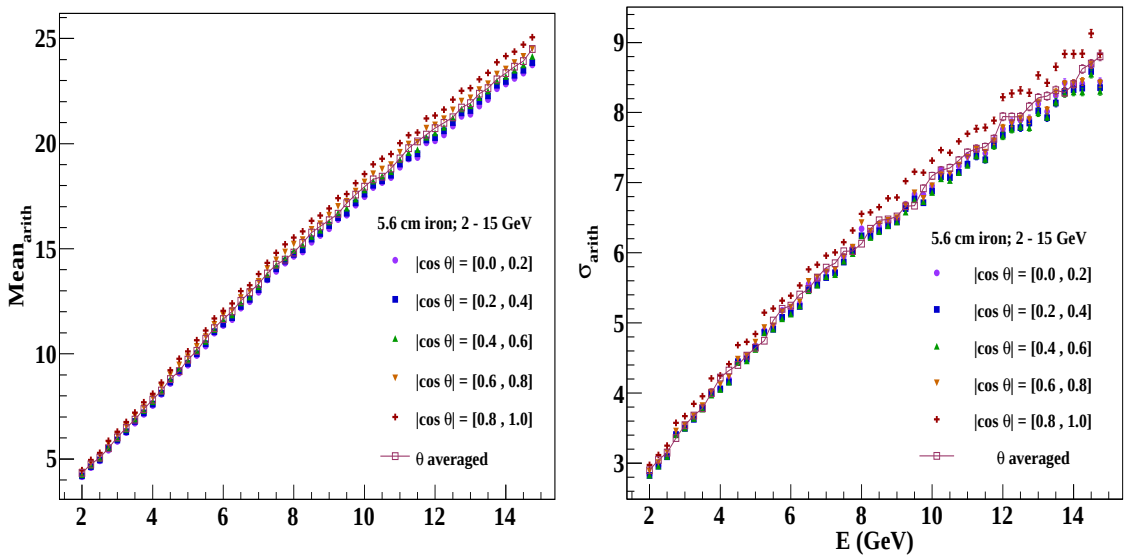

Figure 3.18: Mean hits and widths of the hit distributions for the default 5.6 cm thick iron plate in different $\cos\theta$ bins.

The energy resolutions in different angular bins are found out as in section 3.6. The energy resolution for a 5 GeV pion in different angular bins as a function of plate thickness (t (cm)) is shown in Fig. 3.19.

Several observations are made. The hadrons in the horizontal bins have the worst resolution as expected. Again as expected, the resolution generically improves with increasing $|\cos\theta|$, except in the vertical $\cos\theta$ bin ($|\cos\theta| = [0.8\text{–}1.0]$) for all thicknesses. This

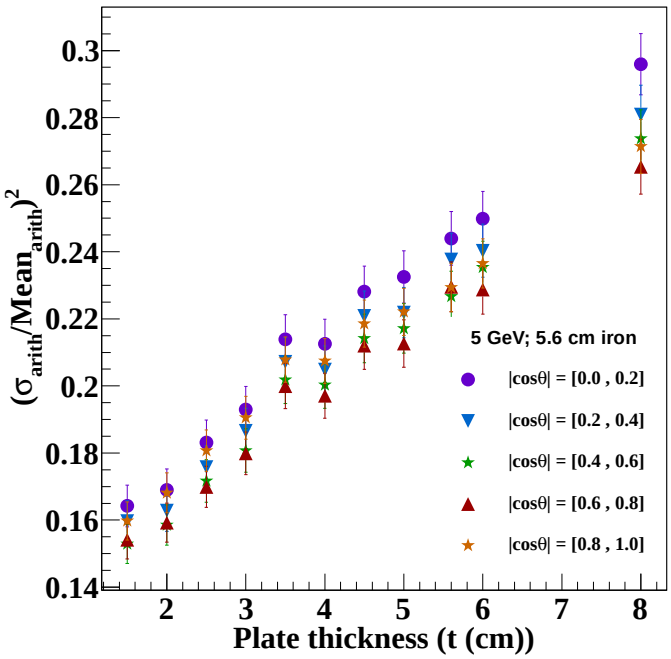

Figure 3.19: Energy response of a 5 GeV pion in different incident $\cos\theta$ bins of the pion as a function of iron plate thicknesses (t in cm).

is due to the presence of support structures as mentioned before. It can also be seen that, even though the hadron traverses an effective thickness of $t/\cos\theta$, the resolution does not exhibit such a naive scaling behaviour. It is seen that, for the same value of $t/\cos\theta$, the resolution is better at smaller thicknesses than at larger thicknesses. This is again because of the non-trivial geometry of the detector and other factors.

The energy resolutions in different $\cos\theta$ bins in the different energy ranges [2 – 4.75 GeV], [5 – 15 GeV] and the combined range [2 – 15 GeV] is shown in Fig. 3.20, for the default thickness of $t = 5.6$ cm. The thickness dependence in angular bins can be observed most conveniently in terms of the stochastic coefficient a as determined from fits in these three energy ranges. This dependence is also illustrated in Fig. 3.20. The analyses in different $\cos\theta$ bins in the three different energy ranges show that the dependence on hadron direction is mild in all these energy ranges. Hence the direction averaged results for energy resolution, presented in earlier sections are realistic.

The results discussed above are all with fixed energy single pions. But the ICAL detector is mainly a neutrino detector in which the interactions of (anti-)neutrinos with iron produce both charged leptons and multiple hadrons, from either resonance or deep inelastic scatterings, in the final state. It is interesting to see the thickness dependence with multiple hadrons even though the sharing of energy by multiple hadrons will bring

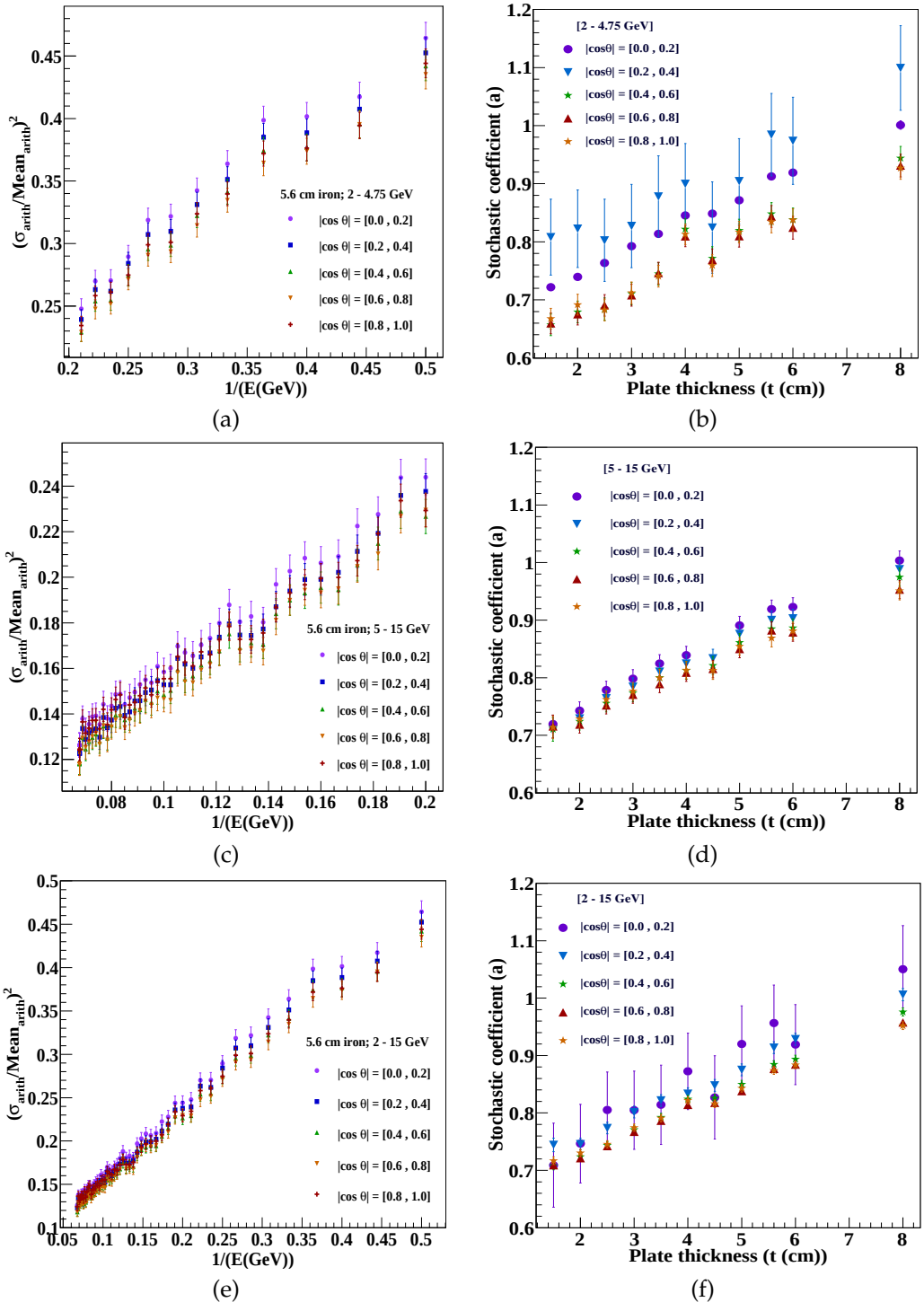

Figure 3.20: Left panels (a), (c) and (e) show the energy resolution ($(\sigma_{arith}/Mean_{arith})^2$) as a function of $1/E(GeV)$ in various $\cos\theta$ bins for the default iron thickness of 5.6 cm, in the three different energy ranges [2 – 4.75 GeV], [5 – 15 GeV] and [2 – 15 GeV] energy range respectively. Right panels (b), (d), and (f) show the plots of stochastic coefficient a as a function of iron plate thickness t (cm) in different $\cos\theta$ bins, for all thicknesses in the three different energy ranges.

additional uncertainty in the study of thickness dependence. The next section elucidates the thickness dependence of hadron energy in the case of multiple hadrons produced in

neutrino interactions.

3.8 Study of thickness dependence of hadron energy resolution for multiple hadrons produced in neutrino interactions

In the earlier study [20] for the fixed absorber thickness of $t = 5.6$ cm, a comparison of single pion resolutions with those of multiple hadrons generated in neutrino events generated by NUANCE neutrino event generator was carried out [20]. This study is presented elsewhere. In the case of multiple hadrons there is a non-trivial partition of energy between different hadronic final states. In this section, the thickness dependence of multiple hadrons for the direction averaged case is discussed. The trends in the thickness dependence of the resolution quantified by $(\sigma/E)^2$ and stochastic coefficient a are found to be similar in both cases.

3.9 Effect of different hadron models on hadron energy resolution

The effect of different hadronisation models was investigated for the default iron thickness of 5.6 cm. In this regard, the LHEP model used in GEANT4 was replaced [23] with QGSP (for hadrons with energy $>$ 12 GeV) and QGSP_BERT (for the lower energy hadrons). The energy resolution was found to be reasonably model independent, with a variation in the mean (rms) of less than 4% (5%) among different models in the energy range from 2–15 GeV for $t = 5.6$ cm.

3.10 Comparison of the simulation studies using ICAL with other experiments

To validate the analysis presented above, the hadron resolutions from ICAL simulation studies have been compared with simulations of both MONOLITH and MINOS collaborations and also to their test beam data. In the current simulation study ICAL with 8 cm iron plate has a resolution of $98.5\%/\sqrt{E} \oplus 29.4\%$. This is roughly comparable to the angle-averaged result of $90\%/\sqrt{E} \oplus 30\%$ obtained from the simulation studies of MONOLITH [128] with the same iron plate thickness. For the convenience in comparing, the convention $a/\sqrt{E} \oplus b \equiv \sqrt{a^2/E + b^2}$ has been used.

The angle averaged results of ICAL cannot be directly compared with the test beam data since beams are highly directional (with $\cos\theta = 1$ as the beam divergence is typically small). For direct comparison with test beam data, hadrons incident normally on the detector plates are simulated (i.e the hadrons are incident in a fixed direction and there is no direction smearing).

The test beam data of Baby MONOLITH (of MONOLITH collaboration) having 5 cm iron plates, with T7-PS beam at CERN has been used here for comparison [129, 130]. This beam has pions of energies ranging from 2–10 GeV which are exactly normally incident on the iron plates. The run reported an energy resolution of $68\%/\sqrt{E} \pm 2\%$. The simulation studies of ICAL detector with 5 cm thick iron plates with fixed energy single pions in the energy range 2–10 GeV incident normally on the detector at a fixed vertex $(100, 100, 0)$ cm, is shown in Fig. 3.21. The analysis gives a similar energy resolution of $66.3\%/\sqrt{E} \oplus 8.7\%$.

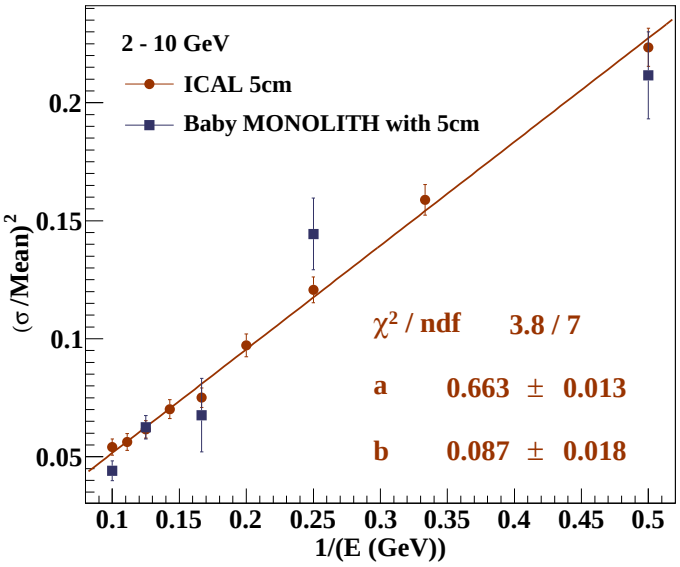

Figure 3.21: Energy response of ICAL detector with 5 cm iron plates with fixed energy single pions in the energy range 2–10 GeV, propagated from the vertex fixed at $(100, 100, 0)$ cm in the vertical direction, compared with the data from MONOLITH test beam run [129, 130].

The simulation studies with gaseous detectors in MINOS collaboration have reported a hadron energy resolution of $70\%/\sqrt{E}$ with 1.5″ (i.e., 3.8 cm) iron plates [131]. The test beam run of MINOS with Aluminium Proportional Tubes (APT) active detectors and 1.5″ steel plates in the energy range 2.5–30 GeV reported a hadron energy resolution of $71\%/\sqrt{E} \oplus 6\%$ [127]. ICAL simulation with 4 cm iron plates in the energy range 2–30 GeV provides a resolution of $61\%/\sqrt{E} \oplus 14\%$. The results are compatible, considering that there are differences in detector geometries. The results of the simulation studies

with ICAL detector thus agree with those of MINOS and MONOLITH simulations and test beam results within statistical errors. The slight differences in the resolutions can be attributed to differences in the details of the detector configuration. it should be noted that fixed vertex data tend to give smaller values of b than the smeared vertex case. This is because the hadrons see more inhomogeneities in the detector geometry owing to the fact that the vertices are spread over a region and hence the effects due to detector geometry also come in. This is reflected in the larger residual resolution.

The study of hadron energy resolution is important owing to the fact that the inclusion of hadron energy information in the atmospheric neutrino oscillation analysis enables the improvement in the precision measurements of θ_{23} and $\Delta {m^2}_{32}$ as well as affecting the hierarchy determination. This will be discussed in detail in Chapter6. It is equally important to determine the direction resolution of hadrons also, since this is the determining piece in the reconstruction of neutrino direction. The following section elucidates the determination of direction resolution of hadrons using hit information and timing of those hits. However, this information has not been included in the physics analysis in Chapter 6.

3.11 e/h ratio in ICAL

Since the atmospheric neutrinos contain ν_μ and ν_e in the 2:1 ratio, there are charged current electron neutrino interactions also in ICAL, which produce electrons in the final state according to Table 3.1 to in Section 3.2. These electrons produce showers and hence cannot be distinguished directly from hadrons in ICAL. The hadronic shower in ICAL also contains an electromagnetic component since the neutral pions (π^0) decay in two gammas (γ) which then produce electromagnetic showers by pair production. Studying the ratio of electron response to charged pion response, i.e, e/h ratio helps the characterisation of the effect of neutral hadrons on hadron energy resolution. The hit distributions of electrons, gammas and neutral pions are similar in ICAL. This is illustrated in Fig. 3.22, where the hit distributions from electrons, gammas, and neutral pions at 5 GeV energy are shown.

The simulation studies of e/h ratio in ICAL have been conducted using fixed energy single electrons and charged pions (π^+), 1,00,000 single particles, for each energy, generated in the energy range 2–15 GeV, with vertices randomised over a fiducial volume of 2

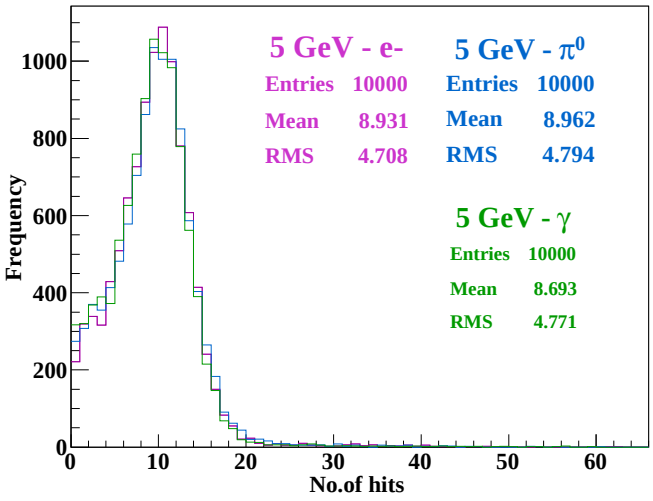

Figure 3.22: Hit distributions of electrons, gammas and π^0s of 5 GeV energy.

m $\times$ 2 m $\times$ 2 m in the central region of the detector. The directions of the particle are also smeared with θ smeared from 0 – π and ϕ from 0 – 2π. The study has been done for all the eleven plate thicknesses discussed in Section 3.6. Since the response as a function of thickness is very smooth, the cases for only three sample thicknesses 2.5 cm and 5.6 cm are discussed in detail here. The direction averaged hit distributions for 2, 5, 10, and 14 GeV electrons in 2.5 cm, 4 cm and 5.6 cm iron are shown in Fig. 3.23. The left panel of the figure shows hit distributions with no layer cut. The distributions of π^+ at 5 GeV are illustrated in Fig. 3.11.

On comparison it is seen that the positions of peaks are not very different for charged pion and electron distributions, but electrons have more zero hits compared to the former, as the thickness increases. This is visible for higher thicknesses like 5.6 cm, since with the increase of thickness electrons lose more energy in iron. The zero hits can be removed from the distribution by imposing a layer cut of $l > 2$, where there should be hits in at least three layers of each event. This cut makes the histograms more symmetric about the peak which is shifted to the right. It should be noted that while this improves the distribution, it reduces the reconstruction efficiency. This layer cut is mainly significant for higher thicknesses and lower energies; with smaller thickness this is significant only for low energies below about 5 GeV.

As in the case of fixed energy charged single pions, the electron energy is calibrated to the mean number of hits. The e/h ratio, which is the ratio of the response of electrons

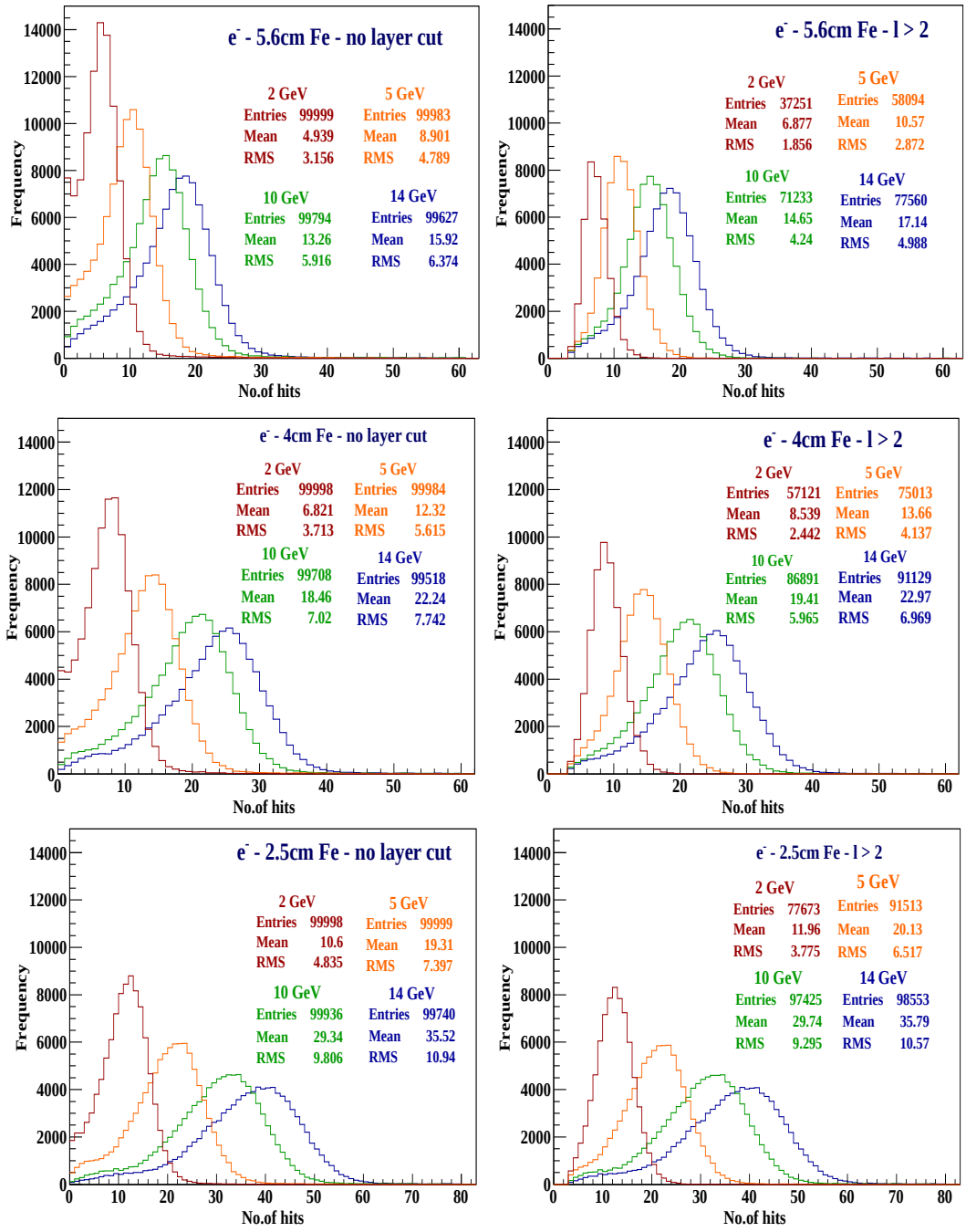

Figure 3.23: Hit distributions of 2, 5, 10 and 14 GeV electrons in ICAL with 2.5, 4 and 5.6 cm thick iron plates. Left panels show the distributions without any layer cut whereas the right ones show those with a layer cut of $l > 2$, where l is the minimum number of layers to be traversed. It should be noted that the layer cut does not alter the peak, but only the width of the distributions.

to that of charged pions is obtained as :

$$e/h \;=\; e^{-}_{mean}/\pi^{+}_{mean}, \tag{3.11}$$

where e^{-}_{mean} = arithmetic mean of the hit distribution of electrons and π^{+}_{mean} = arithmetic

mean of charged pion hit distribution. A detector is called compensating if e/h = 1.

The values of e/h ratio as functions of incident energy for 2.5, 4 and 5.6 cm are shown in Fig. 3.24. The values e/h decreases with increase in energy. Since there is no direct mea-

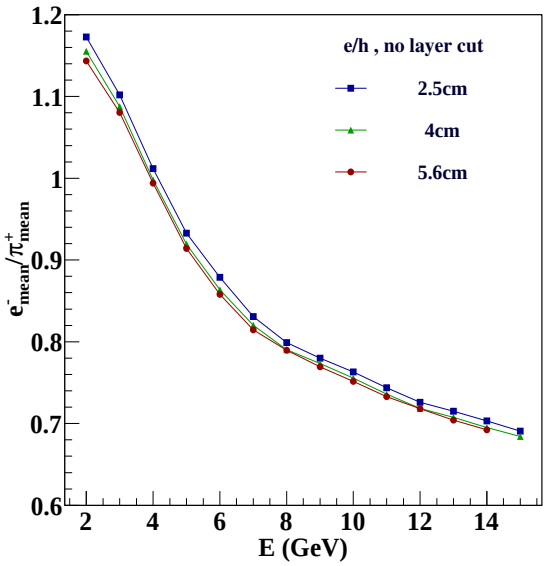

Figure 3.24: Comparison of e/h ratio as a function of incident energy for three different plate thicknesses namely 2.5, 4 and 5.6 cm, with no layer cut. The ratio decreases with increasing energy for all thicknesses. The layer cut marginally changes the results at lower energies and larger plate thicknesses.

surement of energy deposited in ICAL (as the amount of charge deposited by a particle), the shower energy is calibrated to the number of hits. In a high Z material like iron, electrons travel smaller distances than charged pions (radiation length). At lower energies, both electron and hadron showers are concentrated around a small region, the latter due to the low energy hadrons not travelling much distances owing to hadronic interactions. Thus the mean of electron hit distribution will be roughly the same or slightly larger than that of the π^+ hit distribution. As energy increases, π^+s travel more distance and hence more layers, giving more hits. This is because the hadronic interaction length is much more than the electromagnetic interaction length at higher energies. So the value of the ratio decreases with increase in energy. The layer cut only affects the results at energies lower than about 4 GeV (i.e E <4 GeV), which results in a marginal decrease in the value of e/h at higher thicknesses.

3.11.1 e/h ratio and energy resolution of hadrons from neutrino interactions

Since different types of hadrons can be produced in a neutrino interaction (although the dominant component are pions), the energy response of ICAL to hadrons will depend on

the relative fractions of charged and neutral pions. Charged current atmospheric muon neutrino events for 100 years in ICAL of default plate thickness 5.6 cm were generated using NUANCE neutrino generator. Different types of hadrons obtained from the sample occur by the fraction $\pi^+ : \pi^- : \pi^0 :: 0.38 : 0.25 : 0.34$, with the remaining 3% contribution mainly from kaons. The average hadron response from charged current muon neutrino interaction is :

$$\begin{aligned} R_{had} &= \left[(1 - F_0) \times h + F_0 \times e\right], \\ &= h\left[(1 - F_0) + F_0 \times \frac{e}{h}\right], \end{aligned} \tag{3.12}$$

where e is the response of electrons , h the response of charged hadrons and F_0 is the fraction of neutral pions in the sample.

The atmospheric neutrino events of interest in ICAL are dominantly low energy events mostly with hadrons of energies $E < 10$ GeV. The average value of e/h at these energies is $e/h \approx 0.9$. Using $F_0 = 0.34$ in Eq. (3.13), the average hadron response for NUANCE-generated events is obtained to be $R_{had} = 0.97h$. This value is not very different from h. Hence, the analysis of energy response of multiple hadrons in NUANCE-generated events was not very different from that of the single pions case, as discussed in Ref. [20].

3.12 Chapter summary

ICAL detector at INO is designed mainly to detect muons of GeV range energy produced in the interactions of atmospheric neutrinos with the iron target of the detector. Hadron showers are also produced in these interactions. GEANT-4 based simulation studies of fixed energy single pions and multiple hadrons from neutrino interactions, propagating in ICAL detector have been conducted to characterise hadron energy resolutions. Since the only information available about hadrons is the shower hit information, this has been used to estimate the responses. Total number of hits are calibrated to energy in the case of energy response and fitted with Vavilov distribution function to obtain the mean and σ of the distribution which are used in the calculation of energy resolution. The resolution of fixed energy single pions at 1 GeV is found out to be $\sim 0.86/\sqrt{E}$ and $\sim 0.36/\sqrt{E}$ at 15 GeV. Studies on the direction dependence of hadron energy resolution as well as on the

thickness of iron plate have also been conducted.

This study is relevant in the context of physics potential of ICAL, since the inclusion of hadron energy as an observable in the oscillation analysis improves ICAL sensitivities [27]. Thus the effect of plate thickness is crucial for both hadron and muon energies since any improvement in their resolutions will further better ICAL results. The study shows that the dependence on thickness is not a trivial $\sqrt{t}$ one but is mostly driven by a "residual resolution" which is due to the intrinsic uncertainties of strong interactions, fluctuations and detector geometry, which means that there will be a finite uncertainty in the measurement of hadron energy even if the thickness is reduced to infinitesimally small values. The study also shows that due to the presence of support structures in the vertical direction corresponding to the $\cos\theta = 0.9 \pm 0.1$ bin, the resolution in this direction is not the best one as expected. The comparison of ICAL simulations with the simulations of MONOLITH and MINOS and their test beam runs are found to match. The ratio of electron response to pion response, i.e., the e/h ratio has been calculated and used to cross check the resolutions of multiple hadrons produced in neutrino interactions.

4 Simulation studies of direction resolution of hadrons in ICAL

4.1 Overview

As mentioned in Chapter 3, the energy and direction of the hadrons in the final state of a neutrino interaction have to be reconstructed in order to reconsrtuct the energy and direction of the interacting neutrino. Since the only information available about hadrons in ICAL is the shower hit information, it has to be utilised to determine the energy and direction resolutions of hadrons in ICAL. The detailed description of how to use the number of hits in the shower to determine the energy resolution of hadrons was presented in Chapter 3. This chapter describes the simulation studies on how to use the position and timing information of the hadron hits to reconstruct the shower direction. A method called "raw hit" method which makes use of only the position and timing of hadron hits is used to reconstruct the direction of hadrons. The studies on the resolution of the opening angle between the muon and hadron shower in charged current muon neutrino and anti-neutrino interactions are also discussed in detail. The work reported in this chapter forms a part of Ref.[28].

4.2 Direction resolution of hadrons using hit and timing information of the hits (the raw hit method)

As discussed in previous sections, hadrons only leave showers in the detector. Since the only information available on hadrons are their hit positions and timings, in ICAL, these have to be made use of in the reconstruction of the hadron shower direction. Again as in the case of energy resolution, the hit information is used, but with the difference that they are not counted, but their actual positions and timing are used to reconstruct the hadron shower. This method is called the Raw Hit Method (RHM). This method has the advantage that it can be used in the reconstruction of direction of hadrons produced in both charged current and neutral current interactions, since it doesn't require a vertex

with respect to which the direction can be reconstructed. The simulation studies with both fixed energy single pions and multiple hadrons from atmospheric neutrino interactions generated using NUANCE neutrino generator have been conducted for the default iron plate thickness of 5.6 cm. (Hadron direction resolution studies have been conducted only using 5.6 cm.) The reconstruction of hadron direction is discussed in detail below.

4.2.1 Raw hit method (RHM)

The real advantage of this method is that it can be used in the reconstruction of the direction of hadrons produced in both charged current and neutral current interactions. There is no need for a vertex (especially a charged lepton vertex) with respect to which the direction can be reconstructed. Only the hit information in the $X-Z$ and $Y-Z$ planes and the timings of the hits are required for direction reconstruction. Analysing the hits separately in two different planes eliminates the problem of *ghost hits* by double counting of hits taken in 3-D. This problem arises because of the large multiplicity of hits per layer with hadrons in contrast to the minimum ionising muon. The problem is exacerbated with multiple hadrons as obtained in a realisitic neutrino interaction. Since $X-$ and $Y-$ hit information are obtained from different (upper and lower) strips in a layer (Z), it is not obvious which $X-$ and $Y-$ are to be paired to give (x, y, z) information. Allowing for all possible combinations gives rise to spurious hits in that layer, these are *ghost hits*. Timing information is crucial in telling if the hadron is traveling UP or DOWN.

To avoid the ghost-hits problem, the analysis was done separately in both X-Z and Y-Z planes. The true hits are separated out first. While doing this, only hits within a time window of $\leqslant$ 51 ns in a layer are selected. This is done to avoid taking into account hits which are far away in time hits separated by upto 2.2μs (the muon life time may be seen in a layer) and make sure that the hits are actually due to a single interaction.

The x - positions in a single layer are averaged to get the mean x - position in that layer. i.e.,

$$x[i]_{average} = \frac{x[1] + x[2] + ...x[nhits]}{nhits[i]}, \tag{4.1}$$

where $x[i]_{average}$ is the average x position in the i^{th} layer of an event (position in cm ; obtained from the hit output from ICAL code). Similarly

$$y[i]_{average} = \frac{y[1] + y[2] + ...y[nhits]}{nhits[i]}, \tag{4.2}$$

where, $y[i]_{average}$ is the average y position in the i^{th} layer of an event and $nhits[i]$ is the number of hits in a layer. The mean hits $x[i]_{average}$ and $y[i]_{average}$ are plotted separately in $X-Z$ and $Y-Z$ planes with asymmetric error bars in each layer. In a layer, the lower error bar is distance between the position of the first hit from the mean position and the higher error bar is the distance of the last hit from the mean position. If there is only one hit in a layer, the error on it is taken to be 0.015 m (1.5cm) , which is half the width of a strip in RPC (the actual strip width that will be used in ICAL is 3 cm, even though simulation studies have 1.96 cm wide strips; here the half strip width of the actual value is taken into account). The error on z position is taken to be 0.001 m (1 mm), that is half the gas gap in the RPCs. These graphs are then fitted with straight lines $x = m'_x z + c_1$ and $y = m'_y z + c_2$ respectively. The inverses of the slopes m'_x and m'_y are used to reconstruct the direction. Let these inverses be called m_x and m_y respectively and let ω be the angle made by a line with the X axis, in the $X-Z$ plane and λ be the angle made by a line with the Y axis in the $Y-Z$ plane. This is shown in Fig. 4.1. In spherical polar coordinates,

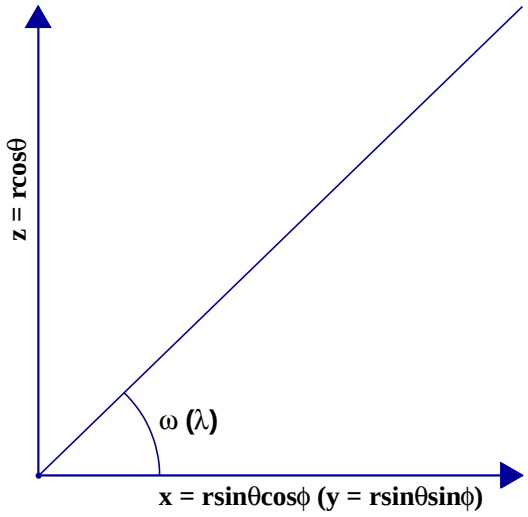

Figure 4.1: Angle ω (λ) in the $X-Z$ ($Y-Z$) plane.

$x = r\sin\theta\cos\phi$; $y = r\sin\theta\sin\phi$; $z = r\cos\theta$. The slopes m_x and m_y in the $X-Z$ and $Y-Z$ planes respectively can be expressed as :

$$m_x = r\cos\theta/r\sin\theta\cos\phi = \tan\omega \ ; \ m_y = r\cos\theta/r\sin\theta\sin\phi = \tan\lambda. \tag{4.3}$$

Thus, θ and ϕ can be obtained as :

$$\tan\phi = \tan\omega/\tan\lambda \ ; \ \phi = \tan^{-1}(\tan\phi) \tag{4.4}$$

$$\cot\theta = \tan(\omega)\cos(\phi) \ ; \ \tan\theta = \frac{1}{\cot\theta} \tag{4.5}$$

$$\text{Hence, } \theta = \tan^{-1}\tan(\theta). \tag{4.6}$$

The slopes m_x and m_y being products of trigonometric functions are degenerate. This is illustrated as follows: $m_x = \cot\theta\sec\phi \ ; \ m_y = \cot\theta\text{cosec}\phi$.

$$\begin{gathered}\text{Since } \cot\theta \text{ is } +\text{ve in } 0 \leqslant \theta \leqslant \tfrac{\pi}{2} \quad \& \quad \cot\theta \text{ is } -\text{ve in } \tfrac{\pi}{2} \leqslant \theta \leqslant \pi, \\ \text{when } 0 \leqslant \phi \leqslant \tfrac{\pi}{2} : \text{cosec}\phi \text{ is } +\text{ve} \ ; \sec\phi \text{ is } +\text{ve}, \\ \text{when } \tfrac{\pi}{2} \leqslant \phi \leqslant \pi : \text{cosec}\phi \text{ is } +\text{ve} \ ; \sec\phi \text{ is } -\text{ve}, \\ \text{when } \pi \leqslant \phi \leqslant \tfrac{3\pi}{2} : \text{cosec}\phi \text{ is } -\text{ve} \ ; \sec\phi \text{ is } -\text{ve} \\ \text{and when } \tfrac{3\pi}{2} \leqslant \phi \leqslant 2\pi : \text{cosec}\phi \text{ is } -\text{ve} \ ; \sec\phi \text{ is } +\text{ve} \ .\end{gathered}$$

Thus, depending on the sign of these trigonometric functions, there are eight different cases as listed in Table 4.1: Hence, the sign of m_x and m_y, which are products of these,

1.	m_x + ; m_y +	($\theta \rightarrow 1^{st}$ quad ; $\phi \rightarrow 1^{st}$ quad) *OR* ($\theta \rightarrow 2^{nd}$ quad ; $\phi \rightarrow 3^{rd}$ quad)
2.	m_x - ; m_y +	($\theta \rightarrow 1^{st}$ quad ; $\phi \rightarrow 2^{nd}$ quad) *OR* ($\theta \rightarrow 2^{nd}$ quad ; $\phi \rightarrow 4^{th}$ quad)
3.	m_x - ; m_y -	($\theta \rightarrow 1^{st}$ quad ; $\phi \rightarrow 3^{rd}$ quad) *OR* ($\theta \rightarrow 2^{nd}$ quad ; $\phi \rightarrow 1^{st}$ quad)
4.	m_x + ; m_y -	($\theta \rightarrow 1^{st}$ quad ; $\phi \rightarrow 4^{th}$ quad) *OR* ($\theta \rightarrow 2^{nd}$ quad ; $\phi \rightarrow 2^{nd}$ quad)

Table 4.1: Possible signs of m_x and m_y for (θ, ϕ) in different quadrants.

will also change accordingly. To get around this problem, the quadrant of θ, to which the event belongs to has to be known. This can be determined by making use of the the following fact :

- **all events with $zlayer[0] < zlayer[l]$ correspong to up-going hadrons (this corresponds to θ in quadrant 1) and and those with $zlayer[0] > zlayer[l]$ are down-going (θ in quadrant 2).**

Using this information the quadrant degeneracy is broken and the signs of the slopes are obtained correctly. These corrected slopes are used to find ϕ, and θ is reconstructed using the information whether the event is upcoming or down going.

It is the hit timing of hadrons which determines whether they are propagating upwards or downwards. The mean timing of hits in a layer are found by averaging over all

the hit timings in the layer. i.e.,

$$tx[i]_{average} = \frac{tx[1] + tx[2] + ...tx[nhits]}{nhits[i]}; \tag{4.7}$$

$$ty[i]_{average} = \frac{ty[1] + ty[2] + ...ty[nhits]}{nhits[i]}. \tag{4.8}$$

This is plotted as a function of z - position and fitted with a straight line. If the slope of the fitted line is positive, the event is flagged as up-going and if the slope is negative, it is flagged as down-going. The significance of the time-window constraint is now clear. A minimum of two layers or more is required to reconstruct the direction using the raw hit method. Also only those events in which both the $X - Z$ slope and the $Y - Z$ slope have been reconstructed are considered for analysis. The resolutions are obtained by fitting the distribution of the reconstructed direction with a Gaussian distribution function in appropriate ranges.

The significance of the raw hit method is that it can used even when there is no information about the muon vertex (for example neutral current events). Since positions and timings are obtained from a real detector, we can use this method in scenarios where the hit information alone is sufficient.

4.2.2 Direction resolution of fixed energy single pions

As in the case of energy resolution, the simulation studies using fixed energy single positive pions (π^+) produced and propagated through the ICAL detector simulated using GEANT4 have were first conducted. The specifications of the simulations are as follows. Fixed energy single pions of energies ranging from 1 – 10 GeV are propagated from randomised vertices inside the volume 2 m $\times$ 2 m $\times$ 2 m in the central region of the ICAL detector. Unless stated otherwise there are 10000 events per energy. The energy of the single pion is not smeared here. Since this study is to determine the direction resolution two cases are considered; one with both the zenith angle θ and the azimuthal angle ϕ fixed at certain values, and the other with only θ fixed at different values namely $|\cos\theta| =$ 0.1, 0.3, 0.5, 0.7 and 0.9, with ϕ smeared from 0–2π. The $\cos\theta$ values represent the most horizontal to the most vertical directions in ascending order. The study is done for ICAL with default plate thickness of 5.6 cm. The results are discussed in detail here.

4.2.2.1 Fixed θ - fixed ϕ

Fixed energy single pions of different energies are propagated in eight different directions which are the combinations of two different θs namely 30° and 150° and four different ϕs namely 30°, 120°, 220° and 340°. To obtain θ resolution, the value of θ is reconstructed using raw hit method as explained in Section 4.2 and the distribution of the difference $\Delta\theta$ in degrees, between the input θ and the reconstructed θ is fitted with a Gaussian distribution in the appropriate range. To reconstruct the direction, there should be at least two or more layers in the event. The resolutions obtained for the eight different cases as a function of hadron energy are shown in Fig. 4.2. It is seen that the best resolutions

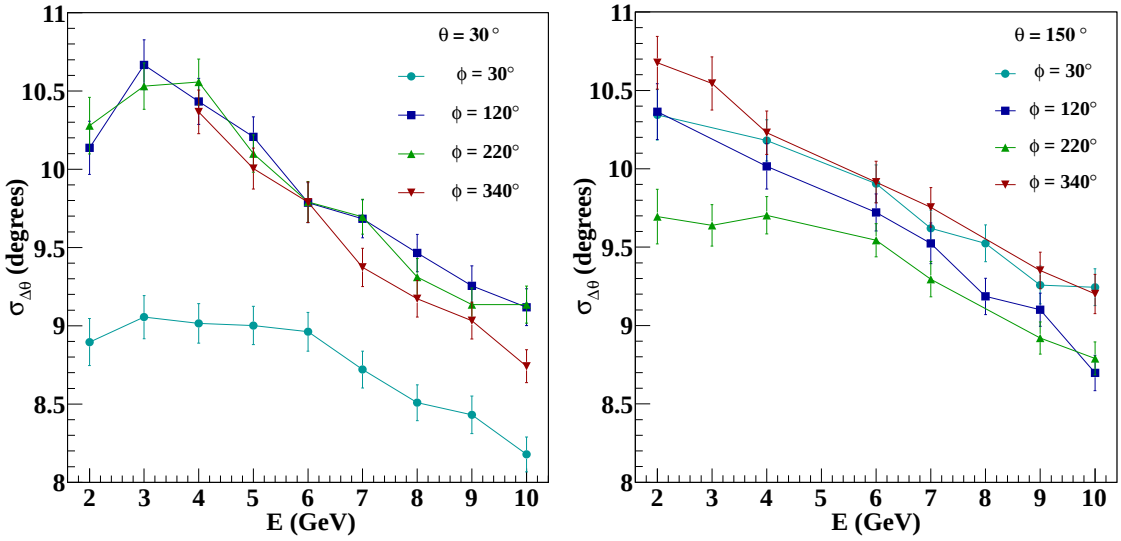

Figure 4.2: Zenith angle resolution $\sigma_{\Delta\theta}$ in degrees for fixed energy single pions propagated in eight different directions with $\theta = 30°$ (left) and $\theta = 150°$ (right) and $\phi = 30°$, $120°$, $220°$ and $340°$ plotted as a function of pion energy in GeV.

are for the directions $(\theta, \phi) = (30°, 30°)$ and $(150°, 220°)$, with the requirement that there should be $\geqslant 2$ layers in the event to have the direction reconstructed. Since $\theta = 150°$ is symmetrically downwards compared to $\theta = 30°$, the results are similar for the two cases as expected. The definition of the ϕ quadrants changes when the up/down direction is flipped, as quadrants (I,II,III,IV) for up-hadron goes to quadrants (III,IV,I,II). Hence the resolutions of the hadrons are similar for up and down directions. It can also be seen that the resolution improves with energy as also can be seen from $\Delta\theta$ distributions. This is because of the fact that showers from higher energy hadrons are better directional than lower energy hadrons. The efficiency of direction reconstruction is illustrated in Fig. 4.3. Total reconstructed fraction is the fraction of events for which direction could be recon-

structed, out of the 10000 events propagated through GEANT4. It can be seen that this fraction increases with hadron energy. At 1 GeV, only 65% of the events can be reconstructed whereas by 5 GeV, this increases to about 94% and by 10 GeV it reaches about 98%, for all eight directions. Not all the hadrons will be reconstructed in the right direc-

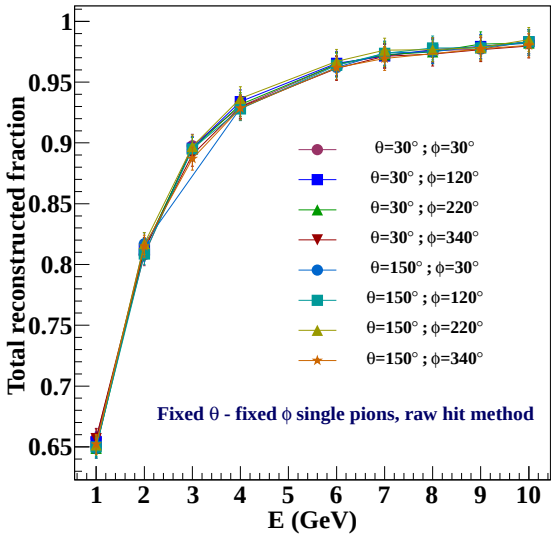

Figure 4.3: Fraction of total events reconstructed out of 10000 events propagated in different fixed directions through GEANT4. More number of events are reconstructed as the energy increases.

tion. There will always be a small fraction of events which are reconstructed in the wrong direction. The fraction of wrongly reconstructed events reduce with the increase in the energy as can be seen in Fig. 4.4. Complementarily the number of correctly reconstructed events increase with energy.

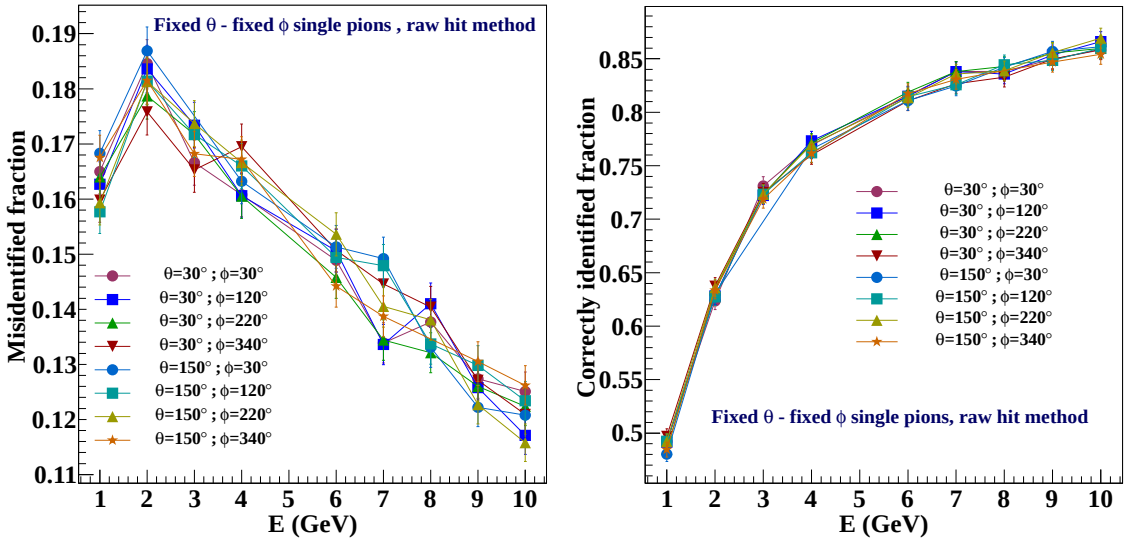

Figure 4.4: Wrongly identified and correctly identified fraction of events among the 10000 fixed θ fixed ϕ single pion events propagated through GEANT4.

4.2.2.2 Direction resolution of fixed energy single pions with smeared azimuthal angle ϕ

In this section the analysis of θ resolution for fixed energy single pions propagated in directions with fixed values of $\cos\theta$ namely 0.1, 0.3, 0.5, 0.7, and 0.9, but ϕ smeared from 0–2π. Here the directions are mentioned in $\cos\theta$ for ease of binning. The θ values corresponding to the $\cos\theta$ values 0.1, 0.3, 0.5, 0.7 and 0.9 are 84.26°, 72.54°, 60°, 45.57° and 25.84° respectively. Again 10000 fixed energy single pion (π^+) events in the energy range 1 – 10 GeV are propagated from vertices randomised over a volume of 2 m $\times$ 2 m $\times$ 2 m in the central region of ICAL. The zenith angle θ is reconstructed using raw hit method and the distribution of the reconstructed direction, i.e., θ_{rec} is fitted with a Gaussian function and the mean and σ of of the fit are obtained. Here also $\sigma_{\theta_{rec}}$ is plotted as a function of hadron energy. As required for the fixed θ - fixed ϕ case, the event must have atleast 2 layers hit for direction reconstruction. It can be seen that the direction resolution is the best in the vertical direction corresponding to $\cos\theta$ = 0.9 and the worst in the horizontal direction, i.e., in the $\cos\theta$ = 0.1 direction. The reconstructed values of ϕ are distributed uniformly like the input values of ϕ. The improvement in direction resolution as energy increases can be seen here also.

The distributions θ_{rec}, the reconstructed angle in degrees for sample energies and different $\cos\theta$ values are shown in Fig. 4.5. An important observation is that, for the same $\cos\theta$ value, more and more events are reconstructed as the energy increases. Also for a given energy, the number of reconstructed events increase as the direction becomes more and more vertical. This is expected since there is more hit information available as $\cos\theta$ increases since the events will traverse more layers and thus leave more number of hits in the detector. The distribution becomes narrower as the energy and $\cos\theta$ increases, thus giving the best resolution at high energies and in the most vertical direction. The fraction of events reconstructed in the wrong quadrant also behaves the same. In the analysis presented here, the direction is best reconstructed for 10 GeV single pions with $\cos\theta$ = 0.9.

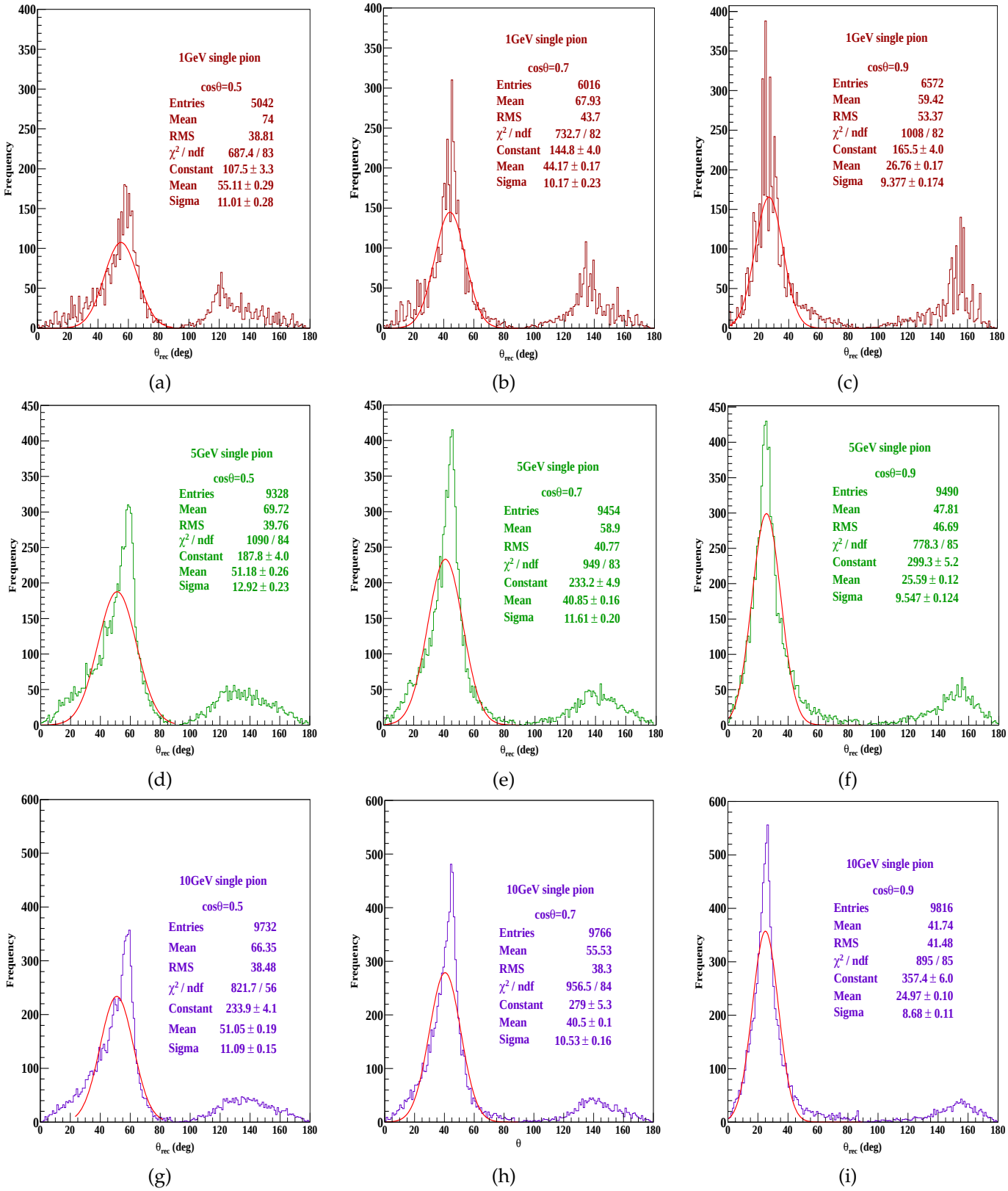

Figure 4.5: Distributions of θ_{rec} in degrees at three different pion energies, 1 GeV, 5 GeV and 10 GeV, in the directions, $\cos\theta = 0.5 \pm 0.1,\ 0.7 \pm 0.1,\ 0.9 \pm 0.1$, for fixed energy single pions with azimuthal angle ϕ smeared from 0–2π. The second peak which is small is due to the events reconstructed in the wrong quadrant. The first peak is fitted with a Gaussian pdf and the σ of this fit is taken to be the direction resolution. The last four fit parameters listed in each histogram correspond to the Gaussian fit.

The direction resolution $\sigma_{\theta_{rec}}$ obtained from a gaussian fit to the reconstructed theta distribution as well as the rms of the histogram (the rms is obtained only for the correctly reconstructed θ), in degrees as a function of hadron energy in (GeV) is shown in Fig. 4.6.

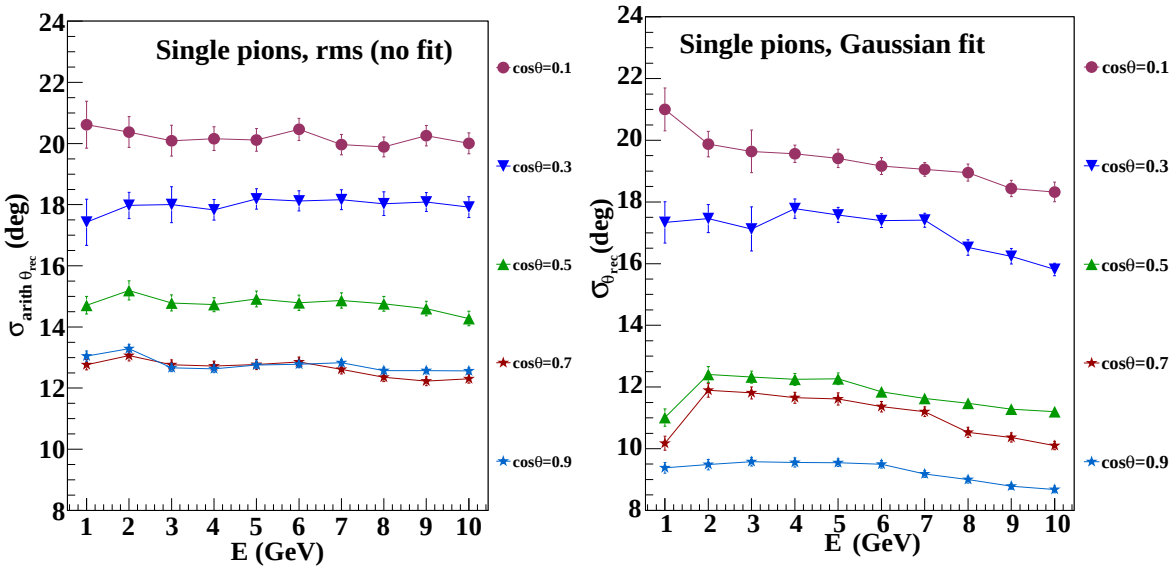

Figure 4.6: Direction resolution $\sigma_{arith_{\theta_{rec}}}$, the rms of the distribution of reconstructed θ in degrees (left) and $\sigma_{\theta_{rec}}$ obtained from a Gaussian fit to the distribution of reconstructed θ (right) for fixed energy single pions in fixed $\cos\theta$ directions with a ϕ smearing in the range 0-2π. The minimum number of layers required to reconstruct direction is two.

The main observations about the resolutions in this case are the following. Taking only the rms of the distribution into account, it can be seen that the resolutions improve as $\cos\theta$ increases but saturate to about 13° for $\cos\theta \geqslant 0.7$. In the very horizontal directions the resolutions are worse owing to the fact that there are fewer number of hits and layers in these horizontal directions, hence making the reconstruction in these directions difficult.

If $\sigma_{\theta_{rec}}$, which is the σ obtained from a Gaussian fit to the reconstructed θ distribution is considered, the resolution is the best for hadrons propagating in the vertical direction, with $\sigma_{\theta_{rec}}$ varying from about $9.38^\circ \pm 0.17^\circ$ at 1 GeV to about $8.68^\circ \pm 0.11^\circ$ at 10 GeV. This implies that the direction resolution improves with energy which is expected. For $\cos\theta \geqslant 0.5$, the Gaussian resolutions are better than the rms value indicating that there are large non-Gaussian tails in the distributions as can be seen from Fig. 4.5.

It is also interesting to see the actual reconstructed mean values as functions of hadron energy E (GeV). The reconstructed arithmetic and Gaussian means as functions of hadron energy E (GeV) are shown in Fig. 4.7. It can be seen that θ is reconstructed around the correct value for $\cos\theta$ = 0.5, 0.7 and 0.9, but are completely off from the actual input value

in the case of the horizontal directions $\cos\theta$ = 0.1 and 0.3. This means that both direction resolution and the actual reconstruction is very poor in the horizontal directions.

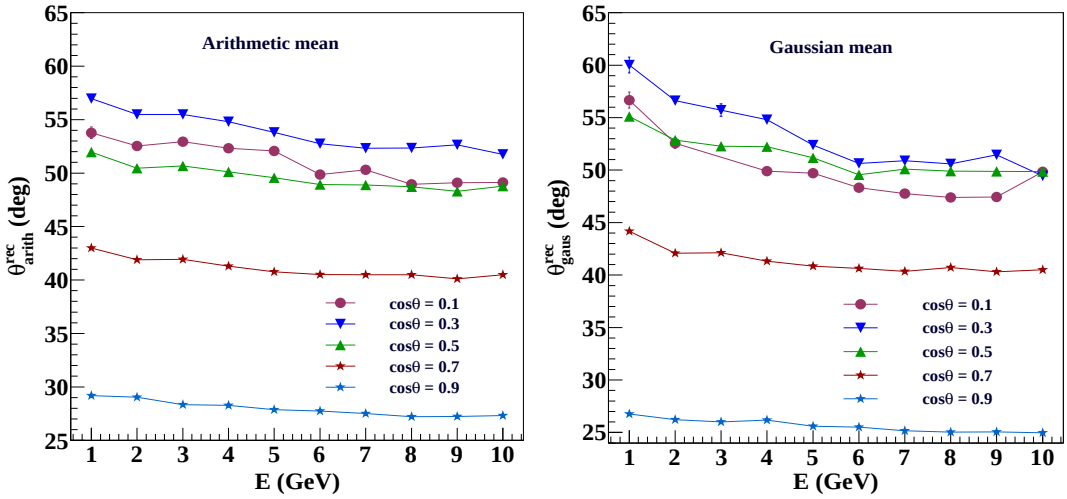

Figure 4.7: Mean values of the reconstructed direction θ_{rec} for fixed energy single pions in fixed $\cos\theta$ directions with ϕ smeared fro 0–2π. The arithmetic mean is shown in the left panel, whereas the mean obtained from a Gaussian fit is shown in the right panel. A layer cut of lmin $\geqslant$ 2 is imposed for reconstructing the direction.

The total fraction of events reconstructed out of the propagated 10000 events and the fraction of events reconstructed in the correct and wrong quadrants as functions of energy are shown in Fig. 4.8 and Fig. 4.9 respectively, with direction reconstructed only if there are two or more layers in the event. The trend is similar to the fixed θ - fixed ϕ case. The fraction of events reconstructed in the correct quadrant increases with both energy and $\cos\theta$ in this case also.

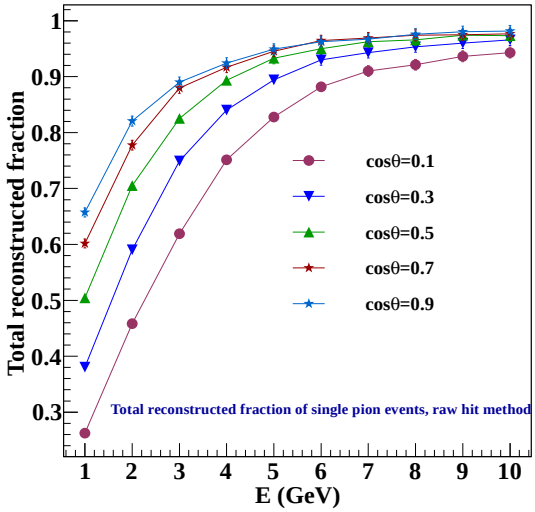

Figure 4.8: Fraction of total events reconstructed out of 10000 events as a function of hadron energy E (GeV) for different $\cos\theta$ values with lmin$\geqslant$2, where lmin is the minimum number of layers required to reconstruct direction.

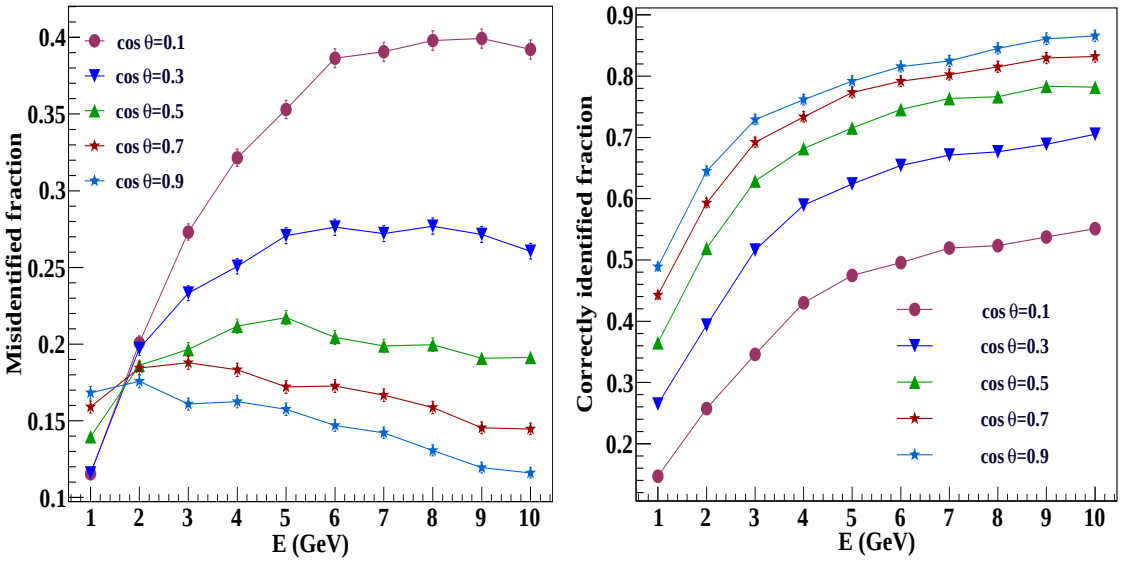

Figure 4.9: Fraction of events reconstructed in the wrong quadrant (left) and in the right quadrant (right) out of 10000 events as a function of hadron energy E (GeV) for different $\cos\theta$ values with lmin$\geqslant$2, where lmin is the minimum number of layers required to reconstruct direction. It should be noted that the y-axes in the two graphs are different.

4.2.3 Direction resolution of hadrons generated in neutrino interactions

So far the discussions were focused on the direction resolution of single pions with fixed energy. A study of the direction resolution of multiple hadrons produced in neutrino interactions was also conducted and is reported in this section. Charged current muon neutrino events generated using the NUANCE neutrino generator have been used for the study. The events are generated for 100 years in ICAL of default iron thickness 5.6 cm. Unlike the fixed energy single pion case, the events are generated all over the detector. Events are binned in different $\cos\theta^{in}_{h'}$ bins namely, [0, 0.2], [0.2, 0.4], [0.4, 0.6], [0.6, 0.8] and [0.8 , 1.0]. These correspond to the $\theta^{in}_{h'}$ bins [90°, 78.46°], [78.46°, 66.42°], [66.42°, 53.13°], [53.13°, 36.87°] and [36.87°, 0.0°] respectively. Still the $\cos\theta$ notation is used in the analysis for ease of depiction. The hadron shower energy defined as $E'_{had} = E_\nu - E_\mu$. The difference between the actual direction of the hadrons and the reconstructed direction $\Delta\theta_{h'} = \theta^{rec}_{h'} - \theta^{in}_{h'}$ in degrees is plotted and fitted with a Gaussian as in sections 4.2.2.1 and 4.2.2.2. Again the direction resolution improves with energy and is the best for the vertical directions.

Distributions of $\Delta\theta_{h'}$ in three input (true) directions $\cos\theta^{t}_{h'} = 0.5 \pm 0.1,\ 0.7 \pm 0.1$ and 0.9 ± 0.1 in different bins of hadron shower energy are shown in Fig. 4.10.

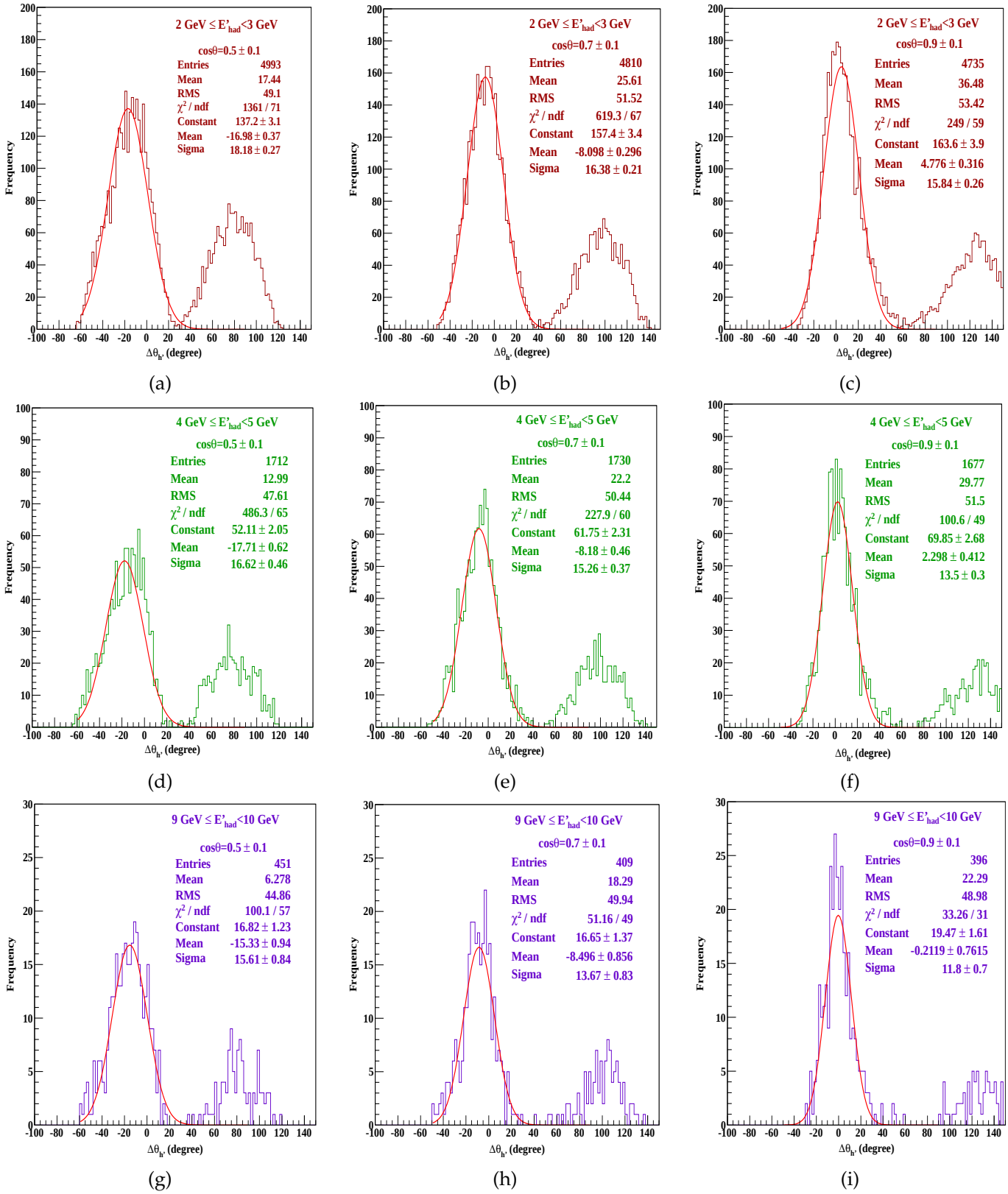

Figure 4.10: Distributions of $\Delta\theta_{h'}$ in degrees in three different hadron energy bins namely 2–3 GeV, 4–5 GeV and 9–10 GeV in the directions $\cos\theta^{t}_{h'} = 0.5 \pm 0.1,\ 0.7 \pm 0.1,\ 0.9 \pm 0.1$, for hadrons from charged current muon neutrino interactions generated using NUANCE. The distributions are fitted with a Gaussian PDF to and the σ of the fit is taken as the direction resolution. The second peak which is small is due to the events reconstructed in the wrong quadrant. It should be noted that the axes scales are not the same in all the plots.

The important observations are the following. Since these are hadrons from neutrino interactions, the number of events decrease as the energy increases. It can be readily observed that as $\cos\theta^t_{h'}$ and shower energy increase, the distributions become narrower. Hence the direction resolution also increases with energy and is the best in the most vertical direction $\cos\theta^t_{h'} = 0.9 \pm 0.1$. However, the fraction of events reconstructed in the wrong quadrant is larger than in the case of fixed energy single pions. This is because there are multiple hadrons, each propagating in a different direction, and the net direction is the vector sum of these. The direction resolution of multiple hadrons from a neutrino interaction as a function of E'_{had} is shown in Fig. 4.11.

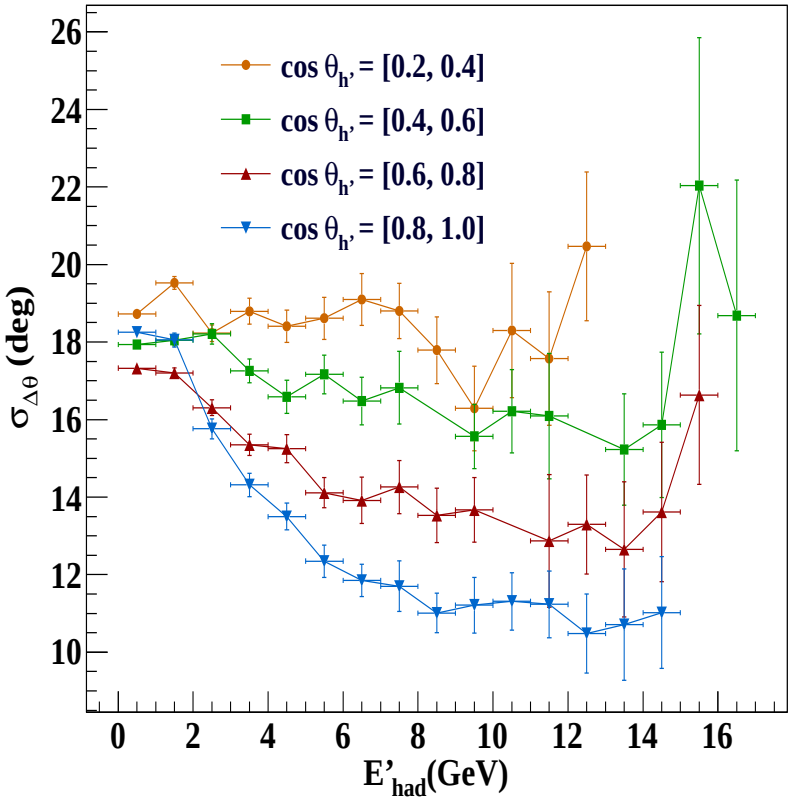

Figure 4.11: Direction resolution $\sigma_{\Delta\theta}$ (deg) of multiple hadrons produced in (anti-)neutrino interactions generated using NUANCE neutrino generator as a function of hadron energy E'_{had} (GeV), where $E'_{had} = E_\nu - E_\mu$. At least 2 layers are required to be in the event to reconstruct the direction.

For the multiple hadrons also, the resolution is the worst in the horizontal bins $\cos\theta$ = [0.0, 0.2] (this bin is not shown in the figure, for the resolutions are poor) and [0.2, 0.4] and improves with increasing $\cos\theta$. The θ resolution of multiple hadrons is observed to be worse than that of fixed energy single pions, especially at low energies. However, at large $\cos\theta$ (nearly vertical) and higher energies, the resolution of the multiple hadrons is distinctly better (and improves with energy in contrast to the rather flat energy depen-

dence of single pions. This can be attributed to the fact that the hadrons produced in neutrino interactions are forward boosted compared to fixed energy single pions. Also direction resolution becomes very good after about 8 GeV which is the region corresponding to deep inelastic scatterings. The best resolution is for the $\cos\theta_{h'} = [0.8,\ 1]$ bin with $\sigma_{\Delta\theta} \approx 15.6^{\circ}$ in the E'_{had}=2–3 GeV energy range and $\sigma_{\Delta\theta} \approx 11^{\circ}$ in the E'_{had}=14–15 GeV bin.

The fraction of events reconstructed in the correct and wrong quadrants of θ, for different values of $\cos\theta_{h'}$ bin are also plotted as a function of E'_{had} (GeV) and are shown in Fig. 4.12. These fractions are calculated with respect to the number of events for which a direction was reconstructed with a cut on the minimum number of layers in an event as 2. It can be seen that the number of events reconstructed in the correct quadrant increases with the increase in shower energy E'_{had} and $\cos\theta_{h'}$ (i.e., as the direction becomes more and more vertical). The number of events reconstructed in the wrong quadrant decreases with the increase in E'_{had} and $\cos\theta_{h'}$. Thus the most vertical direction $\cos\theta = [0.8,\ 1]$, for which the direction resolution is also the best has the maximum (least) number of events with correctly (wrongly) reconstructed direction.

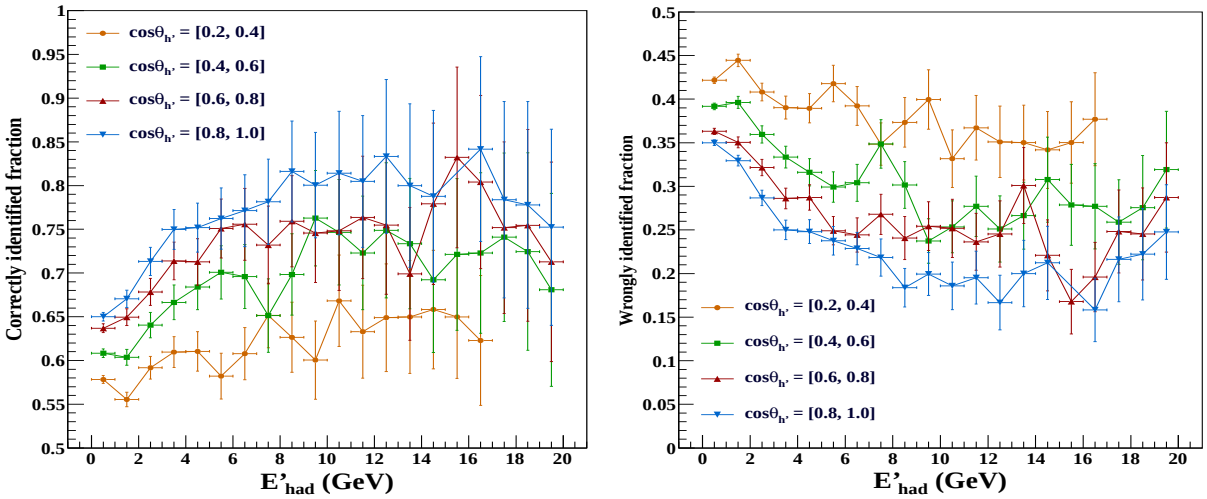

Figure 4.12: Fraction of charged current muon neutrino events generated using NUANCE neutrino generator, in which the hadron shower direction was reconstructed in the correct quadrant (left) and in the wrong quadrant (right) as a function of hadron shower energy E'_{had} (GeV) for different values of $\cos\theta_{h'}$. A minimum of two layers or more should be present in an event to reconstruct the direction. It should be noted that the y-scales in the two graphs are different.

4.3 Reconstruction of the angle between the muon and the hadrons produced in a neutrino interaction using the raw hit method.

In a charged current muon neutrino interaction, the incoming neutrino produces a muon and hadron shower in the final state. Depending on the energy of the incoming neutrino and the interaction process, the opening angle between the final states will vary. The reconstruction of this opening angle $\beta_{\mu h'}$ between the muon and the hadron shower is discussed in this section.

The true angle $\beta^t_{\mu h'}$ between the final state muon and hadron can be expressed as :

$$\cos\beta^t_{\mu h'} = \sin\theta^t_\mu \sin\theta^t_{h'} \cos\left(\phi^t_\mu - \phi^t_{h'}\right) + \cos\theta^t_\mu \cos\theta^t_{h'}, \tag{4.9}$$

where $\beta^t_{\mu h'}$ is the true angle between the muon and hadron shower, θ^t_μ and ϕ^t_μ are the true muon directions, $\theta^t_{h'}$ and $\phi^t_{h'}$ are the true hadron directions. The distribution of $\beta^t_{\mu h'}$ in the neutrino energy range $0 \leqslant E_\nu$<20 GeV, obtained using a 100 year sample of charged current muon neutrino events are shown in Fig. 4.13. The distribution of neutrino energy for the same sample is also shown.

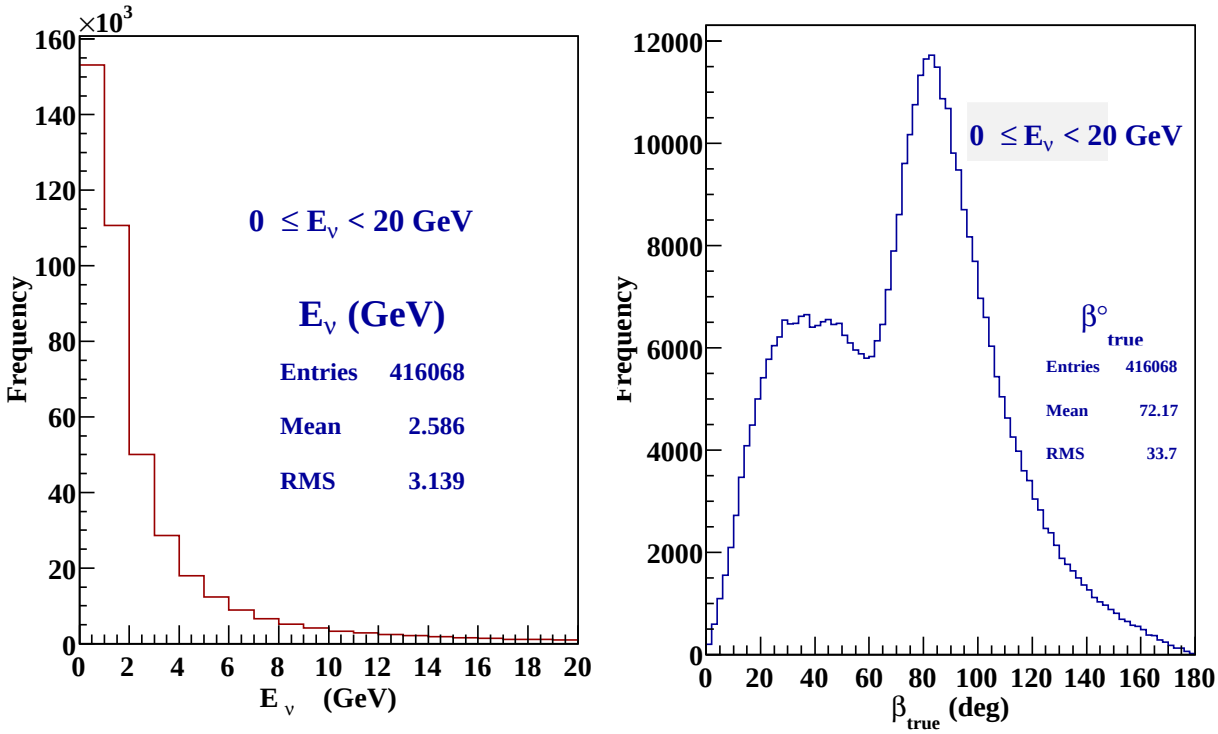

Figure 4.13: The distribution of neutrino energy E_ν in the energy range $0 \leqslant E_\nu < 20$ GeV in a 100 year unoscillated sample of charged current muon neutrino events (left). The distribution of $\beta^t_{\mu h'}$ for the same sample in the same neutrino energy range (right).

It can be seen that the distribution of $\beta^t_{\mu h'}$ has a double peak and cannot be fitted to any functional form simply. Moreover the neutrino interactions of interest in ICAL mostly produce hadrons of energies above $\sim$ 2 GeV. Hence the distribution of $\beta^t_{\mu h'}$ with the hadron shower energy E'_{had} in the range $2 \leqslant E'_{had} 15$ GeV can be plotted and it gives a reasonable distribution. This distribution along with the $\cos\theta^t_{h'}$ of hadrons in the 2–15 GeV energy range are shown in Fig. 4.14. To reconstruct $\beta_{\mu h'}$, only the reconstructed val-

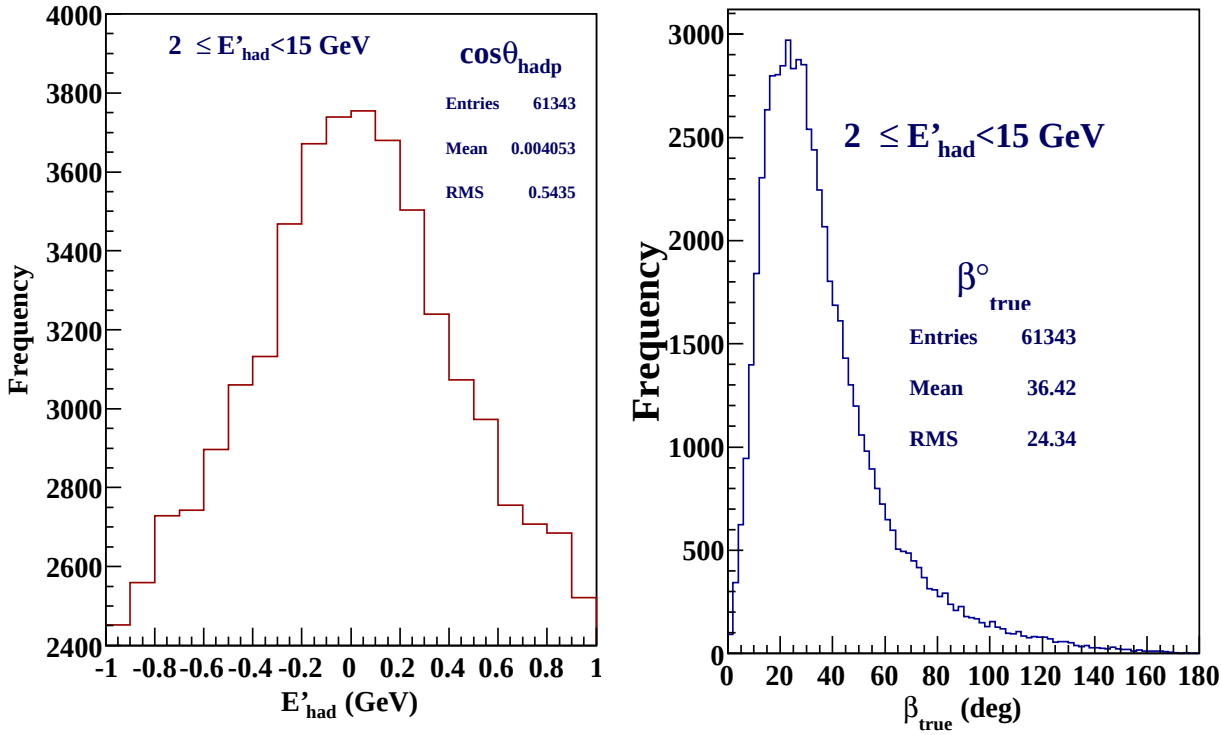

Figure 4.14: The distribution of $\cos\theta^t_{h'}$ of the hadron shower in the energy range $2 \leqslant E'_{had} < 15$ GeV in a 100 year sample of charged current muon neutrino events (left). The distribution of $\beta^t_{\mu h'}$ for the same sample in the same hadron shower energy range (right).

ues $\theta^{rec}_{h'}$ and $\phi^{rec}_{h'}$ of the hadron shower are used and the true values of the corresponding quantities for muon are taken. This is because of the fact that muon have excellent resolution $\sim 1^\circ$ resolution for θ_μ in ICAL and hence the uncertainty in the reconstruction of $\beta_{\mu h'}$ arises only from the uncertainty in hadron direction. For hadrons, the directions $\theta^{rec}_{h'}$ and $\phi^{rec}_{h'}$ obtained using raw hit method are used to reconstruct $\beta_{\mu h'}$. The reconstructed angle is expressed as :

$$\cos\beta^{rec}_{\mu h'} = \sin\theta^t_\mu \sin\theta^{rec}_{h'} \cos\left(\phi^t_\mu - \phi^{rec}_{h'}\right) + \cos\theta^t_\mu \cos\theta^{rec}_{h'}. \tag{4.10}$$

To obtain the resolution, the difference between the true angle and the reconstructed

angle $\Delta\beta_{\mu h'} = \beta^t_{\mu h'} - \beta^{rec}_{\mu h'}$ is calculated and fitted with Landau fitting function in each $\cos\theta^t_{h'}$ bin in the hadron energy range 2–15 GeV. The best results are obtained for $\cos\theta^t_{h'}$ corresponding to vertical directions and in the bin $0^\circ \leqslant \beta^t_{\mu h'} < 45^\circ$. In the bin with $45^\circ \leqslant \beta^t_{\mu h'} < 90^\circ$, the results are worse for the same bin of $\cos\theta^t_{h'}$. The distributions of $\Delta\beta_{\mu h'}$ in the $\cos\theta^t_{h'} = 0.8 \pm 0.1$ bin are shown in Fig. 4.15. One important observation is that in the same $\cos\theta_{h'}$ bin, the number of events in the $0^\circ \leqslant \beta^t_{\mu h'} < 45^\circ$ region is greater than that in the $45^\circ \leqslant \beta^t_{\mu h'} < 90^\circ$. This indicates that most of the events are forward boosted. The energy averaged resolutions of $\Delta\beta_{\mu h'}$ as a function of the input hadron

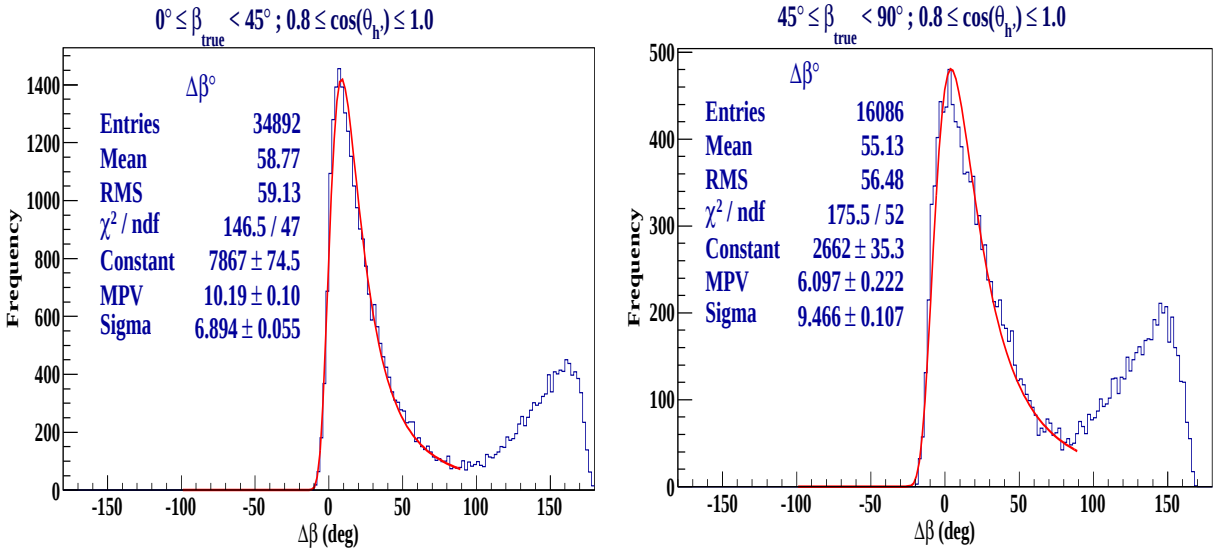

Figure 4.15: Distributions of $\Delta\beta_{\mu h'}$ in the 2–15 GeV range of E'_{had}, in the vertical bin $\cos\theta^t_{h'} = 0.9 \pm 0.1$ (left) when $\beta^t_{\mu h'}$ is between 0° and 45° and (right) when $\beta^t_{\mu h'}$ is between 45° and 90°.

direction $\cos\theta_{h'}$, for the two different cases where $\beta^t_{\mu h'}$ is between 0° and 45°, and 45° and 90° respectively are shown in Fig. 4.16. It can be seen that the resolution is worse for the latter case, when the hadrons are in a more horizontal direction. Again the larger error bars on $\sigma_{\Delta\beta}$ in the $45^\circ \leqslant \beta^t_{\mu h'} < 90^\circ$ case indicates the presence of less number of events. The best resolution achievable in the $0^\circ \leqslant \beta^t_{\mu h'} < 45^\circ$ region is about 10° in the vertical directions $|\cos\theta_{h'}| = [0.8\ ,\ 1.0]$. As expected the worst resolution is in the horizontal direction where there is not enough hit information to reconstruct the direction. The resolution of $\Delta\beta_{\mu h'}$ as a function of neutrino energy E_ν in different bins of input neutrino directions is shown in Fig. 4.17. The resolution of $\Delta\beta_{\mu h'}$ as a function of E'_{had} in different bins of input hadron directions is also shown in the same figure. To obtain the resolution in both cases, the distribution of $\Delta\beta_{\mu h'}$ is fitted with a Landau distribution function and the σ of this fit is taken as the resolution of $\Delta\beta_{\mu h'}$.

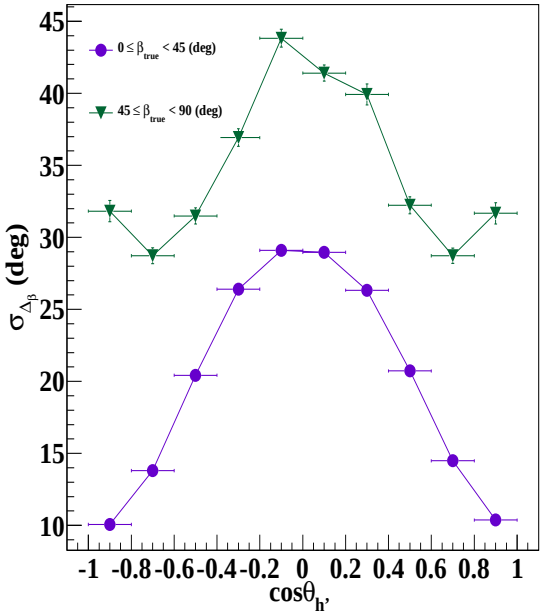

Figure 4.16: Resolution of $\beta_{\mu h'}$ as a function of the input hadron shower direction. This is an energy averaged result.

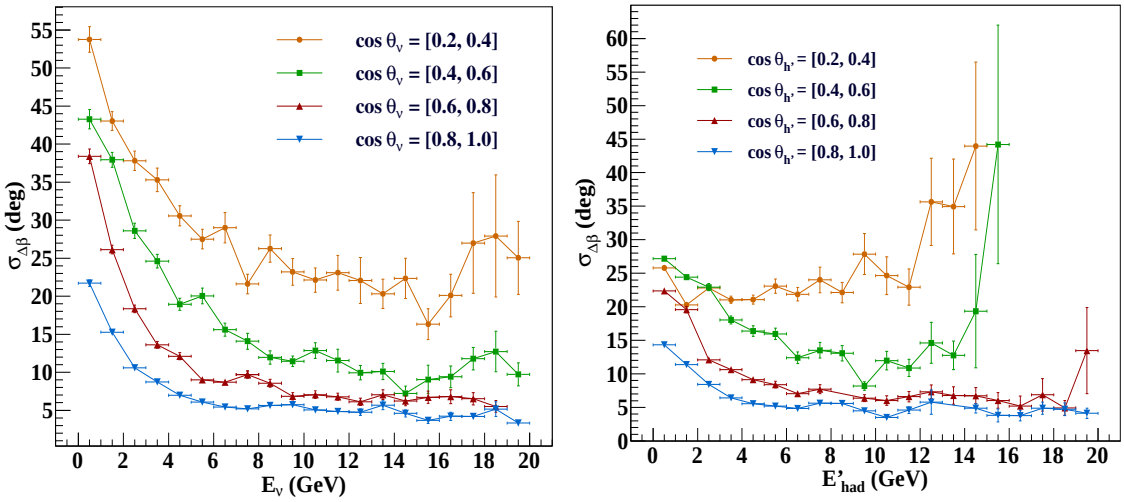

Figure 4.17: (Left) The resolution of $\Delta\beta_{\mu h'}$ as a function of neutrino energy E_ν in GeV in different bins of input neutrino direction, for all $\beta^t_{\mu h'}$. (Right)The resolution of $\Delta\beta_{\mu h'}$ as a function of hadron energy E'_{had} in GeV in different bins of input hadron direction, for $\beta^t_{\mu h'}$.

It can be seen that, on the average, the resolution is the best in the vertical direction $\cos\theta_\nu = [0.8\ ,\ 1.0]$ and the worst in the horizontal direction $\cos\theta_\nu = [0.2\ ,\ 0.4]$. The resolution improves with energy, with $\sigma_{\Delta\beta}$ being about $\sim 3.5^\circ$ at 20 GeV. The result shown is for all $\beta^t_{\mu h'}$. When plotted as a function of E'_{had}, the resolution worsens slightly. On the average the resolution obtained in the direction $\cos\theta_{h'} = [0.8, 1.0]$ is about $\sim 5^\circ$ in the 10–20 GeV energy range. However it should be noted that more detailed analysis is required to see if a functional form other than the Landau distribution can parametrise

the distribution of $\Delta\beta$. For the time being this is out of the scope of this thesis. All the discussions in this chapter are concentrated on the reconstruction of the zenith angle θ of the hadron shower. However, the reconstruction of the azimuthal angle ϕ of the shower can also be done. It is found that in general, both for fixed energy single pions and for hadrons from neutrino interactions generated using NUANCE, the resolution of ϕ is worse than that for θ. This can be attributed to the fact that the pick up strips of the RPCS are 1.96 cm wide (this is in simulations, in the real detector it will be 2.8 cm which is even broader). This increases the uncertainty in the position of the hit in the $X-Y$ plane which in translates to worsening of the ϕ resolution. In contrast the Z-direction uncertainty is only 1 mm. This is true for muons also.

4.3.0.1 Direction resolution of hadrons in neutral current events

Since the "raw hit" method does not require the knowledge of the charged lepton vertex with respect to which to reconstruct the hadron shower direction, it can be used to reconstruct the shower direction of hadrons produced in neutral current interactions. The study on this was conducted with hadrons produced in the neutral current muon neutrino interactions generated using NUANCE. The analysis was carried out in the same way as for hadrons from charged current muon neutrino events. The distribution of the difference $\Delta\theta_{h'} = \theta^{rec}_{h'} - \theta^{t}_{h'}$, where $\theta^{rec}_{h'}$ is the reconstructed direction of the shower and $\theta^{t}_{h'}$ is the true shower direction, in different energy bins for different values of $\cos\theta$ are illustrated in Fig. 4.18. The fraction of the events reconstructed in the wrong quadrand (peak at $\Delta\theta_{h'} \sim 90^{\circ}$ is roughly the same as in the case of hadrons from CC events. As in the case of hadrons from charged current muon neutrino events, these distributions are fitted with a Gaussian pdf and the σ of the fit gives the θ resolution.

The resolution of $\Delta\theta_{h'}$ as a function of E'_{had} for different $\cos\theta_{h'}$ bins is illustrated in Fig. 4.19. As in the case of hadrons from charged current muon neutrino interactions, the resolution is worse in the horizontal bins, and improves as the direction becomes more and more vertical and with the increase in hadron energy. The best achievable resolution is around $\sim$10–11 degrees, in the vertical direction $\cos\theta = [0.8,\ 1.0]$. While the resolutions are comparable for larger values of $\cos\theta$ i.e., $\cos\theta \geqslant 0.6$ to those obtained for hadrons from charged current muon neutrino events (shown in Fig. 4.11), they are worse, especially at higher energies, for more horizontal events. This may also be a consequence of a smaller

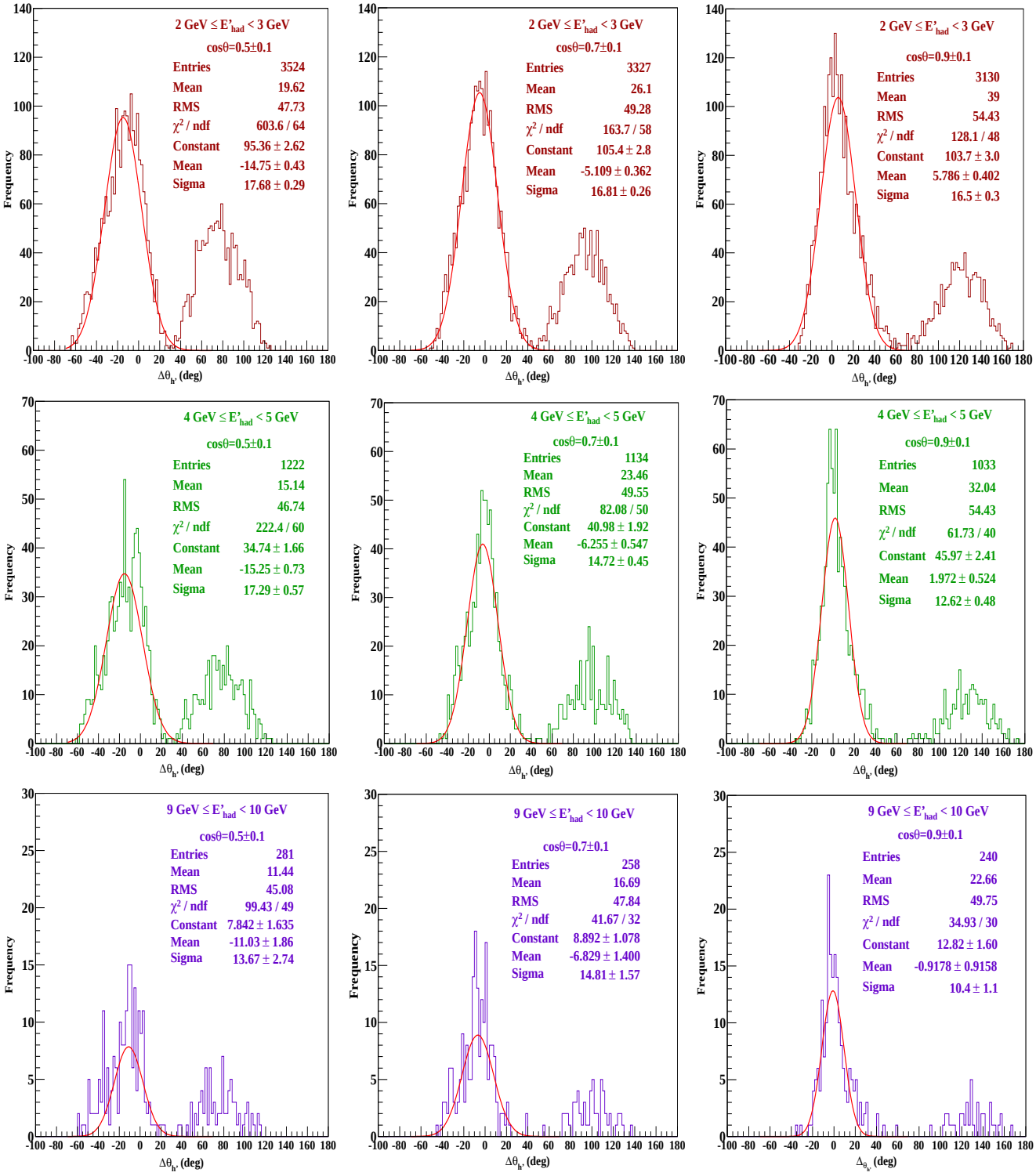

Figure 4.18: Distributions of $\Delta\theta_{h'}$ in degrees in three different hadron energy bins namely 2–3 GeV, 4–5 GeV and 9–10 GeV in the directions $\cos\theta^{t}_{h'} = 0.5 \pm 0.1,\ 0.7 \pm 0.1,\ 0.9 \pm 0.1$, for hadrons from neutral current muon neutrino interactions generated using NUANCE. The distributions are fitted with a Gaussian PDF to and the σ of the fit is taken as the θ resolution of the hadron shower. The second peak which is small is due to the events reconstructed in the wrong quadrant. It should be noted that the axes scales are not the same in the plots.

data sample, as can be seen by comparing Figs. 4.10 and 4.18.

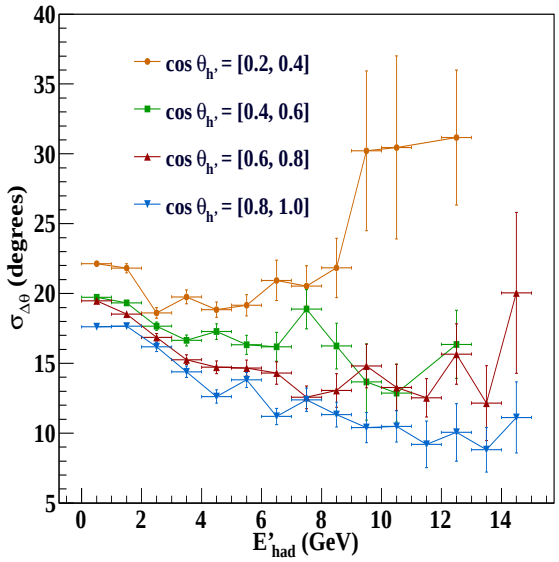

Figure 4.19: The resolution $\sigma_{\Delta\theta}$ in degrees as a function of E'_{had} (GeV) for different $\cos\theta_{h'}$ bins, for hadrons from neutral current muon neutrino interactions generated using NUANCE neutrino generator.

4.4 Chapter Summary

Reconstruction of neutrino direction requires the reconstruction of the directions of the final state particles; in charged current muon neutrino interactions, the directions of the muon and hadron shower have to be reconstructed. Since the muons leave long clean tracks in the detector unlike hadrons which leave a shower, the direction resolution of muons in the ICAL is excellent (less than a degree). The only information about hadrons being hit information, the position and timing of the hits are used to reconstruct the shower direction. The method which makes use of the hit and timing information only is called the "raw hit" method. Since this method does not require any charged lepton vertex with respect to which the direction can be reconstructed, it can be used to reconstruct any type of shower, in the case of hadrons, the showers from both charged current events and neutral current events. Positions of the hits are used to reconstruct the direction whereas their timings have been used to break the quadrant degeneracy of θ.

GEANT-4 simulation studies have been carried out on the direction reconstruction of fixed energy charged single pions with fixed zenith angle θ and azimuthal angle ϕ, as well as fixed energy charged single pions in fixed $\cos\theta$ directions, but with ϕ smeared in the 0–2π range. An energy and ϕ averaged resolution of about $\sim 9^\circ$ is obtained for the

$\theta = 30^\circ$ case and $\sim 9.8^\circ$ in the $\theta = 150^\circ$ case, in the 1–10 GeV energy range. In the case where different $\cos\theta$ directions are considered the best θ resolution is obtained for the $\cos\theta$ value 0.9. At 1 GeV the resolution is about $9.38^\circ \pm 0.17^\circ$ and $8.68^\circ \pm 0.11^\circ$ at 10 GeV, at this $\cos\theta$.

Simulation studies of direction reconstruction of hadron showers from neutrino events generated using NUANCE neutrino generator were also done. Both charged current muon neutrino and neutral current muon neutrino events have been used for this study. The resolutions are again found to be the best in the vertical direction $\cos\theta = [0.8,\ 1]$ with $\sigma_{\Delta\theta} = 15.6^\circ$ in the $E'_{had} = 2.5 \pm 0.5$ GeV bin and $\sim 11^\circ$ in the $E'_{had} = 14.5 \pm 0.5$ GeV bin. It decreases as $\cos\theta_{h'}$ decreases and is worse for the hadrons in the most horizontal direction, i.e., in the $\cos\theta_{h'} = [0,\ 0.2]$ bin. It should be noted that these resolutions correspond to the *actual* polar angle, and not the angle with respect to the neutrino or charged lepton. The resolution is therefore worse (both for hadrons and muons) in the horizontal direction, due to the geometry of ICAL, with its horizontal layers and $X - Y$ magnetic field. Hence the events in which either the muon or the final state hadrons (or both) are mostly in the horizontal direction will be poorly reconstructed.

For hadrons from neutral current muon neutrino events also the trend of θ resolution is the same, with the resolution being the best in the $\cos\theta_{h'} = [0.8,\ 1]$ direction. A resolution of $\sim 16.5^\circ$ is obtained in the 2–3 GeV E'_{had} bin and $\sim 10^\circ$ is obtained in the 12–15 GeV energy range.

The resolution of the opening angle $\beta_{\mu h'}$ between the muon and the hadrons in the final state of a charged current muon neutrino interaction is also obtained using the raw hit method. For this purpose the reconstructed values of only the hadron θ and ϕ are used; the true values of the muon direction are taken for the analysis. The resolution $\sigma_{\Delta\beta}$ is the best in the $|\cos\theta_{h'}| = [0.8,\ 1]$ bin, $\sim 10^\circ$; the $0^\circ \leqslant \beta_{true} < 45^\circ$ region is better compared to the $45^\circ \leqslant \beta_{true} < 90^\circ$ region. The energy dependence of the resolution of $\beta_{\mu h'}$ is such that a fit to the $\Delta\beta_{\mu h'}$ histogram with a Landau distribution in the $E_\nu = 2.5 \pm 0.5$ GeV region yields a resolution of $\sim 10^\circ$ and $\sim 3.3^\circ$ in the $E_\nu = 2.5 \pm 0.5$ in the $\cos\theta_\nu = [0.8,\ 1]$ bin.

Thus it can be seen that the simulation studies can give a good insight into the direction reconstruction of hadrons which in turn will help in the reconstruction of the direction of the incoming neutrino. It can be seen that the uncertainty in the reconstruction of the neutrino direction is driven by that in the reconstruction of hadron direction. Hence, any change in geometry, like varying the strip width or any new algorithm to

improve the shower reconstruction and the direction resolution has to be probed. Even then the results of this study give a good idea of what the hadron direction will be like in the ICAL detector. Currently only the muon energy, direction and the hadron energy are being used as the observables to bin the events in the oscillation physics studies using the ICAL. The effect of adding hadron direction as a fourth observable is worth studying since the addition of hadron energy has proved to significantly improve the sensitivity of the ICAL to oscillation parameters. Also the binning of events in the L/E of the neutrino is always of interest and for this, the reconstruction of both hadron energy and direction are necessary inputs in order to reconstruct fully the L and E of the neutrino from the corresponding charged current lepton and hadron informations.

5 Brief review of muon response in ICAL

5.1 Overview

The main interaction processes of interest in the ICAL detector being the charged current interactions of muon neutrinos and anti-neutrinos (i.e., CC interactions of ν_μ and $\bar{\nu}_\mu$), it is necessary to reconstruct the momentum and direction of the final state muon to reconstruct the incoming neutrino parameters. Also the charge of the muon has to be determined by the direction of its curvature in the magnetic field, since this is the crucial information which determines whether the interaction was that of a neutrino or anti-neutrino and hence forms the basic technique for mass hierarchy distinction. GEANT4 based simulation studies to characterise the muon responses and reconstruction and charge identification efficiencies of the ICAL detector have been performed and have been reported in Refs. [22, 108]. The responses and efficiencies of muons in the central region of the ICAL detector have been tabulated into a look up table and are used in the ICAL oscillation sensitivity analyses. These values as can be seen in the following sections are the best values of muon responses and yield the best oscillation sensitivities because of the uniform magnetic field of 1.5 T. The main highlights of the muon responses in the central of the ICAL detector discussed in [22] are presented in this Chapter for completeness, since they are used in the analysis presented in Chapter 6. In addition, a brief discussion on separating charged current muon neutrino (ccmu) events from charged current electron and neutral current events (cce and nc) is also presented in this Chapter.

5.2 Muons and tracks

The most important quality of muons propagating in ICAL is that they leave clean tracks in the detector unlike the showers by hadrons. This is because of these particles being minimum ionising at the energies of interest to ICAL. As mentioned in Chapter 3, a charged particle leaves a "hit" in the detector, which carries both position and timing

informations; the (x, y) co-ordinates obtained from the pick up strips, z from the layer, and timing with respect to a trigger. Muons in ICAL leave one hit per layer on the average hence avoiding the ghost hit problem seen with hadrons; in addition, they leave a long track in the detector. The reconstruction of muons in the ICAL are done in different steps which include finding the tracks from hits and fitting the tracks.

5.2.1 Track finding

The possible pairing of all adjacent x and y hits in a layer give *clusters*.; a *tracklet* comprises clusters in a few successive layers. Using a simple curve fitting algorithm, tracklets are found by searching for clusters in three adjacent layers. Nearby tracklets are joined together to form a *track* and the longest possible track in an event is obtained by the iteration of this process [132]. The direction of the track is determined by averaging the x and y timings in a plane. To reduce the misidentification of a hadron shower or noise as a muon track the event is required to satisfy the criterion that it should contain at least 5 layers in the muon-like track. For such events, the clusters in each plane are averaged to a single hit per plane and the position and timing information of this average hit point are passed to the track fitter.

5.2.2 Track fitting

Track fitting in ICAL is done using a Kalman filter [133] based algorithm to take into account the bending of tracks in the presence of magnetic field and the effects due to energy losses during propagation. Since the tracks are bent a simple linear fit cannot be applied to fit the tracks and obtain the direction of the muon from it. The Kalman filter algorithm [133–135] treats a track as a state vector paramatrised by hit position, track direction and the particle momentum at a particular position. The starting state vector is defined as $X_0 = (x, y, dx/dz, dy/dz, q/p)$, where (x, y, z) is the position of the first hit recorded by the finder. The charge weighted inverse momentum q/p is taken to be zero at this stage. The initial track direction is calculated using the first two layers of the event assuming that it is straight in this section. This initial state vector X_0 is then extrapolated into the next layer using a 5×5 *propagator matrix* F, whose elements contain information about the magnetic field according to the magnetic field map of ICAL

discussed in Chapter 2 and energy loss of the particle in iron according to Bethe-Bloch equation [120].

The estimated value of the state vector after k planes is given by $X_k = F_{k-1}X_{k-1} + u_{k-1}$. Here u represents the process noise which gives information about multiple scattering and energy loss by the muon. The propagator matrix is calculated for every pair of detector planes. The state covariance matrix C contains the expected error in the state vector. Iterative comparisons of the actual hit location and the extrapolated point are done till they are close enough to call the fit to the track a good one. Further extrapolation of the track backwards is done to half the thickness of the iron layer to determine the interaction vertex (assumed to be at the centre of the iron plate). The best fit value of the muon momentum at the vertex is obtained as the reconstructed momentum (both magnitude and direction). The quantity q/p determines the magnitude of the momentum at the vertex and gives the charge of the muon, whereas dx/dz and dy/dz give $\cos\theta$ and ϕ of the muon. To obtain best reconstructed values a loose cut of $\chi^2/\text{ndf} < 10$ is imposed; a tighter constraint does not alter the results significantly.

5.3 Muon resolutions and efficiencies

As in the case of hadrons, GEANT4 based simulation studies have been conducted to estimate the muon resolutions and efficiencies in the ICAL detector, especially in the central region of each module. Fixed energy single muons propagating from vertices randomised over a region of -4 m $\leqslant$ x $\leqslant$ 4 m, -4 m $\leqslant$ y $\leqslant$ 4 m and -4 m $\leqslant$ z $\leqslant$ 4 m with the origin in the center of the central module are used for this analysis. The muons being minimum ionising particles will travel long distances in the detector that some of the tracks may even go out of the detector volume depending on the energy (mostly around $p_{in} \geqslant 6$ GeV/c), direction and the vertex of the muons. Both fully and partially contained events are analysed together here.

Both μ^- and μ^+ are propagated in the detector at fixed momenta p_{in} in fixed $\cos\theta$ bins with ϕ smeared from 0–2π. The reconstructed muon momentum distribution for $(p_{in}, \cos\theta) = (5\ \text{GeV/c}, 0.65)$ is shown in Fig. 5.1. Since the distributions are similar for both μ^- and μ^+, only μ^- have been used further to determine momentum and direction resolutions. The results of this analysis was tabulated as a look-up table and this table is used in the physics simulation studies discussed in Chapter 6. The detailed analysis of

muon resolutions and efficiencies in the central region with ϕ dependence was done in [22]. However this will not be discussed here since it is out of the scope of this thesis. The results illustrated here are all ϕ averaged, although ϕ dependence has been studied as well.

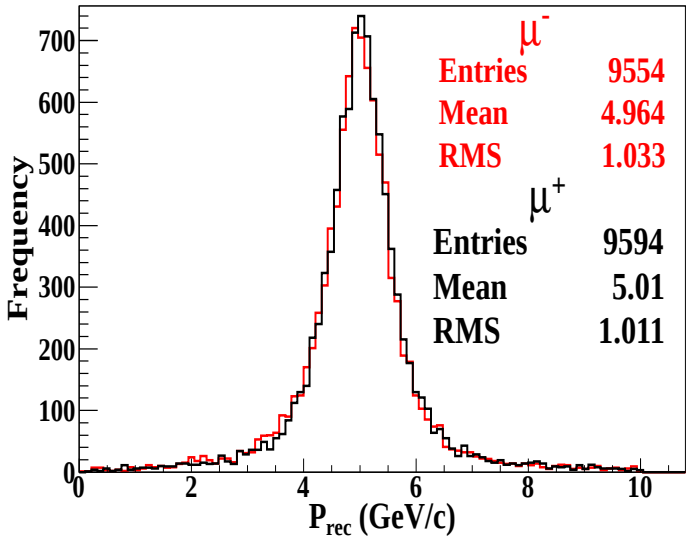

Figure 5.1: Distributions of reconstructed momenta of fixed energy single μ^- and μ^+ with $(p_{in}, \cos\theta) = (5\ \text{GeV/c}, 0.65)$, propagating from vertices randomised in the central region of the detector. Figure taken from Ref. [22].

5.3.1 Momentum resolution

If σ_{rec} is the RMS width of the distribution of the reconstructed momentum p_{rec}, the momentum resolution R, with its error δR is expressed as:

$$R = \frac{\sigma}{p_{in}}; \tag{5.1}$$

$$\frac{\delta R}{R} = \frac{\delta\sigma}{\sigma}, \tag{5.2}$$

where $\delta\sigma$ is the error on the width of the reconstructed momentum distribution. Depending on the energy of the muon the reconstructed momentum distribution can be fitted with an appropriate functional form. The ϕ averaged momentum resolutions as functions of input muon momenta, for μ^- at different values of $\cos\theta$ are shown in Fig. 5.2.

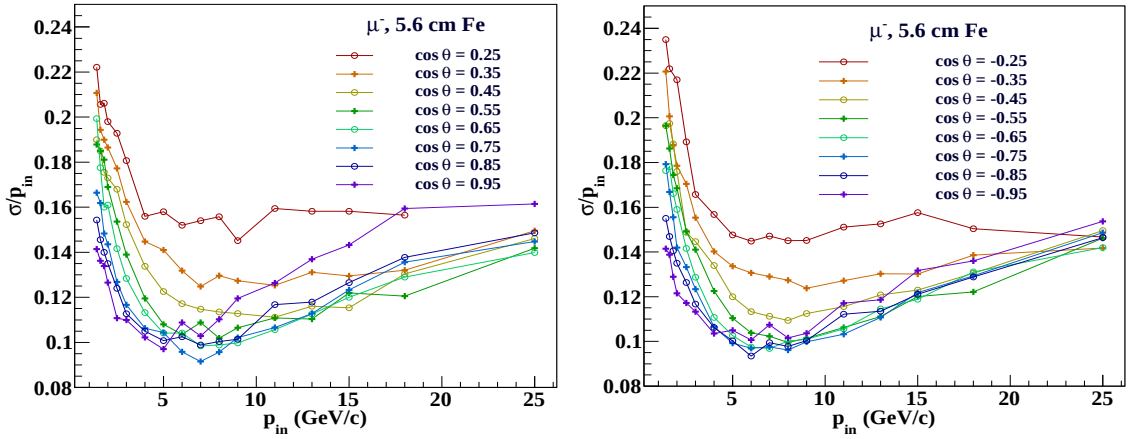

Figure 5.2: Momentum resolution σ/p_{in} as a function of the input momentum p_{in} (GeV/c) for different vlaues of $+\cos\theta$ (left) and $-\cos\theta$ (right). The figures were generated uusing the resolutions as given by the analysis presented in Ref. [22].

5.3.2 Zenith angle (θ) resolution

The distribution of the reconstructed zenith angle θ is fitted with a Gaussian pdf and the width of this fit is taken to be the zenith angle resolution. The distribution of θ_{rec} with a Gaussian fit to it at $(p_{in}, \cos\theta) = (5\ \text{GeV/c}, 0.65)$ is shown in Fig. 5.3. The narrow distribution with a width about less than a degree indicate that the zenith angle resolution of muons in the ICAL detector is extremely good. Zenith angle resolution as a function of input muon momentum is also shown in Fig. 5.3. The resolution improves fast with

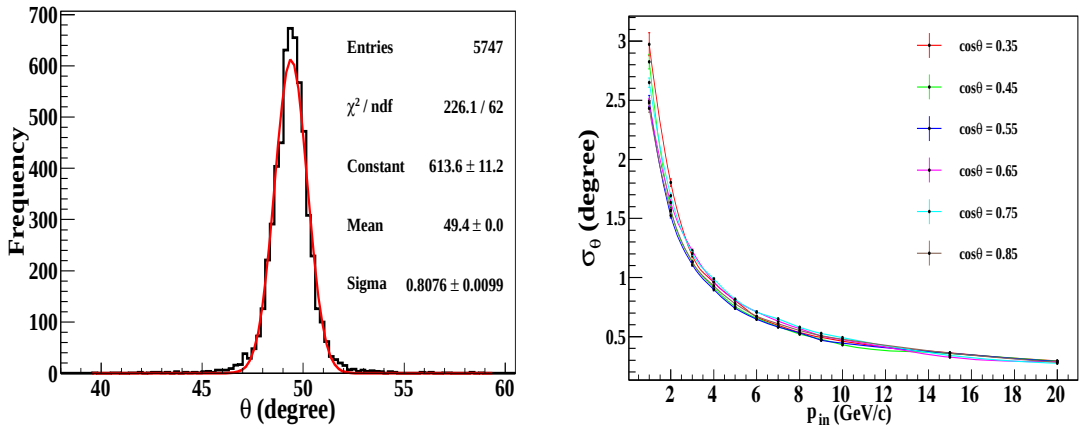

Figure 5.3: (Left) Reconstructed muon θ distribution at $(p_{in}, \cos\theta) = (5\ \text{GeV/c}, 0.65)$ fitted with a Gaussian pdf; the fitted σ gives the direction resolution. (Right) Zenith angle resolution in degrees as a function of muon momentum p_{in} for various $\cos\theta$ values. Figures taken from Ref. [22].

increase in momentum, and is less than $\sim 1^\circ$ for all input angles, beyond 4 GeV/c input momentum. For $p_{in} > 10$ GeV/c, the resolutions are almost the same for all angles.

Also, the fraction of events reconstructed in the wrong quadrant (up/down distinction) is negligible for muons with $E \geqslant 2$ GeV.

5.3.3 Reconstruction efficiency

The efficiency to reconstruct muon momentum (ϵ_{rec}) is defined as the ratio of the number of reconstructed events n_{rec} to the total number of events propagated N_{total}; i.e.,

$$\epsilon_{rec} = n_{rec}/N_{total}; \tag{5.3}$$

$$\delta\epsilon_{rec} = \sqrt{\epsilon(1-\epsilon_{rec})/N_{total}}, \tag{5.4}$$

where $\delta\epsilon_{rec}$ is the error on reconstruction efficiency. Reconstruction efficiency as a function of input muon momentum at different input zenith angles is shown in Fig. 5.4. It can be seen that the reconstruction efficiency depends on the energy of the incident particle, magnetic field strength and direction of propagation. For p_{in} <4 GeV/c, the reconstruc-

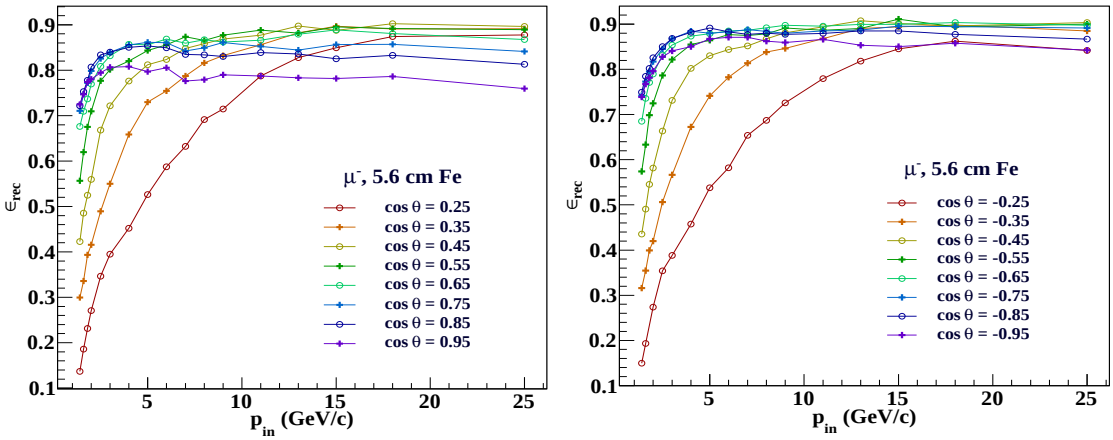

Figure 5.4: Momentum reconstruction efficiency ϵ_{rec} as a function of p_{in} (GeV/c) at different zenith angles for $+\cos\theta$ (left) and $-\cos\theta$ (right). Figure generated according to the muon resolution table obtained from the analysis presented in Ref. [22].

tion efficiency increases with increase in momentum owing to the increase in the number of hits when the muon crosses more number of layers. The efficiency at smaller energies is larger for vertical directions compared to horizontal ones. At higher energies the efficiency becomes almost constant, for vertical directions there is a slight drop due to the fact that the track is only partially contained (track goes out of the detector) and due to the requirement that only a single track should be reconstructed [22].

5.3.4 Relative charge identification (CID) efficiency

The charge of the muon has to be identified correctly to determine whether an interaction is a muon neutrino ν_μ interaction or a muon anti-neutrino $\bar{\nu}_\mu$ interaction, thus enabling mass hierarchy distinction. The direction of bending of a particle in the magnetic field determines its charge. Relative charge identification efficiency is the ratio of the number of events with correctly identified charge n_{cid} to the total number of reconstructed events n_{rec}; i.e.,

$$\epsilon_{cid} = n_{cid}/n_{rec}; \tag{5.5}$$

$$\delta\epsilon_{cid} = \sqrt{\epsilon_{cid}(1-\epsilon_{cid})/n_{rec}}, \tag{5.6}$$

where $\delta\epsilon_{cid}$ is the error on ϵ_{cid}. The relative charge identification efficiency as function of p_{in} at different zenith angles are shown in Fig. 5.5.

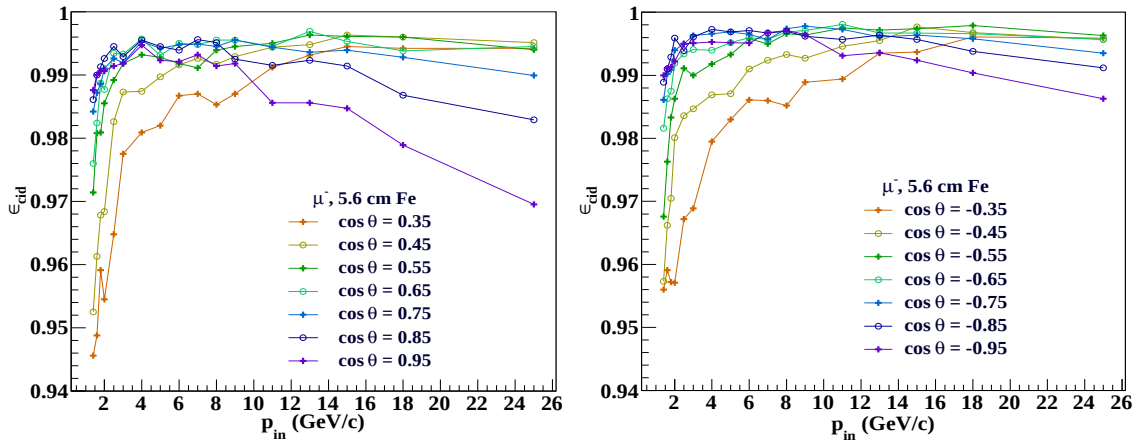

Figure 5.5: Relative charge identification efficiency ϵ_{cid} as a function of p_{in} (GeV/c) at different zenith angles for $+\cos\theta$ (left) and $-\cos\theta$ (right). The figures were generated from the look up table obtained using the analysis in Ref. [22].

Due to multiple scattering of muons during their propagation through the detector, at small momenta where the number of layers having hits is small, the bending direction may be incorrectly reconstructed, thus leading to wrong identification of the muon charge. Even then at 1.4 GeV/c, the charge identification efficiency is around $\sim 95\%$ ($\sim 96\%$) for the horizontal direction $\cos\theta = 0.35$ ($\cos\theta = -0.35$). The efficiency increases significantly with increase in momentum. This is because of the increase in the length of the track thus leading to a correct identification of the bending direction in the magnetic field. The efficiency is roughly constant, about 98–99% beyond a few GeV/c, except for

the very vertical directions $|\cos\theta| = 0.85,\ 0.95$. Even when there is a slight decrease in ϵ_{cid} for these directions, it is does not decrease below 95% in the central region and in the energy range of interest. Subsequently, a complete analysis of the muon response over the entire ICAL detector was also performed [108]. The resolutions and results were marginally worse than those in the central region. While the reconstruction efficiency was substantially lower, the direction and charge identification efficiencies were similar to the results in the central region. Thus ICAL has excellent muon charge identification capability which in turn contributes to the detector's high sensitivity to neutrino mass hierarchy.

The values of resolutions and efficiencies were also found out for lower momenta (p_{in}<1 (GeV/c)) also. These are worse compared to their respective values in the momentum range 1.4 GeV/c and beyond, but it is important to calculate them since the physics simulation studies consider muon energies down to 0.5 GeV also.

5.4 Separation of charged current muon neutrino events in ICAL

The main interactions of interest in ICAL are the charged current interactions of ν_μ and $\bar{\nu}_\mu$. In addition neutral current interactions of ν_μ and $\bar{\nu}_\mu$ will also occur in the detector. Since the atmospheric neutrino flux contains ν_e and $\bar{\nu}_e$ also the charged current and neutral current interactions of these neutrinos with the target iron will also take place. Tau neutrino interactions can also occur in the detector in addition to these but the probability of their being a background for charged current muon neutrino events is small. Thus it becomes important to separate out the channel of interest to study the sensitivity to neutrino oscillations. Each type of event has its own characteristic signatures which can be used to identify and tag it. This section describes the preliminary studies on how to separate different types of events especially charge current muon neutrino events among the others.

Simulation studies using neutrino events generated using the NUANCE [24] neutrino generator are conducted in the ICAL detector with default iron plate thickness of 5.6 cm. The events of interest considered in this study are the charged current and neutral current interactions of ν_μ, $\bar{\nu}_\mu$, ν_e and $\bar{\nu}_e$; ν and $\bar{\nu}$ are taken together and are not distinguished from each other in this study. The events are named as follows for convenience :

1. *ccmu* : charged current muon neutrino and anti-neutrino events $\nu_\mu + N \rightarrow \mu^- + X$, $\bar{\nu}_\mu + N \rightarrow \mu^+ + X$

2. *cce* : charged current electron neutrino and anti-neutrino events $\nu_e + N \rightarrow e^- + X$, $\bar{\nu}_e + N \rightarrow e^+ + X$

3. *ncmu* : neutral current muon neutrino and anti-neutrino events $\nu_\mu + N \rightarrow \nu_\mu + X$, $\bar{\nu}_\mu + N \rightarrow \bar{\nu}_\mu + X$

4. *nce* : neutral current electron neutrino and anti-neutrino events $\nu_e + N \rightarrow \nu_e + X$, $\bar{\nu}_e + N \rightarrow \bar{\nu}_e + X$

Since oscillations have not been turned on, these use no ν_τ events and the sum of nce and ncmu will always accurately represent the total neutral current (NC) events.

5.4.1 Separation using strip and layer multiplicity

The primary information available from the RPCs about an event is the hit information. Since there is no information about the charge deposited by the particles in the detector, this hit information is used in the separation of different types of events in the ICAL. The total number of hits in an event along with the number of layers hit in that event have been used to separate different types of events. This is primarily motivated by the fact that muons being minimum ionising particles leave long tracks in the detector which translates to a large number of layers hit in the event. Compared to *ccmu* events, the other three events do not traverse so many layers, meaning that long tracks will be absent, but the hits will be spread widely within a layer. The focus of this section is to make use of the strip and layer multiplicities of different types of events to identify and tag them.

All the four different types of events were generated in NUANCE neutrino generator and propagated through the GEANT-4 based ICAL detector. The analysis was done using unoscillated events. The hit and layer multiplicities of each event was obtained and used to find out an optimum criterion to identify different types of event. The study was done using the default plate thickness of 5.6 cm.

5.5 Selection criteria based on strip and layer multiplicity

Hit information is the main information available from an event in ICAL. As for the calibration of hadron energy in Chapter 3, the maximum of the hits in the X plane and Y plane, the maximum strip multiplicity of the event (s), along with the number of layers hit in the event (l) are used for this analysis. The 2-dimensional distribution of s and l for ccmu, cce, ncmu and nce events are shown in Fig. 5.6. It can be seen that the charged current muon neutrino (ccmu) events have the maximum number of strips as well as layers hit. For the other three types of events, the number of strips and layers hit are lesser than in ccmu events. Hence it is evident from the figure that ccmu events can be separated by using the number of layers in the event. The number of events having hits in a particular number of layers in all the different types of events are shown in Fig. 5.7. The number of layers is large only in the case of ccmu events, and for all the other events, the hits are confined mostly in less than $\sim$ 10 layers. Only ccmu events have significant amount of events having hits even in 20 layers. Even though the number of hits is a good criterion to separate ccmu events, using only this is not tight enough. Hence the idea of using both l and s/l as selection criteria is probed. To set the optimum values for the selection criteria are set by plotting s/l vs l for a fixed l, where s is the total strip multiplicity and l is the layer multiplicity. This is also illustrated in Fig. 5.7. Several observations can be made from Fig. 5.7. Only ccmu events have l events beyond 10 layers. The small error bars for ccmu events indicate the fact that there are significant number of events also. If an event has more than 4 layers and multiplicity per layer $s/l \leqslant 2$, it is a ccmu event with high probability. Various combination of l and s/l were applied to obtain the corresponding recognition efficiencies and sample purities. All events with $l = 1$ and $s = 1$ are rejected since they cannot be distinguished from noise. Since the events of interest are the charged current muon neutrino events (ccmu) the selection criteria for those events only are discussed here. The criteria for identifying other types of events were also studied but the results were inconclusive and suggestive of the fact that detailed and dedicated analyses are required to separate those events. This will be discussed elsewhere and is currently out of the scope of this thesis. The number and fraction of different classes of events obtained using the criteria $l \geqslant 5$ and $s/l \leqslant 2$ are shown in Table 5.1.

About $\sim$ 29% of the ccmu events satisfy the $l \geqslant 5$ criterion, while only less than 4% of the other three types of events, i.e., cce, ncmu and nce satisfy this criterion. This means

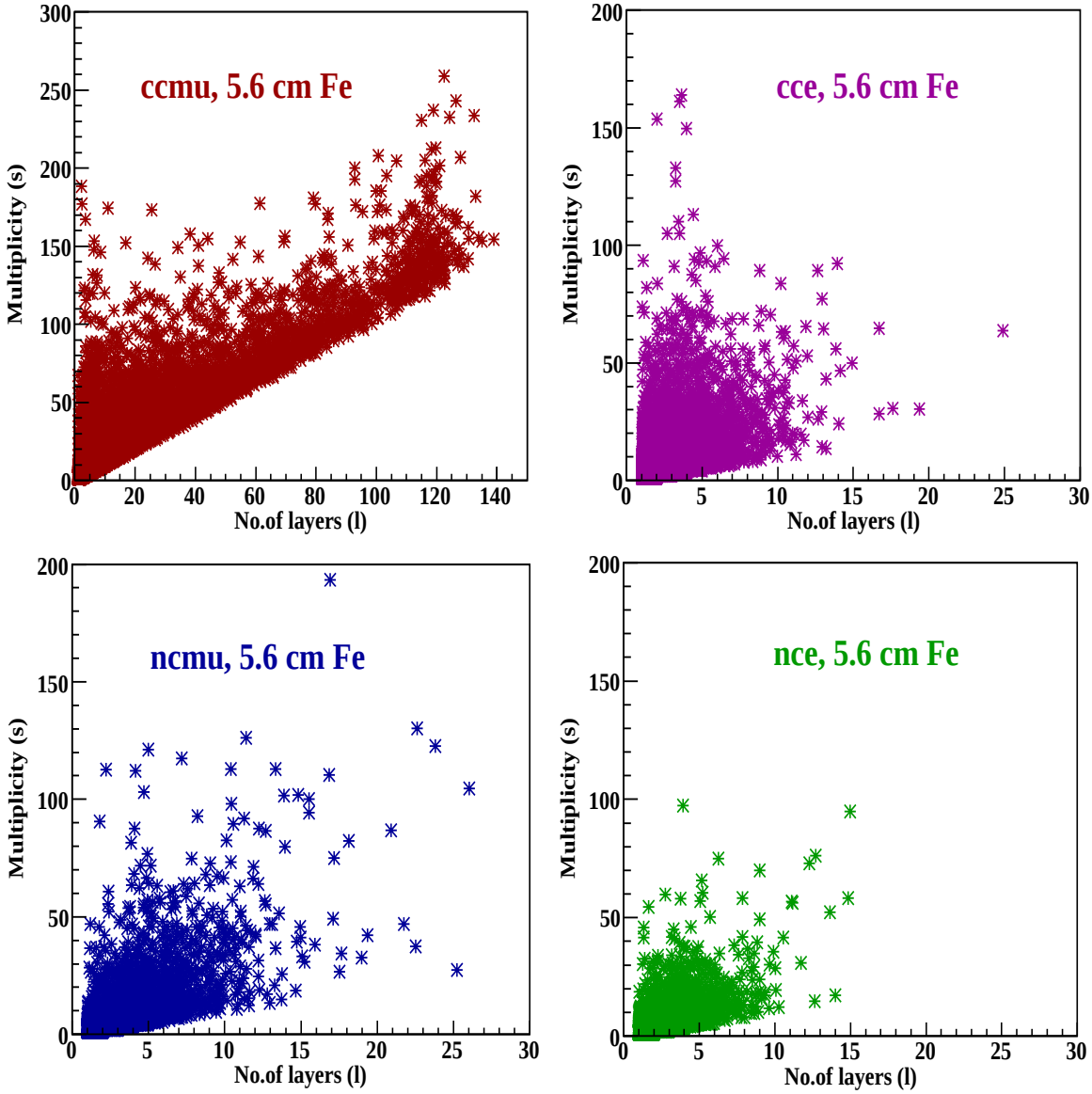

Figure 5.6: Total number of hits s vs the total number of layers in an event, for different types of events in 5.6 cm thick iron. It can be seen that the charged current muon neutrino (ccmu) events have the largest number of hits as well as the largest number of layers. It should also be noted that the ccmu graph has different scales from others both in x and y axes.

Type of event	Total no.of events	$l \geqslant 5$	$l \geqslant 5$(%)	$l \geqslant 5$ & $s/l \leqslant 2$	$l \geqslant 5$ & $s/l \leqslant 2$ (%)
ccmu	79537	23326	29.33	20591	25.89
cce	33729	1089	3.23	418	1.24
ncmu	29464	1045	3.55	430	1.459
nce	12382	265	2.14	129	1.042

Table 5.1: Number and fraction of events with only a layer cut ($l \geqslant 5$) and with both ($l \geqslant 5$ & $s/l \leqslant 2$) for 5.6cm Fe plate.

that $l \geqslant 5$ is a good criterion to select ccmu events. But the purity of the ccmu sample by just applying this cut only is about $\sim 90.6\%$. To improve the sample purity the additional

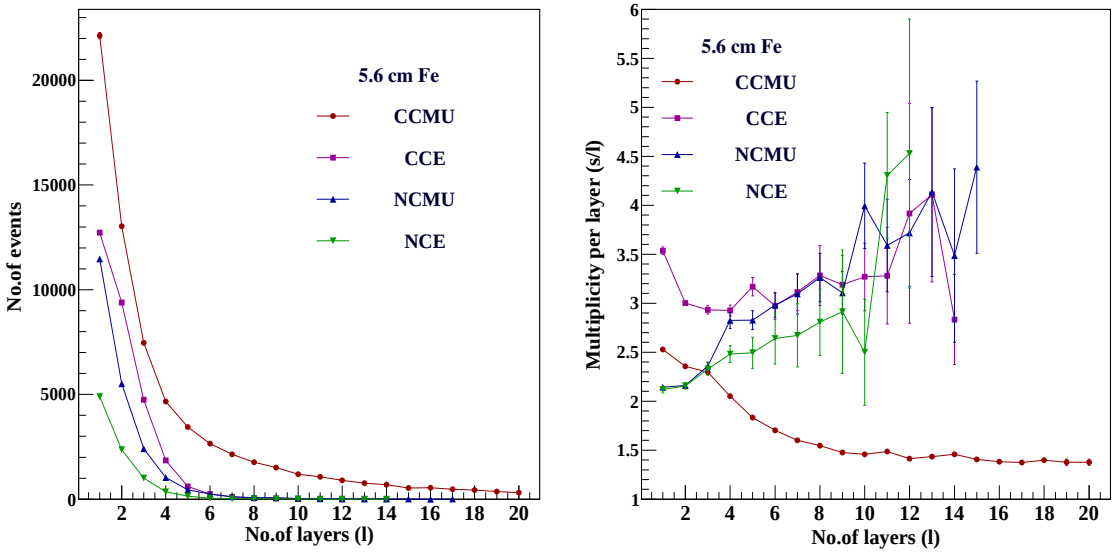

Figure 5.7: (Left) Number of events having hits a given number of layers, for ccmu, cce, ncmu and nce events. Only ccmu events have hits even beyond 10 layers. (Right) Strip multiplicity per layer s/l vs number of layers l for all different types of events in ICAL with 5.6 cm thick iron plates. It is readily visible that ccmu events have the largest l and the smallest s/l among all the events.

cut of $s/l \leqslant 2$ is also imposed. This improves the sample purity to $\sim 95.5\%$, and only marginally reduces the efficiency. It is always true that as the sample purity improves the reconstruction efficiency goes down and vice versa. Finally the recognition efficiency and sample purity for ccmu events are defined as follows and the percentages obtained are:

$$\text{Recognition efficiency of ccmu events} = \frac{\text{No.of events with } l \geqslant 5 \ \& \ s/l \leqslant 2}{\text{No.of events with} \geqslant 5} = 88.3\%$$

$$\text{Purity of ccmu sample} = \frac{\text{No.of ccmu events with } l \geqslant 5 \ \& \ s/l \leqslant 2}{\text{No.of all events with } l \geqslant 5 \ \& \ s/l \leqslant 2} = 95.5\%$$

Thus it is seen that even with just strip and layer multiplicities, it is possible to separate ccmu events from other types of events. The separation of cce and neutral current events are necessary for the study of sterile neutrinos and also for oscillation studies using charged current electron neutrino events (even though the ICAL is not as sensitive to these as to charged current muon neutrino events, adding the effects due to these events can increase the sensitivity of ICAL towards neutrino oscillations). Hence further studies on the separation of events have to be performed in detail since the selection of the correct event will directly have an impact on the physics potential of ICAL. it should be noted that the analysis presented in Chapter 6 assumes that all ccmu events are identified correctly among the other events; including the mis-identified events will marginally worsen the results obtained there. An identical study was undertaken for a plate thickness of 4

cm; a similar behaviour was observed.

5.6 Chapter Summary

The main interactions of interest in the ICAL are the charged current interaction of ν_μ and $\bar{\nu}_\mu$ with the iron target. The muons produced in the final state of these interactions, being minimum ionising particles, leave long clean tracks in the detector unlike the hadrons which shower. These tracks are bent in the magnetic field of the detector and the direction of the bending makes it possible to identify the charge of the muon. The momentum and direction of the muon can be reconstructed using a Kalman filter algorithm. The momentum and direction resolution, and the reconstruction efficiencies and charge identification efficiencies for muons in the central region of each module where the magnetic field is uniform have been estimated elsewhere [22] using a GEANT-4 based simulation studies. The results of this study have been collated for use in Chapter 6. It is seen that the muons have excellent momentum and direction resolution in the ICAL as compared to the hadrons. The charge identification efficiency for muons is always more than $\sim 95\%$ indicating that ICAL is very well optimised for muon detection.

The separation of different types of events in ICAL is also very important. Muons are easily identifiable with their long tracks and lower strip multiplicity whereas the separation of neutral current events from charged current electron events is rather difficult due to the presence of showers in these events. This is studied using simulations by propagating the particles produced from each type of events, generated using NUANCE. Selection criteria based on strip and layer multiplicities of an event are implemented to separate the different types of events from one another. It is seen that most of the charged current muon neutrino events can be identified easily with the large number of layers and lesser strip multiplicity per layer owing to the presence of the minimum ionising muon in the event. However further studies on the separation of the other three types of events namely cce, ncmu and nce have to be done in detail to extract as much information from these events as possible. Both the separation of various types of particles (events) in the ICAL and quantifying their energy and direction resolutions is necessary to be used as inputs to the oscillation physics analysis with ICAL. Any improvement in the efficiencies and resolutions is crucial with respect to the physics potential of ICAL and simulations will throw light on these.

Part III

Simulation studies of the sensitivities of the ICAL detector to neutrino oscillation parameters

6 Precision measurements of θ_{23} and $|\Delta m^2_{32}|$ and mass hierarchy sensitivity of ICAL in the context of adding higher muon energy bins and constraining the neutrino-antineutrino flux ratio

6.1 Overview

The iron calorimeter detector (ICAL) at INO will be a magnetised iron calorimeter mainly sensitive to the interaction of atmospheric neutrinos with the iron target in the detector. The main physics goals of ICAL include probing the earth matter effect on the propagation of atmospheric neutrinos and hence resolve the mass hierarchy puzzle, i.e., the sign of Δm^2_{32} where $\Delta m^2_{32} = m^2_3 - m^2_2$, m_2, m_3 being the mass eigenstates of neutrinos.

ICAL will actually probe the mass ordering in the 2–3 sector, i.e., it will determine the sign of Δm^2_{32}. The determination of the mass hierarchy also requires knowledge of the absolute scale of neutrino masses. These can only be probed in direct detection experiments such as tritium beta decay [136–139] or in neutrinoless double beta decay [140–144]. It is noted that if the lowest mass eigenstate is relatively heavy, all the mass eigenstates are degenerate and roughly of the order of 0.1 eV, i.e., about one third of the limit on the sum of the neutrino masses arising from cosmological observations [145, 146]. On the other hand, if the lightest neutrino is nearly massless, the observed neutrino mass ordering will also determine the hierarchy. In this Chapter, mass ordering and hierarchy are referred to interchangeably.

ICAL will not only determine the 2–3 neutrino mass ordering, but will also perform precision measurements of the atmospheric mixing angle θ_{23} and mass squared difference Δm^2_{32}. This precision measurement will in turn contribute to improving the current precision limits set by MINOS [33] and T2K [147]. MINOS is also a magnetised detector, but it is only 5400 tons whereas ICAL will be 50 ktons in mass which will impact ICAL's

physics reach. Magnetisation will help ICAL in distinguishing neutrino events from anti-neutrino events, by means of having an excellent charge identification efficiency. This distinction improves the sensitivities of ICAL to oscillation parameters. Thus unlike water cherenkov detectors like Super-K [78], ICAL will be able to do precision measurements very well and also determine the neutrino mass ordering efficiently.

The source of neutrinos in ICAL are naturally occuring neutrinos produced over a range of few GeVs to a few 100 GeVs (sub GeV to multi GeV) in the upper atmosphere when primary cosmic ray particles (mainly protons) interact with the nuclei there [113, 117]. These neutrinos while passing through the Earth undergo oscillations and the neutrinos which interact with the iron target carry the signatures of oscillations. Since real data is not available, simulation studies have been carried out to study the sensitivities of ICAL detector to atmospheric oscillation paratmeters. The main steps involved in this are neutrino event generation, inclusion of detector responses and efficiencies, inclusion of oscillations, binning in observables and χ^2 analysis. The analysis is discussed in detail in the following sections. This work will also be reported in Ref. [35].

6.2 Neutrino events generation

NUANCE neutrino event generator (version 3.5) [24] is used to generate the required interactions of atmospheric neutrinos in ICAL. Atmospheric neutrino flux at the Super Kamiokande site, as provided by Honda et al. [117] is used to generate the events. The energy range of the generated neutrinos is 0.4 – 500 GeV. The composition of ICAL detector (mainly RPC glass and iron) is fed into NUANCE as input. NUANCE generates all possible interactions for all neutrino flavours in different materials which constitute the detector, by knowing the the differential cross sections for different types of interactions. Both charged current (CC) and neutral current (NC) interactions are generated, and the different classes in each channel include quasi-elastic (QE), resonance (RES), deep inelastic (DIS), coherent scattering (CO) and diffractive scattering (DF). The event rates for all scattering processes with the target nuclei are calculated by multiplying neutrino fluxes read from Honda flux tables with the interaction cross sections. The kinematics of each event is generated depending upon the flux and differential cross section. The output of NUANCE consists of particle id number (pid), interaction process id, information whether a particle belongs to the initial, intermediate and final state, four-momentum

(p^μ) of the initial and final state particles, interaction vertex and time of interaction of the particles. For the purpose of physics analysis (and as input to GEANT-4 simulation code for ICAL), only the information about particle id, interaction vertex, four momentum and time are retained. Particle ids of the initial and final state particles are important to determine whether the interaction is charged current or neutral current. Also pid is important to determine whether the interaction is that of a neutrino or anti-neutrino ; this along with the four-momentum information of the neutrino is used to call the appropriate oscillation probabilities while applying oscillations on each events. Four-momentum information is required to determine the true energy and direction of the final state particles which will further be used to determine the bins to which these events belong to and to smear these values accordingly. Even though the analyses are done for a smaller number of years (say 5, 10, 15, 20), NUANCE data sample for exactly these years are not generated. Instead a huge data sample for a very large number of years (here 1000 years) is generated and scaled down to the required number of years during the analysis. This is mainly done to reduce the effect of statistical (Monte Carlo) fluctuations on sensitivity studies, which may alter the results. A detailed discussion about the effect of fluctuations on oscillation sensitivity studies will be discussed in section 6.10.

6.3 Oscillation probabilities

The oscillation probabilities calculated by considering full three flavour oscillations in the presence of matter effects, as discussed in Section 1.4.1 are used for the analysis. The Preliminary Reference Earth Model (PREM) profile [148] has been used to model the varying Earth matter density encountered by the neutrinos during their travel through the Earth. For the precise measurement of the oscillation parameters, the neutrino oscillation probabilities in matter can be calculated to a high degree of accuracy using numerical methods. The Runge-Kutta solver method is used to calculate the oscillation probabilities for various energies E and distances L/or equivalently $\cos\theta$ (θ being the zenith angle). The results obtained in the analyses presented in the following sections make use of the evolution of flavour eigenstates through Earth's varying matter density as described by the PREM profile. The PREM profile as a function of the radius r from the center of the Earth is shown in Fig. 6.1. The discontinuity at the inner-outer core as well as the core-mantle transitions can also be seen. An up-going neutrino which is of interest in atmospheric

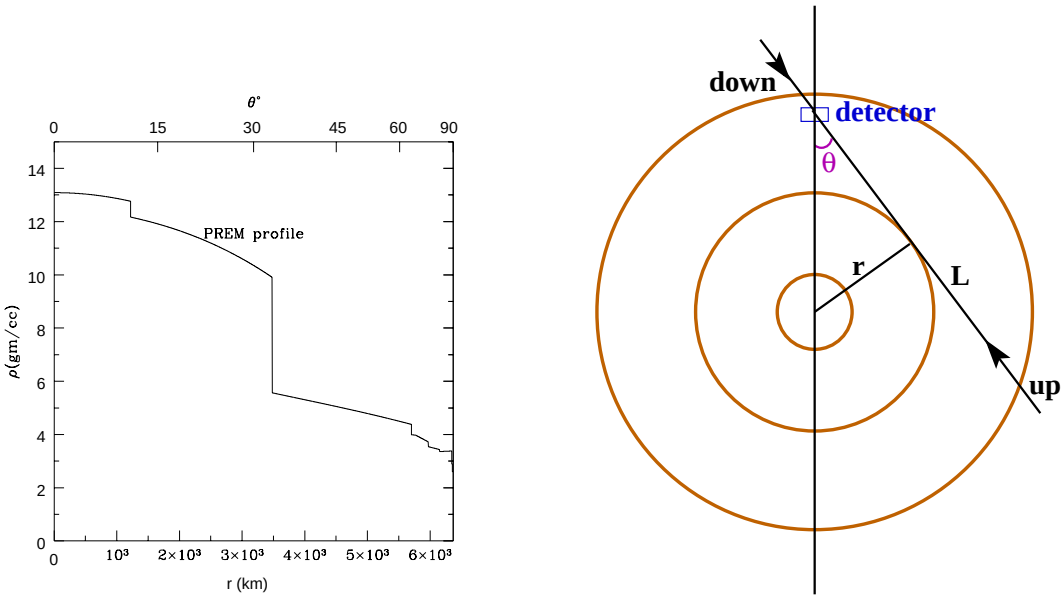

Figure 6.1: (Left) Earth matter density profile as a function of the radius r (km) from the center of the Earth, in PREM model, assuming that the Earth is spherically symmetric. The largest zenith angle equivalent to this distance r, just grazing a shell, is also shown [31]. (Right) An empirical depiction of the shell structure of the Earth along with the zenith and nadir angle (θ) for neutrinos traveling in the down and up direction respectively. The up-coming neutrinos travel more distance and hence encounter more matter density than the down-going neutrinos. This is the reason why the matter effects as well as oscillations are seen in the up-coming neutrinos in the case of atmospheric neutrinos whose energies are in the few GeV range.

neutrino oscillations, with a zenith angle θ that just grazes the shell of radius r travels through all density zones of radii larger than this radius r. Thus, a neutrino with $\theta = 33^{\circ}$, just grazes the core-mantle boundary whereas a neutrino at a smaller angle θ will traverse the core [31].

6.4 The oscillation analysis

Since Earth is made up of matter, neutrinos and anti-neutrinos interact differently with matter. The difference in this interaction shows up as a "matter effect". It is this effect which in turn will determine neutrino mass hierarchy. The phenomenon of matter dependence of mixing angles and mass squared differences and the MSW resonance and how it helps in determining neutrino mass hierarchy have been discussed in detail in Section 1.4.1.

The source of neutrinos in ICAL are the atmospheric neutrinos which are produced by the decay of pions and kaons produced in the atmosphere during the interaction of primary cosmic rays with the nuclei in the upper atmosphere. A discussion about the atmospheric neutrino fluxes and their asymmetries have been presented in Section 2.5.

The atmospheric neutrino flux used for the analyses presented here are the Honda-3D fluxes at the Kamioka site. The fluxes at Theni where INO will be located are marginally different, especially they are smaller at lower energies. These fluxes are just being made available and hence is beyond the scope of this thesis.

6.4.1 Total number of neutrino events for a given exposure time

The interactions of interest in ICAL are the charged current interactions of ν_μ and $\bar{\nu}_\mu$ with the iron target in ICAL. These ν_μ ($\bar{\nu}_\mu$) in ICAL come from both ν_μ and ν_e atmospheric fluxes via $\nu_\mu \rightarrow \nu_\mu$ and $\nu_e \rightarrow \nu_\mu$ oscillations. The first channel gives the number of ν_μ events which have survived and the second one gives the number from oscillations of ν_e to ν_μ. The number of events ICAL sees will be a sum of these events. Thus,

$$\frac{d^2N}{dE_\mu\, d\cos\theta_{\mu\nu}} = t \times n_d \times \int dE_\nu\, d\cos\theta_\nu\, d\phi_\nu \times \left[P_{\mu\mu} \frac{d^3\Phi_{\nu_\mu}}{dE_\nu\, d\cos\theta_\nu\, d\phi_\nu} + P_{e\mu} \frac{d^3\Phi_{\nu_e}}{dE_\nu\, d\cos\theta_\nu\, d\phi_\nu} \right] \times \frac{d\sigma_{\nu\mu}(E_\nu)}{dE_\mu\, d\cos\theta_{\mu\nu}}, \tag{6.1}$$

where, t is the exposure time, n_d is the number of targets in the detector, σ_{ν_μ} is the differential neutrino interaction cross section in terms of the energy and opening angle of the CC lepton, Φ_{ν_μ} and $\Phi_{\nu_e} = \nu_e$ are the ν_μ and ν_e fluxes and $P_{\alpha\beta}$ is the oscillation probability of $\nu_\alpha \rightarrow \nu_\beta$. The number of events in a bin of $(E_\mu, \cos\theta_{\mu\nu})$ is obtained by integrating over the bin, Before doing this, the final state variables are transformed to $(E_\mu, \cos\theta_\mu)$ so that the events are binned in the observable polar angle of the muon rather than the unobservable $\theta_{\mu\nu}$, the opening angle of the muon with respect to the neutrino. These transformations are performed within NUANCE and the output of NUANCE lists events as discussed earlier. These are taken and binned accordingly.

The expression in Eq. 6.1 is for the ideal case when the detector has perfect resolutions and 100% efficiencies. To get the actual number of events, realistic resolutions and efficiencies obtained from GEANT-4 based simulation studies of ICAL have to be incorporated as discussed in the following sections.

6.5 Inclusion of detector responses and efficiencies

Every detector has its own resolution with which it can distinguish different energies and directions. The efficiencies with which the final state particles can be detected are also important and affect the calculation of no.of oscillated events. The energy and direction resolutions of muons, to the detection of which the detector is optimised is excellent [22]. Hadrons which are also produced in the charged current interactions have worse energy and direction resolutions [20]. Even then the inclusion of hadron information has proved to enhance ICAL sensitivities [27]. These resolutions and efficiencies have been tabulated and these tables are used to smear the true energies of the final state particles (muons and summed hadrons) to the values that will be seen in the detector and used in the analysis. It should be noted that muon resolutions and efficiencies vary in different regions of the detector according to the strength and direction of magnetic field [22, 108]. This analysis uses the responses and efficiencies of muons in the central region of the detector, discussed in Chapter 5. These are the best of all possible muon responses in the ICAL detector. While the energy and direction resolutions of muons as well as their charge identification efficiency is similar in the peripheral regions, the reconstruction efficiency is smaller because of edge effects including smaller magnetic field. Hence including the entire volume of ICAL will marginally reduce the total number of events for a given exposure time – the consequences of this reduction have not been discussed in this thesis. In addition to muon momentum and direction, the energy of the multiple hadrons produced in ICAL are used as observables in the analysis. Since hadrons traverse relatively few layers, the results on hadron energy resolutions obtained in Chapter 3 in the central region of ICAL apply over entire ICAL without much impact due to edge effects etc. Hence the energy resolutions of multiple hadrons propagating in the central part of the detector, which were estimated using GEANT-4 based simulation studies[20] are used. These realistic values obtained from simulating the propagation of muons and hadrons in ICAL simulated using GEANT-4 have been used in the analysis presented here.

6.5.1 Smearing of energies and direction: inclusion of detector resolutions

At the time this calculation was begun, the responses of both muons and hadrons in the peripheral parts of ICAL was not completely understood. Hence, instead of propagating the NUANCE events through the simulated ICAL detector in GEANT and obtaining a

more realistic set of "observed" values of the energy and momentum of the final state particles, the true values of these variables were smeared according to the resolutions obtained in the earlier studies using random number generators. Subsequently, the peripheral regions of ICAL have also been well understood. However, the extension of the study to perform a full GEANT4-based analysis is beyond the scope of this work.

In the analysis, the energy and direction of muons and energy of hadrons in the final state of interaction have been used as observables. The reconstructed values of these observables will depend on detector resolutions. The better the detector resolution, the closer will be the observed value to the true value. To take into account the fact that the detector has a certain resolution, the true values are smeared using the look up tables prepared from ICAL GEANT4 simulations.

6.5.1.1 Smearing of muon momentum and direction

The muon look up table lists the mean and σ of the reconstructed distribution obtained from simulations of fixed energy muons for fixed true values of $(E_\mu^i, \cos\theta_\mu^j)$ as well as the reconstruction and CID efficiencies in those bins. For each NUANCE event, a uniform random number generator is used to generate the smeared/observed value of each of $E_\mu, \cos\theta_\mu$ with a probability consistent with the distribution in the table whose $(E_\mu^i, \cos\theta_\mu^j)$ corresponds closest to the true $(E_\mu, \cos\theta_\mu)$ of that event. While the smeared values of E_μ and $\cos\theta_\mu$ are henceforth used in place of the original values, the information on reconstruction and CID efficiencies (again taken from the look-up table) is retained for each event for later use.

In the case of muon energy and direction, the smearing is done consistent with the Gaussian distribution function using the true particle energy E_μ obtained from NUANCE as the mean and σ of the nearest E_μ^i from the look-up table as the width. Only positive values of smeared energy E_μ^{obs} are allowed; if the smeared energy happens to be negative, the random number is called repeatedly till a positive value is obtained. A smeared $\cos\theta_\mu$ value is obtained in a similar fashion. Since the allowed range of $\cos\theta$ is from $[-1, +1]$ only, for cases when the smeared value of $\cos\theta_\mu^{obs} < -1$ and $\cos\theta_\mu^{obs} > +1$, the conditions $\cos\theta_\mu^{obs} = -1$ and $\cos\theta_\mu^{obs} = +1$ are imposed so as to confine the smeared values of $\cos\theta_\mu^{obs}$ also in the allowed range $[-1, +1]$. This is preferred to wrapping the $\cos\theta > 1$ values back into the correct range since the distributions are very narrow in $\cos\theta$ ($\sigma \sim 1^\circ$).

In the case of hadrons, the smearing is not done directly. Momentum of muons can be measured directly in ICAL by using curvature method (using Kalman filter technique). But in the case of hadrons, energy is calibrated to the number of hits in the hadron shower. Hence the smearing of hadron cannot be done directly, but only by smearing the number of hits and recalibrating them to energy. A brief description of hadron energy smearing is given here.

6.5.1.2 Hadron energy smearing

First the true energy of the hadrons produced in a charged current muon neutrino interaction is determined as $E_{had}^{\prime true} = E_{\nu}^{true} - E_{\mu}^{true}$, where E_{ν}^{true} is the true energy of the incident neutrino and E_{μ}^{true} is the true energy of the final state muon. This true hadron energy is binned into a true hadron energy bin. If $E_{had}^{\prime true} < 1$ GeV, then the energy is taken to be $E_{had}^{obs} = 0$ GeV. If $E_{had}^{\prime true} \geqslant 1$ GeV, the hadron look up table is used and the Vavilov parameters corresponding to the true energy bins are read and used to implement smearing via Vavilov distribution function. The smearing is indirect since the number of hits corresponding to the true bin is generated from these parameters and the energy is then calibrated to the number of hits. To generate such a hit distribution, the following procedure is adopted. Let the mean number of hits calculated from Vavilov parameters for a given $E_{had}^{\prime true}$ which is the central bin value (from hadron look-up table) be:

$$mean_{vav} = (\gamma - 1 - \ln P_0 - P_1)\, P_3 + P_2 = \bar{x}_N + P_2, \tag{6.2}$$

where $\gamma = 0.57721$ (Euler's constant) and P_i, with $i = 0, 1, 2, 3$ are Vavilov parameters as described in Section. A.0.1. This equation generates the mean number of hits in the given true hadron energy bin. However, the hadron energy of the actual event may not be the same as the bin centre. Hence to generate the mean number of hits corresponding to a given true hadron energy, a linear approximation of the number of hits to the true hadron energy is used :

$$\bar{n}^t = n_h^0 \times E_{had}^{\prime true} + n_h^{\prime}, \tag{6.3}$$

where, n_h^0 = 1.6 is the slope and $n_h^{\prime}$ = 5.7, the intercept of the linear fit. Thus, for the true hadron energy $E_{had}^{\prime true}$, the mean number of hits corresponding to this particular energy is given by $\bar{n}^t$ and the Vavilov distribution is thus rescaled to have this mean value. That is the shifted Vavilov distribution has $P_2^{\prime} = \bar{n}^t - \bar{x}_N$, where $P_2^{\prime}$ is the modified P_2,

$\bar{x}_N = (\gamma - 1 - \ln P_0 - P_1)\, P_3$. This P_2' is used to generate hits distributed according to a Vavilov distribution, distributed about the shifted mean :

$$vdis = (vinv \times P_3) + P_2', \tag{6.4}$$

where $vinv$ is a Vavilov random number with P_0 and P_1 as κ and β^2 respectively. Now the smeared hits are calibrated back to energy using the expression :

$$E_{had}^{\prime obs} = \frac{vdis - n_h'}{n_h^0}. \tag{6.5}$$

. If the smeared value of energy happens to be negative, i.e., if $E_{had}^{\prime obs} < 0$, a new random number is generated and the whole process is repeated as in the case of muon energy smearing until a positive value is obtained.

6.5.2 Applying neutrino oscillations

A sample of 1000 years of unoscillated data was generated using NUANCE. Two data sets were generated :

1. CC muon events using the Φ_μ flux and

2. CC muon events using the swapped $\Phi_e \rightarrow \Phi_\mu$ flux.

This generates the so-called muon- and swapped-muon events that corresponds to the two terms in Eq. 6.1. Oscillations were then applied in two different ways. In the first study, the $P_\mu\mu$ (or $\bar{P}_{\mu\mu}$) was calculated given the $(E_\nu, \cos\theta_\nu)$ of the event. A random number r was generated. If $P_{\mu\mu} > r$, then the event was retained; else it was dropped. A similar procedure was carried out for the swapped events with respect to $P_{e\mu}$ (and for anti-neutrinos as well). The surviving events were then binned in the appropriate observed bins for analysis.

In the second approach which was finally used in the analysis, the generated event was simply multiplied by $P_{\mu\mu}$ (or $P_{e\mu}$) and then binned. This procedure gave similar results to the first one for the thousand year data with a 10 year data set, however the first approach gave rise to random fluctuations (as expected) which gave appreciably different data sets on each iteration. As discussed in [27], using the first approach generates the statistical mean distribution with respect to which an unbiased analysis can be performed.

The oscillation is applied event by event (for both muon and swapped muon events) and it is a time consuming process since the actual sample contains 1000 years of data.

6.5.3 Binning in observed energies and direction

It is always in terms of observables that the analysis is done. It is because of this that the energies and direction of the final state particles had to be smeared according to detector resolutions. The observables used in the analysis discussed here are muon energy E_μ^{obs}, muon direction $\cos\theta_\mu^{obs}$ and hadron energy $E_{had}^{\prime obs}$. There are two different binning schemes, one in which only the muon energy and direction are used, i.e., the $(E_\mu^{obs}, \cos\theta_\mu^{obs})$ called the 2D (mu only) binning scheme and the other in which all the three observables $(E_\mu^{obs}, \cos\theta_\mu^{obs}, E_{had}^{\prime obs})$ are used, which is also known as the 3D (with hadron) binning scheme. Previous analyses of ICAL physics [27, 29, 30], were done in the observed muon energy range of E_μ^{obs} = 0.8 – 10.8 GeV and 1 – 11 GeV (both being approximately same). The analysis discussed here takes into consideration, the extended energy region of the observed muon energy E_μ^{obs} = 0.5 – 25 GeV. Even though this includes the lower energy region which contains larger neutrino flux, it will be seen that it is the inclusion of the higher energy bins beyond 11 GeV, which contributes to the improved results discussed in Section. 6.6. The motivation to use the extended energy range of the observed muon energy can be justified from Fig. 6.2 where the number of ν_μ and $\bar{\nu}_\mu$ events in various $\log(L_\mu^{obs}/E_\mu^{obs})$ bins, where L_μ^{obs} is the observed muon path length and E_μ^{obs} is the observed muon energy are shown. The events are calculated after applying oscillation probabilities (using the central values of oscillation parameters) and detector efficiencies in each bin. The comparison of the number of events in different $\log(L_\mu^{obs}/E_\mu^{obs})$ bins when E_μ^{obs} is 1–11 GeV only and with E_μ^{obs} extended to 0.5–25 GeV, for ν_μ and $\bar{\nu}_\mu$ are shown in the figure. [Roughly speaking, the left peak corresponds to down-going events and the right one to up-coming events.] It can be seen that the with the extension of the energy range, a larger range of $\log(L_\mu^{obs}/E_\mu^{obs})$ is spanned, which increases the sensitivities to oscillation parameters. The number of events also increases with the extension of the energy range, again giving a better sensitivity to oscillation parameters. It should be noted that the binning in $\log(L_\mu^{obs}/E_\mu^{obs})$ is used for representational purposes only. For the actual analysis separate bins of E_μ^{obs} and $\cos\theta_\mu^{obs}$ along with $E_{had}^{\prime obs}$ are used as described below.

The binning scheme is discussed now. As mentioned earlier, there are two binning

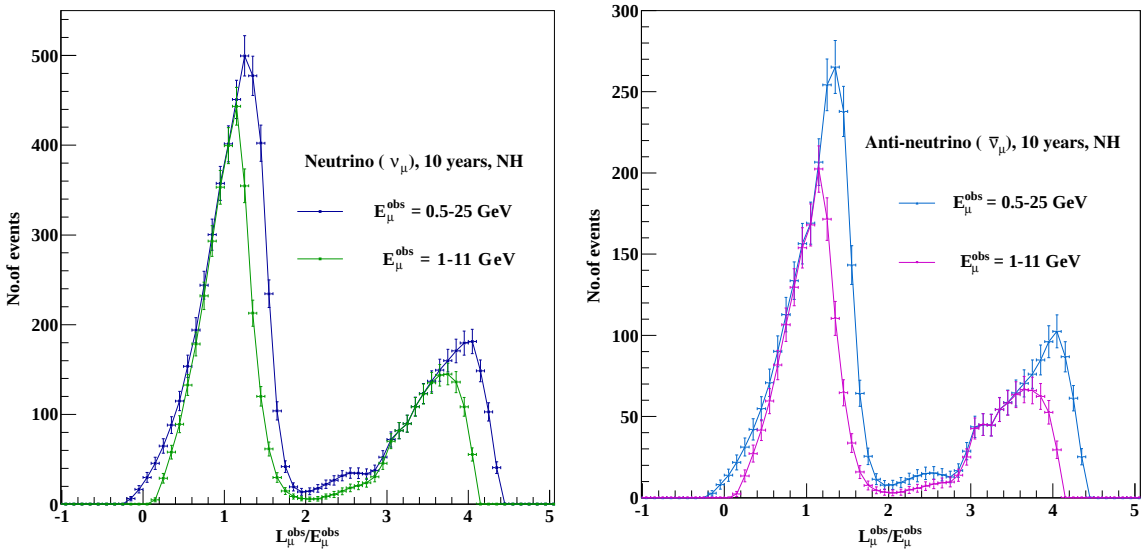

Figure 6.2: Number of ν_μ events (left) and $\bar{\nu}_\mu$ events (right) in each $\log(L_\mu^{obs}/E_\mu^{obs})$ bin after applying oscillation probabilities and detector efficiencies, with the observed muon energy in the 1–11 GeV and 0.5–25 GeV ranges, for 500 kton year exposure of ICAL. The extension of the observed muon energy range increases the number of events as well as the range of $\log(L_\mu^{obs}/E_\mu^{obs})$ spanned. This leads to an improvement in the sensitivities to oscillation parameters.

schemes. The observed energy of muons E_μ^{obs} is from 0.5–25 GeV, observed muon direction $\cos\theta_\mu^{obs}$ from $[-1,+1]$ and observed hadron energy $E_{had}^{\prime obs}$ is from 0–15 GeV. There are 15 bins of E_μ^{obs}, 21 bins of $\cos\theta_\mu^{obs}$ and 4 bins of $E_{had}^{\prime obs}$. The binning scheme is listed in detail in Table 6.1. In the mu only (2D) analysis there are $15 \times 21 = 315$ bins and in the one including hadrons (3D), there are $15 \times 21 \times 4 = 1260$ bins. It should be noted that in the current analysis the direction $\cos\theta_\mu^{obs} = [0,+1]$ is taken as the up direction where as $\cos\theta_\mu^{obs} = [-1,0]$ is taken as the down direction. Since atmospheric neutrino oscillations are mainly in the up direction, more bins are assigned in this region than in the down direction. The binning scheme is an extension of that used in Ref. [27].

Observable	Range	Bin width	No.of bins
E_μ^{obs} (GeV) (15 bins)	[0.5, 4]	0.5	7
	[4, 7]	1	3
	[7, 11]	4	1
	[11, 12.5]	1.5	1
	[12.5, 15]	2.5	1
	[15, 25]	5	2
$\cos\theta_\mu^{obs}$ (21 bins)	[-1.0, 0.0]	0.2	5
	[0.0, 0.4]	0.10	4
	[0.4, 1.0]	0.05	12
$E_{had}^{\prime obs}$ (GeV) (4 bins)	[0, 2]	1	2
	[2, 4]	2	1
	[4, 15]	11	1

Table 6.1: Bins of the three observables muon energy and direction and hadron energy in detail.

6.5.4 Detection efficiencies and number of events

Every detector has a certain value of detection efficiency for each particle with a given energy and traveling in a given direction. Thus out of a given sample only a certain fraction will be reconstructed at a given energy and in a given direction. This is called *reconstruction efficiency* ϵ_r. The values of ϵ_r for each true energy and $\cos\theta$ bins for muons are read from the look up table and used in the analysis. Here, reconstruction efficiency of an event is taken to be the ability to see a muon, that is to be able to reconstruct it. Hence when hadron energy is added as the third observable, the efficiency in detecting an event remains the same.

The main characteristic of ICAL which makes it a special detector and suited for mass hierarchy determination is its ability to distinguish between neutrino and anti-neutrino events by separating muons from anti-muons by means of a magnetic field. Thus it identifies the charge of the final state muons using a magnetic field. The ability of the detector to identify events of a particular charge is known as *charge identification* ϵ_{cid} efficiency. This is incorporated to calculate the number of ν_μ and $\bar{\nu}_\mu$ events separately. First the number of events in the 2D binning scheme can be found out. The total number of ν_μ events in each bin will be a sum of ν_μ events correctly identified as ν_μ events and $\bar{\nu}_\mu$ events wrongly identified as ν_μ events. Thus charge identification efficiency comes into play in determining the number of events per bin. Similarly, the number of $\bar{\nu}_\mu$ events in each bin is the sum of correctly identified $\bar{\nu}_\mu$ events and ν_μ events wrongly identified as $\bar{\nu}_\mu$ events. The number of events per bin depends on the reconstruction efficiency in each bin. This is also taken into account while determining the number of events per bin. Thus,

$$N^{tot}_{\mu^-}(E^{obs}_\mu, \cos\theta^{obs}_\mu) = N_{\mu^-}\epsilon_{rec}\epsilon_{cid} + N_{\mu^+}\epsilon_{rec}(1-\epsilon_{cid}), \tag{6.6}$$

$$N^{tot}_{\mu^+}(E^{obs}_\mu, \cos\theta^{obs}_\mu) = N_{\mu^+}\epsilon_{rec}\epsilon_{cid} + N_{\mu^-}\epsilon_{rec}(1-\epsilon_{cid}), \tag{6.7}$$

$$\tag{6.8}$$

where, $N^{tot}_{\mu^-}$ ($N^{tot}_{\mu^+}$) is the total number of ν_μ ($\bar{\nu}_\mu$) CC muon events in the bin $(E^{obs}_\mu, \cos\theta^{obs}_\mu)$, N_{μ^-} and N_{μ^+} are the number of events in this bin for an ideal detector with 100% reconstruction and CID efficiencies. The quantity ϵ_{rec} is the reconstruction efficiency of muons with a given energy and direction and ϵ_{cid} is the charge identification efficiency of the same. The reconstruction and charge identification efficiencies for μ^- and μ^+ have been

taken to be the same. It is straightforward to include unequal values fro them, but the studies show that they are only marginally different in a few energy-$\cos\theta$ bins. Finally, the events in a bin are considered non-zero if there is at least one event in that bin. This procedure is used both N are the data events D and theory events T.

The number of oscillated events in the bin observed bin $(E_\mu^{obs}, \cos\theta_\mu^{obs})$ is given by:

$$N_{\mu^-}^{osc} = N_{\mu^-} \times P_{\alpha\beta}, \tag{6.9}$$

$$N_{\mu^+}^{osc} = N_{\mu^+} \times \bar{P}_{\alpha\beta}, \tag{6.10}$$

where $P_{\alpha\beta}$ is the probability of oscillation from a neutrino flavour ν_α to a neutrino flavour ν_β and $\bar{P}_{\alpha\beta}$ is the probability of oscillation from an anti-neutrino flavour $\bar{\nu}_\alpha$ to a flavour $\bar{\nu}_\beta$; α, β are μ, μ and e, μ.

These events are used for the physics analysis. Now this 1000 year data sample is scaled to the same number of years as the data, for comparison and calculation of χ^2. The current precision analysis is done for 10 years of exposure of 50 kton ICAL (500 kton year). For the χ^2 analysis, the oscillation parameters are changed and the aforementioned processes are repeated. This new data is called "theory" and different theories are generated by changing the oscillation parameters.

6.6 χ^2 analysis

The χ^2 analysis is done in the observed bins discussed in Section 6.5.3. Since neutrino experiments are low counting events, Poissonian χ^2 is used in the analysis. There are two χ^2 analyses here; one with 10 systematic pulls and the other with 11 pulls. In the former, χ^2s from neutrino events and anti- neutrino events are uncorrelated and can be defined separately and summed. In the case of the latter, a 11^{th} pull is added as a constraint on the neutrino anti-neutrino flux ratio, hence there are no separate χ^2s for these events. Analyses are done for both 2D and 3D binning schemes, but the expressions are similar except for the bins. The expression for χ^2 for the 10 pulls case is :

$$\chi^2_{\pm} = min_{\xi^{\pm}_l} \sum_{i=1}^{N_{E^{obs}_{\mu}}} \sum_{j=1}^{N_{\cos\theta^{obs}_{\mu}}} \left(\sum_{k=1}^{N_{E'^{obs}_{had}}} \right) 2 \left[\left(T^{\pm}_{ij(k)} - D^{\pm}_{ij(k)} \right) - D^{\pm}_{ij(k)} \ln \left(\frac{T^{\pm}_{ij(k)}}{D^{\pm}_{ij(k)}} \right) \right] + \sum_{l^{\pm}=1}^{5} \xi^2_{l^{\pm}}, \tag{6.11}$$

where, $T^{\pm}_{ij(k)} = T^{0\pm}_{ij(k)} \left(1 + \sum_{l^{\pm}=1}^{5} \pi^{l^{\pm}}_{ij(k)} \xi_{l^{\pm}} \right)$,
$T^{\pm}_{ij(k)}$ is the number of theory (expected) events in each bin with systematic errors,
$T^{0\pm}_{ij(k)}$ is the number of theory (expected) events in each bin without systematic errors,
$D^{\pm}_{ij(k)}$ is the number of "data" (observed) events in each bin,
i, j, k are the observed bin indices, $\xi_{l^{\pm}}$ are the pulls, $\pi_{l^{\pm}}$ are the systematic uncertainties;
$l = 1, ..., 5$.

The five systematic uncertainties π_l used in the analysis are :

1. $\pi_1 : 20\%$ flux normalisation error,

2. $\pi_2 : 10\%$ cross section error,

3. $\pi_3 : 5\%$ tilt error,

4. $\pi_4 : 5\%$ zenith angle error,

5. $\pi_5 : 5\%$ overall systematics,

and these have been implemented using method of pulls [32]. The "tilt error" is included as follows. First the event spectrum is calculated with the predicted values of atmospheric neutrino fluxes. Then the spectrum is shifted according to the relation :

$$\Phi_{\delta}(E) \; = \; \Phi_0(E) \left(\frac{E}{E_0} \right)^{\delta} \simeq \Phi_0(E) \left(1 + \delta \ln \frac{E}{E_0} \right), \tag{6.12}$$

where E_0 = 2 GeV, δ = 1σ systematic tilt error taken as 5%. The difference $\Phi_{\delta}(E) - \Phi_0(E)$ is included as the flux error. Now the total χ^2 is defined as :

$$\chi^2 \; = \; \chi^2_{+} + \chi^2_{-}, \tag{6.13}$$

where, χ^2_{+} is the contribution from anti-neutrino events and χ^2_{-} is that from neutrino events. Thus far, the analysis is an extension of that in Ref. [27] with larger muon energy range.

An 11$^{\text{th}}$ pull is implemented in the analysis as a constraint on the flux ratio of ν_μ and $\bar{\nu}_\mu$. This has been considered for the first time in such an analysis. The uncertainty in the ratio is taken as 5%. Now the χ^2 definition becomes :

$$\chi^2 = min_{\xi_l^\pm,\xi_6} \sum_{i=1}^{N_{E_\mu^{obs}}} \sum_{j=1}^{N_{\cos\theta_\mu^{obs}}} \left(\sum_{k=1}^{N_{E'^{obs}_{had}}} \right) 2 \left[\left(T^+_{ij(k)} - D^+_{ij(k)} \right) - D^+_{ij(k)} \ln \left(\frac{T^+_{ij(k)}}{D^+_{ij(k)}} \right) \right] +$$
$$2 \left[\left(T^-_{ij(k)} - D^-_{ij(k)} \right) - D^-_{ij(k)} \ln \left(\frac{T^-_{ij(k)}}{D^-_{ij(k)}} \right) \right] + \sum_{l^+=1}^{5} \xi^2_{l^+} + \sum_{l^-=1}^{5} \xi^2_{l^-} + \xi^2_6, \tag{6.14}$$

where,

$$T^+_{ij(k)} = T^{0+}_{ij(k)} \left(1 + \sum_{l^+=1}^{5} \pi^{l^+}_{ij(k)} \xi_{l^+} + \pi_6 \xi_6 \right) \tag{6.15}$$

$$T^-_{ij(k)} = T^{0-}_{ij(k)} \left(1 + \sum_{l^-=1}^{5} \pi^{l^-}_{ij(k)} \xi_{l^-} - \pi_6 \xi_6 \right), \tag{6.16}$$

where, π_6 = 2.5% and ξ_6 is the 11$^{\text{th}}$ pull. The effect of the new pull can be understood by considering its contribution alone on the ration of neutrino to anti-neutrino events :

$$\frac{T^-}{T^+} \simeq \frac{T^{0-}}{T^{0+}} \frac{(1 - \pi_6 \xi_6)}{(1 + \pi_6 \xi_6)} \tag{6.17}$$

$$\simeq \frac{T^{0-}}{T^{0+}} (1 - 2\pi_6 \xi_6). \tag{6.18}$$

This pull accounts for the uncertainty in the flux ration and corresponds to the 1σ value when $\xi_6 = +1$; this gives the 1σ error on the ratio to be 5%. In the earlier case with 10 pulls, the overall normalisation of the fluxes was freely allowed to float by 20% separately for T^- and T^+ and that for the cross section by 10% allowing a best fit where the pulls for T^- and T^+ could be large and in opposite directions. The introduction of the 11$^{\text{th}}$ constrains the ration and hence does not permit this anymore.

Since the new pull acts as a constraint to the T^-_μ/T^+_μ ratio, the expressions for χ^2 from neutrino and anti-neutrino events cannot be written separately.

For χ^2 minimisation, the oscillation parameters are varied within the ranges as given in Table 6.2, to simulate the theory events represented by $T_{ij(k)}$. The parameters which will not affect the results of this analysis, i.e, the solar mixing angle and mass squared difference θ_{12}, Δm^2_{21} (bot magnitude and sign) are kept "fixed". Earlier studies have shown

that the atmospheric neutrino events are insensitive to the CP violation phase δ_{CP} and so this has been kept fixed at $\delta_{CP} = 0$. The central values of the other parameters given in the Table 6.2 i.e., θ_{23}, Δm^2_{eff} and θ_{13} are used to generate "data" and varied to generate the "theory". The effective mass squared difference Δm^2_{eff} is related to Δm^2_{31} and Δm^2_{21} as [149, 150] :

$$\Delta m^2_{\text{eff}} = \Delta m^2_{31} - \Delta m^2_{21} \left(\cos^2\theta_{12} - \cos\delta_{CP} \sin\theta_{13} \sin 2\theta_{12} \tan\theta_{23}\right). \tag{6.19}$$

When Δm^2_{eff} is varied within its 3σ range, the mass-squared differences are determined according to

$$\Delta m^2{}_{31} = \Delta m^2{}_{eff} + \Delta m^2_{21} \left(\cos^2\theta_{12} - \cos\delta_{CP} \sin\theta_{13} \sin 2\theta_{12} \tan\theta_{23}\right); \tag{6.20}$$

$$\Delta m^2{}_{32} = \Delta m^2{}_{31} - \Delta m^2{}_{21}, \tag{6.21}$$

for normal hierarchy when $\Delta m^2{}_{eff} > 0$, with $\Delta m^2{}_{31} \leftrightarrow -\Delta m^2{}_{32}$ for inverted hierarchy when $\Delta m^2{}_{eff} < 0$.

An 8% prior at 1σ is also added on $\sin^2 2\theta_{13}$, since this quantity is known to this accuracy [11, 151]. No prior is imposed on θ_{23} and Δm^2_{32}, since the precision measurements of these parameters are to be carried out in ICAL. The contribution to χ^2 due to prior is defined as :

$$\chi^2_{\text{prior}} = \left(\frac{\sin^2 2\theta_{13} - \sin^2 2\theta^{\text{true}}_{13}}{\sigma(\sin^2 2\theta_{13})}\right)^2, \tag{6.22}$$

where, $\sigma(\sin^2 2\theta_{13}) = 0.08 \times \sin^2\theta^{\text{true}}_{13}$. Thus the total χ^2 is defined as:

$$\chi^2_{\text{ICAL}} = \chi^2 + \chi^2_{\text{prior}}. \tag{6.23}$$

During χ^2 minimisation, χ^2_{ICAL} is first minimised with respect to the pull variables ξ_l, then marginalised over the ranges of the oscillation parameters $\sin^2\theta_{23}$, Δm^2_{eff} and $\sin^2 2\theta_{13}$ given in Table 6.2. The third column of the table shows the 3σ range over which the parameter values are varied. These along with the best fit values of θ_{12} and Δm^2_{21} are obtained from the global fits in Refs. [107, 152–154]. The parameter δ_{CP} is kept fixed at zero all throughout this analysis.

Statistical significance of the obtained result is denoted by $n\sigma$, where, $n = \sqrt{\Delta\chi^2}$, which is given by;

$$\Delta\chi^2(\lambda) = \chi^2_{ICAL}(\lambda) - \chi^2_0, \tag{6.24}$$

Parameter	True value	Marginalization range
θ_{13}	8.729°	[7.671°, 9.685°]
$\sin^2\theta_{23}$	0.5	[0.36, 0.66]
Δm^2_{32}	2.4×10^{-3} eV^2	[2.1, 2.6] $\times 10^{-3}$ eV^2 (NH)
$\sin^2_{12}$	0.304	Not marginalised
Δm^2_{21}	7.6×10^{-5} eV^2	Not marginalised
δ_{CP}	0°	Not marginalised

Table 6.2: Main oscillation parameters used in the current analysis. In the second column are the true values of these parameters used to simulate the "observed" data set. True value is the value at which the data is simulated. More details are given in the main text. For precision measurement of each parameter, all others are varied except that parameter in the analysis. Normal hierarchy is taken as the true hierarchy.

χ^2_0 being the minimum value of χ^2_{ICAL} in the allowed parameter range. With no statistical fluctuations, $\chi^2_0 = 0$.

6.7 Results : precision measurement of $\sin^2\theta_{23}$ and Δm^2_{eff}

The precision measurement of oscillation parameters in the atmospheric sector in the energy range 0.5 – 25 GeV is done using the current analysis for 500 kton year exposure of ICAL detector. Comparisons with previous analyses in the 1 – 11 GeV energy range are also done. Hence the results will be for the combinations of binning scheme, energy ranges and pulls. Sensitivities for the oscillation parameters θ_{23} and $|\Delta m^2_{eff}|$ can be found out separately, when the other parameter and θ_{13} are marginalised over their 3σ ranges. Normal hierarchy (NH) is taken to be the true hierarchy and 500 kton years of exposure is used (10 years of running the experiment).

The relative precision achieved on a parameter λ (here λ being $\sin^2\theta_{23}$ or $|\Delta m^2_{eff}|$) at 1σ is expressed as :

$$p(\lambda) = \frac{\lambda_{max-2\sigma} - \lambda_{min-2\sigma}}{4\lambda_{true}}, \tag{6.25}$$

where $\lambda_{max-2\sigma}$ and $\lambda_{min-2\sigma}$ are the maximum and minimum allowed values of λ at 2σ; λ_{true} is the true choice.

6.7.1 Precision measurement of $\sin^2\theta_{23}$

The relative 1σ precision on $\sin^2\theta_{23}$ obtained from different analyses are discussed here. The analyses are done in two different ranges of observed muon energy E^{obs}_{μ}, i.e., 1–11 GeV and 0.5–25 GeV. Two different binning schemes, the muon only (2D) and with hadron (3D) analyses are used with 10 pulls and 11 pulls in both cases. The plots of

$\Delta\chi^2_{ICAL}$ vs $\sin^2\theta_{23}$, with normal hierarchy as the true hierarchy, are shown in Fig. 6.3 for different cases which are the combinations of energy ranges, binning schemes and number of pulls.

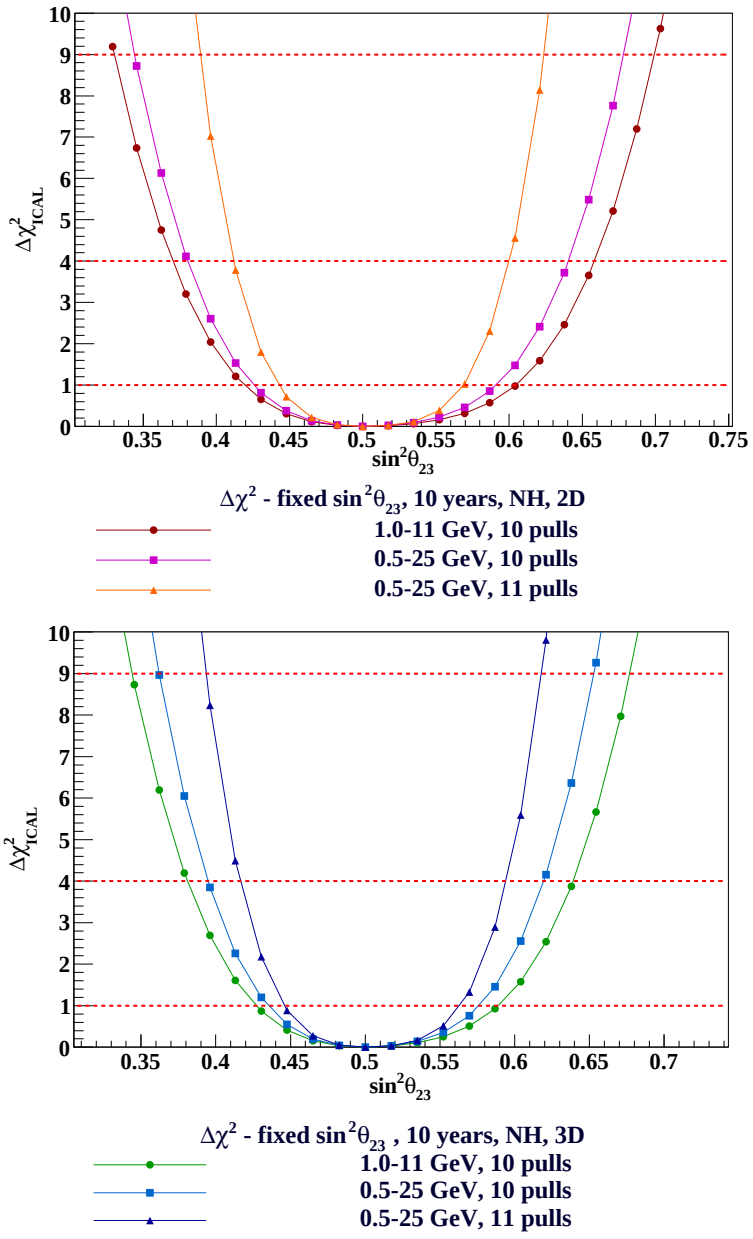

Figure 6.3: The values of $\Delta\chi^2_{ICAL}$ at different values of $\sin^2\theta_{23}$ with true $\sin^2\theta_{23} = 0.5$ and with normal hierarchy as the true hierarchy. The top panel shows the results for muon only (2D) analyses and the bottom panel shows those for the analyses with hadrons also (3D). The results for all possible combinations of energy ranges, pulls and binning schemes are shown. It can be seen that the addition of higher energy observed muon bins improve the results, both in the 2D and 3D cases as compared to the cases with muon energy in 1 – 11 GeV only. The addition of an extra pull as a constraint on the neutrino anti-neutrino flux ratio further improves the results.

The other parameters $|\Delta m^2_{eff}|$ and θ_{13} have been marginalised over their 3σ ranges

given in Table 6.2. Percentage precisions on $\sin^2\theta_{23}$ at 1σ obtained with different analyses are shown in Table 6.3. The comparison of the precisions from 2D and 3d analyses in the energy range 0.5 – 25 GeV with 11 pulls is shown in Fig. 6.4.

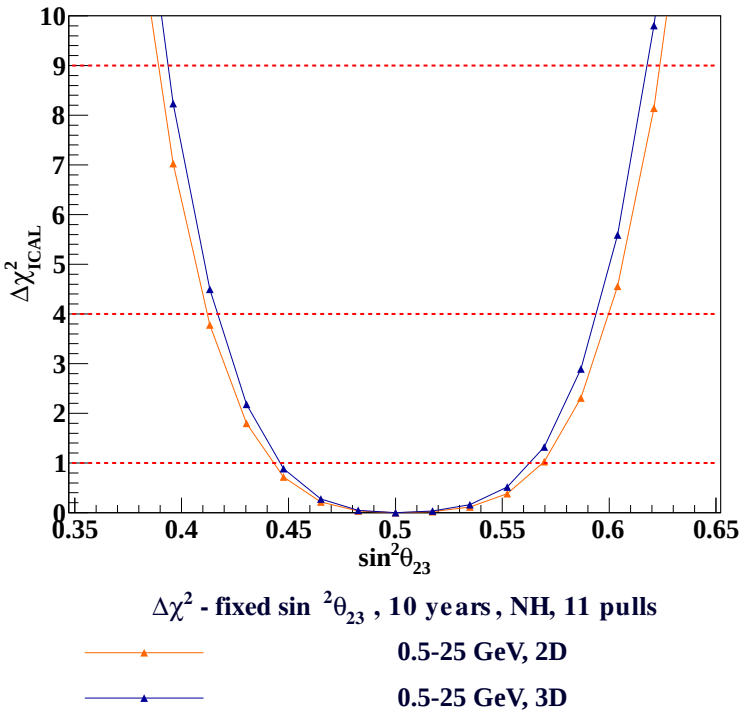

Figure 6.4: The precision on $\sin^2\theta_{23}$ obtained from 2D and 3D analyses in the energy range E_μ^{obs} = 0.5 – 25 GeV and with 11 pulls. It can be seen that the analysis with 3D binning and 11 pulls in this energy range yields the best precision on $\sin^2\theta_{23}$.

Binning	E_μ^{obs} (GeV)	No.of pulls	$\sin^2\theta_{23_{min}}(2\sigma)$	$\sin^2\theta_{23_{max}}(2\sigma)$	Precision at 1σ (%)
2D $(E_\mu^{obs}, \cos\theta_\mu^{obs})$	1–11	10	0.370	0.658	14.40
	0.5–25	10	0.380	0.640	13.00
	0.5–25	11	0.412	0.599	9.35
3D $(E_\mu^{obs}, \cos\theta_\mu^{obs}, E_{had}^{obs})$	1–11	10	0.381	0.639	12.85
	0.5–25	10	0.394	0.619	11.25
	0.5–25	11	0.416	0.594	8.90

Table 6.3: Precision of $\sin^2\theta_{23}$ at 1σ, obtained using Eq. 6.25, from different analyses. The maximum and minimum values of $\sin^2\theta_{23}$ at 2σ in each case are also shown. The true value of $\sin^2\theta_{23}$ is taken to be 0.5 with normal hierarchy as the true hierarchy.

The following observations can be made about the precision on $\sin^2\theta_{23}$. The 2D analysis is discussed first. The relative 1σ precision on $\sin^2\theta_{23}$ improves from $\sim 14.40\%$ to $\sim 13\%$ when higher energy bins are added in the analysis with muons only (2D) and 10 pulls. The precision is further improved by the addition of higher energy bins (i.e the analysis in 0.5 – 25 GeV range), to 9.35% which is obvious. Thus the observations are that

the inclusion of higher energy ranges in observed muon energy improves the precision on $\sin^2\theta_{23}$, which is further improved by the addition of the 11$^{\text{th}}$ pull, in the 2D analysis.

In the case of 3D analysis the inclusion of hadron energy bins improves the precision as discussed in Ref. [27]. Further the inclusion of higher energy muon bins in the 3D analysis with 10 pulls improve the precision to $\sim 11.25\%$ percent. This improvement is expected since addition of higher energy bins in E_μ^{obs} ought to improve the precision. Further inclusion of the 11$^{\text{th}}$ pull significantly improves the precision to $\sim 8.9\%$. Thus the analysis with E_μ^{obs} in the 0.5 – 25 GeV, and 3D binning scheme and 11 pulls gives the best 1σ precision on $\sin^2\theta_{23}$. This is a remarkable achievement by ICAL given the fact that it is in general hard to improve the precision on $\sin^2\theta_{23}$. It should also be noted that the 2D analysis with 10 pulls only in the 0.5 – 25 GeV energy range gives a precision comparable to that obtained with the 3D analysis with 10 pulls only in the 1 – 11 GeV. So, what the 3D analysis can achieve in the 1 – 11 GeV only range can be achieved by extending the energy range and obviously the 3D analysis in this range will give better precision. The inclusion of the 11$^{\text{th}}$ pull is also remarkable, since the precisions achieved in the same energy range by both 2D and 3D with the addition of this pull are comparable.

6.7.2 Precision on $|\Delta m^2_{eff}|$ (or $|\Delta m^2_{32}|$)

Since ICAL is a magnetised iron calorimeter, it can measure $|\Delta m^2_{eff}|$ (or $|\Delta m^2_{32}|$) with very good precision. As in the case of $\sin^2\theta_{23}$, there are six different analyses which give the results as shown in Fig. 6.5. The percentage precisions obtained for the magnitude of Δm^2_{eff} are shown in Table 6.4.

Binning	E_μ^{obs} (GeV)	No.of pulls	$\Delta m^2_{eff_{min}}(2\sigma) eV^2$ $\times 10^{-3} eV^2$	$\Delta m^2_{eff_{max}}(2\sigma) eV^2$ $\times 10^{-3} eV^2$	Precision at 1σ (%)
2D $(E_\mu^{obs}, \cos\theta_\mu^{obs})$	1–11	10	2.176	2.665	5.09
	0.5–25	10	2.219	2.599	3.95
	0.5–25	11	2.221	2.597	3.91
3D $(E_\mu^{obs}, \cos\theta_\mu^{obs}, E'^{obs}_{had})$	1–11	10	2.259	2.552	3.05
	0.5–25	10	2.282	2.525	2.53
	0.5–25	11	2.282	2.525	2.53

Table 6.4: Precision of $|\Delta m^2_{eff}|$ at 1σ, obtained using Eq. 6.25, from different analyses. The maximum and minimum values of Δm^2_{eff} at 2σ in each case are also shown. The true value of Δm^2_{eff} is taken to be $2.4 \times 10^{-3} eV^2$ with normal hierarchy as the true hierarchy.

The following observations can be made. The first observation is that ICAL can determine $|\Delta m^2_{eff}|$ with a greater precision than $\sin^2\theta_{23}$, in all energy ranges. The relative

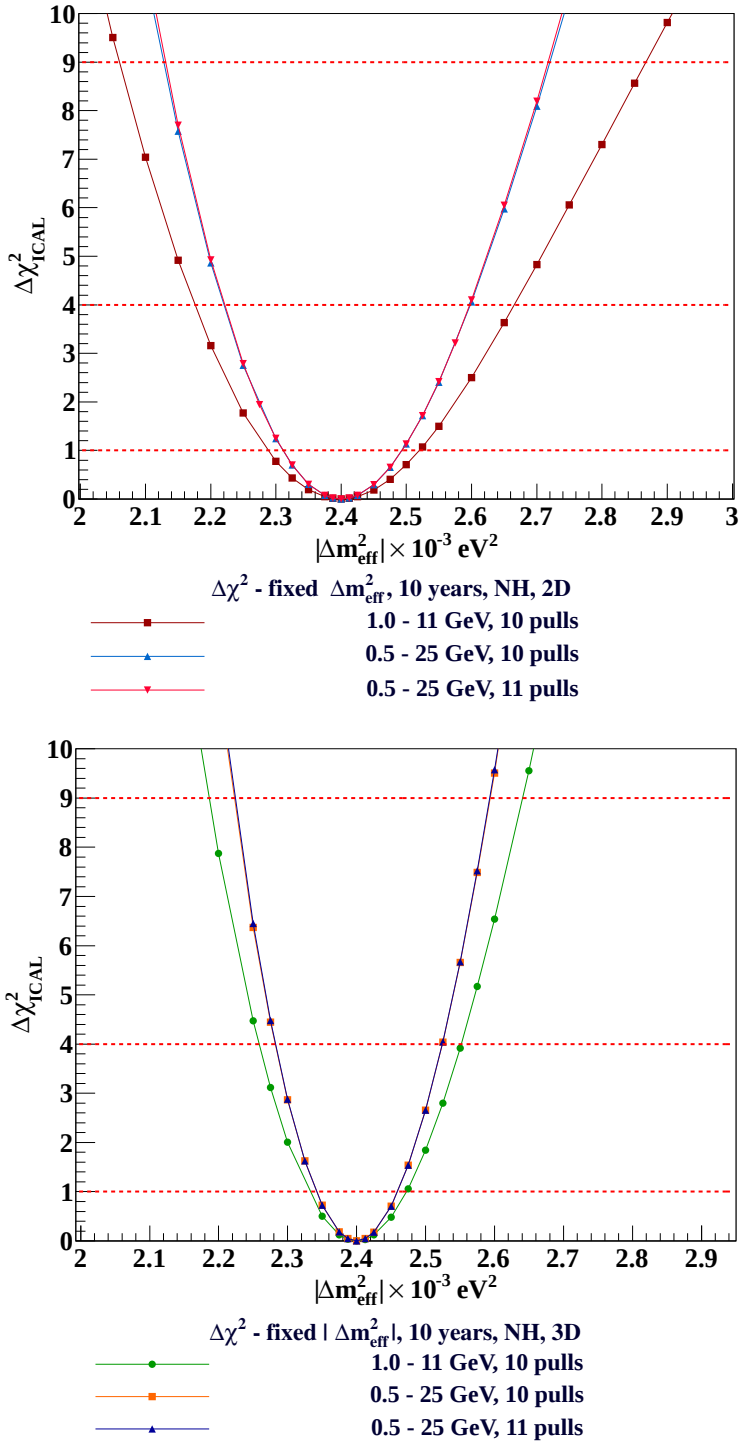

Figure 6.5: The values of $\Delta\chi^2$ at different values of Δm^2_{eff} with true $\Delta m^2{}_{eff} = 2.4 \times 10^3 eV^2$ with normal hierarchy as the true hierarchy. Top panel shows the results for the 2D analyses and the bottom one shows those for the 3D analyses. The results for all possible combinations of energy ranges, pulls and binning schemes are shown. It can be seen that the addition of higher energy observed muon bins improve the results, both in the 2D and 3D cases as compared to the cases with muon energy in 1 – 11 GeV only. The addition of the 11$^{\text{th}}$ pull doesn't make any difference in the precision of $|\Delta m^2_{eff}|$. The X axes are not the same in the top and bottom panels.

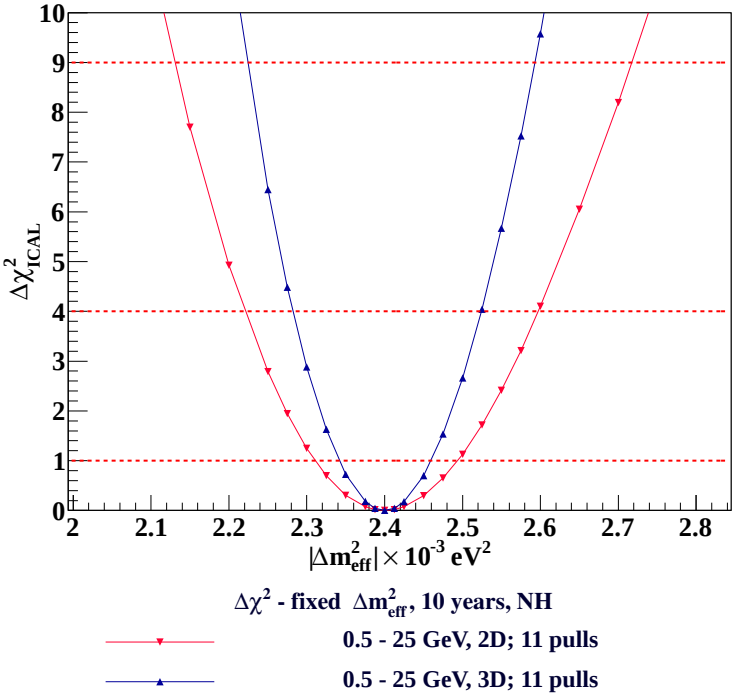

Figure 6.6: Comparison of $\Delta\chi^2_{ICAL}$ obtained from 2D and 3D analyses in the energy range E_μ^{obs} = 0.5–25 GeV and with 11 pulls. The best result is for the 3D analysis. It should be noted that these are same as the results obtained in the same energy with 10 pulls only, since the addition of the extra pull does not affect the precision on $|\Delta m^2_{eff}|$.

1σ precision is 5.09% in the 1–11 GeV energy range of observed muon, with 2D analysis and 10 pulls only. This improves to 3.95% on the extension of E_μ^{obs} to 0.5–25 GeV, still with 10 pulls and with 2D analysis. However the addition of the 11$^{\text{th}}$ pull in both the energy ranges does not significantly improve the precision from the values obtained with 10 pulls only. This is in contrast to $\sin^2\theta_{23}$, whose precision is improved by the addition of the extra pull.

The analysis with 10 pulls and 3D binning scheme gives a precision of 3.05% in the E_μ^{obs} = 1–11 GeV range as discussed in Ref. [27]. This is a significant improvement from the precision given by the muon-only analysis. The addition of higher energy bins in the observed muon energy improves the precision on Δm^2_{eff} by about 0.52%, the value being 2.53%. Further adding the 11$^{\text{th}}$ pull does not improve the precision on $|\Delta m^2_{eff}|$ in both E_μ^{obs} = 1 – 11 GeV and 0.5 – 25 GeV energy ranges.

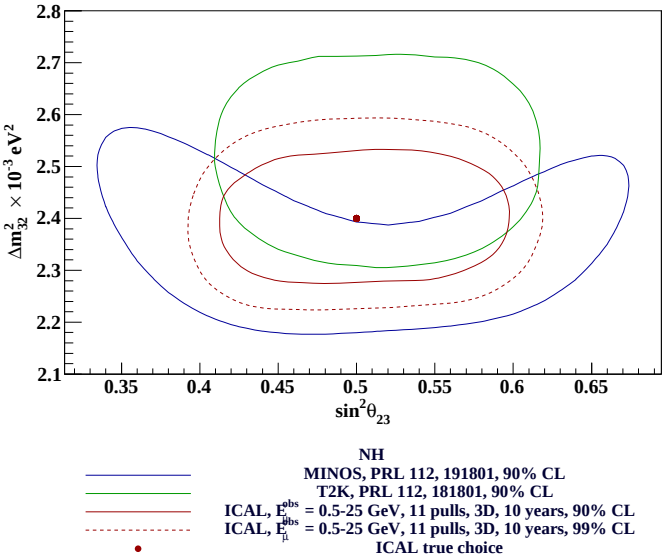

Figure 6.7: The $\Delta\chi^2_{ICAL}$ contours at 90% and 99% confidence levels (CL) in the $\sin^2\theta_{23} - |\Delta m^2_{eff}|$ plane for 500 kton yrs exposure of ICAL and the 3D analysis with E_μ^{obs} = 0.5–25 GeV and the inclusion of the 11$^{\text{th}}$ pull. The 90% confidence contours from MINOS [33] and T2K [34] are also shown for comparison. The red dot shows the true choice of parameters for the ICAL analysis, $(\sin^2\theta_{23}, |\Delta m^2_{eff}|) = (0.5, 2.4 \times 10^{-3}\text{eV}^2)$. It can be seen that the addition of the 11$^{\text{th}}$ pull gives a significant improvement in the precision of $\sin^2\theta_{23}$ obtainable by ICAL. For 500 kton yrs of exposure, this projected precision is similar to the current precision on this parameter by T2K.

6.7.3 Simultaneous precision on $\sin^2\theta_{23}$ and Δm^2_{eff}

The results discussed in the previous sections were for fixed values of either of the oscillation parameters $\sin^2\theta_{23}$ and Δm^2_{eff}. The precision obtained by allowing all parameters to vary is shown in this section. The analysis was done for the 11 pull case with E_μ^{obs} = 0.5–25 GeV and with hadrons, for 500 kton yrs of ICAL exposure. Normal hierarchy is assumed to be the true hierarchy. The precision $p(\lambda)$ on a parameter λ at a given confidence level (CL) is expressed as:

$$p(\lambda) = \frac{\lambda_{max} - \lambda_{min}}{\lambda_{max} + \lambda_{min}}, \tag{6.26}$$

where λ_{min} and λ_{max} are the minimum and maximum values of the parameter λ at that given confidence level.

The 90% and 99% confidence contours of $\sin^2\theta_{23}$ vs $\Delta m^2{}_{eff}$ for 500 kton years of exposure and the analysis with hadrons with 11 pulls and E_μ^{obs} = 0.5–25 GeV are shown in Fig. 6.7. A comparison of these projected results for ICAL with the current results from MINOS [33] and T2K [34] are also shown in the figure.

It can be seen that the extension of the energy range for analysis and constraining the $\nu_\mu - \bar{\nu}_\mu$ flux ratio improve the precision on both parameters. The significant improvement

is in $\sin^2\theta_{23}$ precision, which is 18.3% at 90% CL and 22.37% at 99% CL. The projected ICAL precision on $\sin^2\theta_{23}$ is comparable to the current T2K precision. The ICAL precision on Δm^2_{eff} at 90% CL is 5.34% and that at 99% CL is 7.66%. It can be seen that this is better than the precision on $\sin^2\theta_{23}$, since ICAL being a magnetised detector will always measure Δm^2_{eff} more precisely than $\sin^2\theta_{23}$. This is slightly worse than the precision obtained by MINOS. With more years of data ICAL can improve its precision on the oscillation parameters.

6.8 Results: sensitivity to neutrino mass hierarchy

Studies on the sensitivity to neutrino mass hierarchy have been conducted in the extended energy range and with the extra pull. Normal hierarchy is taken as the true hierarchy for the analysis. Studies with exposures of 5, 10, 15 and 20 years were done and $\Delta\chi^2_{MH-ICAL}$ in each case were plotted as a function of exposure time in years. The ability of ICAL to distinguish true hierarchy from wrong hierarchy is given by:

$$\Delta\chi^2_{MH-ICAL} = \chi^2_{false-MH} - \chi^2_{true-MH}, \tag{6.27}$$

where $\chi^2_{false-MH}$ is the χ^2 from the false hierarchy, which is taken to be the inverted hierarchy here and $\chi^2_{true-MH}$ is the χ^2 from the true mass hierarchy which is taken to be the normal hierarchy in the current analysis. The plot of $\Delta\chi^2_{MH-ICAL}$ as a function of number of years of exposure is shown in Fig. 6.8.

The observations about hierarchy determination are as follows. The muon-only analysis (2D) in the 1–11 GeV energy range of observable muons with 10 pulls only gives a $\Delta\chi^2_{MH-ICAL}$ of ~ 4.65 only for 10 years of ICAL exposure. The addition of higher energies in the muon only analysis with 10 pulls improves $\Delta\chi^2_{MH-ICAL}$ to ~ 5.21 for the same 10 years' exposure. The addition of the 11^{th} pull does not improve $\Delta\chi^2_{MH-ICAL}$ in both energy ranges in the 2D analysis.

The addition of hadron energy as the third observable increases the $\Delta\chi^2_{MH-ICAL}$ to ~ 7.69, in the energy range 1–11 GeV with 10 pulls, for an exposure time of 10 years. It should be noted that the values of $\Delta\chi^2_{MH-ICAL}$ are lower than those reported in Ref. [27], for the same exposure time. This is due to the fact that the two analyses use two different values of input θ_{13}, the one in Ref. [27] being $\theta_{13} \sim 9.097^\circ$ and the one used in the current

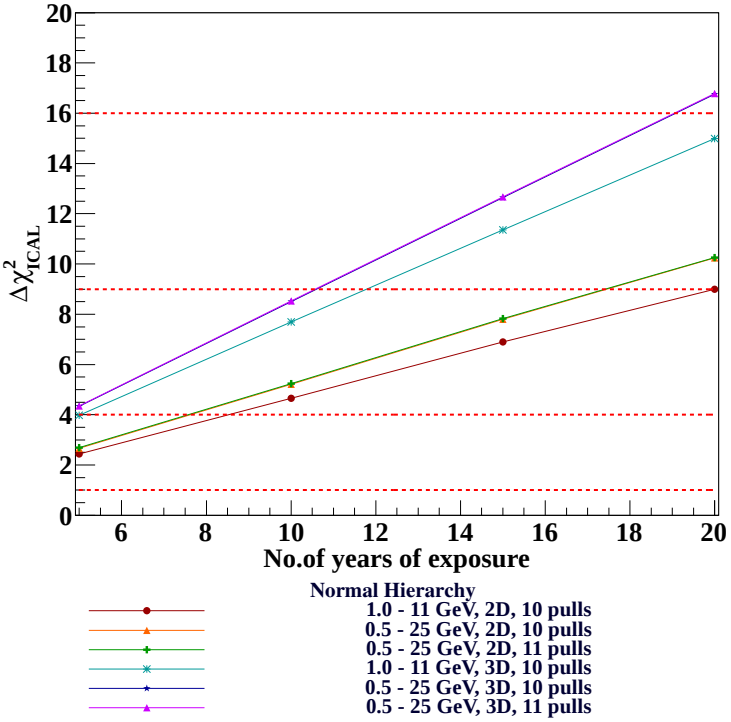

Figure 6.8: $\Delta\chi^2_{MH-ICAL}$ as a function of exposure time in years. It can be seen that the sensitivity to mass hierarchy increases linearly with exposure time. The extension of observed muon energy range to 0.5 – 25 GeV increases the sensitivities in the case of both 2D and 3D. The extra pull doesn't improve hierarchy sensitivity.

analysis is the current best fit value [120] $\theta_{13} \sim 8.729°$. It has been shown in Ref. [27] that $\Delta\chi^2_{MH-ICAL}$ decreases with the decrease in θ_{13} value. In the energy range 0.5–25 GeV, with only 10 pulls in the analysis, $\Delta\chi^2_{MH-ICAL}$ improves to about 8.5 for 10 years of exposure of ICAL. Again the addition of the 11$^{\text{th}}$ pull has no effect on hierarchy sensitivity.

To summarise, the mass hierarchy sensitivity improves with the addition of higher energy bins in the analysis, but constraining the $\nu_\mu - \bar{\nu}_\mu$ flux ratio does not improve the sensitivity to mass hierarchy in any energy range. Even then, the ICAL's ability to determine mass hierarchy is significant owing to its magnetisability and its 50 kton mass. Improvement in energy resolutions will further improve ICAL's mass hierarchy sensitivity further. Also in ICAL hierarchy can be determined independent of the CP violating phase δ_{CP} because of the baselines involved in atmospheric neutrinos [19].

6.9 Impact of the 11th pull on determination of θ_{23}

The 11th pull accounts for the fact that the *ratios* of the ν_μ and $\overline{\nu}_\mu$ fluxes are better known that the absolute fluxes themselves. This is implemented by using a pull $\pi_6 = 0.025$ (2.5%),

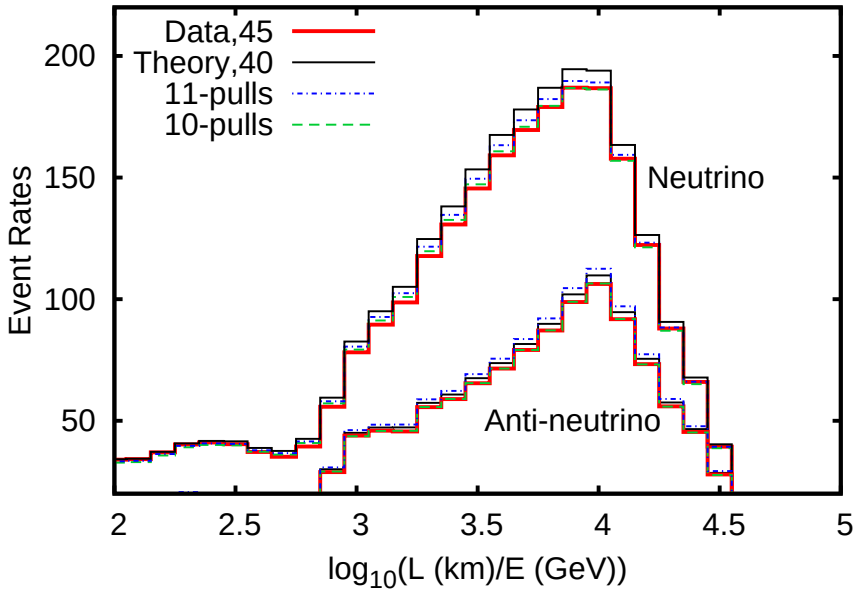

Figure 6.9: The rates from CC ν_μ and $\overline{\nu}_\mu$ events over 10 years in ICAL are shown as a function of $\log_{10}(L(\text{km})/E(\text{GeV}))$ where L and E are the "path length" and energy of the final state muon. The red (thick solid) lines correspond to the "data" set with $\theta_{23} = 45°$ and the black (thin solid) one to the "theory" with $\theta_{23} = 40°$ (and other parameters held fixed). The discrepancy between the theory and data (and hence whether $\theta_{23} = 40°$ yields an acceptable fit) can be improved by changing the overall normalisation. The green (dashed) lines show the fit with normalisation independently reduced by 4% and 3% on neutrino and anti-neutrino fits. The blue (dot-dashed) lines show the fit with normalisation reduced (increased) by 2.5% correspondingly, thus mimicing the effect of the 11th pull. It is seen that the fits are worse in this latter case.

but this pull contributes *with the opposite sign* for neutrino and anti-neutrino events.

It is seen that the inclusion of the 11th pull is most visible in the determination of θ_{23} which becomes more constrained when this pull is included. One way to understand this is to rebin the events in a single variable L/E (of the final state muon) rather than its direction and energy separately. Since the muon did not travel this path length, it is simply to be understood as a function of its direction ($\cos\theta$) so the L/E of the muon is equivalent to that of the initial neutrino. Fig. 6.9 shows the effect of θ_{23} on both the neutrino and anti-neutrino events. The "data" corresponds to $\theta_{23} = 45°$ while the "theory" corresponds to a fit with $\theta_{23} = 40°$. In both cases, reducing θ_{23} from the true value increases the event rate (the opposite will hold with the inverted hierarchy; here the normal hierarchy is shown). Note that the down-going events are not shown here.

The curves marked 11- and 10-pulls show the effect of changing the normalisation of the theory with and without the 11th pull. The overall normalisation of the events in the 10-pull case can be *independently* varied for neutrinos and anti-neutrinos (4% and 3% in figure) to improve the agreement of the $40°$ theory line to the data, resulting in smaller χ^2

in this fit.

On the other hand, a 2.5% decrease in the normalisation of neutrino-induced events in the 11-pull case is accompanied by a 2.5% *increase* in the anti-neutrino case, so that the agreement with the neutrino data becomes better, but that with the anti-neutrino data becomes worse. (Of course, it can be applied vice versa, but the smaller χ^2 is obtained with this choice since there are about twice as many neutrino events as anti-neutrino ones due to the smaller cross section of the latter.) Hence it is not possible to improve the agreement of the 40° theory with data by tuning the normalisation; this results in a larger χ^2 compared to the 10-pull case where the normalisations of neutrino- and anti-neutrino-induced events can be independently varied. This gives rise to the tighter constraints on θ_{23} when the 11th pull is added.

In addition, it can be seen from Fig. 6.9 that there is sensitivity to oscillation parameters near and beyond $\log_{10}(L(\text{km})/E((GeV)) \sim 4$. This is precisely the region that is included when E_μ^{obs} is extended from 1–11 GeV to 0.5–25 GeV. Similarly, (smaller) sensitivity to the parameters is also seen for $\log_{10}(L(\text{km})/E((GeV))$ ~2–3, which corresponds to the extension in the higher energy end.

6.10 The effect of fluctuations

As discussed in Section 6.5.4, the analyses in the previous sections were done by taking a 1000 year sample of charged current muon neutrino events and scaling it down to the required number of years. Since the analysis uses realistic detector resolutions and efficiencies smearing effects will already affect the results. Hence it is very important to have a sample with less "theory" fluctuation so as to obtain a genuine result from the analysis. The effect of fluctuations on neutrino oscillation parameters are discussed in this section. The effect of taking different years of data samples to be scaled to 10 years on precision measurement of θ_{23} and $|\Delta m^2_{eff}|$ is shown in Fig. 6.10. It can be seen that a smaller data sample yields a large value of $\Delta\chi^2_{ICAL}$ for a given parameter thus giving too good a precision on the oscillation parameter which is false. The larger data sample takes care of this by reducing the fluctuations in the theory itself. The χ^2 saturates at a point when the data sample is fairly large and this is the number of years of data to be taken and scaled down for the analysis. Ideally this happens to be 1000 year data sample and thus the analyses have made use of such a sample of charged current muon neutrino events.

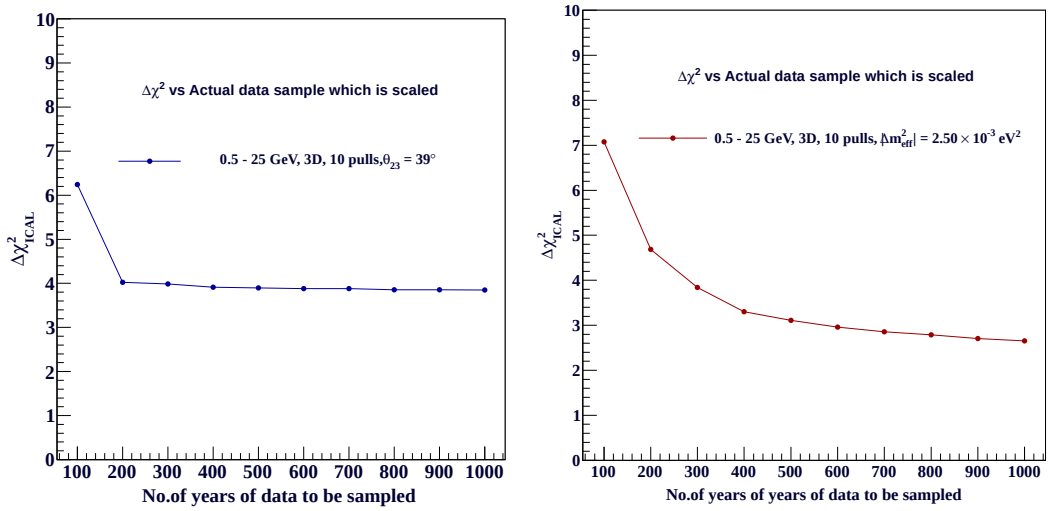

Figure 6.10: The value of $\Delta\chi^2_{ICAL}$ vs the number of years of data to be scaled to 10 years for $\theta_{23} = 39°$ (left) and $|\Delta m^2{}_{eff}| = 2.5 \times 10^{-3}\text{ev}^2$ (right). It can be seen that the scaling of only 100 years of data gives too high a χ^2 which is even more prominent in the case of $\Delta m^2{}_{eff}$. As the number of years of data sample to be scaled increases, the value of χ^2 also comes down as well as saturates for large enough data samples.

6.11 Chapter Summary

The proposed magnetised Iron Calorimeter detector (ICAL) at INO aims to probe the neutrino oscillation parameters by observing atmospheric neutrino oscillations and studying their Earth matter effects as they propagate through the Earth. This will be done by detecting (mainly) the charged current interactions of ν_μ and $\bar{\nu}_\mu$ in the detector by means of the final state muons. The detector, which is optimised for the detection of muons in the GeV energy range will have a magnetic field which will enable the distinction of ν_μ and $\bar{\nu}_\mu$ events by identifying the charge of the muon in the final state, thus making ICAL an excellent detector to determine neutrino mass hierarchy. Not only this, the magnetic field helps to improve the precision measurement of the mixing angle θ_{23} and $|\Delta m^2_{eff}|$ ($|\Delta m^2_{32}|$). Muons are not the only final state particles in the charged current interactions. Hadrons which produce a shower unlike the clean tracks of muons, are also present. Thus to study the sensitivities of the ICAL to neutrino oscillation parameters two different types of analyses can be used, one with muon energy and direction only as the observables used to bin events (2D binning scheme); and the other in which hadron energy, along with muon energy and direction (3D binning scheme) is used as an observable to bin the events. It has been shown elsewhere that the use of hadron energy improves the sensitivities of ICAL significantly [27]. But these studies have been conducted in the restricted energy range of 1 – 11 GeV and with 10 systematic pulls only. It should be noted that instead of re-

constructing the neutrino energy and direction and then binning in neutrino energy the analyses have been done by taking all the observables separately. This is because of the poor energy and direction resolution of neutrinos in ICAL detector owing to the fact that they are driven by the responses of ICAL detector to hadrons, which are worse compared to those of muons. Still the addition of the extra information regarding hadrons improves the sensitivity of ICAL to oscillation parameters.

Knowing that hadron energy information can improve the sensitivities it is interesting to probe new possibilities of improving the detector's sensitivities since any improvement in the sensitivities is going to impact the global values of these parameters and it is important that we extract as much information as possible from different analyses. Thus the study of the effect of extending the observed muon energy E_μ^{obs} range to 0.5 – 25 GeV along with the addition of a pull in the form of a constraint on the ratio of atmospheric ν_μ - $\bar{\nu}_\mu$ fluxes becomes significant. Both 2D and 3D binning scheme are used for the analyses and the results for E_μ^{obs} = 1 – 11 GeV and 0.5 – 25 GeV are compared with one another. The 2D binning scheme with $(E_\mu^{obs}, \cos\theta_\mu^{obs})$, where $\cos\theta_\mu^{obs}$ represents the observed muon direction, has 15 non-uniform bins in E_μ^{obs} and 21 uniform bins in $\cos\theta_\mu^{obs}$. In the 3D binning scheme with $(E_\mu^{obs}, \cos\theta_\mu^{obs}, E_{had}^{obs})$, the same muon bins along with 4 bins in observed hadron energy are used.

The relative 1σ precision on $\sin^2\theta_{23}$ and $|\Delta m^2_{eff}|$ ($|\Delta m^2_{32}|$) improves with the extension of energy range, the major effect coming from the addition of higher energy bins beyond 11 GeV. Though the precision on $|\Delta m^2_{eff}|$ ($|\Delta m^2_{32}|$) is very good, it is the precision on $\sin^2\theta_{23}$ which improves significantly, which is also the main highlight of this analysis. The effect on precisions attainable with 500 kton year exposure (10 years of run) are mentioned here. In the 2D case with 10 pulls only, the 1σ precision on $\sin^2\theta_{23}$ which was $\sim$14.40% in the 1 – 11 GeV range, improves to $\sim$13.00% on extending the energy range to 0.5 – 25 GeV. Similarly in the 3D case with 10 pulls only, the same precision improves from $\sim$12.85% to $\sim$ 11.25% on increasing the energy range. The addition of the extra pull improves the precision further in all energy ranges. The best best precision on $\sin^2\theta_{23}$ achievable with 500 kton years of ICAL $\sim$8.90% with the 3D binning scheme, in the 0.5 – 25 GeV energy and with 11 systematic pulls. This is a significant improvement over all the previous analyses of ICAL physics and will contribute to the global fits of neutrino oscillation parameters.

The relative precision of $|\Delta m^2_{eff}|$ ($|\Delta m^2_{32}|$) in the 1 – 11 GeV range with 10 pulls only, is

$\sim$5.09% with 2D binning scheme. The extension of energy range to 0.5 – 25 GeV improves this precision to $\sim$3.95%. The 3D binning scheme with 10 pulls only yields a precision of $\sim$3.05% in the 1 – 11 GeV energy range, the precision slightly improves to $\sim$2.53% in the 0.5 – 25 GeV. Addition of the 11$^{\text{th}}$ pulls does not improve the precisions on $|\Delta m^2_{eff}|$ ($|\Delta m^2_{32}|$) from their values obtained with 10 pulls only. Thus unlike $\sin^2\theta_{23}$, the constraint on the flux ratio of ν_μ and $\bar{\nu}_\mu$ has no effect on $|\Delta m^2_{eff}|$ ($|\Delta m^2_{32}|$).

The neutrino mass hierarchy sensitivity of ICAL was also shown to improve significantly with the 3D binning scheme in the energy range 1 – 11 GeV [27]. The extension of E^{obs}_μ to 0.5 – 25 GeVs improves the hierarchy sensitivity in both 2D and 3D analyses with 10 pulls. The best value of $\Delta\chi^2_{ICAL}$ achievable with 500 kton years of exposure is $\sim$8.523 obtained from 3D analysis in the 0.5 – 25 GeV range of observed muon energy. Addition of the 11$^{\text{th}}$ pulls does not affect mass hierarchy determination.

The studies presented here assume that there is perfection separation between different types of events. The event identification efficiency will also affect the results of the analysis since they will determine the number of events in each bin. Also the resolutions for hadrons and muons used in this analysis were obtained from simulations of the INO ICAL detector using GEANT-4. Improvements in the reconstruction efficiencies and resolutions will definitely give better results. It is also worthwhile thinking about alterations in detector geometry if needed and plausible to make the detector more efficient and one with better resolutions. Also the current studies are all done with the atmospheric neutrino flux at the Super Kamiokande site. The fluxes at Theni where ICAL will be built have to be used for next level of analysis. Also the effect of adding hadron direction as a fourth observable in the analysis still have to be studied, it remains to be checked if this information will give better or worse results than the existing ones. The physics results of ICAL have the capability to impact global fits to neutrino data and thus any new analysis will open a window to understanding the neutrino oscillation parameters better on the whole.

Part IV

Summary and future scope

7 Summary and Future Scope

Many neutrino oscillation experiments all over the world are probing neutrinos from various sources, over different regions of L/E to get more insight into the intrinsic properties of neutrinos such as their masses, mixing angles and mass ordering and also to probe CP violation through the leptonic sector via studying neutrinos. The proposed Iron-CALorimater (ICAL) experiment at the upcoming India-based Neutrino Observatory (INO) is a large scale Neutrino Physics experiment which aims to determine neutrino mass hierarchy and perform precision measurements of neutrino oscillation parameters $|\Delta m^2{}_{32}|$ and θ_{23}, by observing atmospheric neutrinos coming from the other side of the Earth. The 50 kilo ton magnetisable, detector, to be situated under the 1595 m peak of Bodi West Hills in Theni District of Tamil Nadu has tremendous physics potential. The simulation studies on the physics of hadrons in the ICAL detector and the physics reach of ICAL to neutrino oscillations have been discussed in this thesis. A summary of these discussions is given in the first part of this chapter. Since ICAL is such a huge detector, it is interesting to explore what other physics it can do other than neutrino oscillations. The future scopes are discussed in the second part of this thesis.

7.1 Summary

As mentioned above, the ICAL detector at INO will be a 50 kton magnetisable detector which will detect atmospheric neutrinos and probe Earth matter effects on their propagation to determine neutrino mass hierarchy and conduct precision measurements of the mixing angle θ_{23} and $|\Delta m^2{}_{32}|$. Due to its magnetisability, ICAL can distinguish between μ^- and μ^+ produced in the final state of the charged current interactions of ν_μ and $\bar{\nu}_\mu$ with the iron in the detector. This imparts to ICAL the capability to determine neutrino mass hierarchy.

Not only muons but hadrons are also produced in the final state of these charged current interactions. Even though the ICAL detector is optimised for muon detection

and has excellent muon momentum and direction resolutions, it is necessary to extract as much information from the hadrons as possible. Simulation studies of single pions propagated through the ICAL detector simulated using a GEANT-4 based simulation frames work was done. From the studies it was seen that the energy resolution of fixed energy single pions is $0.86/\sqrt{E}$ at 1 GeV and $0.36/\sqrt{E}$ at 15 GeV for the default iron plate thickness of 5.6 cm.

Studies on the dependence of hadron energy resolution on iron plate thickness were done. The studies showed that the dependence is not a naive square root dependence as seen in the case of hadrons of very high energies. The dependence of the stochastic coefficient a from the relation $(\sigma/E)^2 = a^2/E + b^2$, was studied and it was found to have the following properties. For the direction averaged case, in the low energy range of 2–4.75 GeV, the value of a increases from $a = 0.651$ for 1.5 cm thick iron to $a = 0.969$ for 8 cm iron. In the higher energy range 5–15 GeV, the value of a varies between 0.702 and 0.974. In the full energy range 2–15 GeV, the variation is between $a = 0.709$ to $a = 0.985$. The parametrisation of the thickness dependence of this stochastic coefficient a using the relation $a(t) = p_0 t^{p_1} + p_2$ shows that the dependence is not a $\sqrt{t}$ (where t is the iron plate thickness) as in the case of very high energies. Rather it is energy dependent and the thickness dependent term has an exponent p_1 which is $\sim$ 1.13 in the 2–4.75 GeV energy range and $\sim$ 0.73 in the 5–15 GeV energy range. The smallness of the coefficient p_0 makes the contribution of this term less significant than that of the constant term p_2 which is always around $\sim$ 0.6. The term p_2 attributes to the residual resolution which is due to the intrinsic uncertainties of strong interactions, fluctuations and detector geometry, indicating that there will always be a finite uncertainty the estimation of hadron energy even if the plate thickness is reduced to infinitesimally small values. An alternate parametrisation of the plate thickness dependence of $\sigma/\sqrt{E}$ as, $\sigma/\sqrt{E} = q_0 t^{q_1} + q_2$ also showed that the effect of the presence of the residual resolution on hadron energy response.

The direction dependence of the thickness dependence was also studied. For a given thickness it was found that the energy response is the worst for the most horizontal directions as expected, improves with the increase in $\cos\theta$ values, but the resolution for the $\cos\theta$ bin [0.8, 1.0] was found to be worse than that in the bin $\cos\theta$ = [0.6, 0.8]. This is because of the non-trivial geometry of the detector, with vertical support structures at regular intervals which causes the lose of signal and thus hits, thus affecting the hadron energy calibration. The studies on the e/h ratio of the ICAL detector were also con-

ducted since this shows the effect of neutral pions on the energy resolution of multiple hadrons produced in neutrino interactions with iron. The ratio of the electron response to charged pion response of ICAL was found to be energy dependent. On the average, taking e/h ratio to be $\sim$ 0.9 and using this value to calculate the energy response of multiple hadrons produced in the charged current interactions of muon neutrinos yielded a value of $\sim 0.97h$, where h is the response of single pions in ICAL, consistent with the values obtained in [20].

Simulation studies of fixed energy single pions propagated along a fixed direction with nominal smearing, was done for different iron plate thicknesses. These were compared with the test beam runs of other experiments, and were found to be comparable. The effect of different hadronisation models in GEANT-4 on the hadron energy response was also studied. Different hadron models were found to have no significant effect on the energy response of hadrons in the energy range 2–15 GeV in the ICAL detector. These results have all been discussed in detail in Chapter 3.

GEANT-4 based simulation studies of fixed energy single pions and also multiple hadrons produced in neutrino interactions generated using NUANCE were conducted to reconstruct the direction of hadrons in the ICAL detector. A method called the "raw hit method", which uses both the position and timing information of the hadron shower hits was used for the purpose of direction reconstruction. Since this method does not require a vertex with respect to which the direction has to be reconstructed, it can be used in the case of charged current neutrino interactions as well as neutral current interactions. Studies show that the direction resolution is the best in the most vertical direction with $|\cos\theta|$ = [0.8, 1.0] and gradually decreases as the direction becomes more and more horizontal. A θ resolution of $9.38^\circ \pm 0.17^\circ$ at 1 GeV and $8.68^\circ \pm 0.11^\circ$ at 10 GeV, were obtained for fixed energy single pions in the direction $\cos\theta = 0.9$ with the azimuthal angle ϕ smeared from 0–2π.

In the case of hadrons from charged and neutral current muon neutrino interactions, the best resolutions were obtained for the vertical direction $\cos\theta = [0.8,\ 1]$ with $\sigma_{\Delta\theta} = 15.6^\circ$ in the $E'_{had} = 2.5 \pm 0.5$ GeV bin and $\sim 11^\circ$ in the $E'_{had} = 14.5 \pm 0.5$ GeV bin. In the case of hadrons from neutral current interactions also the best θ resolution was obtained for the $\cos\theta = [0.8,\ 1]$ bin with $\sim 16.5^\circ$ in the 2–3 GeV E'_{had} bin and $\sim 10^\circ$ is obtained in the 12–15 GeV energy range. In addition to the θ resolutions, the resolution of the opening angle β between the muon and hadrons in a charged current muon neutrino interaction

was determined. These works have been discussed in detail in Chapter 4.

The resolutions of muon momentum and direction along with the reconstruction efficiency and charge identification efficiency of muons were determined elsewhere and have been reviewed briefly in Chapter 5 for completeness since they are used in the physics analysis in Chapter 6. The momentum and direction resolutions of muons in ICAL are found out to be excellent, with about $\sim 10\%$ momentum resolution and less than 1° direction resolution. The charge identification efficiency of ICAL with respect to the charge of muons is also extremely good, in the range 95–99%, indicating that the detector is highly optimised for muon detection.

A method to separate charged current muon neutrino events based on the number of strips and layers hit in an event was also discussed in detail. It was found that the application of a criterion which takes into account both the strip and layer multiplicity effectively separates charged current muon neutrino events from other types of events in the detector.

The oscillation sensitivities of the ICAL detector have been discussed in detail in Chapter 6. Unlike the previous analyses of ICAL to oscillation sensitivities which were done only in the 1–11 GeV energy range of the observed muon, the analysis discussed in this thesis has taken into account the extended energy range of 0.5–25 GeV of the observed muon and the effect of constraining the ν_μ-$\bar{\nu}_\mu$ flux ratio. As a consequence, a larger kinematic region with sensitivity to the neutrino oscillation parameters gets included in the analysis. Two types of analyses with muon momentum and direction only as the observables, along with another in which muon momentum, direction and hadron energy have been used as observables have been discussed. Studies on the precision measurement of θ_{23} and $|\Delta m^2{}_{32}|$, as well as sensitivity to neutrino mass hierarchy were also conducted. The relative 1σ precision obtained for 500 kton year exposure of ICAL are as follows. For θ_{23}, in the 0.5–25 GeV muon energy range, a precision of 13.0% is obtained for the muon only analysis without the constraint on the ν_μ-$\bar{\nu}_\mu$ flux ratio (10 pulls only) and 9.35% when the constraint on the flux ratio is applied. For the analysis with hadrons, the relative precision on θ_{23} is 11.25% for the 10 pull analysis whereas the precision improves to 8.90% when the flux ratio is constrained. Similarly, the precision on $|\Delta m^2{}_{eff}|$ improves on extending the muon energy bins, but are roughly the same for the 10 pull and 11 pull analyses. For the muon only analysis, the precisions are 3.95% and 3.91% for the 10 pull and 11 pull analyses respectively, whereas the precisions are 2.53% and 2.53%

respectively for the 10 pull and 11 pull analyses with hadrons also. It can be seen that that addition of the extra pull has no effect on the precision of $|\Delta m^2{}_{eff}|$ whereas it improves the precision on θ_{23} considerably.

Mass hierarchy sensitivity of ICAL also improves with the extension of the observed muon energy range. The best sensitivity to hierarchy is obtained for the with hadron analysis with the muon energy range extended to 0.5–25 GeV. A $\Delta\chi^2_{MH-ICAL}$ of ~ 8.5 is obtained for 10 years for the best case. The 11^{th} pull is found not to have any major effect on the hierarchy sensitivity. The most important finding of the analysis presented in this chapter is the improvement in the precision measurement of θ_{23}, the precision on which is very hard to determine.

The summary of the works discussed in all the previous chapters has been presented in this section. These studies are mainly about the physics potential of the ICAL detector with respect to determining the neutrino oscillation parameters. The analysis discussed in Chapter 6 is mainly through the muon detection channel. However, charged current muon neutrino interactions are not the only interactions which will occur in ICAL. Hence it is important to think about the scope of the things that can be done in future. A discussion on the future scopes are presented in the next section.

7.2 Future scope

The ICAL detector is mainly optimised for the detection of muons. However in reality there will be charged current interactions of both muon and electron neutrinos in the detector, since there are electron neutrinos in the atmospheric neutrino flux. Hence it is important to extract as much information about oscillation parameters as possible by probing the charged current interactions of electron neutrinos in the ICAL detector. It is a hard task given the fact that electrons produced in the final state of these interactions will produce showers like the final state hadrons. But these are electromagnetic showers whose characteristics differ from those of the hadron shower. Still given the coarse position resolution of the ICAL detector, it is hard, but not impossible to separate electrons and hadrons in the detector. Detailed studies to separate the events without muons, or rather the charged current electron events from neutral current events have to be done in detail and the input of these studies have to be fed into the oscillation analysis to study the sensitivity of ICAL to $P_{\mu e}$ ($\bar{P}_{\mu e}$) oscillations. This is a future scope and will be an

interesting one.

It was seen that the addition of the hadron energy as the third observable enhanced the sensitivities of ICAL to the oscillation parameters. It will be interesting to study the effect of adding the hadron direction as the fourth observable in the oscillation analysis. Till now all the oscillation sensitivity studies with ICAL have been conducted with the muon momentum, direction and hadron energy as separate observables. Reconstructing the initial neutrino energy and momenta from the final state muon and hadron information and conducting the oscillation sensitivity studies in the L_ν/E_ν bins will be interesting. Even though the uncertainties in the reconstruction of neutrino energy and direction are driven by those in the hadron energy and direction, this analysis is interesting. This also opens up a prospect of improving the hadron responses of the detector. In addition to providing a better neutrino reconstruction, improving the hadron responses by themselves will improve the sensitivities even when used as separate observables along with the final state muon momentum and direction. This also means that the sensitivity to electrons will also improve and thus the overall sensitivity of the ICAL to neutrino oscillation parameters will improve.

As of now there is no direct measurement of the charge deposited by the particles in the detector due to the mode in which it is operated. Hence due to the absence of any direct measurement of the energy deposited during the propagation of a charged particle, the energy of hadrons are calibrated to the number of hits only. By making small but optimal changes in the detector geometry like using scintillators as active detectors instead of RPCs, the energy of the hadrons can be measured in a better manner. It is not necessary that the entire detector geometry and structure be changed to implement this, but this can be implemented in a small portion of the detector and checked. In fact simulation studies with such a geometry can be done and the effect of these changes can be studied and it will help deciding if such changes will make a major difference in the oscillation sensitivities or not.

Another possibility is to reduce the width of the copper pick up strips used in the RPCs. Currently all ICAL simulation studies use 1.96 cm wide strips and the real prototype of ICAL has RPCs with 3 cm wide pick up strips. The major uncertainty in the reconstruction of the azimuthal angle ϕ of the final state particles, both muons and hadron shower is due to the large width of the pick up strips. The studies on the effect of varying the pick up strip width on both the energy and direction resolution of particles can be

done. Again simulation studies can be done in this regard to decide whether to keep the current width or whether it can be changed if varying the strip width will improve the resolutions. This is another future scope.

The studies presented in this thesis show that the sensitivities of the ICAL to oscillation parameters improve with the extension of the observed muon energy range from 1-11 GeV to 0.5–25 GeV. The effect of these improved values on the global values of these parameters has to be studied. It is sure that these improved values will have an impact on the global values of these parameters obtained from other neutrino oscillation experiments as well. ICAL can also be used to study sterile neutrinos and dark matter. Since ICAL will be a huge detector, the prospects of dark matter and magnetic monopole detection using the ICAL are interesting. Some of these studies are going on and are out of the scope of this thesis.

7.3 Summary

Neutrino physics all over the world has reached an interesting stage, where the absolute unknowns among the neutrino oscillation parameters are the mass hierarchy of neutrinos and the δ_{CP}, which is the CP violating phase. The precision measurements of θ_{23} and $|\Delta m^2{}_{32}|$ by various experiments all over the world are putting tighter and tighter bounds on their values each day. The proposed India-based Neutrino Observatory (INO) to be located in the Theni district of Tamil Nadu district in India will also make its mark in the history of neutrino physics by determining the neutrino mass hierarchy with its giant magnetisable 50 kton Iron CALorimater (ICAL) detector by probing the Earth matter effects on the propagation of atmospheric neutrinos through the Earth. The physics of potential of the ICAL detector is tremendous and the impact it will have on the global neutrino oscillation parameters is high. The detector with its simple yet powerful technique of magnetisation is very well suited for the easy determination of neutrino mass hierarchy. The physics is again interesting because of the myriad energies and baselines offered by atmospheric neutrinos.

The optimisation of the detector to the interaction channels of interest is necessary. The simulation studies of various particles propagated through the detector is required to estimate the performance of the detector and thus understand its full physics potential. Both studies, the simulations studies of the detector itself along with the simulation

studies of the neutrino oscillation physics to be probed by the ICAL were discussed in detail in the different chapters of this thesis. Simulations throw light upon the unknown, predict what all can happen in the detector, and how sensitive the detector will be, but the real fun starts with real data. Let us wait for and watch what all stories the ICAL detector will tell us about the tiny neutrinos.

A The Vavilov distribution function

A.0.1 The Vavilov distribution function

Vavilov distribution function is used to explain the energy loss of particles in thick absorbers [25, 26]. The standard Vavilov probability density function is defined as :

$$P(x;\kappa,\beta^2) = \frac{1}{2\pi i}\int_{c-i\infty}^{c+i\infty}\phi(s)e^{xs}ds, \tag{A.1}$$

where

$$\phi(s) = e^{C}e^{\psi(s)}, \quad C = \kappa(1+\beta^2\gamma) \tag{A.2}$$

and

$$\psi(s) = s\ln\kappa + (s+\beta^2\kappa)\cdot\left[\int_0^1 \frac{1-e^{-st/\kappa}}{t}\,dt \;-\; \gamma\right] - \kappa\, e^{-s/\kappa} \tag{A.3}$$

where $\gamma = 0.5772156649\ldots$ is the Euler's constant. The mean and variance (σ^2) of the distribution in Eq. (A.1) are given by

$$\text{mean} = \gamma - 1 - \ln\kappa - \beta^2; \quad \sigma^2 = \frac{2-\beta^2}{2\kappa}. \tag{A.4}$$

For $\kappa \leqslant 0.05$, Vavilov approximates to Landau distribution and for $\kappa \geqslant 10$, it tends to a Gaussian.

To fit to the hit distribution, Vavilov parameters have been redefined as follows: The original Vavilov pdf, $\mathrm{P}(\mathrm{x};\ \kappa,\ \beta^2)$ is modified into $(\mathrm{P_4}/\mathrm{P_3})\ \mathbf{P}(\mathrm{x}-\mathrm{P_2}/\mathrm{P_3};\ \mathrm{P_0},\ \mathrm{P_1})$. These account for normalization ($\mathrm{P_4}$) and the shift of mean to a non-zero value. Hence, the modified mean and variance are :

$$\text{Mean} = (\gamma\ -\ 1\ -\ \ln\mathrm{P_0} - \mathrm{P_1})\,\mathrm{P_3} + \mathrm{P_2}; \quad \sigma^2 = (2-\mathrm{P_1})\,\frac{\mathrm{P_3^2}}{2\mathrm{P_0}}. \tag{A.5}$$

The errors on mean and σ therefore arise from highly correlated parameters P_i. These have been determined using standard analytical formulae [155].

To calculate the mean and sigma, the hit distribution is fitted with the Vavilov density function in MINUIT modified to generate a function with mean at a non-zero value. After obtaining all the parameters, mean and sigma are calculated using Eq. A.5.

Bibliography

[1] W. Pauli, "Letter to the participants of workshop at Tuninfen, Germany," (1930).

[2] F. Reines and C. L. Cowan Jr., The Neutrino, Nature **178**, 446 (1956).

[3] C. L. Cowan Jr. *et al.*, "Detection of the Free Neutrino: a Confirmation", Science **20**, 103-104 (1956).

[4] B. Pontecorvo, "Mesonium and antimesonium", J.Exptl. Theoret. Phys. **33** 549 (1957) [Sov. Phys. JETP **6** 429 (1958)].

[5] B. Pontecorvo, "Inverse beta processes and nonconservation of lepton charge", J.Exptl. Theoret. Phys. **34** 247 (1958) [Sov. Phys. JETP **7** 172 (1958)].

[6] J. N. Bahcall and R. Davis Jr., "Solar Neutrinos: A Scientific Puzzle", Science **191**, 264-267 (1976).

[7] Q. R. Ahmad *et al.*, "Direct Evidence for Neutrino Flavor Transformation from Neutral-Current Interactions in the Sudbury Neutrino Observatory", Phys. Rev. Lett. **89**, 011301 (2002).

[8] Y. Fukuda *et al.*, "Evidence for Oscillation of Atmospheric Neutrinos", Phys. Rev. Lett. **81**, 1562 (1998).

[9] K. Eguchi *et al.*, "First Results from KamLAND: Evidence for Reactor Antineutrino Disappearance", Phys. Rev. Lett. **90**, 021802 (2003).

[10] T. Araki **et al.**,"Measurement of Neutrino Oscillation with KamLAND: Evidence of Spectral Distortion", Phys. Rev. Lett. **94**, 081801 (2005).

[11] F. P. An *et al.*, "Observation of Electron-Antineutrino Disappearance at Daya Bay", Phys. Rev. Lett. **108**, 171803 (2012).

[12] J. K. Ahn *et al.*, "Observation of Reactor Electron Antineutrinos Disappearance in the RENO Experiment", Phys. Rev. Lett. **108**, 191802 (2012).

[13] Y. Abe *et al.*, "Indication of Reactor $\bar{\nu}_e$ Disappearance in the Double Chooz Experiment", Phys. Rev. Lett. **108**, 131801 (2012).

[14] Y. Abe *et al.*, "Reactor $\bar{\nu}_e$ disappearance in the Double Chooz experiment", Phys. Rev. D **86**, 052008 (2012).

[15] Matthew Bass, Daniel Cherdack, Robert J. Wilson, "Future Neutrino Oscillation Sensitivities for LBNE", DPF2013-256, arXiv:**1310.6812** [hep-ex].

[16] S. K. Agarwalla *et al.* LAGUNA-LBNO Collaboration, "Optimised sensitivity to leptonic CP violation from spectral information: the LBNO case at 2300 km baseline", [arXiv:1412.0593] (2014).

[17] K. Abe *et al.*, "Neutrino oscillation physics potential of the T2K experiment", Prog. Theor. Exp. Phys. **4**, 043C01 (2015).

[18] M. S. Athar *et al.*, "India-based Neutrino Observatory: Project Report. Volume I.", INO-2006-01 (2006).

[19] S Ahmed *et al.*, "Physics Potential of the ICAL detector at the India-based Neutrino Observatory (INO)", INO/ICAL/PHY/NOTE/2015-01, arXiv:**1505.07380** [physics.ins-det] (2015).

[20] M. M. Devi *et al.*, "Hadron energy response of the Iron Calorimeter detector at the India-based Neutrino Observatory", JINST **8**, P11003 (2013).

[21] S. M. Lakshmi *et al.*, "Simulation studies of hadron energy resolution as a function of iron plate thickness at INO-ICAL", JINST **9** T09003 (2014).

[22] A. Chatterjee *et al.*, "A simulations study of the muon response of the Iron Calorimeter detector at the India-based Neutrino Observatory", JINST **9**, P07001 (2014).

[23] S. Agostinelli *et al.*, "GEANT4: A Simulation toolkit", Nucl. Instrum. Meth. A **506**, 250 (2003).

[24] D. Casper, "The Nuance neutrino physics simulation and the future", Nucl. Phys. Proc. Suppl. **112**, 161 (2002). [hep-ph/0208030]

[25] B. Schorr, "Programs for the Landau and the Vavilov distributions and the corresponding random numbers", Comp. Phys. Commm. **7**, 215 (1974);

[26] A. Rotondi, P. Montagna, "Fast calculation of Vavilov distribution", Nucl. Instr. & Meth. B **47**, 215 (1990).

[27] M. M. Devi *et al.*, "Enhancing sensitivity to neutrino parameters at INO combining muon and hadron information", Journal of High Energy Physics **10**, 189 (2014).

[28] M. M. Devi, S. M. Lakshmi, A. Dighe, D. Indumathi, "The physics reach of ICAL using hadron direction resolution", Paper under preparation.

[29] Anushree Ghosh, Tarak Thakore, Sandhya Choubey, "Determining the neutrino mass hierarchy with INO, T2K, NOvA and reactor experiments", Journal of High Energy Physics **4**, 009 (2013).

[30] Tarak Thakore, Anushree Ghosh, Sandhya Choubey and Amol Dighe, "The Reach of INO for Atmospheric Neutrino Oscillation Parameters", Journal of High Energy Physics **5**, 058 (2013).

[31] D. Indumathi, M. V. N. Murthy, G. Rajasekaran, and Nita Sinha, "Neutrino oscillation probabilities: Sensitivity to parameters", Phys. Rev. D **74**, 053004 (2006).

[32] M. C. Gonzalez-Garcia and Michele Maltoni, "Atmospheric neutrino oscillations and new physics", Phys. Rev. D **70**, 033010 (2004).

[33] P. Adamson *et al.*, "Combined Analysis of ν_μ Disappearance and $\nu_\mu \rightarrow \nu_e$ Appearance in MINOS Using Accelerator and Atmospheric Neutrinos", Phys. Rev. Lett. **112**, 191801 (2014).

[34] K. Abe *et al.*, "Precise Measurement of the Neutrino Mixing Parameter θ_{23} from Muon Neutrino Disappearance in an Off-Axis Beam", Phys. Rev. Lett. **112**, 181801 (2014).

[35] S. M. Lakshmi, D. Indumathi, N. Sinha, "Probing sensitivities to atmospheric neutrino oscillation parameters by the addition of higher energies in muons and constraining the neutrino-antineutrino flux ratio", Paper under preparation.

[36] L. Meitner and W. Orthmann, "Über eine absolute Bestimmung der Energie der primren β - Strahlen von Radium E, Z. Phys. **60**, 143 (1930).

[37] Sheldon L. Glashow, "Partial-symmetries of weak interactions", Nuclear Physics **22**, 579 (1961).

[38] F. Englert and R. Brout, "Broken symmetry and the mass of gauge vector mesons", Phys. Rev. Lett. **13**, 321 (1964).

[39] Peter W. Higgs, "Broken symmetries and the masses of gauge bosons", Phys. Rev. Lett. **13**, 508 (1964).

[40] G. S. Guralnik, C. R. Hagen, and T. W. B. Kibble, "Global Conservation Laws and Massless Particles", Phys. Rev. Lett. **13**, 585 (1964).

[41] Steven Weinberg, "A Model of Leptons", Phys. Rev. Lett. **19**, 1264 (1967).

[42] M. Gell-Mann, "A schematic model of baryons and mesons", Physics Letters **8**, 214 (1964).

[43] G. Zweig, "An SU(3) model for strong interaction symmetry and its breaking", Developments in the Quark Theory of Hadrons **1**, 22-101 (1964).

[44] Dvaid N. Schramm and Gary Steigman, "Relic neutrinos and the density of the universe", The Astrophysical Journal **243**, 1-7 (1981).

[45] Amand Faessler *et al.*, "Beta Decay and the Cosmic Neutrino Background", EPJ Web of Conferences **71**, 00044 (2014).

[46] Gianni Fiorentini *et al.*, "Geo-neutrinos and earth's interior", Physics Reports **453**, 117172 (2007).

[47] J. N. Bahcall *et al.*, "Solar Neutrino Flux", ApJ 137, No. 1, pp. 344-346 (1963 January)

[48] J. N. Bahcall, "Solar Neutrinos. I. Theoretical", Phys. Rev. Lett. **12**, 300-302 (1964).

[49] J. N. Bahcall, "Solar Neutrinos", Phys. Rev. Lett. **17**, 398-401 (1966).

[50] H. A. Bethe, "Energy Production in Stars", Phys. Rev. **55**, 434-456 (1939).

[51] Raymond Davis, Don S. Harmer, Kenneth C. Hoffman, "Search for neutrinos from the sun", Phys. Rev. Lett. **20**, 1205-1209 (1968).

[52] P. Anselmann *et al.*, "Solar neutrinos observed by GALLEX at Gran Sasso", Physics Letters B **285**, 376-389 (1992).

[53] P. Anselmann *et al.*, "GALLEX solar neutrino observations. The results from GALLEX I and early results from GALLEX II", Physics Letters B **314**, 445-45 (1993).

[54] Marc Herant *et.al.*, "Neutrinos and Supernovae", Los Alamos Science **25**, 64-78 (1997).

[55] H. A. Bethe, "Supernova mechanisms", Rev. Mod. Phys. **62**, 801 (1990).

[56] K. Hirata *et al.*, "Observation of a neutrino burst from the supernova SN1987A", Phys. Rev. Lett. **58**, 1490-1493 (1987).

[57] R. M. Bionta *et al.*, "Observation of a neutrino burst in coincidence with supernova 1987A in the Large Magellanic Cloud", Phys. Rev. Lett. **58**, 1494-1496 (1987).

[58] E. N. Alekseev **et al.**, "Possible Detection of a Neutrino Signal on 23 February 1987 at the Baksan Underground Scintillation Telescope of the Institute of Nuclear Research", JETP Lett. **45** 589-592 (1987).

[59] Thomas K. Gaisser, "Atmospheric Neutrinos", AIP Conf. Proc. **944**, 140 (2007).

[60] C.V. Achar *et al.*, "Detection of muons produced by cosmic ray neutrinos deep underground", Physics Letters **18**, 196-199 (1965).

[61] M. G. Aartsen *et al.*, "First observation of PeV-energy neutrinos with IceCube", Phys. Rev. Lett. **111**, 021103 (2013).

[62] M. G. Aartsen *et al.*, "Evidence for High-Energy Extraterrestrial Neutrinos at the IceCube Detector", Science **342**, 1242856 (2013).

[63] M. G. Aartsen *et al.*, "Observation of High-Energy Astrophysical Neutrinos in Three Years of IceCube Data", Phys. Rev. Lett. **113**, 101101 (2014).

[64] E. Fermi, "Fermi's Theory of Beta Decay", American Journal of Physics **36** 1150-1160 (1968). [Translation of Enrico Fermi's paper "Versuch einer Theorie der beta-Strahlen (in German), Z. Phys. **88**, 161 (1934), by Fred L. Wilson.]

[65] Y. Fukuda *et al.*, "Study of the atmospheric neutrino flux in the multi-GeV energy range", Physics Letters B **436**, 33-41 (1998).

[66] Y. Fukuda, *et al.*, "Evidence for Oscillation of Atmospheric Neutrinos", Phys. Rev. Lett. **81**, 1562 (1998).

[67] Ziro Maki, Masami Nakagawa and Shoichi Sakata, "Remarks on the Unified Model of Elementary Particles", Prog. Theor. Phys. **28** 870-880 (1962).

[68] B. Pontecorvo, "Neutrino Experiments and the Problem of Conservation of Leptonic Charge", Soviet Physics JETP **26**, 984 (1968).

[69] http://antares.in2p3.fr/users/pradier/orca.html

[70] D. Indumathi and M. V. N. Murthy, "Question of hierarchy: Matter effects with atmospheric neutrinos and antineutrinos", Phys. Rev. D **71**, 013001 (2005).

[71] L. Wolfenstein, "Neutrino oscillations in matter", Phys. Rev. D **17**, 2369-2374 (1978).

[72] S. P. Mikheyev, A. Yu. Smirnov, "3ν oscillations in matter and solar neutrino data", Physics Letters B **200**, 560564 (1988).

[73] Bruce T. Cleveland *et al.*, "Measurement of the Solar Electron Neutrino Flux with the Homestake Chlorine Detector", ApJ **496**, 505-526 (1998).

[74] R. Davis, "Solar neutrinos. II: Experimental", Phys. Rev. Lett. **12**, 303-305 (1964).

[75] R. Davis, "A review of the Homestake solar neutrino experiment", Prog. Part. Nucl. Phys. **32**, 1332 (1994).

[76] Q. R. Ahmad *et al.*, "Measurement of the Rate of $\nu_e + d \rightarrow p + p + e$ Interactions Produced by ^8B Solar Neutrinos at the Sudbury Neutrino Observatory", Phys. Rev. Lett. **87**, 071301 (2001).

[77] S. N. Ahmed *et al.*, "Measurement of the Total Active ^8B Solar Neutrino Flux at the Sudbury Neutrino Observatory with Enhanced Neutral Current Sensitivity", Phys. Rev. Lett. **92**, 181301 (2004).

[78] S. Fukuda *et al.*, "The Super-Kamiokande detector", Nuclear Instruments and Methods in Physics Research Section A **501**, Pages 418462 (2003).

[79] Y. Fukuda *et al.*, "Measurements of the Solar Neutrino Flux from Super-Kamiokande's First 300 Days", Phys. Rev. Lett. **81**, 1158-1162 (1998). [Erratum : Phys. Rev. Lett. **81**, 4279 (1998).]

[80] Y. Fukuda *et al.*, "Measurement of the Solar Neutrino Energy Spectrum Using Neutrino-Electron Scattering", Phys. Rev. Lett. **82**, 2430 (1999).

[81] Y. Fukuda *et al.*, "Constraints on Neutrino Oscillation Parameters from the Measurement of Day-Night Solar Neutrino Fluxes at Super-Kamiokande", Phys. Rev. Lett. **82**, 1810 (1999).

[82] Y. Fukuda *et al.*, "Study of the atmospheric neutrino flux in the multi-GeV energy range", Physics Letters B **436**, 3341 (1998).

[83] Y. Fukuda *et al.*, "Evidence for Oscillation of Atmospheric Neutrinos", Phys. Rev. Lett. **81**, 1562 (1998).

[84] S. H Ahn *et al.*, "Detection of accelerator-produced neutrinos at a distance of 250 km", Physics Letters B **511**, 178184 (2001).

[85] M. H. Ahn *et al.*, "Measurement of neutrino oscillation by the K2K experiment", Phys. Rev. D **74**, 072003 (2006).

[86] K. Abe *et al.*, "The T2K experiment", Nuclear Instruments and Methods in Physics Research Section A **659**, 106135 (2011).

[87] K. Abe *et al.*, "Neutrino oscillation physics potential of the T2K experiment", Prog. Theor. Exp. Phys. **4**, 043C01 (2015).

[88] S. Fukuda *et al.*, "Determination of solar neutrino oscillation parameters using 1496 days of Super-Kamiokande-I data", Physics Letters B **539**, 179187 (2002).

[89] M. B. Smy *et al.*, "Precise measurement of the solar neutrino day-night and seasonal variation in Super-Kamiokande-I", Phys. Rev. D **69**, 011104 (2004).

[90] S. Abe *et al.*, "Precision Measurement of Neutrino Oscillation Parameters with KamLAND", Phys. Rev. Lett. **100**, 221803 (2008).

[91] T. Araki *et al.*, "Experimental investigation of geologically produced antineutrinos with KamLAND", Nature **436**, 499-503 (2005).

[92] Daya Bay Collaboration, "A Precision Measurement of the Neutrino Mixing Angle θ_{13} using Reactor Antineutrinos at Daya Bay", BNL-77369-2006-IR, LBNL-62137, TUHEP-EX-06-003, arXiv:hep-ex/**0701029**

[93] F. P. An *et al.*, "A side-by-side comparison of Daya Bay antineutrino detectors", Nuclear Instruments and Methods in Physics Research Section A **685**, 7897 (2012).

[94] J. K. Ahn *et al.*, "RENO: An Experiment for Neutrino Oscillation Parameter $theta_{13}$ Using Reactor Neutrinos at Yonggwang", arXiv:1003.1391 (2010).

[95] F. Ardellier *et al.*, "Double Chooz, A Search for the Neutrino Mixing Angle θ_{13}", arXiv:hep-ex/**0606025** (2006).

[96] D. G. Michael *et al.*, "The magnetized steel and scintillator calorimeters of the MINOS experiment", Nuclear Instruments and Methods in Physics Research Section A **596**, 190228 (2008).

[97] Sacha E. Kopp, "The NuMI Neutrino Beam at Fermilab", arXiv:physics/**0508001** (2005).

[98] P. Adamson *et al.*, "Measurement of Neutrino Oscillations with the MINOS Detectors in the NuMI Beam", Phys. Rev. Lett. **101**, 131802 (2008).

[99] D. Ayres *et al.*, "NOvA Proposal to Build a 30 Kiloton Off-Axis Detector to Study Neutrino Oscillations in the Fermilab NuMI Beamline", arXiv:hep-ex/**0503053**.

[100] Ryan B. Patterson, "First Oscillation Results from NOvA', Fermilab JETP Seminar (2015).

[101] K. Abe *et al.*, "Physics potential of a long-baseline neutrino oscillation experiment using a J-PARC neutrino beam and Hyper-Kamiokande", Prog. Theor. Exp. Phys., 053C02 (2015).

[102] The IceCube-Pingu collaboration, "Letter of Intent: The Precision IceCube Next Generation Upgrade (PINGU)", arXiv:**1401.2046** (2014).

[103] Yu-Feng Li, Jun Cao, Yifang Wang, and Liang Zhan, "Unambiguous determination of the neutrino mass hierarchy using reactor neutrinos", Phys. Rev. D **88**, 013008 (2013).

[104] N. Agafonova *et al.*, "Evidence for appearance in the CNGS neutrino beam with the OPERA experiment", Phys. Rev. D **89**, 051102 (2014).

[105] R. Bailey *et al.*, "The CERN Neutrino beam to Gran Sasso (NGS)", CERN-SL/99-034(DI), INFN/AE-99/05.

[106] M. C. Gonzalez-Garcia, Michele Maltoni, Thomas Schwetz, "Updated fit to three neutrino mixing: status of leptonic CP violation", Journal of High Energy Physics **52**, 2014.

[107] http://www.nu-fit.org/

[108] R. Kanishka *et al.*, "Simulations study of muon response in the peripheral regions of the Iron Calorimeter detector at the India-based Neutrino Observatory", JINST **10**, P03011 (2015).

[109] Infolytica Corp., Electromagnetic field simulation software, http://www.infolytica.com/en/products/magnet/

[110] V. M. Datar *et al.*, "Development of glass resistive plate chambers for INO experiment", Nucl. Instrum. Meth. A **602** 744 (2009).

[111] J. A. Formaggio and G. P. Zeller, "From eV to EeV: Neutrino cross sections across energy scales", Rev. Mod. Phys. **84**, 1307 (2012).

[112] Takaaki Kajita, "Atmospheric Neutrinos", Advances in High Energy Physics **2012** 504715, (2012).

[113] M. Honda, T. Kajita, K. Kasahara, and S. Midorikawa, "Improvement of low energy atmospheric neutrino flux calculation using the JAM nuclear interaction model", Phys. Rev. D **83**, 123001 (2011).

[114] M. Honda, T. Kajita, K. Kasahara, S. Midorikawa, and T. Sanuki, "Calculation of atmospheric neutrino flux using the interaction model calibrated with atmospheric muon data", Phys. Rev. D **75**, 043006 (2007).

[115] G. Barr *et al.*, "A Three - dimensional calculation of atmospheric neutrinos", Phys. Rev. D **70** 023006 (2004).

[116] G. Battistoni, A. Ferrari, T. Montaruli, and P. Sala, "The FLUKA atmospheric neutrino flux calculation", Astropart. Phys. **19**, 269290 (2003).

[117] T. K. Gaisser and M. Honda, "Flux of atmospheric neutrinos", Annual Review of Nuclear and Particle Science **52**, 153-199 (2002).

[118] M. Sajjad Athar, M. Honda, T. Kajita, K. Kasahara, and S. Midorikawa, "Atmospheric neutrino flux at INO, South Pole and Pyhásalmi", Phys. Lett. B **718**, 13751380 (2013).

[119] M. Honda, M. Sajjad Athar, T. Kajita, K. Kasahara, and S. Midorikawa, "Atmospheric neutrino flux calculation using the NRLMSISE-00 atmospheric model", Phys. Rev. D **92**, 023004 (2015).

[120] K. A. Olive *et al.*, "The Review of Particle Physics", Chin. Phys. C **38**, 090001 (2014).

[121] http://www.hecr.tifr.res.in/samuel/html/vice.html

[122] Moon Moon Devi, "Enhancing ICAL Potential with hadrons, and development of multigap RPC", Ph.D. Thesis, Homi Bhabha National Institute (HBNI) (2015).

[123] D. Green, "Physics of Particle Detectors", Cambridge Monographs on Particle Physics, Nuclear Physics and Cosmology, (Cambridge University Press, 2000).

[124] D. Green, "Hadron calorimeter performance with a $PbWO_4$ EM compartment", FERMILAB-TM-1958 (1996), http://lss.fnal.gov/archive/test-tm/1000/fermilab-tm-1958.pdf.

[125] C. W. Fabjan, "Calorimetry in high energy physics", CERN-EP/85-54 (1985).

[126] K. Kleinknecht, "Particle detectors", Phys. Rept. **84**, 85 (1982).

[127] P. Schoessow *et.al.*, *Results from an iron-proportional tube calorimeter prototype*, NUMI-Note , MINOS Document 335-v1

[128] N. Y. Agafonova *et al.*, "MONOLITH: a massive magnetised iron detector for neutrino oscillation studies", Monolith Proposal, LNGS P26/2000, CERN/SPSC 2000-031, SPSC/M657 (2000).

[129] M. Ambrosio *et al.*, "The MONOLITH prototype", Nucl. Instrum. Meth. A **456**, 67 (2000).

[130] G. Bari *et al.*, "Analysis of the performance of the MONOLITH prototype", Nucl. Instrum. Meth. A **508**, 170 (2003).

[131] D. A. Petyt, "A study of parameter measurement in a long-baseline neutrino oscillation experiment", Ph.D. Thesis, University of Oxford, Preprint FERMILAB-THESIS-1998-66 (1998), http://www.physics.ox.ac.uk/neutrino/Petyt/Petyt.htm.

[132] J. S. Marshall, "A study of muon neutrino disappearance with the MINOS detectors and the NuMI neutrino beam", Ph.D. Thesis, University of Cambridge (2008).

[133] R. E. Kalman, "A new approach to linear filtering and prediction problems", J. Basic Eng. **82**, 35 (1960).

[134] E. J. Wolin and L. L. Ho, "Covariance matrices for track fitting with the Kalman filter", Nucl. Instrum. Meth. A **329**, 493 (1993).

[135] Kolahal Bhattacharya, Arnab K Pal, Gobinda Majumder and Naba K Mondal, "Error propagation of the track model and track fitting strategy for the iron calorimeter detector in India-based neutrino observatory", Computer Physics Communications **185**, 3259-3268 (2014).

[136] E W Otten and C Weinheimer, "Neutrino mass limit from tritium β decay", Rep. Prog. Phys. **71** 086201 (2008).

[137] C. Weinheimer and K. Zuber, "Neutrino masses" Ann. Phys. **525**565575 (2013).

[138] A. Osipowicz *et al.*, "KATRIN: a next generation tritium beta decay experiment with sub-eV sensitivity for the electron neutrino mass (Letter of Intent)", arXiv:hep-ex/0109033 (2001).

[139] J. Angrik *et al.*, "KATRIN Design Report 2004", FZKA **7090** (2005).

[140] K. Alfonso *et al.*, "Search for Neutrinoless Double-Beta Decay of ^{130}Te with CUORE-0", Phys. Rev. Lett. **115**, 102502 (2015).

[141] K. -H. Ackermann *et al.*, "The GERDA experiment for the search of $0\nu\beta\beta$ decay in ^{76}Ge", Eur. Phys. J. C **73**, 2330 (2013).

[142] M. Agostini *et al.*, "Results on Neutrinoless Double-β Decay of ^{76}Ge from Phase I of the GERDA Experiment", Phys. Rev. Lett. **111**, 122503 (2013).

[143] A. Gando et al., "Measurement of the double-β decay half-life of ^{136}Xe with the KamLAND-Zen experiment", Phys. Rev. C **85**, 045504 (2012).

[144] Vandana Nanal, "Search for neutrinoless double beta decay in ^{124}Sn", EPJ Web of Conferences **66**, 08005 (2014).

[145] Julien Lesgourgues and Sergio Pastor, "Massive neutrinos and cosmology", Physics Reports **429**, 307379 (2006).

[146] Julien Lesgourgues and Sergio Pastor, "Neutrino cosmology and Planck", New Journal of Physics **16**, 065002 (2014).

[147] K. Abe *et al.*, "Measurements of neutrino oscillation in appearance and disappearance channels by the T2K experiment with 6.6×10^{20} protons on target", Phys. Rev. D **91**, 072010 (2015).

[148] A. M. Dziewonski and D. L. Anderson, "Preliminary reference Earth model (PREM)", Phys. Earth Plan. Int. **25**, 297 (1981).

[149] A. de Gouvea, J. Jenkins and B. Kayser, "Neutrino mass hierarchy, vacuum oscillations and vanishing $|U_{e3}|$", Phys. Rev. D **71**, 113009 (2005).

[150] H. Nunokawa, S. J. Parke and R. Zukanovich Funchal, "Another possible way to determine the neutrino mass hierarchy", Phys. Rev. D **72**, 013009 (2005).

[151] F. P. An *et al.*, "Spectral Measurement of Electron Antineutrino Oscillation Amplitude and Frequency at Daya Bay", Phys. Rev. Lett. **112**, 061801 (2014).

[152] D. V. Forero, M. Tórtola, and J. W. F. Valle, "Neutrino oscillations refitted", Phys. Rev. D **90**, 093006 (2014).

[153] M. C. Gonzalez-Garcia, Michele Maltoni, Jordi Salvado and Thomas Schwetz, "Global fit to three neutrino mixing: critical look at present precision", Journal of High Energy Physics **12**, 123 (2012).

[154] F. Capozzi, G. L. Fogli, E. Lisi, A. Marrone, D. Montanino, and A. Palazzo, "Status of three-neutrino oscillation parameters, circa 2013", Phys. Rev. D **89**, 093018 (2014).

[155] R. J. Barlow, "Statistics: A Guide to the Use of Statistical Methods in the Physical Sciences", Wiley publications.